Parametric Forcing of Confined and Stratified Flows

by

Jason Yalim

A Dissertation Presented in Partial Fulfillment
of the Requirements for the Degree
Doctor of Philosophy

Approved April 2019 by the
Graduate Supervisory Committee:

Bruno D. Welfert, Co-Chair
Juan M. Lopez, Co-Chair
Donald Jones
Rodrigo Platte
Wenbo Tang

ARIZONA STATE UNIVERSITY

May 2019

ABSTRACT

A continuously and stably stratified fluid contained in a square cavity subjected to harmonic body forcing is studied numerically by solving the Navier–Stokes equations under the Boussinesq approximation. Complex dynamics are observed near the onset of instability of the basic state, which is a flow configuration that is always an exact analytical solution of the governing equations. The instability of the basic state to perturbations is first studied with linear stability analysis (Floquet analysis), revealing a multitude of intersecting synchronous and subharmonic resonance tongues in parameter space. A modal reduction method for determining the locus of basic state instability is also shown, greatly simplifying the computational overhead normally required by a Floquet study. Then, a study of the nonlinear governing equations determines the criticality of the basic state's instability, and ultimately characterizes the dynamics of the lowest order spatial mode by the three discovered codimension-two bifurcation points within the resonance tongue. The rich dynamics include a homoclinic doubling cascade that resembles the logistic map and a multitude of gluing bifurcations.

The numerical techniques and methodologies are first demonstrated on a homogeneous fluid contained within a three-dimensional lid-driven cavity. The edge state technique and linear stability analysis through Arnoldi iteration are used to resolve the complex dynamics of the canonical shear-driven benchmark problem. The techniques here lead to a dynamical description of an instability mechanism, and the work serves as a basis for the remainder of the dissertation.

DEDICATION

To my friends and family.

ACKNOWLEDGMENTS

Thank you to Arizona State University, for providing me the opportunity to obtain a PhD and teach.

Thank you to my co-chairs, Professors Bruno Welfert and Juan Lopez, for guiding me through the PhD process. I wouldn't have had this opportunity without the two of you, and together you make one hell of a mathematical and scientific powerhouse.

Thank you to my committee, Professors Donald Jones, Rodrigo Platte, and Wenbo Tang, for all their support and guidance. Professor Donald Jones provided me with one of my first research projects: modeling the two-dimensional shallow water equations with openMPI and Fortran 90, an experience which helped me realize my ideal career path. Professor Rodrigo Platte regularly allowed me to be his Teaching Assistant for the Graduate computational methods course here, an honor I have not taken lightly. Professor Wenbo Tang was always willing to humor my questions on partial differential equations and linear algebra and provide deep insight.

Thank you to Doctor Renate Mittelmann and her staff, for allowing me to compute on all the machines I did. While I joke that the machines in ECA 221 and 216 are my children, Doctor Renate Mittelmann and her staff kept them and all of the servers that I asked for in great health.

Thank you to Doctor Gil Speyer and Research Computing for providing the additional computing resources I needed. At the time of this writing I have about thirty terabytes of storage on Agave and over twelve hundred month long jobs running on the Open Science Grid, and the contents of my `.project` and `.plan` files are elucidating:

`Flip all the bits` (ノ°□°)ノ ⌒_└┘_

My research would not be the same without these resources, and I look forward to our future collaboration.

Thank you again to ASU for the Teaching Associate support. It has been an incredible experience being able give back to students and I will always appreciate Doctor Katie Kolossa for her trust and guidance.

Thank you to Ke Wu for providing the original Navier-Stokes solving software. I am happy to have inherited your work, but if I go bald in the near future I am blaming it on not starting completely from scratch instead. Thank you to Paloma Gutierrez Castillo for all her support and discussions and most importantly helping me tease Ke.

Thank you to my Grandfather, Bulent Yalim, for sharing his optimistic curiousity and humorous wisdom. His saying, "humor is the pillar of the sky", has carried me through some of the more onerous times.

Thank you to Marcus Mccaw and Keri McKiernan, you both were instrumental in guiding my career path all those years ago, and had seemingly bottomless patience when answering my questions on mathematics and physics. My life and career choices would have been completely different without the both of you.

Finally, thank you to all my friends and family who have supported me throughout this experience. Special shoutouts to Alex Fryer, Justin Greene, Tom Hart, Dakota and Michael Hilton, Andrew Lawson, Courtney Robinson, Laura Yalim, and of course my wonderful and hardworking mother Zeynep Yalim.

You are all the best.

TABLE OF CONTENTS

CHAPTER Page

CHAPTER Page

LIST OF TABLES

LIST OF FIGURES

Figure Page

Figure Page

Figure Page

Figure Page

Figure Page

Chapter 1

INTRODUCTION

Internal gravity waves play a fundamental role in many fluid domains. In geophysics, the mixing or redistribution of energy or momentum in the ocean and atmosphere are often attributed to the dynamics of internal gravity waves [108, 96, 49, 22]. While internal waves do not play a dominant role in weather or climate modeling, meteorological models without them fail to predict atmospheric wind speeds and temperatures, and internal wave breaking in the atmosphere can lead to clear-air turbulence [96]. Also, the Lee waves generated in the wake of a stratified fluid moving over an obstacle and the valley winds formed by the solar heating of a valley blanketed by a stratified atmosphere are additional examples of internal wave phenomena [23].

Internal waves may be generated by locally forcing a stratified fluid, and in particular by oscillating cylinders, spheres, slats, flaps, paddles, or camshafts within a stratified fluid [97, 36, 69, 71, 84, 95, 22]. Local forcing usually is associated with internal gravity wavebeams emanating from the local interfaces, which has spawned a lot of theoretical interest [22].

Internal gravity waves may also be generated by globally forcing a stratified fluid, usually through the harmonic oscillation of the fluid's container [72, 7]. However, despite the fundamental importance of these responses to understanding resonances and internal wave breaking, the internal waves obtained in this fashion are underrepresented in the literature.

Hoping to better understand wave dynamics in stratified fluids, Yih studied a variety of geometries with different stratifications and was one of the first to study the parametric instability of a continuously stratified fluid [114]. He investigated the

dynamics a laterally unbounded and continuously stratified inviscid fluid subjected to vertical vibration and showed that the resultant inviscid Mathieu equations governed the instability of the flow. This essentially extended what Benjamin and Ursell had shown for the homogeneous inviscid problem [8], who were motivated by understanding the parametric instabilities of interfacial waves that were first studied by Faraday [28].

After first considering Faraday's interfacial waves, Thorpe extended Yih's work by analytically determining the inviscid eigenmodes for a fully confined and continuously stratified fluid to third order [97]. Thorpe also conducted an experiment of a linearly stratified fluid, locally forcing the system with paddles, and was able to resonate viscous modes of a certain parity near the predicted inviscid frequencies. Using pumps at the top of a salt stratified tank of fluid, Keunecke was able to validate additional modes, such as the 1:1 (one half-wavelength horizontally and vertically) and the 2:2 (two half-wavelengths horizontally and vertically) [40].

Interested in understanding the mechanisms of internal gravity wave energy transfer, McEwan [69] (and later with Mander and Smith [71]) affirmed the existence of localized parametric instability in McEwan's experiments of continuously and stably stratified fluids. Further motivated by their understanding of the role that parametric instabilities play in the dynamical aspects of the ocean and atmosphere, McEwan and Robinson studied the parametric instability of internal gravity waves for a stably and continuously stratified fluid in a confined cylinder geometry subjected to either horizontal harmonic motion or swinging the apparatus as a fluid filled pendulum bob, ultimately validating the previously proposed parametric instability theory [72].

Mostly interested in understanding the instability mechanism of wave-breaking modes Bouruet-Aubertot, Sommeria, and Staquet [13] performed one of the first numerical investigations of continuously and stably stratified fluid, by solving the

two-dimensional Boussinesq-Navier-Stokes equations with Thorpe's eigenmodes [97] as initial conditions. The experiment of Benielli and Sommeria [7] was one of the first that properly globally forced a rectangular container of a continuous and stably stratified fluid. In the first half of their study [7] considered the parametric instability of Faraday's interfacial waves, but in the second half focused on the parametric instabilities of internal gravity waves. Within small forcing frequency intervals, they observed the basic state lose stability via parametric resonance to subharmonic modes strongly resembling Thorpe's two-dimensional inviscid eigenmodes [97]. At larger amplitudes they observed the modes succumbing to internal wave breaking, generating secondary waves which were compared to the previous numerical study [13]. They also observed intermittent behavior as the flow violently transitioned between different harmonics of the system, intermittently relaminarizing into a $2m$:m mode (two m half-wavelengths horizontally and m half-wavelengths vertically) between drifts.

This dissertation is concerned with expanding the theory of internal gravity waves for stably and continuously stratified fluids confined within square cavities. By harmonically vertically forcing the square cavity, wave beams are not produced, and the dynamics of initial instabilities primarily involve parametrically resonated viscous and nonlinear modes resembling the inviscid eigenmodes of Thorpe [97].

Further, this investigation is carried out with heat instead of salt as a stratifying agent, counter to the preceding experiments [97, 69, 7]. By using salt instead of heat, the initial stratification is transient, which makes a dynamical analysis of the flow's behavior overly difficult. Stratification with salt (mass concentration) requires normal no-flux conditions for the top and bottom walls of the container which results in the eventual homogenization of the fluid on a timescale related to the Schmidt number (ratio of viscous and mass concentration diffusivities). Thus, any result without a homogenized density field is transient. By using heat with constant temperatures on the

endwalls, Dirichlet conditions are imposed, allowing for an explicit nonhomogeneous basic state.

1.1 Nondimensional Governing Equations for Square Confined Flows

Consider a stably stratified incompressible fluid confined in a square cavity subject to an arbitrary periodic forcing. The square has sides of length L, and the origin is defined at the square's center with nondimensionalized horizontal coordinate x and vertical coordinate z both defined in the interval $[-0.5, 0.5]$. These Cartesian coordinates may be expressed in tensor format as $\boldsymbol{x} = x\hat{\boldsymbol{e}}_x + z\hat{\boldsymbol{e}}_z$, where $\hat{\boldsymbol{e}}_x$ and $\hat{\boldsymbol{e}}_z$ are unit vectors in the horizontal and vertical directions respectively. Homogeneous Dirichlet (no-slip) boundary conditions will be assumed for the velocity $\boldsymbol{u} = u\hat{\boldsymbol{e}}_x + w\hat{\boldsymbol{e}}_z$, as well as homogeneous Neumann (no-flux) boundary conditions for the temperature T on the side-walls and conducting (Dirichlet) conditions for the top walls such that stable linear stratification $T(x, z) = z$ is a valid initial condition.

The above quantities of temperature T, velocity $\boldsymbol{u}$, and space $\boldsymbol{x}$ have all been nondimensionalized. For completeness, the nondimensional Navier–Stokes–Boussineseq governing equations will be derived. Let the presence of a star in the superscript of a variable denote a dimensional quantity to be nondimensionalized, e.g. $\boldsymbol{u}^*$ refers to the velocity vector measured in some arbitrary S.I. units (such as meters per second) that will eventually be expressed as $\boldsymbol{u}$. The dimensional momentum equation is defined as,

$$\rho\left(\frac{\partial \boldsymbol{u}^*}{\partial t^*} + (\boldsymbol{u}^* \cdot \nabla^*)\boldsymbol{u}^*\right) = -\nabla^* p^* + \mu \nabla^{2^*} \boldsymbol{u}^* - \rho g \boldsymbol{f}(t^*), \tag{1.1}$$

with time t^*, density ρ, velocity vector $\boldsymbol{u}^*$, pressure p^*, dynamic viscosity μ, and $\boldsymbol{f}(t^*) = F(\Omega t^*)\hat{\boldsymbol{e}}_x + G(\Omega t^*)\hat{\boldsymbol{e}}_z$ where F and G are sinusoidal forcing terms that modulate gravity g at respective angular frequency Ω. The remaining dimensional equations

are the continuity equation,

$$\nabla^* \cdot \boldsymbol{u}^* = 0, \tag{1.2}$$

and temperature T^* equation,

$$\frac{\partial T^*}{\partial t^*} + (\boldsymbol{u}^* \cdot \nabla^*)T^* = \kappa {\nabla^2}^* T^*, \tag{1.3}$$

where κ is the thermal diffusivity coefficient. Note that the starred 'del' operator is also dimensional, since, $\nabla^* = \frac{\partial}{\partial x^*}\hat{\boldsymbol{e}}_x + \frac{\partial}{\partial z^*}\hat{\boldsymbol{e}}_z$.

Let σ be a characteristic length scale of the system and τ be a characteristic time scale. Then the general nondimensional space and time coordinates are,

$$x = \frac{x^*}{\sigma}, \qquad z = \frac{z^*}{\sigma}, \qquad t = \frac{t^*}{\tau}, \tag{1.4}$$

which implies,

$$\boldsymbol{u}^* = \frac{\sigma}{\tau}\boldsymbol{u}, \qquad \nabla^* = \frac{1}{\sigma}\nabla. \tag{1.5}$$

Applying these to the momentum equation (1.1) and dividing both sides by σ/τ^2 yields

$$\rho\left(\frac{\partial \boldsymbol{u}}{\partial t} + (\boldsymbol{u}\cdot\nabla)\boldsymbol{u}\right) = -\frac{\tau^2}{\sigma^2}\nabla p^* + \tau\frac{\mu}{\sigma^2}\nabla^2\boldsymbol{u} - \rho\tau^2\frac{g}{\sigma^2}\boldsymbol{f}(\tau t). \tag{1.6}$$

Recalling the Boussinesq approximation [46] with reference density ρ_0, thermal coefficient of volume expansion β, and bottom wall reference temperature ${T_0}^*$,

$$\rho = \rho_0(1 - \beta[T^* - {T_0}^*]), \tag{1.7}$$

with the condition $|\beta(T^* - T_0^*)| << 1$, equation (1.7) applied to equation (1.6) in the usual manner and dividing by ρ_0 results in,

$$\frac{\partial \boldsymbol{u}}{\partial t} + (\boldsymbol{u}\cdot\nabla)\boldsymbol{u} = -\frac{\tau^2}{\rho_0\sigma^2}\nabla p^* + \frac{\tau}{\tau_\nu}\nabla^2\boldsymbol{u} - \frac{\tau^2}{\tau_g^2}(1 - \beta[T^* - {T_0}^*])\boldsymbol{f}(\tau t), \tag{1.8}$$

where $\tau_g = \sqrt{\sigma/g}$ is the *free-fall* timescale, $\tau_\nu = \sigma^2/\nu$ is the *viscous* timescale, and $\nu = \mu/\rho_0$ is the kinematic viscosity. The nondimensional temperature may be defined

as,

$$T = \frac{T^* - T_0^*}{\Delta T} + z_0 = \frac{T^* - T_0^*}{T_1^* - T_0^*} - 0.5, \tag{1.9}$$

where T_1^* is the dimensional temperature at the top wall, and z_0 is the nondimensional position of the bottom wall. Allowing $p^* = p\rho_0\sigma^2/\tau^2$, $\boldsymbol{x} = x\hat{\boldsymbol{e}}_x + z\hat{\boldsymbol{e}}_z$, and grouping all of the gradient terms results in,

$$\begin{aligned} \frac{\partial \boldsymbol{u}}{\partial t} + (\boldsymbol{u}\cdot\nabla)\boldsymbol{u} = &-\nabla\left(p + \frac{\tau^2}{\tau_g^2}[1+\beta\Delta T z_0]\boldsymbol{f}(\tau t)\cdot\boldsymbol{x}\right) \\ &+ \frac{\tau}{\tau_\nu}\nabla^2\boldsymbol{u} \\ &+ \frac{\beta\Delta T\tau^2}{\tau_g^2}\boldsymbol{f}(\tau t)T, \end{aligned} \tag{1.10}$$

which may be simplified by letting P represent the gradient terms and also by simultaneously defining the *Archmedian* timescale $\tau_A = 1/N = \sqrt{\tau_g/(\beta\Delta T)}$ (note that N is the buoyancy or Brunt–Väisälä frequency),

$$\frac{\partial \boldsymbol{u}}{\partial t} + (\boldsymbol{u}\cdot\nabla)\boldsymbol{u} = -\nabla P + \frac{\tau}{\tau_\nu}\nabla^2\boldsymbol{u} + \frac{\tau^2}{\tau_A^2}\boldsymbol{f}(\tau t)T. \tag{1.11}$$

Likewise, nondimensionalizing the continuity equation (1.2),

$$\nabla\cdot\boldsymbol{u} = 0, \tag{1.12}$$

and since $T^* = \Delta T(T + z_0) + {T_0}^*$, equation (1.3) becomes,

$$\frac{\partial T}{\partial t} + (\boldsymbol{u}\cdot\nabla)T = \frac{\tau}{\tau_\kappa}\nabla^2 T, \tag{1.13}$$

where $\tau_\kappa = \sigma^2/\kappa$ is the *thermal diffusivity* timescale. The final timescale in the nondimensionalization of the momentum equation, the *inertial* timescale $\tau_i = 1/\Omega$, is contained in the forcing, here generalized as,

$$\boldsymbol{f}(\tau t) = \alpha_x \sin\left(\frac{\tau}{\tau_i}t\right)\hat{\boldsymbol{e}}_x + \left[1 + \alpha_z\cos\left(\frac{\tau}{\tau_i}t\right)\right]\hat{\boldsymbol{e}}_z, \tag{1.14}$$

Time scales	
Viscous time	$\tau_\nu = \sigma^2/\nu$
Archimedian time	$\tau_A = \tau_\nu/N = \sqrt{\sigma/(\beta\Delta T g)} = 1/N$
Inertial time	$\tau_i = 1/\Omega = \ell/U$
Thermal Diffusion time	$\tau_\kappa = \sigma^2/\kappa$
Free Fall time	$\tau_g = \sqrt{\sigma/g}$

Table 1.1: The physical timescales of the system.

Nondimensional Parameters	
Brunt–Väisälä Number	$R_N = \tau_\nu/\tau_A$
Grashof Number	$Gr = (\tau_\nu/\tau_A)^2 = {R_N}^2$
Prandtl Number	$Pr = \tau_\kappa/\tau_\nu = \nu/\kappa$
Rayleigh Number	$Ra = GrPr = \tau_\nu\tau_\kappa/\tau_A^2$
Reynolds Number	$Re = \tau_\nu/\tau_i = \omega\sigma^2/\nu$
Nondim. Forcing Amplitude	$\alpha = (\tau_g/\tau_i)^2 = \ell\Omega^2/g$
Nondim. Forcing Frequency	$\omega = \tau_A/\tau_i = \Omega/N$
Richardson Number	$Ri = (\tau_i/\tau_A)^2 = (1/\omega)^2$
Froude Number	$Fr = \tau_g/\tau_i = \omega\sqrt{\sigma/g}$
Galilei Number	$Ga = (\tau_\nu/\tau_g)^2 = \sigma^3 g/\nu^2$
Amplitude Aspect Ratio	$\varepsilon = \ell/\sigma$

Table 1.2: The various nondimensional parameters resulting from ratios of introduced physical timescales and length scales.

where $\alpha_x = \ell_x \Omega^2/g$ and $\alpha_z = \ell_z \Omega^2/g$ are nondimensional forcing amplitudes that are related to the square of the Froude number. Note as well that the forcing amplitudes are essentially ratios of the inertial and free-fall timescales squared.

The various physical timescales of the system are summarized in table 1.1. It was shown how these are coefficients of physical terms in the governing equations that are balanced out by a choice of timescale (e.g. $\tau = \tau_A$). The ratios of these timescales lead to many different nondimensional parameters which ultimately become the coefficients of the governing equations, and these are summarized in table 1.2.

In practice, τ and σ are not left in the general form presented above. Usually one will chose a length scale (e.g. the side length of the square L) and a timescale (e.g. the Archmedian timescale τ_A). $\sigma = L$ and $\tau = \tau_A$ were chosen for nondimensionalization in chapters 3 and 5 for the study of the stably stratified fluid confined square cavity under vertical harmonic motion, which results in the following governing equations,

$$\begin{aligned} &\frac{\partial \boldsymbol{u}}{\partial t} + \boldsymbol{u} \cdot \nabla \boldsymbol{u} = -\nabla P + \frac{1}{R_N} \nabla^2 \boldsymbol{u} + [1 + \alpha \cos(\omega t)] T \boldsymbol{e}_z, \quad \nabla \cdot \boldsymbol{u} = 0, \\ &\frac{\partial T}{\partial t} + \boldsymbol{u} \cdot \nabla T = \frac{1}{Pr R_N} \nabla^2 T. \end{aligned} \tag{1.15}$$

The governing equations 1.15 are fully characterized by the four parameters ω, α, R_N, and Pr, forming a four-dimensional parameter space.

1.2 Numerical Methodology

1.2.1 Spatial Discretization

For all of the problems investigated in this dissertation, a collocated Chebyshev spatial discretization was used such that the unscaled domain $x \in [-1, 1]$ would be discretized by a Chebyshev polynomial of degree M into $M + 1$ points:

$$x_k = \cos\left(\frac{k\pi}{M}\right),$$

where $k \in [0, M] \subset \mathbb{Z}$ is an integer index. The barycentric representation was employed [9], resulting in weights $w_k = (-1)^k$ with $w_0 = 0.5$ and $w_M = 0.5(-1)^M$. To further improve numerical stability, the explicit first derivative operator D^1 was computed in the manner specified by Bayliss et. al [6] and Trefethen [99], constructing D^1 with its anti-centrosymmetry property and then correcting the diagonal with the matrix product from its nullspace vector of all ones (the so called *negative sum trick*). Explicitly, this is the same as what was given by [4]:

$$D^1_{jk} = \begin{cases} \frac{w_k}{w_j} \frac{1}{x_j - x_k} & \text{if } j \neq k, \\ \sum_{i=0, i\neq j}^{M} \frac{w_i}{w_j} \frac{1}{x_j - x_i} & \text{if } j = k. \end{cases}$$

It is also important to reduce numerical error by constructing the second derivative operator D^2 in a similar fashion [105, 4, 104, 16] (see [4] for a discussion, but note that their off-diagonal elements are incorrect and require a factor of two, or see the errata to the first edition of [16, pg. 91]):

$$D^2_{jk} = \begin{cases} \frac{1}{x_j - x_k} \left(\frac{w_j}{w_k} D^1_{kk} - D^1_{jk} \right) & \text{if } j \neq k, \\ 2 \left((D^1_{jj})^2 + \sum_{i=0, i\neq j}^{M} D^1_{ji} \frac{1}{x_j - x_i} \right) & \text{if } j = k. \end{cases}$$

Note that when building the finite operators, one may also take advantage of the centrosymmetry of the D^2 matrix. It is also common to construct D^2 by matrix multiplying D^1 with D^1 (Peyret [81, §3.3.5]), but centrosymmetry should be enforced and the diagonal corrected with the negative sum trick. To enforce centrosymmetry, one may overwrite D^2:

$$D^2 = \frac{1}{2} \left(D^2 + J D^2 J \right),$$

where $J \in \mathbb{R}^{M+1, M+1}$ is the *exchange* matrix with ones on the counter-diagonal and zeros elsewhere.

1.2.2 Numerical Solver

For the following subsection, consider the following governing equation for the velocity $\boldsymbol{u}$, pressure P, temperature T, forcing associated with gravity $\boldsymbol{f}$, and additional body forcing $\boldsymbol{F}$ for a three dimensional stratified flow of an incompressible fluid:

$$\begin{aligned}
\partial_t \boldsymbol{u} + (\boldsymbol{u}\cdot\nabla)\boldsymbol{u} &= -\nabla P + \frac{\tau}{\tau_\nu}\nabla^2\boldsymbol{u} + \left(\frac{\tau}{\tau_A}\right)^2 T\boldsymbol{f} + \left(\frac{\tau}{\tau_F}\right)^2 \boldsymbol{F},\\
\partial_t T + (\boldsymbol{u}\cdot\nabla)\boldsymbol{u} &= \frac{\tau}{\tau_\kappa}\nabla^2 T,\\
\nabla\cdot\boldsymbol{u} &= 0
\end{aligned}$$

where τ is the choice of timescale to nondimensionalize the system and τ_F is a timescale associated with the additional body forcing. Assume the boundary conditions for the velocity and temperature are Robin conditions. Choosing the viscous timescale $\tau = \tau_\nu$ results in the nondimensionalized momentum equation, temperature transport equation, and continuity equation:

$$\begin{aligned}
\partial_t \boldsymbol{u} + (\boldsymbol{u}\cdot\nabla)\boldsymbol{u} &= -\nabla P + \nabla^2\boldsymbol{u} + GrT\boldsymbol{f} + \gamma\boldsymbol{F},\\
\partial_t T + (\boldsymbol{u}\cdot\nabla)\boldsymbol{u} &= \frac{1}{Pr}\nabla^2 T,\\
\nabla\cdot\boldsymbol{u} &= 0
\end{aligned} \tag{1.16}$$

where γ is the nondimensional parameter associated with the additional body forcing and the chosen viscous timescale.

The system (1.16) is then discretized using a spectral-collocation method in all spatial directions. The velocity, temperature, and pressure are approximated by Chebyshev polynomials of degree M written in barycentric form with weights $w_0 = 0.5$, $w_k = (-1)^k$ for $k \in [1, M-1] \subset \mathbb{Z}$, and $w_M = 0.5(-1)^M$, associated to the Chebyshev–Gauss–Lobatto grid. Spatial nodes are given by $x_k = \Gamma\cos(k\pi/M)/2$, where Γ is the appropriate aspect ratio of the system and the $1/2$ comes from rescaling the Chebyshev domain from $[-1, 1]$ to unit length $[-0.5, 0.5]$. Spatial differen-

tiation is performed via direct matrix-matrix or matrix-vector multiplication by the pseudospectral differentiation matrix (common to all three directions). These matrices are computed explicitly and have skew-centrosymmetry enforced and are diagonal corrected [99, 14, 81].

The fractional-step improved projection method of [35] as extended for thermal convection in cylindrical geometries by [74] is used to integrate in time. It is based on a linearly implicit and stiffly stable, second-order accurate scheme [102, 39] utilizing a backward differentiation formula for the time derivative with implicit treatment for the linear terms and explicit Adams–Bashforth extrapolation for the nonlinear convective terms (AB2/BDF2). (Note that Peyret refers to this temporal discretization as AB/BDI2–see equation (4.51) in [81].) In the predictor stage of the fractional step method a discretized Helmholtz equation (Sylvester equation) is solved for the pressure field with Neumann boundary conditions consistent with the governing equations applied at the walls. The corrector stage then projects the resulting predicted velocity field onto the space of (discretely) divergence-free polynomials via a Stokes problem, which is also handled by solving a Helmholtz equation for the corrected pressure, albeit with homogeneous Neumann boundary conditions. Further details may be found in [35, 89]. The applied scheme was first validated on a homogeneous (unstratified) three dimensional lid-driven cavity flow [60], and later applied to two-dimensional stratified lid-driven cavity flow [107], as well as modified for a linear stability analysis of the instabilities of a basic state associated with the flow in a stratified cavity subject to harmonic gravity modulation [109].

Below is a general outline of the method. For problems that do not have stratification, the temperature field T may be ignored without loss of generality along with the forcing term $\boldsymbol{f}$ that is associated with it. Likewise the term $\boldsymbol{F}$ is only included for additional body forces and may be neglected in their absence. Let $NL(\boldsymbol{u})$ repre-

sent the nonlinear (convective) terms of the momentum equation and $NL(\boldsymbol{u}, T)$ the nonlinear terms of the temperature transport equation. Likewise, let $L(\boldsymbol{u})$ and $L(T)$ represent the linear (viscous) terms from the momentum and temperature transport equations as well. Note that only the momentum linear terms are computed and only on the boundary (required for the preliminary pressure's boundary conditions). Further, the momentum linear term is expressed with the vector calculus identity,

$$L(\boldsymbol{u}) = \nabla^2 \boldsymbol{u} = \nabla(\nabla \cdot \boldsymbol{u}) - \nabla \times \nabla \times \boldsymbol{u},$$

which simplifies due to incompressibility and is preferred for numerical stability [82, 39]. Finally, superscripts of the velocity $\boldsymbol{u}$, pressure P, T, $\boldsymbol{f}$, and $\boldsymbol{F}$ denote time indexing (e.g. $\boldsymbol{u}^n$ is the velocity at time $t_n = t_0 + nh$), and let h be the timestep:

Step 1: Compute implicitly T^{n+1} from the temperature equation

$$\left(\nabla^2 - \frac{3Pr}{2h}\right) T^{n+1} = Pr\left(2NL(\boldsymbol{u}^n, T^n) - NL(\boldsymbol{u}^{n-1}, T^{n-1}) - \frac{4T^n - T^{n-1}}{2h}\right),$$

then enforce the boundary conditions for T^{n+1}.

Step 2: Compute the preliminary pressure $P^\star$ by solving Poisson equation (obtained by taking the divergence of the momentum equation):

$$\nabla^2 P^\star = \nabla \cdot \left(-2NL(\boldsymbol{u}^n) + NL(\boldsymbol{u}^{n-1}) + GrT^{n+1}\boldsymbol{f}^{n+1} + \gamma \boldsymbol{F}^{n+1}\right),$$

then enforce Neumann boundary conditions:

$$\frac{\partial P^\star}{\partial \hat{n}} = \boldsymbol{n} \cdot \Bigg(\frac{3\boldsymbol{u}^{n+1} - 4\boldsymbol{u}^n + \boldsymbol{u}^{n-1}}{2h} - 2NL(\boldsymbol{u}^n) + NL(\boldsymbol{u}^{n-1}) + 2L(\boldsymbol{u}^n) - L(\boldsymbol{u}^{n-1}) + GrT^{n+1}\boldsymbol{f}^{n+1} + \gamma \boldsymbol{F}^{n+1} \Bigg),$$

where $\hat{n}$ is the normal unit vector along the relevant boundary.

Step 3: Implicitly predict the preliminary velocity field $\boldsymbol{u}^\star$ by solving the Helmholtz equation:

$$\left(\nabla^2 - \frac{3}{2h}\right)\boldsymbol{u}^\star = 2NL(\boldsymbol{u}^n) - NL(\boldsymbol{u}^{n-1}) + \nabla P^\star - GrT^{n+1}\boldsymbol{f}^{n+1} - \gamma \boldsymbol{F}^{n+1} - \frac{4\boldsymbol{u}^n - \boldsymbol{u}^{n-1}}{2h},$$

then enforce boundary conditions.

Step 4a: Correction for $\boldsymbol{u}^{n+1}$, P^{n+1} involves solving the following Darcy problem:

$$\frac{3}{2h}(\boldsymbol{u}^{n+1} - \boldsymbol{u}^\star) = -\nabla(P^{n+1} - P^\star).$$

In the first stage, define the intermediate variable $\phi = \frac{2h}{3}(P^{n+1} - P^*)$, take divergence of above with definition of ϕ to obtain Poisson equation:

$$\nabla^2 \phi = \nabla \cdot \boldsymbol{u}^\star,$$

and enforce pure Neumann boundary conditions for ϕ. Note $\nabla \cdot \boldsymbol{u}^{n+1} = 0$ by the continuity equation (and is being enforced).

Step 4b: Stage 2 correction for P^{n+1} and $\boldsymbol{u}^{n+1}$,

$$P^{n+1} = P^\star + \frac{3}{2h}\phi$$
$$\boldsymbol{u}^{n+1} = \boldsymbol{u}^\star - \nabla\phi.$$

The implicit equations are in general inhomogeneous Helmholtz equations of field $v \in \mathbb{R}^n$ with scalar ξ,

$$(\nabla^2 + \xi)v = f$$

which are solved using diagonalization, and upon discretization the equations become the Sylvester equations. Special care was taken to solve the Sylvester equation, as is detailed in the next section. Note that the diagonalization only needs to be computed initially rather than every timestep.

Solving the Sylvester equation

Without loss of generality, the Sylvester equation for a two dimensional field of $(x, z) \in \mathbb{R}^2$ will be considered here (see [81] for additional details, as well as a three dimensional description). In two dimensions, the Sylvester equation is an implicit matrix equation of the form,

$$AX + XB = C, \tag{1.17}$$

where $A \in \mathbb{R}^{m\times m}$, $B \in \mathbb{R}^{n\times n}$, and $X, C \in \mathbb{R}^{m\times n}$. X is a set of unknowns and is to be solved for. When discretizing the Helmholtz equation pseudospectrally with the barycentric Chebyshev–Gauss–Lobatto formulation, the second derivative operators $\partial_{\star\star}$ become finite linear operators $D_{\star\star}$, and one obtains the Sylvester system (in two dimensions x and z):

$$\begin{aligned}
\nabla^2 v + \xi v &= f, \\
D_{xx}V + VD_{zz} + \xi V &= F, \\
P_{xx}\Lambda_{xx}P_{xx}^{-1}V + VP_{zz}\Lambda_{zz}P_{zz}^{-1} + \xi V &= F, \\
\Lambda_{xx}P_{xx}^{-1}VP_{zz} + P_{xx}^{-1}VP_{zz}\Lambda_{zz} + \xi P_{xx}^{-1}VP_{zz} &= P_{xx}^{-1}FP_{zz}, \\
\Lambda_{xx}Y + Y\Lambda_{zz} + \xi Y &= G,
\end{aligned} \tag{1.18}$$

where $Y = P_{xx}^{-1}VP_{zz}$, $G = P_{xx}^{-1}FP_{zz}$, and the $P_{\star\star}$ and diagonal $\Lambda_{\star\star}$ matrices are the eigenspectrum of the specified second order operator $D_{\star\star}$ (with boundary conditions applied). This technique is well-documented in the literature, even specifically for incompressible Navier-Stokes solvers (full treatment for two-dimensions and three-dimensions described in [81, §3.7.2 & §3.7.3]). The eigenspectrum also has well documented symmetric properties [77].

Note that the eigenspectrums of the second order spatial derivative operators applied here are very special: they are purely real, distinct, and the eigenvalues are

non-positive. Further, the second order spatial derivative operators are centrosymmetric. In [74, §4, last paragraph], the real spectrum is noted and it is emphasized that the accuracy in the computation of the eigenspectrum is essential in treating the pole condition from the authors cylindrical set-up. Recently, it was proven that these derivative operators have these spectral properties [20, 21].

Traditionally, the diagonalization of these spatial operators is computed initially and stored: $D_{\star\star} = P_{\star\star}\Lambda_{\star\star}P_{\star\star}^{-1}$, including the numerically obtained inverse of the eigenvector matrix [81, §3.7.1]. However, this goes against common numerical linear algebra practice as the matrix inverse is notorious for relative lack of numerical precision (compared to an implicit factorization solve), and numerical spectra also suffer from a similar fate.

It was found in practice that using a pivoting LU factorization of the eigenvector matrix $P_{\star\star}$ to implicitly solve in the place of an explicit matrix inverse product resulted in increased numerical stability. Further, it is likely that utilizing the special spectral properties of the Chebyshev second-order operators will result in improved stability, as the spectrum of centrosymmetric matrices may be partitioned and has symmetries that may be leveraged. Further, using a singular value decomposition or Schur decomposition of the eigenvector matrix $P_{\star\star}$ instead of a pivoting LU factorization may result in further stability improvements. Another possibility is to a Schur decomposition of the second order operator instead of matrix diagonalization, which is how the Sylvester equation is commonly numerically solved [5].

Also, on a subtle note, the explicitly treated, extrapolated nonlinear terms NL are represented in their convective form, e.g. $NL(\boldsymbol{u}) = \boldsymbol{u} \cdot \nabla \boldsymbol{u}$ for the momentum equation. It is well established in the literature that using an incompressible skew-symmetric representation ($NL(\boldsymbol{u}) = 0.5\boldsymbol{u}\cdot\nabla\boldsymbol{u}+0.5\nabla\cdot[\boldsymbol{u}\otimes\boldsymbol{u}]$) may improve numerical stability, especially in flow regimes of strong nonlinearity (see Zang [115] for a discus-

sion, also note that these representations are obtained from vector calculus identities and $NL(\boldsymbol{u}) = \nabla \cdot [\boldsymbol{u} \otimes \boldsymbol{u}]$ is referred to as the 'divergence' representation).

Zang [115] also discussed using an alternating representation of the nonlinear terms, such that convective and divergence representations would be used for alternating timesteps. In practice, it was found that the full skew-symmetric representation and alternating representation were essentially equivalent to one another. Note that these representations were consistently applied to the $NL(\boldsymbol{u}, T)$ term associated to the temperature equation. Further, the best performance and stability was achieved for the vertically oscillating stratified cavity by using the convective representation for two consecutive timesteps and then using the divergence representation (divergence form every third timestep). However, the best representation appears to be problem dependent as is noted in the literature [115].

1.2.3 Edge State Technique

The Edge State Technique (EST), is a numerical method for approximating unstable states of a dynamical system,

$$\partial \boldsymbol{u}/\partial t = \boldsymbol{f}(t, \boldsymbol{x}, \boldsymbol{u}; \boldsymbol{\mu}), \qquad \boldsymbol{u}(0, \boldsymbol{x}) = \boldsymbol{u}_0, \tag{1.19}$$

where $\boldsymbol{u} \in \mathbb{R}^N$, $\boldsymbol{f} : \mathbb{R}^N \to \mathbb{R}^N$, t is time, $\boldsymbol{x} \in \mathbb{R}^N$ is space, and $\boldsymbol{\mu} \in \mathbb{R}^M$ is a vector of parameters (note boundary conditions may also be specified). EST becomes useful when for a given $\boldsymbol{\mu}$ two co-existing stable states, $\mathcal{S}_0$ and $\mathcal{S}_1$, are solutions to system (1.19). In such a case, there must exist an unstable solution $\mathcal{U}_0$ somewhere intermediate the stable solutions. For such a solution space, $\mathcal{U}_0$ may be approached arbitrarily closely by optimizing for parameter $\gamma \in (0, 1)$,

$$\mathcal{U}_0 = \gamma \mathcal{S}_0 + (1 - \gamma)\mathcal{S}_1. \tag{1.20}$$

To illustrate, consider the following ordinary differential system,

$$\dot{x}(t) = x - x^3, \qquad x(0) = x_0. \tag{1.21}$$

The potential for this bistable system is given by,

$$V(x) = \frac{x^4}{4} - \frac{x^2}{2} + C, \tag{1.22}$$

where we allow $C = 0$ without loss of generality. From both equations (1.21) and (1.22), it is clear that there are three equilibria $x^* \in \{-1, 0, 1\}$, and from the derivative of (1.21) with respect to x or from (1.22), it is also clear that $x^* \in \{-1, 1\}$ are stable equilibria while $x^* = 0$ is unstable. Figure 1.1 illustrates this well.

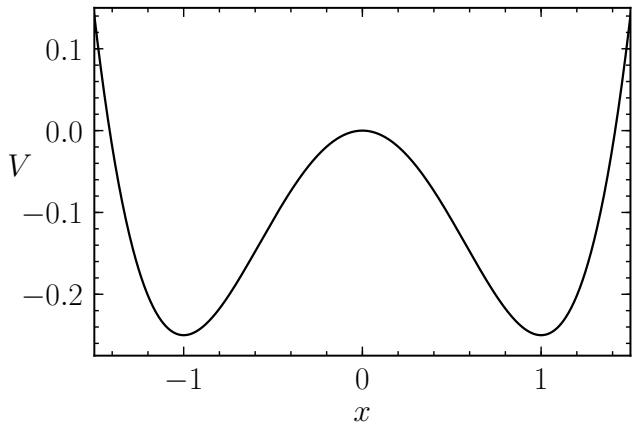

Figure 1.1: Illustration of the bistable potential from equation (1.22), graphically demonstrating the stable equilibria at $x = -1$ and $x = 1$, as well as the unstable equilibrium at $x = 0$.

For system (1.21), the equilibria are analytically obtainable. However, in most practical applications this will not be the case and direct numerical simulation (DNS) of the underlying system would be necessary to apprehend dynamical information. As the stable solutions for this problem are globally attracting, DNS would resolve them well. If the initial condition for the unstable equilibrium was perfectly specified, then the DNS would resolve that well also. This is illustrated in figure 1.2 where ten

estimates of γ are utilized as initial conditions. Numerically integrating (1.21) with a Runge-Kutta 4 scheme, it is clear that all flows between the two stable states will end at one of the two stable states, unless $\gamma = 0.5$ which provides $\mathcal{U}_0$.

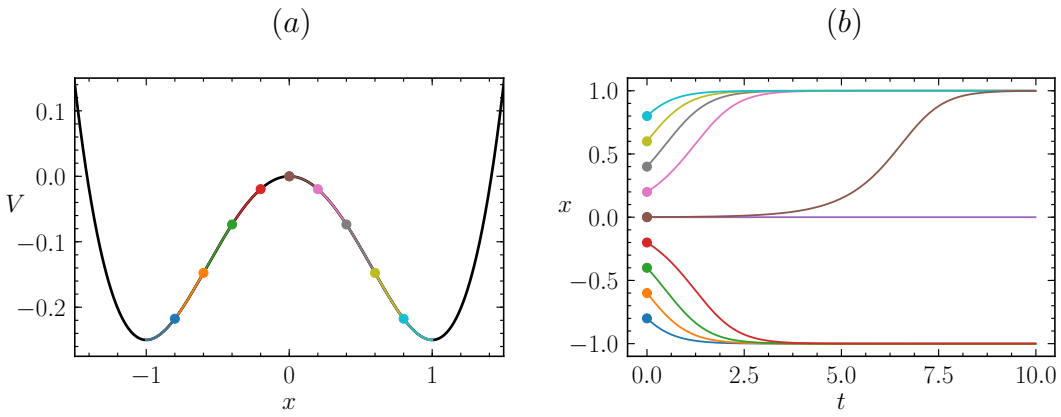

Figure 1.2: Illustration of running ten estimates of EST optimization parameter γ such that $\gamma_k = k/10$ for integer $k \in [1, 9]$ as well as $\gamma_j = 0.001$. In this toy model, $k = 5$ results in the analytical $\gamma = 0.5$, and the unstable equilibrium is obtained. However, $\gamma_j = 0.001$ nicely demonstrates how approaching the unstable edge state affects the flow.

While in this example $\mathcal{U}_0$ was directly obtainable, for more complicated dynamical systems, such as the Navier-Stokes equations, the chances of exactly finding γ are not good. However, as is also demonstrated by figure 1.2, as the estimated γ approaches the optimal γ, flows stay closer to the unstable state for longer. Thus, one may compute as close to the optimal γ as finite precision allows.

1.3 Outline

This dissertation primarily focuses on the numerical study of a stably stratified fluid confined in a square geometry, subjected to vertical oscillation via harmonic body forcing. The remainder of this monograph is organized as follows.

Chapter 2 first validates the numerical solver and various techniques to resolve

dynamics on a three-dimensional lid-driven cavity flow involving an unstratified, homogeneous incompressible fluid. The flow goes unsteady around a Reynolds number of 1910, appearing periodic unless simulated sufficiently long enough to observe intermittent bursting. This behavior was previously an open question, that was resolved by work that was published in [60]. I contributed the three-dimensional flow visualizations, the linear stability analysis with Arnoldi iteration, and the edge state technique (EST) results. My collaborator Ke Wu provided the original software for the direct numerical simulation, and this was modified for the linear stability analysis and EST. Note that Ke Wu also computed the unstable steady states using the selective frequency damping (SFD) method, which I made use of for the linear stability analysis and as a partial initial condition for some of the EST results.

Chapter 3 investigates the linear stability of the basic state for the stably stratified two-dimensional square cavity under vertical harmonic body forcing. The basic state is analytically known and exists for all parameter values, however, previous theory struggled to describe the loci of the basic state's instability. Utilizing Floquet theory, the critical forcing frequencies ω and forcing amplitudes α were determined for a specific Prandtl number $Pr = 1$ and buoyancy number $R_N = 2 \times 10^4$. Then, for the main subharmonic modal instability, various (R_N, ω, α) loci were obtained, demonstrating self-similar (power law) behavior. This work was published in [109].

Chapter 4 builds on the linear stability of the basic state by developing a modal analysis method to estimate the loci of instability without performing a Floquet analysis. With the correct ansatz, the non-commutation of the confinement with the diffusion operator may be approximated in this way to very quickly (matter of compute minutes versus weeks) determine the loci of instability for a family of modes. This work was submitted to be published [112].

Chapter 5 studies the nonlinear dynamics of the flow, determining the criticality

of the instability as well as discovering dynamics that cannot be described with linear theory, such as a homoclinic doubling cascade. This work was accepted for publication in the Journal of Fluid Mechanics [113]. Conclusions and future directions are presented in Chapter 6.

Chapter 2

LID-DRIVEN CAVITY FLOW IN THE CUBE

ABSTRACT

The onset of time dependence in the cubic lid-driven cavity is surprisingly complicated, given the simplicity of the geometry and the modest value of the Reynolds number at which it occurs. The onset is characterized by finite amplitude oscillations which appear to be stable for long times, but are subjected to intermittent bursts at irregular times during which the reflection symmetry about the spanwise midplane is broken. The complex dynamics are shown to be intimately related to the subcritical nature of the instability of the steady basic state. We use a spectral collocation numerical technique, solving both in the full three-dimensional space as well as in the symmetric subspace, and use selective frequency damping and Arnoldi iterations about the unstable basic state to determine its bifurcations. Edge tracking is also used to investigate a number of time-dependent saddle states. Putting all this together, we show that the complex dynamics are organized by two successive Hopf bifurcations, the first of which is shown to be subcritical. All local states are unstable in the full space at higher Reynolds numbers, leading to the intermittent bursting behavior.

2.1 Introduction

The lid-driven cavity flow, consisting of the flow in a rectangular cavity driven by the steady translation of one of the cavity walls, is a canonical flow for the study of the stability of separated shear layers. The idealized situation where the cavity is

of infinite spanwise extent and the flow is assumed to be invariant in the spanwise direction has been studied extensively; see the review article by [88].

In the cubic cavity, the spanwise confinement effects are pronounced, and for Reynolds numbers Re $\sim 10^3$, the flow is steady with a single pair of streamwise vortices centered about the spanwise midplane, together with vortical structures along the edges where the spanwise walls meet the other walls. When the Reynolds number is increased beyond approximately 1910, the flow becomes unsteady, manifesting long periods of essentially periodic flow with intermittent bursts, and for slightly larger Re, the flow is persistently chaotic. A number of numerical investigations have contributed to the details of the flow dynamics in this regime where the flow in the cubic lid-driven cavity becomes unsteady. In the earliest such study, [31] report that the steady flow loses stability at a subcritical Hopf bifurcation, with unsteady flow appearing for Re $\gtrsim 1914$. The more recent studies of [42], [50], and [52] reproduce some aspects of the flows reported by [31], but note that the periodic state of [31] is not stable beyond the Hopf bifurcation, and that it undergoes sudden bursts at random times. They conclude that the simulations of [31] were not run long enough for the intermittent bursts to manifest; near onset, it takes several viscous times for this to happen. Also, near onset the intervals between bursts can be very long (several viscous times). Following a burst, another essentially periodic state with larger amplitude and smaller frequency that persists for a relatively short time is observed before another burst occurs. The dynamics involved remain unclear; [50] suggests that it is some type of intermittency that requires further investigation to unravel, [42] calls for further investigations to clarify the situation, and [52] concludes that the origin of the intermittent events is still unknown. The numerical studies each use very different methods with a wide range of spatial and temporal resolutions; [31] uses finite differences, [42] uses Chebyshev spectral collocation, and [50, 52] use spectral elements.

The results from the spectral collocation and the spectral elements methods, which were run for sufficiently long times, are in agreement. There are minor variations in the precise value of Re at which things happen, but this is readily accounted for by differences in resolution and the treatment of the discontinuous boundary condition at the edges where the moving lid meets the stationary walls. Thus, the transition from steady flow to intermittent bursting when Re is increased beyond a critical value is consistently observed by the various computations. The only experiment specifically designed to address this onset of unsteady flow in the lid-driven cube [48] is broadly consistent with the numerical results, but the resolution in Re available in the experiment was insufficient to resolve the details.

Linear stability analysis of the types so far employed have been incapable of capturing the nature of the onset of the intermittent bursting reported from nonlinear simulations in the cubic cavity. In part, the problem is that linear stability analysis only gives the eigenstructure near instability, and for the cubic lid-driven cavity, the studies all agree that instability is via a subcritical Hopf bifurcation. Since the bifurcation is subcritical, the subsequent flow evolution is not well described by the bifurcating eigenmode. The previous nonlinear studies of the cubic cavity flow all report that the reflection symmetry about the spanwise midplane is broken to some degree in the unsteady nonlinear states, but they do not provide details about the nature of this symmetry breaking nor how it is related to the onset of unsteadiness.

Here, we use a Chebyshev spectral collocation method, similar in many ways to that used in [42] but with a different treatment of the boundary condition discontinuity, and our nonlinear results are in very close agreement with [42, 50, 52]. By computing in both the full three-dimensional space as well as in the reflection-symmetric subspace, we are able to show that the second periodic oscillations that are observed briefly following the bursts in fact correspond to a limit cycle that is unstable to sym-

metry breaking, and exists for much lower Re than that at which the basic state first loses stability. As was done in [50, 52] we also compute the unstable basic state via selective frequency damping (SFD) [67] and then use Arnoldi iterations [86] to study its linear stability. In agreement with [50, 52], the limit cycle reported by [31] corresponds to the first pair of complex-conjugate eigenvalues to acquire positive real part as Re is increased. As noted by [31, 42], this Hopf bifurcation is subcritical, and we re-confirm this by computing the lower branch down to the cyclic-fold bifurcation at lower $\mathrm{Re} \approx 1872$ using an edge state technique (EST) [38, 87]. We have also located a second Hopf bifurcation at $\mathrm{Re} \approx 2089$ whose eigenfrequency is very close to that of the intermittent large-amplitude oscillations that are observed following a burst in the nonlinear simulations. This was also noted by [50, 52], but they did not study the linear stability of the basic state beyond $\mathrm{Re} = 2000$, and so missed this second bifurcation. By monitoring the symmetry of the nonlinear solutions, it is clear that the large-amplitude oscillations immediately following a burst are unstable to symmetry breaking. So, we have also computed the nonlinear solutions in the symmetry subspace and indeed find that these large-amplitude oscillations correspond to a limit cycle solution. We have continued this limit cycle down to much lower $\mathrm{Re} \approx 1872$ where it undergoes a cyclic-fold bifurcation. Then, using EST in the symmetric subspace with combinations of the limit cycle and the basic state as initial conditions, we have been able to capture the details of the lower-branch saddle limit cycle for a small range in Re. The lower-branch limit cycle undergoes a Neimark–Sacker bifurcation and acquires two unstable directions, thus compromising the effectiveness of EST to track it. However, at the Neimark–Sacker bifurcation, a quasiperiodic state is spawned, that has one unstable direction in the symmetry subspace. We have tracked this state using EST to slightly higher Re where it is absorbed in a subcritical Neimark–Sacker bifurcation of the upper branch of the other (low-amplitude) limit

cycle, rendering that limit cycle unstable. By taking the various edge states computed in the symmetry subspace as initial conditions for nonlinear simulations in the full space, we have also been able to extract crucial information about which states are unstable to symmetry breaking. By piecing all this information together, we are able to provide a fairly complete and consistent picture of what is responsible for the bursting behavior.

2.2 Governing Equations and Numerical Techniques

Consider the flow in a cube of sides of length L, completely filled with an incompressible fluid of kinematic viscosity ν, driven by the motion of one wall at constant velocity U. Using L as the length scale and L/U as the time scale, the non-dimensional governing equations are

$$\partial \boldsymbol{u}/\partial t + \boldsymbol{u} \cdot \boldsymbol{\nabla} \boldsymbol{u} = -\boldsymbol{\nabla} p + \mathrm{Re}^{-1} \nabla^2 \boldsymbol{u}, \quad \boldsymbol{\nabla} \cdot \boldsymbol{u} = 0, \tag{2.1}$$

where the Reynolds number

$$\mathrm{Re} = UL/\nu, \tag{2.2}$$

is a ratio of two time scales: the viscous time scale L^2/ν and the convective time scale L/U. For the most part, we will present results using the convective time scale, but the time series of flow quantities will be shown in terms of the viscous time scale. As such, we introduce $\tau = t/\mathrm{Re}$, where one time unit in τ is a viscous time.

The Cartesian coordinate system, $\boldsymbol{x} = (x, y, z)$, with the origin at the center of the cube is used; x is the direction in which the wall at $y = 0.5$ is moving, z is the spanwise direction, and the velocity field is $\boldsymbol{u} = (u, v, w)$. See Fig. 2.1 for a schematic.

The boundary conditions on the stationary walls at $x = \pm 0.5$, $y = -0.5$, and $z = \pm 0.5$ are no-slip, i.e. $\boldsymbol{u} = \boldsymbol{0}$ on these walls. Nominally, on the moving wall $(u, v, w) = (1, 0, 0)$, resulting in a jump discontinuity along the four edges, $(x, y, z) =$

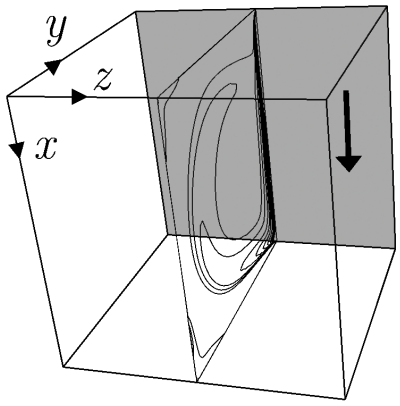

Figure 2.1: Schematic of the cubic lid-driven cavity. The perspective shown, with the back wall (at $y = 0.5$, shaded gray) moving downwards ($+x$-direction), is that used in all subsequent three-dimensional renderings of the results. In the spanwise midplane (at $z = 0$), typical streamlines of a low-Re steady-state flow are shown.

$(\pm 0.5, 0.5, z)$ and $(x, 0.5, \pm 0.5)$, where the moving wall meets the streamwise and spanwise walls.

The system (2.1), together with the boundary conditions, is equivariant with respect to a reflection symmetry $\mathcal{K}$ about the spanwise midplane $z = 0$. The action of this Z_2 symmetry on the velocity, vorticity $\nabla \times \boldsymbol{u} = (\xi, \eta, \zeta)$, and helicity $\mathcal{H} = \boldsymbol{u} \cdot (\nabla \times \boldsymbol{u})$ is

$$\mathcal{A}(\mathcal{K})(u, v, w)(x, y, z) = (u, v, -w)(x, y, -z), \tag{2.3a}$$

$$\mathcal{A}(\mathcal{K})(\xi, \eta, \zeta)(x, y, z) = (-\xi, -\eta, \zeta)(x, y, -z), \tag{2.3b}$$

$$\mathcal{A}(\mathcal{K})\mathcal{H}(x, y, z) = -\mathcal{H}(x, y, -z). \tag{2.3c}$$

The flow in the cubic lid-driven cavity is inherently three dimensional for all $\mathrm{Re} \neq 0$. It is interesting to visualize the flow in terms of the helicity, which for the idealized spanwise invariant case is identically zero since the velocity and vorticity vectors are orthogonal.

A convenient global measure of the flow is the kinetic energy

$$E = \frac{1}{2} \int_{\mathcal{C}} |\boldsymbol{u}|^2 \, d\boldsymbol{x} \,, \tag{2.4}$$

where $\mathcal{C}$ is $\boldsymbol{x} \in [-0.5, 0.5] \times [-0.5, 0.5] \times [-0.5, 0.5]$. It is also convenient to introduce a symmetry parameter in order to measure the relative departure from symmetry of a solution:

$$S = \frac{1}{2E} \int_{\mathcal{C}} |\boldsymbol{u} - \mathcal{A}(\mathcal{K})\boldsymbol{u}|^2 \, d\boldsymbol{x} \,. \tag{2.5}$$

This symmetry parameter is proportional to the kinetic energy in the skew-symmetric component of the flow relative to the total kinetic energy of the flow.

2.2.1 Numerics

The Navier–Stokes system (2.1) is discretized using a spectral-collocation method in all spatial directions. Both velocity and pressure are approximated by polynomials of degree N $(\mathcal{P}_N, \mathcal{P}_N)$, written in barycentric form with weights $w_0 = 0.5$, $w_n = (-1)^n$ for $n \in [1, N-1]$, and $w_N = 0.5(-1)^N$, associated to the Chebyshev–Gauss–Lobatto grid. Spatial differentiation is performed via direct matrix-vector multiplication by the pseudospectral differentiation matrix (common to all three directions).

The time integration scheme used is the fractional-step improved projection method of [35], based on a linearly implicit and stiffly stable, second-order accurate scheme combining a backward differentiation formula for the linear terms and an explicit mix, equivalent to linear extrapolation, of Adams–Moulton and Adams–Bashforth steps for the nonlinear convective terms [102]. The predictor stage of the fractional step method solves a Helmholtz equation for a pressure field, for which Neumann conditions consistent with (2.1) are applied at the walls. The corrector stage then projects the resulting predicted velocity field onto the space of (discretely) divergence-free polynomials via a Stokes problem, which is also handled by solving a Helmholtz

equation for the corrected pressure, albeit with homogeneous Neumann boundary conditions. Further details can be found in [35].

The boundary condition for the streamwise component of velocity for the moving wall, $u = 1$, is discontinuous where it meets the four stationary walls. Discontinuous boundary conditions can lead to numerical problems when using spectral methods, and so we regularized it by using

$$u(x, 0.5, z) = \left[1 - 2\exp\left(\frac{-1}{\epsilon}\right)\cosh\left(\frac{2x}{\epsilon}\right)\right] \times \left[1 - 2\exp\left(\frac{-1}{\epsilon}\right)\cosh\left(\frac{2z}{\epsilon}\right)\right]. \tag{2.6}$$

The small positive number ϵ controls the distance over which the discontinuity is smoothed. This is a standard technique used in spectral methods [58]. As ϵ is decreased for a given Re, the accuracy of the spectral method becomes dominated by the need to resolve the steep variation in (2.6) rather than the flow. For the results presented here, with $\mathrm{Re} \leq 2100$, we have used $\epsilon = 0.01$, for which $N = 48$ is sufficient to resolve (2.6), having 5 collocation points in the gap. When using local methods, such as finite differences and finite volume techniques, the gap is the grid spacing at the edge, so that the gap decreases as the resolution is increased. An alternative treatment for global spectral methods is to try to account for the discontinuity asymptotically [14]. [42] implement such an approach, but were unable to account for the discontinuity at the four corners where the edges meet, $(x, y, z) = (\pm 0.5, 0.5, \pm 0.5)$. They noted that their spectral accuracy was considerably reduced as a consequence. The size of the gap has a direct impact on, for example, the critical Re for the onset of instability; a smaller gap results in a smaller critical $\mathrm{Re}_{\mathrm{H1}}$. In their finite volume study, [31] found by direct simulation that for their highest resolution (and hence their smallest gap), the basic state loses stability via a subcritical Hopf bifurcation H_1 at $\mathrm{Re} = \mathrm{Re}_{\mathrm{H1}} \approx 1927$. This compares very well with $\mathrm{Re}_{\mathrm{H1}} \approx 1929$

that we find using $\epsilon = 0.01$ and $N = 48$. They then used Richardson extrapolation to estimate $\mathrm{Re}_{\mathrm{H1}} = 1914$. [42] report $\mathrm{Re}_{\mathrm{H1}} \approx 1920$ using $N = 72$, although their $N = 48$ result is very close (≈ 1918). With all of this under consideration, our choice of ϵ represents a 1% gap along the edges and about a 0.5% increase in $\mathrm{Re}_{\mathrm{H1}}$ over what it would be with a zero gap. This allows us to have good spectral resolution with a relatively modest $N = 48$. In the following sections, we demonstrate excellent agreement with the previous numerical studies of the cubic lid-driven cavity. Small quantitative differences correspond to small shifts in the given Re due to the gap size differences. Most importantly, the details of the intermittent bursts for $\mathrm{Re} > \mathrm{Re}_{\mathrm{H1}}$ that we find are in agreement with those reported in [42, 50, 52].

For $\mathrm{Re} < \mathrm{Re}_{\mathrm{H1}} \approx 1929$ the stable basic state BS can be determined via direct numerical simulation (DNS). At $\mathrm{Re} = \mathrm{Re}_{\mathrm{H1}}$, BS loses stability via a (subcritical) Hopf bifurcation and cannot be computed via DNS. However, it can be computed by introducing a feedback control $\boldsymbol{v}$ into (2.1) and using the selective frequency damping (SFD) technique described in [67]. Specifically, we solve the augmented system

$$\partial \boldsymbol{u}/\partial t + \boldsymbol{u} \cdot \boldsymbol{\nabla} \boldsymbol{u} = -\boldsymbol{\nabla} p + \mathrm{Re}^{-1} \nabla^2 \boldsymbol{u} + \omega_c (\boldsymbol{v} - \boldsymbol{u}), \tag{2.7a}$$

$$\partial \boldsymbol{v}/\partial t = \omega_c (\boldsymbol{u} - \boldsymbol{v}), \quad \boldsymbol{\nabla} \cdot \boldsymbol{u} = 0, \quad \boldsymbol{\nabla} \cdot \boldsymbol{v} = 0, \tag{2.7b}$$

with $\boldsymbol{v} = \boldsymbol{u}$ on all boundaries. Equation (2.7b) represents a low-pass filter applied to $\boldsymbol{u}$, with cut-off frequency ω_c. The selection $\omega_c = \omega/2$ optimizes damping of unstable modes of (2.7) oscillating at a target frequency ω close to the Hopf frequency associated to H_1. The velocity and feedback control fields, $\boldsymbol{u}$ and $\boldsymbol{v}$, are (pseudo) spectrally collocated and (2.7) is solved using the same technique as that used for (2.1). In the time-splitting scheme, the high-frequency term $\omega_c(\boldsymbol{v} - \boldsymbol{u})$ in (2.7a) is treated implicitly, while $\omega_c(\boldsymbol{u} - \boldsymbol{v})$ in (2.7b) is treated as a nonlinear term, using linear extrapolation.

The linear stability of the unstable BS found via SFD is analyzed using a standard Arnoldi iteration [86] applied in two different ways. In one, the Navier–Stokes equations are linearized around BS and subjected to a small perturbation [100]. In the other implementation, the action of the Jacobian is approximated with a divided difference constructed from the full nonlinear flow (2.1), evaluated at BS in the direction of the small perturbation, as described in [34]. In both implementations, the corresponding Krylov subspaces consisted of $m = 96$ modes. Each mode was obtained using 1000 time steps in a time window of 2×10^{-3} viscous times, guaranteeing a sufficiently high Nyquist frequency to accurately resolve the frequencies of interest while avoiding aliasing effects for this choice of m. The nonlinear implementation has an additional time window constraint due to nonlinear growth effects, but allows the original DNS solver to be used with only minor modifications. With the time window and m used, both implementations gave comparable results.

2.3 Results

2.3.1 Onset of Unsteadiness

The flow in the cubic lid-driven cavity for sufficiently small Re is steady and symmetric. This basic state, BS, has been shown to be stable for $\mathrm{Re} \lesssim 1900$ [31, 42, 50, 52]. We find that for $\mathrm{Re} \lesssim 1929$, static continuation converges to stable BS. However, for $\mathrm{Re} = 1930$, using BS at $\mathrm{Re} = 1929$ as initial condition, the evolution does not converge to a steady state. There is an initial adjustment to a state that is very similar to BS, and then over a long time (several viscous time units) there are small oscillations about BS that are slowly amplified. These oscillations are damped for $\mathrm{Re} \lesssim 1929 \approx \mathrm{Re}_{\mathrm{H1}}$. Similar behavior was reported in [31], who found $\mathrm{Re}_{\mathrm{H1}} = 1927$ from direct simulations.

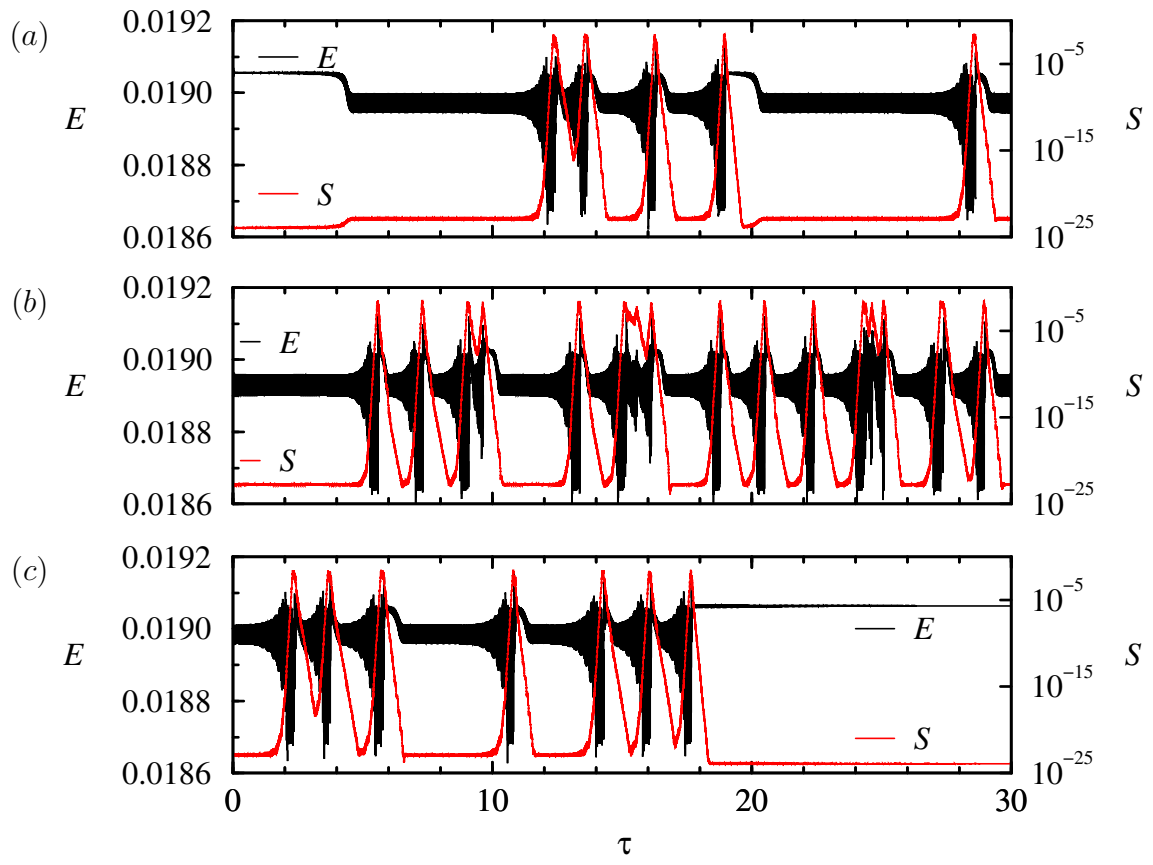

Figure 2.2: Time series of E (black) and S (red) for (a) $\mathrm{Re} = 1930$, (b) $\mathrm{Re} = 1940$ and (c) $\mathrm{Re} = 1927$.

Figure 2.2(a) shows the temporal evolution of both the kinetic energy E and the symmetry parameter S in the $\mathrm{Re} = 1930$ case, using BS at $\mathrm{Re} = 1929$ as initial condition. Note that we plot all time series with respect to the viscous time τ. During the early evolution ($\tau \lesssim 4$), the flow consists of very slowly amplified oscillations about the unstable BS, during which time the flow is symmetric, as indicated by $S \sim 10^{-24}$, which is essentially machine epsilon squared. Then for $\tau \in (4, 4.5)$, there is a rapid evolution away from the unstable BS, and by $\tau \approx 5$, the flow appears to have settled into a periodic limit cycle state, called LC1. There is a very slight increase in S from about 10^{-24} to 10^{-23}, but this level is still very close to being essentially zero. For

a very long time (up to $\tau \sim 11$), it appears that LC1 is a stable symmetric limit cycle state. This behavior was also reported by [31], but as pointed out by [42], LC1 is unstable for $\mathrm{Re} > \mathrm{Re}_{\mathrm{H1}}$. By $\tau \approx 11$, there is a rapid exponential growth in S, accompanied by rapidly growing oscillations in E which saturate at $\tau \approx 12$ to what appears to be another limit cycle LC2, and S has nonlinearly saturated to a level of order 0.01. The LC2 state persists for a very short time, about 10 oscillations or 0.2 viscous times, after which the flow evolves back toward LC1 with S decaying exponentially. A sequence of bursts, during which S grows exponentially again, then occurs. At about $\tau = 19$, Fig. 2.2(a) shows that following another burst, the flow evolves very close to BS, and then settles near LC1 for several viscous times before executing another burst visiting LC2 and BS.

The timing between the bursts is not uniform. This intermittent bursting behavior has been reported in [42, 50, 52], and all studies note that the flow is essentially symmetric when near the unstable BS and LC1 states, and the broken symmetry is only strongly evident while it is near the LC2 state. None of the studies were able to determine the nature of the intermittency in the bursting behavior, but noted that the bursts become more frequent with increased Re, with the time intervals between bursts remaining irregular. Figure 2.2(b) shows a time series of E and S of the bursting state at $\mathrm{Re} = 1940$, when started from the bursting state at $\mathrm{Re} = 1930$.

For $\mathrm{Re} < \mathrm{Re}_{\mathrm{H1}}$, evolutions starting from a bursting state at higher Re eventually tend to converge to BS. Figure 2.2(c) shows the evolution of E and S for $\mathrm{Re} = 1927$ starting again from the bursting state at $\mathrm{Re} = 1930$. The flow continues to burst for a long time (approximately 18 viscous times) before an excursion visiting the phase space neighborhood of BS. Since BS is stable at $\mathrm{Re} = 1927$, it ends up attracting the flow.

During the time that the flow is evolving close to LC1 or LC2, one is able to

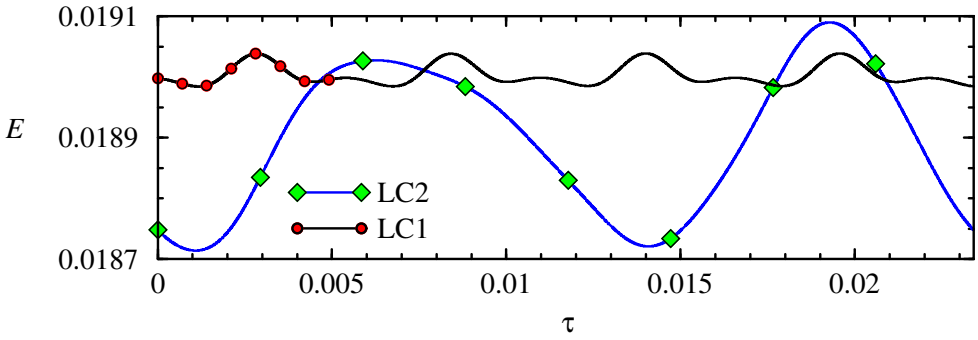

Figure 2.3: Time series of E for LC1 and LC2 at Re = 1930; the symbols correspond to the snap-shots over one period shown in Figs. 2.4 and 2.5.

characterize these two unstable limit cycles. Figure 2.3 shows snippets of the times series of E at Re = 1930, taken from Fig. 2.2(a) at times when the flow is evolving close to either LC1 or LC2. The time origin in this figure has been shifted so as to directly compare the energy evolutions. The amplitude and period of the oscillation of LC2 are about four times those of LC1. Specifically, the period ratio of LC2 to LC1 at Re = 1930 is 4.18, which is very close to the values reported in [42, 50, 52]. Also, the oscillations associated with LC1 and LC2 are very nonlinear, even though the value of Re is very close to $\mathrm{Re}_{\mathrm{H1}}$ where BS loses stability.

To better identify the flow features associated with the unsteadiness in LC1 and LC2, we consider the deviations away from their mean. Figures 2.4 and 2.5 show ten snap-shots over one period of the deviation in the helicity, $\mathcal{H} - \langle \mathcal{H} \rangle$, for LC1 and LC2, respectively, where $\langle \cdot \rangle$ denotes the time average over one period. The deviations are of comparable strength to the means; these are not small perturbations about the mean. For both limit cycles, the deviation is associated with the streamwise vortices; the helicity associated with the spanwise endwall regions remains essentially steady throughout the oscillations. For both limit cycles, the deviations are $\mathcal{K}$-symmetric, but the details differ for the two. For LC1, the deviation rollers for the most part remain in their spanwise location, but progressively change their sign through the

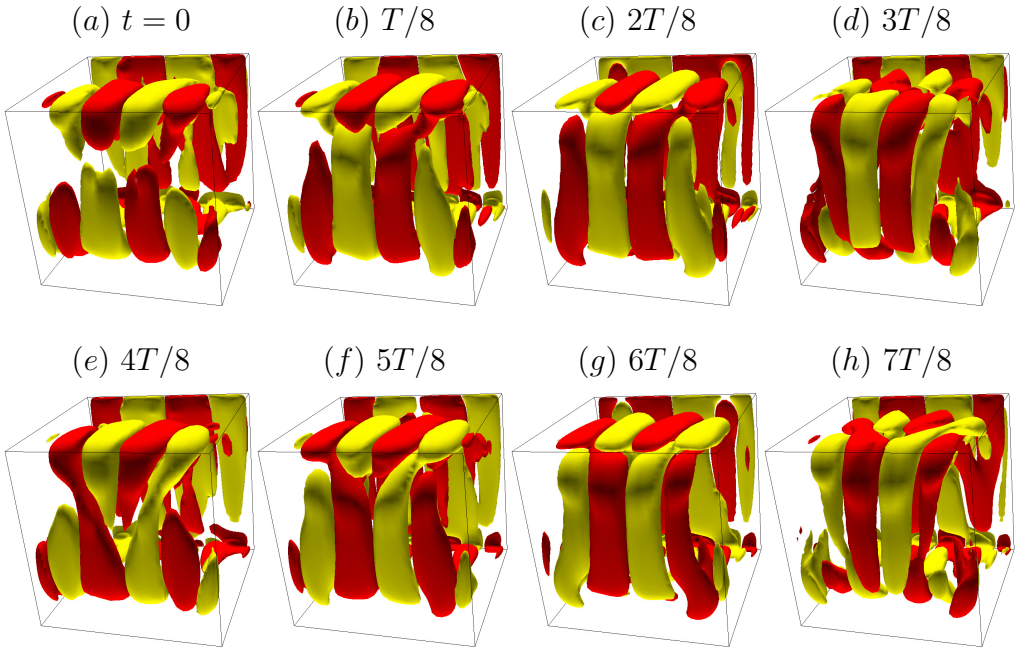

Figure 2.4: Isosurfaces of $\mathcal{H} - \langle \mathcal{H} \rangle$ at $\pm 10^5$ of LC1 at Re = 1930, over one period $T = 10.8$ (convective time units). See Supplemental Material [59] for an animation.

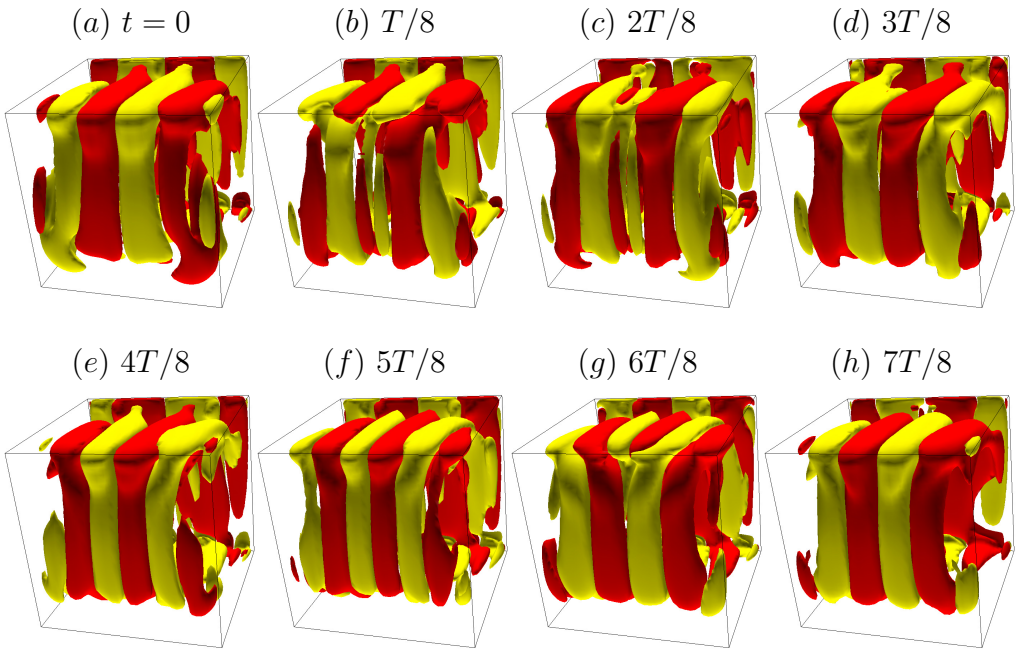

Figure 2.5: Isosurfaces of $\mathcal{H} - \langle \mathcal{H} \rangle$ at $\pm 10^5$ of LC2 at Re = 1930, over one period $T = 45.2$ (convective time units). See Supplemental Material [59] for an animation.

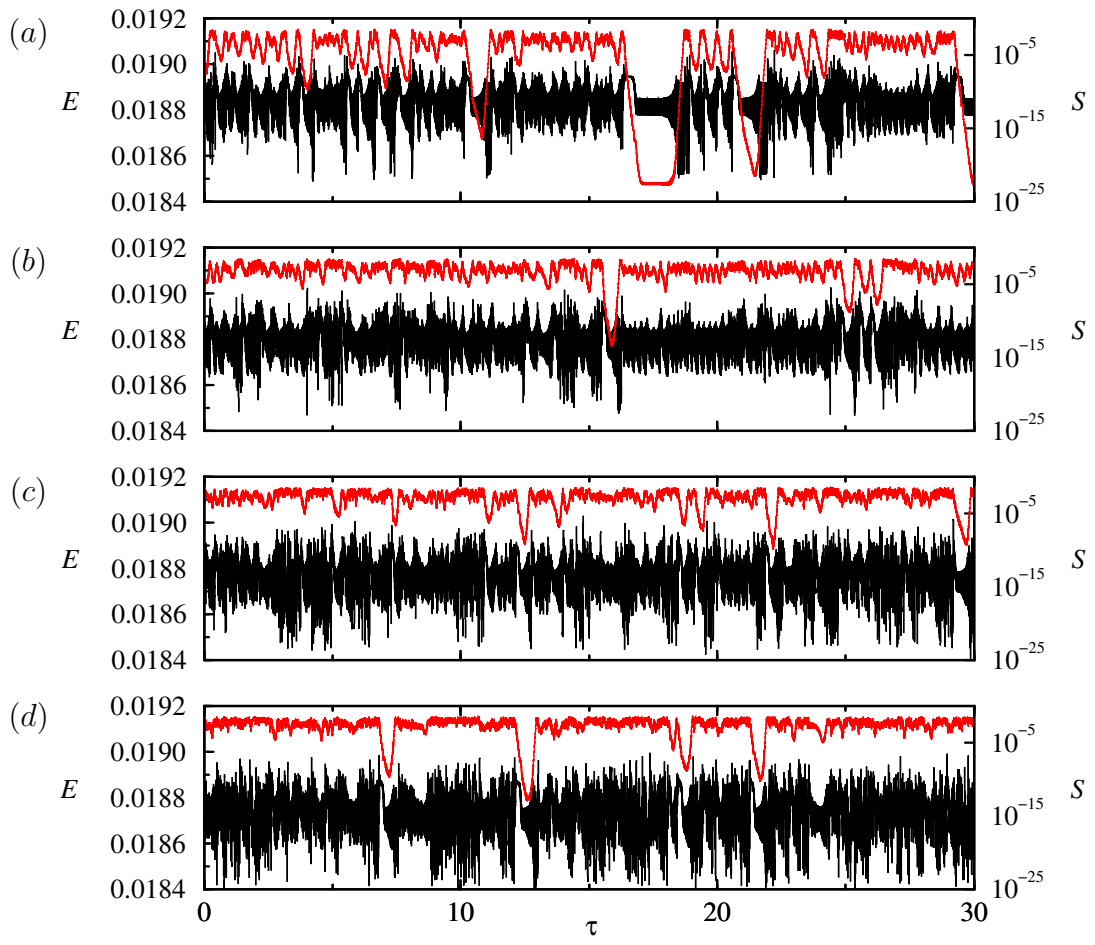

Figure 2.6: Time series of E (black) and S (red) at (a) Re = 1970, (b) Re = 1980, (c) Re = 1990 and (d) Re = 2000.

cycle. In contrast, the deviation rollers of LC2 travel in from the spanwise endwalls, and annihilate at the midplane $z = 0$ as new rollers are spawned at the spanwise endwalls, much like left- and right-traveling waves meeting at the $z = 0$ midplane. These flows are represented in the snap-shots shown in Figs. 2.4 and 2.5, but the associated online movies [59] provide a much clearer picture of their spatio-temporal features.

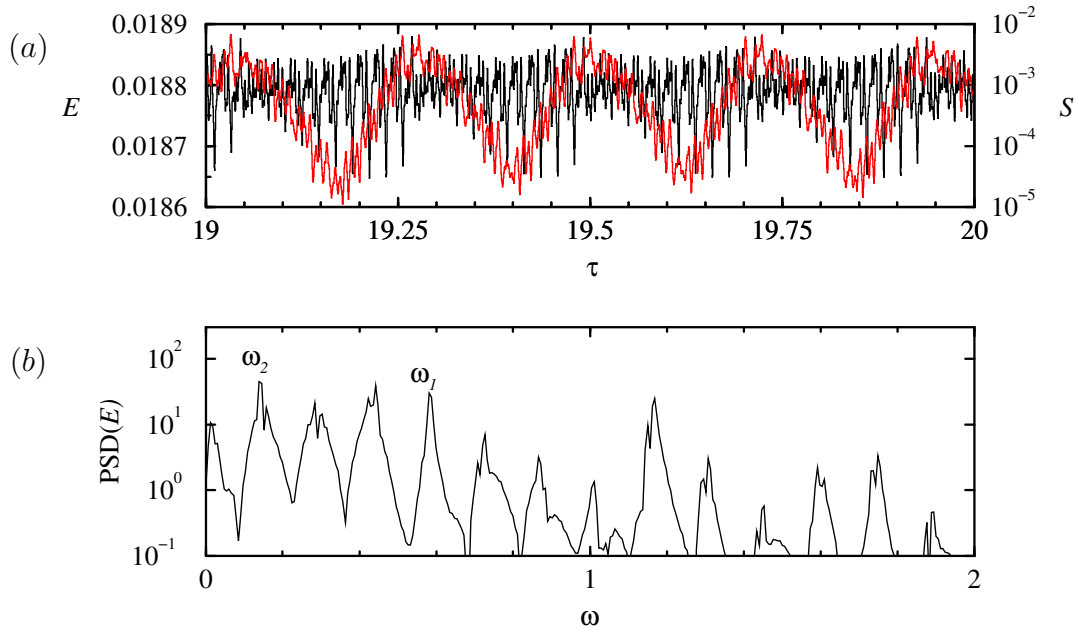

Figure 2.7: (a) Time series of E (black) and S (red) for Re = 1980, zoomed in for a time during which the evolution is close to the mixed mode QPa (with $\sigma(E) \approx 4 \times 10^{-5}$), and ($b$) power spectral density (PSD) of the time series of E shown in (a). The peaks corresponding to the frequencies of LC1 and LC2 are indicated.

2.3.2 Intermittent Bursting

Figure 2.6 shows time series of E and S for a number of cases with Re $\geq$ 1970, where the flow is much more irregular with many excursions away from and back toward the symmetry subspace (exponential decay and growth in S). The approaches to either BS or LC1 occur much less frequently than for the lower Re cases shown in Fig. 2.2. The bursts at these higher Re are occasionally into the symmetry subspace for a very brief period, rather than what was happening at lower Re, with the bursts providing short lived excursions out of the subspace. Also, the excursions are not visiting BS, LC1 or LC2 very often, but instead appear to be visiting quasi-periodic states and more complicated states, such as chaotic saddles.

The evolution at Re = 1980 shown in Fig. 2.6(b) has regular oscillations for

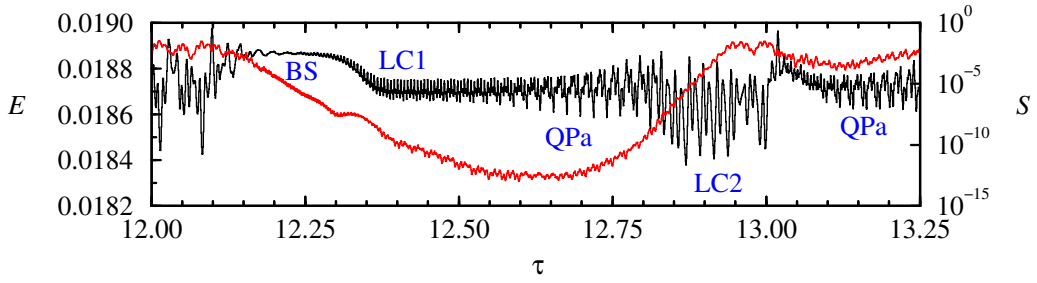

Figure 2.8: Time series of E (black) and S (red) for Re = 2000, zoomed in for a time during which there is a 'regular' burst event.

$\tau \in (19, 20)$ which do not correspond to either LC1 or LC2. Figure 2.7(a) shows details of the E and S time series over this time. The quasi-periodic oscillation is close to being periodic; this is indicated by the low beat frequency modulating the signal. The power spectral density of the E time series over the time shown in Fig. 2.7(a) is presented in Fig. 2.7(b), which consists of peaks at the frequencies corresponding to the two limit cycles LC1 and LC2 (ω_1 and ω_2, respectively), plus linear combinations of these. Also evident is a very low frequency peak corresponding to the beat frequency noticeable in the time series, which also shows up as sidebands to the main peaks. The frequencies ω_1 and ω_2 are close to a 4:1 ratio, and the beat frequency is a measure of how far the ratio is from being rational. In Fig. 2.6(a), the time series for Re = 1970 also shows that the flow is close to this quasi-periodic mixed mode QPa during $\tau \in (26.4, 27.5)$.

At larger Re = 2000, the flow continues being spatio-temporally complicated. The chaotic behavior is similar to that reported in [50]. However, careful inspection reveals episodes of 'orderly' bursts, as illustrated in Fig. 2.8, where at $\tau \approx 12.2$ the flow is very close to BS, then it evolves close to LC1, during which time S is decreasing exponentially to very small values. Then, at $\tau \approx 12.6$, the flow evolves away from LC1 to the mixed mode QPa with S increasing; QPa gives way to LC2 at $\tau \approx 12.9$ for 2 or 3 cycles by which time S has saturated. Then there is a another burst but

the evolution does not make it to the neighborhood of BS this time and instead visits another quasi-periodic unstable state.

The limit cycle LC1 is symmetric, but is unstable to modulations, i.e. a Neimark–Sacker bifurcation, and the new frequency introduced is that of LC2. LC2 is unstable to symmetry breaking. For most of the time, the time series appears to be temporally chaotic, suggesting that the stable and unstable manifolds of the saddle states (BS, LC1, LC2, and QPa) intersect transversely, leading to chaotic dynamics interspersed with regular episodes during which the flow approaches sufficiently close to one or other saddle state, but eventually the dynamics are directed by the unstable manifolds. The mixed mode QPa acts as a gateway in and out of the symmetric subspace and S grows and decays exponentially during the beat cycle. Further evidence supporting this is presented in the following sections where the flow is further analyzed.

2.3.3 Spectral Analysis of BS

Now that we have explored the dynamics as Re is increased beyond $\mathrm{Re}_{\mathrm{H1}}$ via DNS, and have reproduced the DNS results of previous investigations, we analyze the results. As was already done by [50], we begin by using SFD to obtain the unstable BS for $\mathrm{Re} > \mathrm{Re}_{\mathrm{H1}}$, and then we determine its leading eigenmodes using Arnoldi iterations.

Figure 2.9 shows the real and imaginary parts of the three leading eigenvalue pairs as functions of Re. The leading eigenvalue pair (which we simply refer to as λ_1) acquires positive real part at $\mathrm{Re} \approx 1928.9$, which is consistent with the DNS results presented above. The imaginary part is approximately 0.5832 (using the convective time scale), which is very close to the oscillation frequency of LC1 and to the Hopf frequency reported by [50, 52]. The second leading eigenpair, λ_2, has a real part that

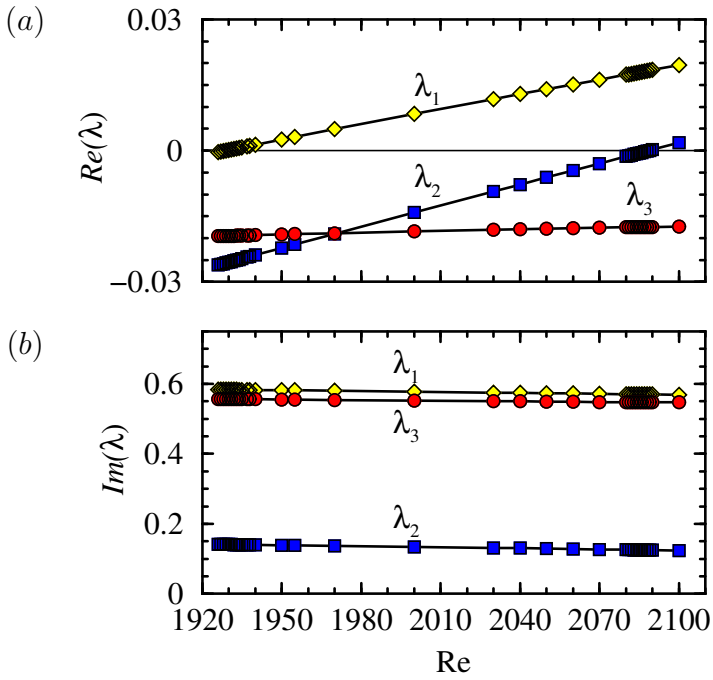

Figure 2.9: Real and Imaginary parts of the three leading eigenvalues of BS as functions of Re, using the convective time scale.

is growing faster with Re than that of λ_1, but starting from a much more negative value. The real part of λ_2 becomes positive via a second Hopf bifurcation, H_2, at $\mathrm{Re} = \mathrm{Re}_{\mathrm{H2}} \approx 2089$. The imaginary part of λ_2 is approximately 0.1407, which is very close to the oscillation frequency of LC2. This value is also very close to the imaginary part of λ_2 reported by [50, 52], however they did not consider the linear stability of BS beyond $\mathrm{Re} = 2000$, and so they did not determine $\mathrm{Re}_{\mathrm{H2}}$. The eigenvectors associated with λ_1 and λ_2 are reflection symmetric. The third leading eigenvalue pair, λ_3, has a real part that remains negative over the Re range considered, and varies very slowly with Re, suggesting that if it is involved in a bifurcation of BS, it would be at a much larger Re and so is not likely to have an impact on the dynamics at the Re values under consideration. It has an imaginary part slightly smaller than λ_1, and the associated eigenvector is anti-symmetric. This is consistent with the findings of

[50, 52]. This is also consistent with the fact that this mode does not show up when the spectral analysis is done in the symmetric subspace.

2.3.4 Details of the Subcritical Hopf Bifurcation to LC1

Linear stability analysis identifies the onset of a bifurcation, but does not give information about whether it is super- or sub-critical; that requires nonlinear information for its determination. Both [31] and [42] presented DNS evidence that the Hopf bifurcation H_1 at which BS first loses stability is subcritical. We now focus on the details of this subcritical Hopf bifurcation. The generic behavior in the neighborhood of a subcritical Hopf bifurcation is that the steady equilibrium (BS) loses stability at $\mathrm{Re} = \mathrm{Re}_{\mathrm{H1}} \approx 1929 \pm 1$ and an unstable limit cycle (LC1) is spawned to lower Re. The next order nonlinear terms in the normal form give that the unstable limit cycle undergoes a cyclic-fold bifurcation (also known as a saddle-node bifurcation of limit cycles) at $\mathrm{Re} = \mathrm{Re}_{\mathrm{CF1}} < \mathrm{Re}_{\mathrm{H1}}$. We have numerically determined (see below for details) $\mathrm{Re}_{\mathrm{CF1}} \approx 1913.5 \pm 0.5$. For $\mathrm{Re} < \mathrm{Re}_{\mathrm{CF1}}$ there are no limit cycles locally in phase space, and for $\mathrm{Re} > \mathrm{Re}_{\mathrm{CF1}}$ there are two limit cycles. One is the unstable lower-branch cycle that was spawned at the subcritical Hopf bifurcation, and the other is a stable upper-branch cycle that continues to exist to higher Re [see 94, Ch. 8.2]. The DNS results presented in the previous section, as well as those of [42, 50, 52], show that the upper-branch LC1 is unstable for $\mathrm{Re} \gtrsim \mathrm{Re}_{\mathrm{H1}}$, but only very weakly so in the sense that there is a very long-lived transient that remains close to LC1 before bursting sets in.

The lower-branch LC1 is not directly accessible via DNS as it is unstable. However, by implementing EST [38, 87] using linear combinations of the upper-branch LC2 (which is stable in the symmetry subspace for $\mathrm{Re} \in [\mathrm{Re}_{\mathrm{CF1}}, \mathrm{Re}_{\mathrm{H1}}]$, see Section 2.3.5) and BS as initial conditions, we have been able to obtain the unsta-

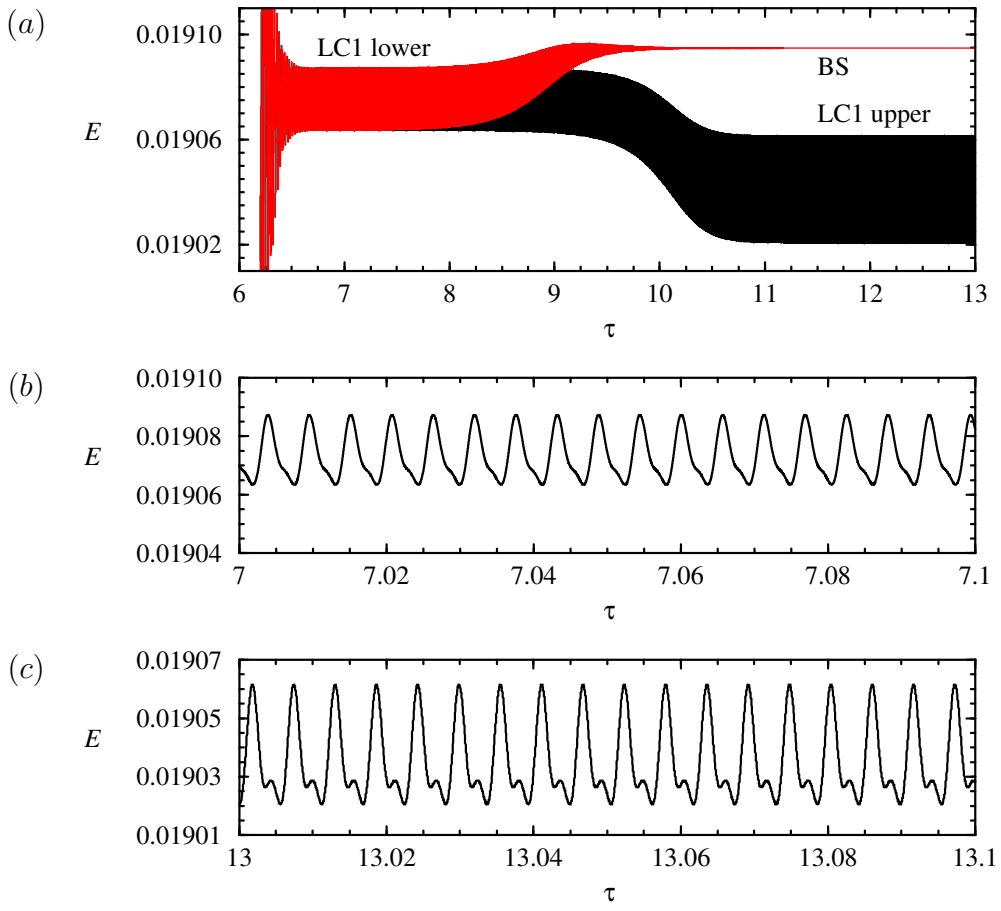

Figure 2.10: Time series of E for EST simulations between BS and upper-branch LC2 at Re $= 1916$, showing (a) two transients using αBS $+ (1 - \alpha)$(LC2 upper) as the initial condition, with $\alpha = 0.644\,442$ (black, evolving to upper-branch LC1) and $\alpha = 0.644\,443$ (red, evolving to BS); (b) shows a close-up of the time series for $\tau \in [7.0, 7.1]$ during which the transients are very close to lower-branch LC1, and (c) shows the upper-branch LC1 oscillations for $\tau \in [13.0, 13.1]$.

ble lower-branch LC1 as a long transient. A pair of transients at Re = 1916 using αBS + $(1-\alpha)$(LC2 upper) as the initial condition, with $\alpha = 0.644\,442$ and $\alpha = 0.644\,443$ are shown in Fig. 2.10. With these two slightly different values of α, the transient remains close to the unstable lower-branch LC1 for about 1.5 viscous times, corresponding to about 270 oscillations, before the transient corresponding to the larger α evolves and converges to BS, while the other transient converges to the upper-branch LC1. Close-ups of the oscillations corresponding to lower- and upper-branch LC1 are shown over 0.1 viscous times in Fig. 2.10(b, c); they both have approximately the same period, and the upper-branch LC1 has larger amplitude and the form of its oscillation is more nonlinear. During the entire duration of these simulations, S remains at machine zero levels, indicating that the dynamics is occurring in the symmetry subspace.

By implementing EST for $\mathrm{Re} \in [\mathrm{Re}_{\mathrm{CF1}}, \mathrm{Re}_{\mathrm{H1}}]$, we have been able to capture the lower-branch LC1. Figure 2.11 is a bifurcation diagram in the neighborhood of the subcritical Hopf bifurcation H_1, using the standard deviation in the energy oscillations $\sigma(E)$ as the state variable and Re as the bifurcation parameter. We use $\sigma(E)$ as a measure of the oscillation amplitude as the oscillations are far from harmonic, and so a peak-to-peak measure is not a good measure as it typically overestimates the average deviation away from the mean. Also shown is the cyclic-fold bifurcation CF_1 where the lower- and upper-branch LC1 meet at $\mathrm{Re}_{\mathrm{CF1}} \approx 1913.5 \pm 0.5$. For $\mathrm{Re} < \mathrm{Re}_{\mathrm{H1}}$, BS is stable, and for $\mathrm{Re} > \mathrm{Re}_{\mathrm{H1}}$, BS loses stability acquiring one unstable (eigen) direction. Since the bifurcation is subcritical, with LC1 being spawned to lower Re, LC1 also has one unstable direction. At CF_1, LC1 folds from the lower to the upper branch and becomes stable (no unstable direction). We verified the stability of LC1 via DNS at Re = 1916 over 120 viscous time units, corresponding to over 20 000 oscillations. LC1 loses stability in a Neimark–Sacker bifurcation NS_1 (a Hopf bifurcation of limit

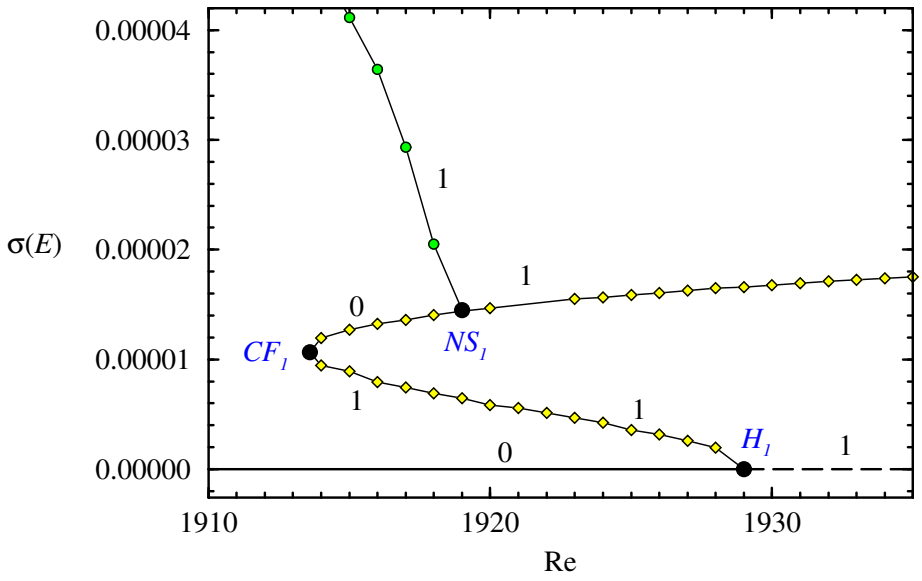

Figure 2.11: Bifurcation diagram in the neighborhood of the subcritical Hopf bifurcation. The solid and dashed lines with $\sigma(E) = 0$ correspond to BS, the curve with the yellow diamonds corresponds to LC1, and the curve with green circles corresponds to a mixed-mode between LC1 and LC2. The subcritical Hopf where BS loses stability is labeled H_1, the cyclic-fold bifurcation between the lower and upper branches of LC1 is labeled CF_1, and the Neimark–Sacker bifurcation on the upper branch of LC1 is labeled NS_1. Along each equilibrium solution branch segment, there is an integer indicating the number of unstable directions associated with the equilibrium.

cycles) at $\mathrm{Re} = \mathrm{Re}_{\mathrm{NS1}} \approx 1919 \pm 1$. For $\mathrm{Re} > \mathrm{Re}_{\mathrm{NS1}}$, LC1 has one unstable direction. The details of how NS_1 is determined will be given below in §2.3.5, but briefly it involved using EST with LC2 (stabilized in the symmetry subspace) and BS. For some combinations, we found a long-lived transient with a quasi-periodic signature, QPs. Figure 2.12 shows two such transients at $\mathrm{Re} = 1916$ that both stay close to QPs for over three viscous times and then one evolves toward LC2 and the other toward LC1. Also shown in the figure are the time series and corresponding power spectral density (PSD) of E over a time interval when the flow is close to QPs. It is clear that QPs is a mixed-mode of LC1 and LC2. EST simulations show that QPs exists for $\mathrm{Re} < \mathrm{Re}_{\mathrm{NS1}}$, i.e. the Neimark–Sacker bifurcation of LC1 is subcritical, and so QPs

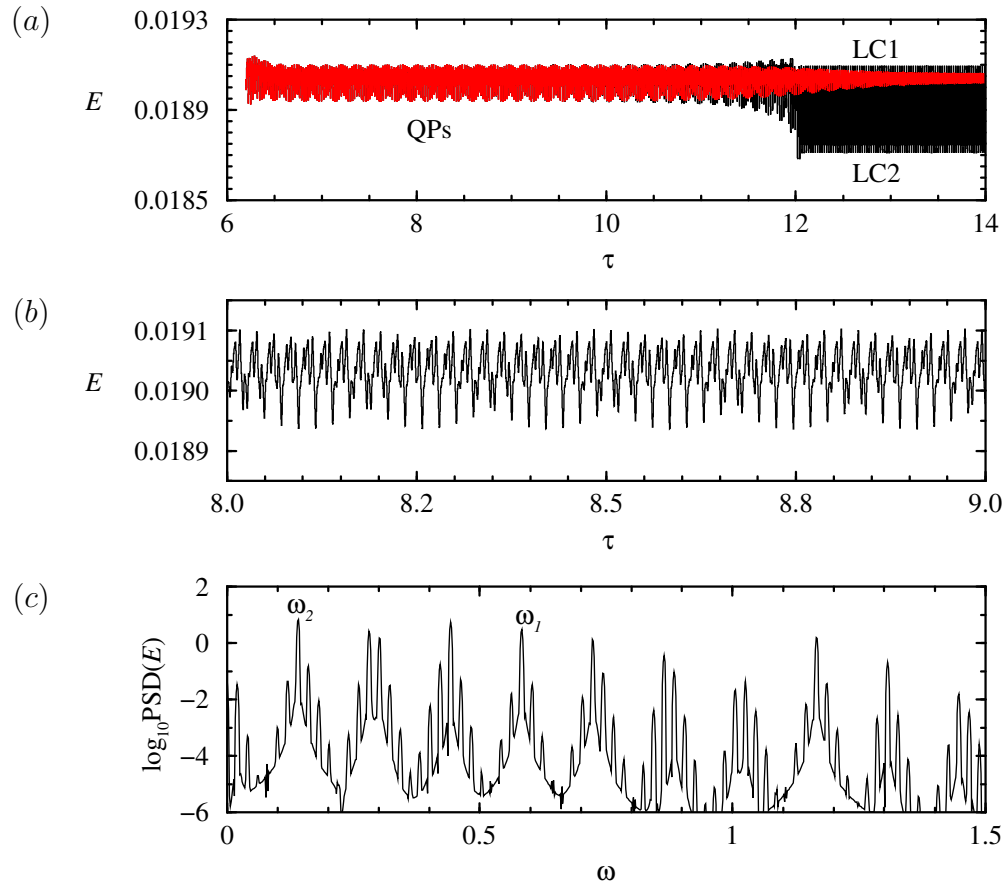

Figure 2.12: Time series of E for EST simulations in the symmetry subspace between BS and upper-branch LC2 at Re = 1916, showing (a) two transients using $\alpha\mathrm{BS}+(1-\alpha)$(LC2 upper) as the initial condition, with $\alpha = 0.629\,428\,5$ (black, evolving to upper-branch LC2) and $\alpha = 0.629\,428\,6$ (red, evolving to upper-branch LC1), (b) shows a close-up of the time series for $\tau \in [8.0, 8.3]$ during which the transients are very close to QPs, and (c) is the power spectral density (PSD) of the time series of E over $\tau \in [7.0, 10.]$.

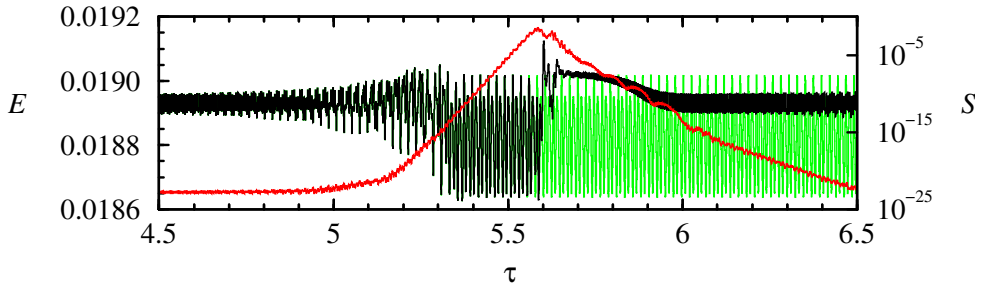

Figure 2.13: Time series of E and S at $\mathrm{Re} = 1940$. Shown are the same time series from Fig. 2.2(b), but zoomed in for $\tau \in [4.5, 6.5]$ (black for E and red for S), as well as the time series starting with the same initial condition at $\tau = 0$, but computed in the symmetry subspace (only E is shown, in green, as $S = 0$ in the subspace).

has one unstable direction. More details are presented in §2.3.5. The important point here is that the upper-branch LC1 had to lose stability for the DNS results showing bursting (as in Fig. 2.2) to make sense. Note that the upper-branch LC1 is only stable over the range $\mathrm{Re}_{\mathrm{CF1}} < \mathrm{Re} < \mathrm{Re}_{\mathrm{NS1}}$, with $(\mathrm{Re}_{\mathrm{NS1}} - \mathrm{Re}_{\mathrm{CF1}})/(\mathrm{Re}_{\mathrm{NS1}} + \mathrm{Re}_{\mathrm{CF1}}) \approx 0.0014$, which is very small and easily missed; [42, 50, 52] do not report LC1 as being stable for any Re.

2.3.5 Dynamics in the Symmetry Subspace

The intermittent bursting behavior for $\mathrm{Re} \approx \mathrm{Re}_{\mathrm{H1}}$, with the bursts correlated with large increases in the flow asymmetry, is a poorly understood feature of the onset of unsteadiness in the cubic lid-driven cavity [42, 50, 52]. In this section we explore the flow dynamics in the symmetry subspace in order to further investigate what dynamics are involved. Numerically, the flow is restricted to the subspace simply by setting $\boldsymbol{u} = 0.5(\boldsymbol{u} + \mathcal{A}(\mathcal{K})\boldsymbol{u})$ at every time step (and intermediate time step) in the simulation.

Figure 2.13 shows a typical evolution in the subspace and compares it to that in the full space. The figure includes the time series from Fig. 2.2(b), cropped to

$\tau \in [4.5, 6.5]$ to focus on the first burst event. From Fig. 2.2(b), we saw that the flow stays very close to LC1 for over 4 viscous times before undergoing a burst. In Fig. 2.13, we now appreciate that the flow starts to depart from LC1 before there is any appreciable increase in its asymmetry, i.e. S does not start to grow until $\tau \approx 4.9$, but by $\tau = 4.6$ there is a significant departure from the periodic signal associated with LC1 due to a modulation. This modulation is due to the Neimark–Sacker bifurcation NS_1 at which QPs is spawned. By $\tau \approx 5.2$, QPs is large and becomes irregular while S is growing exponentially. There is a rapid adjustment in the flow and by $\tau \approx 5.4$, the flow transient approaches close to LC2. During this time, S is still small, but continues to grow exponentially. Over this same period of time, the evolution in the symmetric subspace is virtually identical (except, of course, that $S = 0$). This is clear evidence that the transition from LC1 to LC2 via modulation is not due to symmetry breaking; LC1 is unstable in the subspace, as is BS at this Re, and there is an eventual evolution to LC2 which is virtually identical to that in the full space.

The evolution in the subspace converges onto LC2 at $\tau \approx 5.4$ and remains at LC2 indefinitely. In the full space, LC2 is unstable to symmetry breaking. By $\tau \approx 5.55$, there is an appreciable difference between the kinetic energy of LC2 in the full space and that in the subspace. As S saturates at $\tau \approx 5.6$, the evolution quickly evolves away from the unstable LC2, briefly approaches the unstable BS, which nevertheless is symmetric, and so during the approach to BS S decays exponentially. Since BS is unstable, the evolution ends up tracking an unstable manifold away from BS and approaches LC1. In the full space (at Re = 1940 under consideration) LC1 is unstable, and like BS it too is symmetric. Hence, while the evolution is in the neighborhood of LC1, S continues to decay exponentially, albeit at a different rate. LC1 becomes modulated by $\tau \approx 6.2$, but this modulation is also symmetric and S continues to decay exponentially. As the modulation amplitude grows, another burst is initiated,

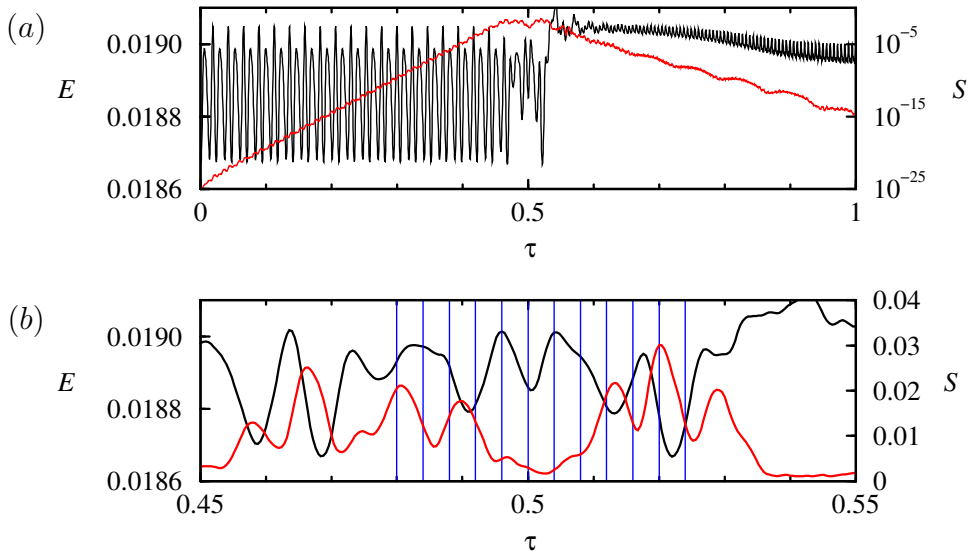

Figure 2.14: Time series of E (black) and S (red) for Re = 1930, (b) is a close-up of (a) near $\tau = 0.5$; the vertical blue lines correspond to the times of the snap-shots shown in Fig. 2.15.

as shown in Fig. 2.2(b). So, in summary, we have for Re $\gtrsim$ 1930 that both BS and LC1 are unstable but symmetric, and LC2 is stable in the subspace, but unstable to symmetry breaking.

It is now interesting to examine the symmetry-breaking of LC2 in the full space. To do this, we have first computed LC2 in the subspace at Re = 1930, and used that solution as initial condition for a simulation in the full space at the same Re = 1930. Figure 2.14(a) shows the evolutions of E and S in this simulation. Initially, S is at machine epsilon squared and grows exponentially. During this early part of the evolution, the flow essentially corresponds to the LC2 state that is stable in the subspace, until $\tau \approx 0.5$ by which time S has grown to $\sim 10^{-3}$ and a bursting event very similar to those shown in Fig. 2.2(a) is initiated. Figure 2.14(b) is a close-up of the evolution shown in Fig. 2.14(a), covering the duration of the burst when S is maximal and just as the flow transitions toward LC1 and S decays exponentially. The twelve vertical (blue) lines in the figure correspond to snap-shots of the helicity

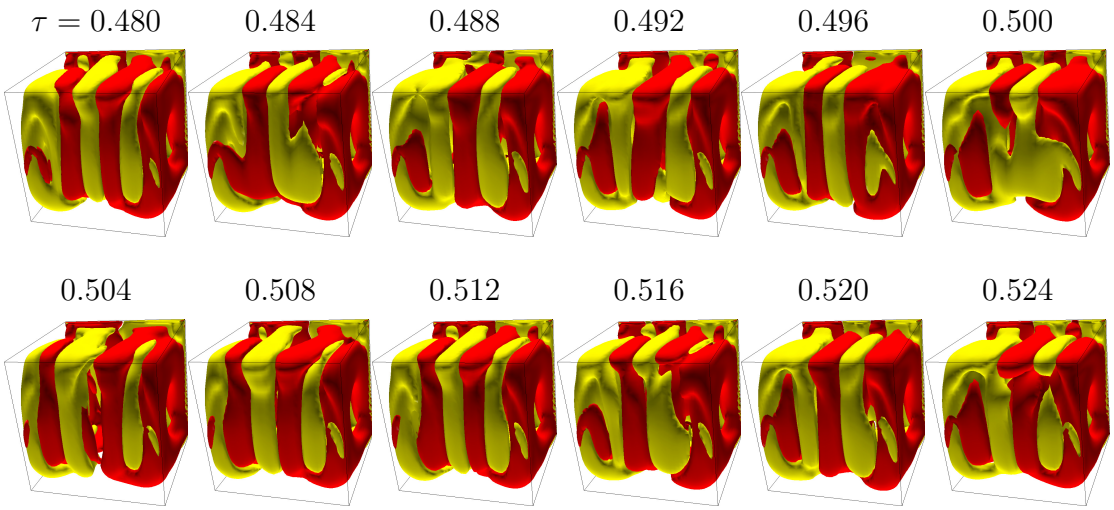

Figure 2.15: Helicity isosurfaces at $\mathcal{H} = \pm 10^5$ for $\mathrm{Re} = 1930$ during the transition from LC2 at times indicated by the blue vertical lines in Fig. 2.14(b). See Supplemental Material [59] for an animation from $\tau = 0.344$ to 0.664.

isosurfaces shown in Fig. 2.15. Note that these isosurfaces are of the full solution, in contrast to those shown in Figs. 2.4 and 2.5 which showed helicity isosurfaces of the deviation away from the mean; during the bursting event, there is no meaningful mean. As such, the isosurfaces include the contribution from the spanwise endwall regions. The nature of the flow is difficult to discern from the twelve snap-shots, but the corresponding online movie [59] is very insightful. The movie starts at $\tau = 0.344$ when the flow is very near LC2 and consists of waves traveling symmetrically in from the two spanwise endwalls and annihilating at the midplane, i.e. the typical LC2 behavior described earlier. Then, in the transitional stage with $\tau \in (4.8, 5.2)$, during which S has saturated, the flow consists of waves traveling from one spanwise endwall to the other. This traveling wave TW is very unstable and only lasts for about one and a half cycles, but it is clearly discernable in the movie. In principle, both left and right traveling waves are possible, and which is observed depends on the details of the symmetry-breaking perturbation at the time. The instability of TW is likely

due to confinement effects in the cubic cavity. Such traveling waves states have been observed experimentally in an oscillatory lid-driven cavity of large spanwise extent [47], and are related to the symmetry breaking dynamics in the spanwise periodic idealization of that flow [10, 64, 11]. Following the instability of TW, the movie shows a rapid transition to oscillations that are converging toward LC1.

The differences between the evolutions in the full space and in the subspace for $\mathrm{Re} < \mathrm{Re}_{\mathrm{H1}} \approx 1929$ also provide significant insight into the dynamics involved. As mentioned in the previous section, evolutions for $\mathrm{Re} \lesssim 1930$ in the full space eventually converge onto the stable BS, independently of initial conditions, as BS is the only stable state at these Re, except for $\mathrm{Re}_{\mathrm{CF1}} < \mathrm{Re} < \mathrm{Re}_{\mathrm{NS1}}$, an interval of only 6 units in Re ($[\mathrm{Re}_{\mathrm{NS1}} - \mathrm{Re}_{\mathrm{CF1}}]/[\mathrm{Re}_{\mathrm{NS1}} + \mathrm{Re}_{\mathrm{CF1}}] \approx 0.0014$), over which LC1 is also stable. In the subspace however, LC2 is stable down to $\mathrm{Re} = \mathrm{Re}_{\mathrm{CF2}} \approx 1872$, where it undergoes a cyclic-fold bifurcation CF_2, and does not exist for lower Re, leaving BS as the only stable state for $\mathrm{Re} < \mathrm{Re}_{\mathrm{CF2}} \approx 1871.5 \pm 0.5$.

For $\mathrm{Re} \gtrsim \mathrm{Re}_{\mathrm{CF2}}$, we have implemented EST in the symmetry subspace, using linear combinations of BS and LC2 in order to localize the lower-branch LC2 involved in the cyclic-fold bifurcation CF_2. In the subspace, near the cyclic-fold bifurcation, the lower-branch LC2 is a saddle limit cycle with one unstable direction. Figure 2.16 shows time series of E for a pair of EST simulations in the subspace at $\mathrm{Re} = 1883$, where the initial conditions were (α)BS+$(1-\alpha)$(LC2 upper) with $\alpha = 0.390\,426\,457\,32$ that ended up evolving to BS and $\alpha = 0.390\,426\,457\,30$ that ended up evolving to upper-branch LC2. With these choices of α, the evolutions remain very close to the saddle lower-branch LC2 for about one viscous time; Fig. 2.16(b) is a close-up of the E time series over $\tau \in [9.4, 9.7]$ to more clearly see the oscillations of lower-branch LC2. From this we have extracted the standard deviation of the oscillation, $\sigma(E)$, and the corresponding frequency. Figure 2.16(c) is a close-up over $\tau \in [10.2, 10.5]$ of the

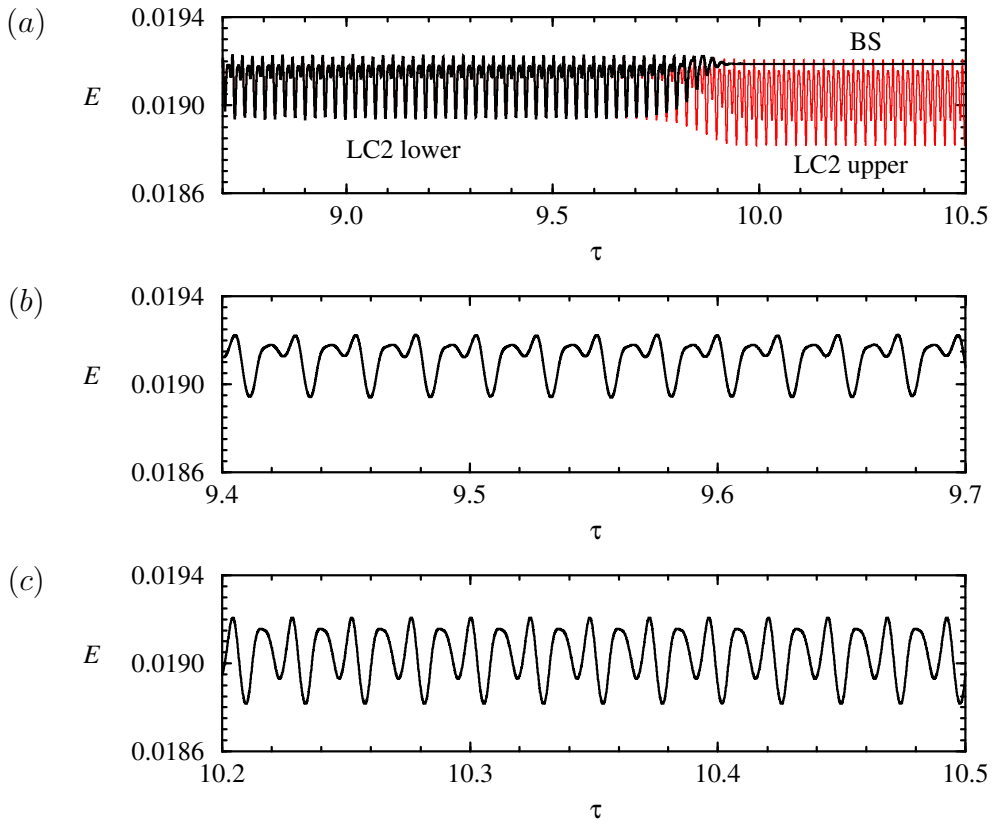

Figure 2.16: Time series of E for EST simulation in the symmetric subspace between BS and upper-branch LC2 at Re = 1883, showing (a) two transients using αBS + $(1-\alpha)$(LC2 upper) as the initial condition, with $\alpha = 0.390\,426\,457\,32$ (black, evolving to BS) and $\alpha = 0.390\,426\,457\,30$ (red, evolving to upper-branch LC2), (b) presents a zoom of the time series for $\tau \in [9.4, 9.7]$ during which the transients are very close to lower-branch LC2, and (c) shows the upper-branch LC2 oscillations for $\tau \in [10.2, 10.5]$.

time series that evolves to LC2. We have made movies of these two oscillations (not shown) and they are essentially the same as the one associated with upper-branch LC2 in Fig. 2.5.

The identification of the unstable lower-branch LC2 emanating from CF_2 is relatively straight-forward because in the symmetry subspace its unstable manifold is only one-dimensional and can parameterized by α: lower-branch LC2 is the edge state between upper-branch LC2 and BS, corresponding to a single value of α. With devia-

tions only in the 11th significant figure away from this value of α, we obtain transients that remain very close to lower-branch LC2 for more than one viscous time. Larger deviations in α reduce this time considerably. Repeating the EST simulations to higher Re also reduces the time spent near lower-branch LC2 for the same level of refinement in α. For $\mathrm{Re} \gtrsim 1886$, EST simulations with refinements of α to different values lead to long transients close to either lower-branch LC2, much as been just described, or to QPs as illustrated in Fig. 2.12 for $\mathrm{Re} = 1916$. This indicates that lower-branch LC2 undergoes a Neimark–Sacker bifurcation, NS_2 (by doing several EST simulations at many Re, we estimate this to occur at $\mathrm{Re} = \mathrm{Re}_{\mathrm{NS2}} \approx 1886 \pm 3$), spawning the mixed-mode QPs supercritically (i.e. to larger Re). The supercriticality of NS_2 means that lower-branch LC2 acquires another unstable direction for $\mathrm{Re} > \mathrm{Re}_{\mathrm{NS2}}$, totaling two in the symmetry subspace, and QPs has the same number of unstable directions as the lower-branch LC2 from which it bifurcates, namely one. Having only one unstable direction, QPs was tracked via EST all the way to NS_1 where it is absorbed by upper-branch LC1 (see Fig. 2.11 and the accompanying text for details). For lower-branch LC2, having two unstable directions for $\mathrm{Re} > \mathrm{Re}_{\mathrm{NS2}}$ means that localizing it using bisection in α is no longer possible. We have been able to localize lower-branch LC2 up to $\mathrm{Re} = 1914$, but for larger Re a different strategy is needed.

The evolution of E and S in the full space at $\mathrm{Re} = 1916$ when started from QPs, which is now unstable in at least two directions, shown in Fig. 2.17. In addition to the unstable direction in the symmetry subspace, QPs now has an additional unstable direction out of the subspace, illustrated by the growth of S associated to the smaller value of α. For that initial condition, QPs loses stability via symmetry breaking, and the dynamics eventually visits the basin of attraction of BS, while the state originating from an initial condition associated to the slightly larger α remains symmetric and

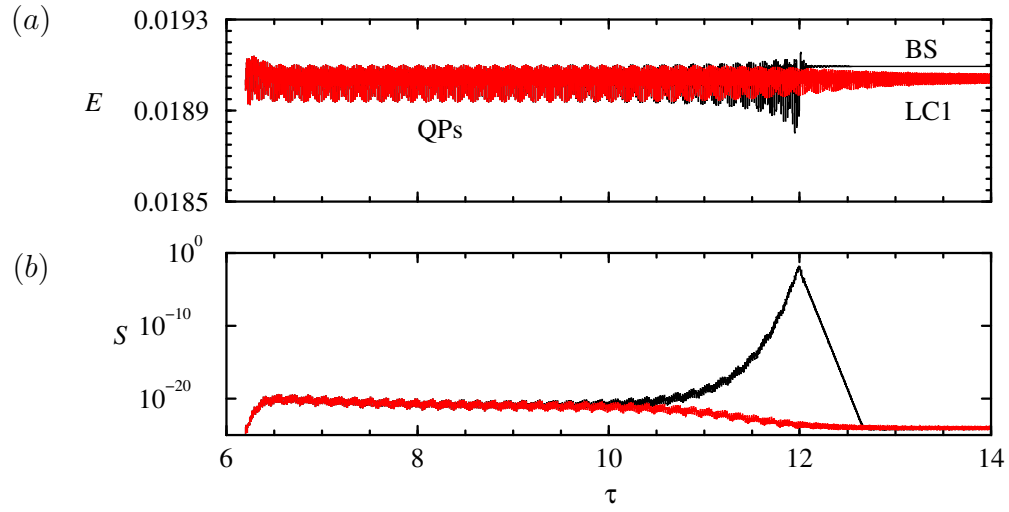

Figure 2.17: Time series of (a) E and (b) S for EST simulations at Re $= 1916$, showing two transients using $\alpha\mathrm{BS} + (1-\alpha)$(LC2 upper) as the initial condition, with $\alpha = 0.629\,428\,5$ (black, evolving to BS) and $\alpha = 0.629\,428\,6$ (red, evolving to upper-branch LC1). These EST runs are the same as those shown in Fig. 2.12, but executed in the full space.

Bifurcation	Re
H_1: first Hopf of BS	1929 ± 1
H_2: second Hopf of BS	2089 ± 1
CF_1: cyclic-fold of LC1	1913.5 ± 0.5
CF_2: cyclic-fold of LC2	1871.5 ± 0.5
NS_1: Neimark–Sacker of LC1 (upper branch)	1919 ± 1
NS_2: Neimark–Sacker of LC2 (lower branch)	1886 ± 3

Table 2.1: List of bifurcations encountered, and the critical Re at which they occur.

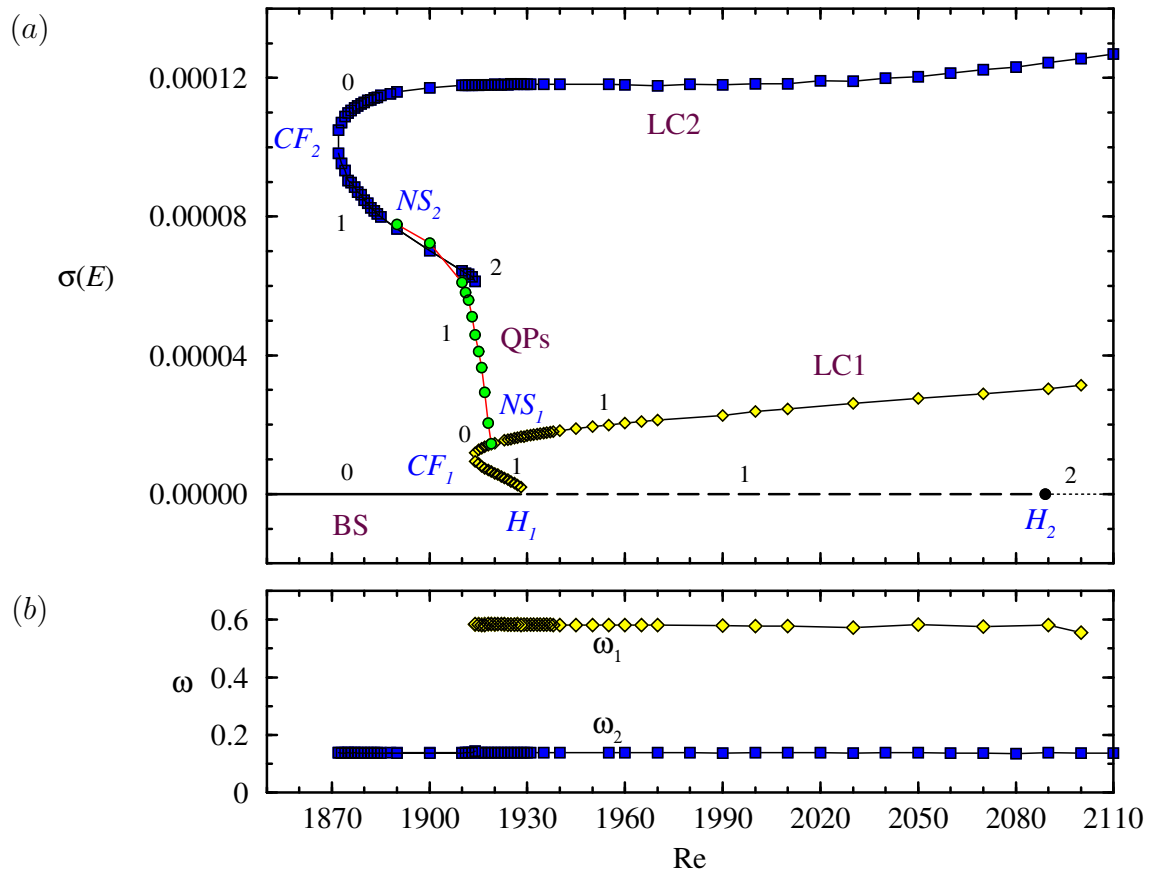

Figure 2.18: Variation with Re of (a) the oscillation amplitudes, $\sigma(E)$, of the various states as indicated, with integer indicating the number of unstable directions associated with each state (unstable states were found by restriction to the symmetry subspace, SFD or EST), and (b) the frequencies ω_1 and ω_2 of LC1 (diamonds) and LC2 (squares). Note that the frequencies of the upper and lower branches of each are virtually the same. The critical Re for the various bifurcations indicated are listed in Table 2.1.

evolves toward LC1, which is the only other stable state in the full space at this Re besides BS. The similarity in spectral signatures between QPs in Fig. 2.12 and QPa in Fig. 2.7 obtained at a slightly lower Re suggests that the symmetry breaking of QPs indeed results in QPa (a pair of them, related by the reflection).

2.3.6 Summary of Identified States

All the information acquired using the various numerical techniques is used to construct Fig. 2.18, showing the standard deviation in the kinetic energy $\sigma(E)$ and the oscillation frequency ω of the states found. A brief overview of the various states in Fig. 2.18, how they were found, and their stability properties that we have been able to educe, now follows:

- BS — the basic state, by definition is symmetric. It first loses stability at $\mathrm{Re} = \mathrm{Re}_{\mathrm{H1}}$ in a subcritical Hopf bifurcation H_1, and then suffers a second Hopf bifurcation H_2 at $\mathrm{Re} = \mathrm{Re}_{\mathrm{H2}}$. The unstable BS was computed via SFD and the bifurcations were identified using Arnoldi iterations.

- LC1 — this limit cycle is spawned from BS at H_1 subcritically toward lower Re. At onset, it has one unstable direction. It undergoes a cyclic-fold bifurcation CF_1 at $\mathrm{Re} = \mathrm{Re}_{\mathrm{CF1}}$, where it (the lower-branch) is folded to continue to higher Re (the upper-branch). The upper-branch is stable for $\mathrm{Re} \in (\mathrm{Re}_{\mathrm{CF1}}, \mathrm{Re}_{\mathrm{NS1}})$; at $\mathrm{Re}_{\mathrm{NS1}}$ it undergoes a Neimark–Sacker bifurcation and for $\mathrm{Re} > \mathrm{Re}_{\mathrm{NS1}}$, LC1 has one unstable direction. Even though it is unstable, the growth rate of small perturbations away from it is very slow, and its characteristics can be determined via DNS with initial conditions that are reasonably close to LC1. The lower branch LC1 was computed using EST with linear combinations of BS and upper-branch LC2 as well as linear combinations of BS and upper-branch

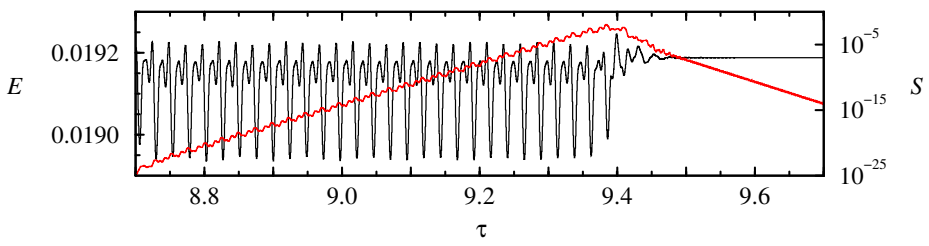

Figure 2.19: Time series of E (black) and S (red) starting from the EST-determined lower-branch LC2 (using αBS + $(1-\alpha)$(LC2 upper) as the initial condition, with $\alpha = 0.390\,426\,457\,30$), but evolving in the full space, at Re = 1883.

LC1. LC1 (both lower and upper branches) are stable to symmetry breaking; this was determined by monitoring S during simulations.

- LC2 — this limit cycle was first found by restricting DNS to the symmetric subspace. For $\mathrm{Re} > \mathrm{Re}_{\mathrm{H1}}$, there are no stable steady or time-periodic solutions in the full space, but in the subspace any initial condition evolves to LC2. LC2 was continued down to $\mathrm{Re} = \mathrm{Re}_{\mathrm{CF2}}$ where it undergoes a cyclic-fold bifurcation CF_2, and is folded to form lower-branch LC2 which has one unstable direction in the subspace for $\mathrm{Re} \in (\mathrm{Re}_{\mathrm{CF2}}, \mathrm{Re}_{\mathrm{NS2}})$. This lower-branch LC2 was computed using EST in the subspace with combinations of BS and upper-branch LC2 as initial conditions. DNS in the full space with LC2 (upper and lower) as initial conditions show that LC2 is unstable to symmetry breaking. An example of such a DNS at Re = 1883 is shown in Fig. 2.19. The initial condition used was close to lower-branch LC2. The figure shows exponential growth in S while the trajectory is near LC2. For $\mathrm{Re} > \mathrm{Re}_{\mathrm{NS2}}$, lower-branch LC2 in the subspace has two unstable directions, and we were not able to continue it very far using EST. However, it is a reasonable conjecture that it continues until it meets BS at H_2, given the similarities in the spatio-temporal structure of lower- and upper-branch LC2 and the eigenfunction that bifurcates at H_2 (see next subsection

for supporting arguments).

- QPs — for Re $\in (\mathrm{Re}_{\mathrm{NS2}}, \mathrm{Re}_{\mathrm{NS1}})$ there is a symmetric quasiperiodic state that is a mixed mode of LC1 and LC2. It was found using EST using certain combinations of BS and LC2 as initial conditions in the symmetric subspace. As is typical of quasiperiodic mixed modes, it is spawned at a Neimark–Sacker bifurcation of one limit cycle (NS_2 on lower-branch LC2) and terminates at another Neimark–Sacker bifurcation of the other limit cycle (NS_1 on upper-branch LC1). QPs in the subspace has one unstable direction. DNS in the full space using QPs as initial conditions show that it also has an unstable direction out of the subspace. This indicates that a pitchfork bifurcation of QPs would spawn a pair of symmetry-related mixed modes in the full space, QPa. QPa would have (at least) two unstable directions. We have seen glimpses of QPa, for example at Re = 1980 (see Fig. 2.7) and Re = 2000 (see Fig. 2.8).

2.3.7 Connection Between LC2 and H_2

The picture summarized in the previous subsection is fairly complete albeit missing some pieces, specifically the possible connection between the lower-branch LC2 and the second Hopf bifurcation H_2. As already noted by [50, 52] and confirmed by our own analysis in § 2.3.3, the Hopf frequency is very close to the oscillation frequency of LC2, suggesting that LC2 is the limit cycle that bifurcates from BS at H_2. To further support this conjecture, we compare the spatio-temporal structure of LC2 with that of the eigenfunction corresponding to λ_2. Figure 2.20 shows the spatio-temporal dynamics of the y-component of the real part of the rotated eigenmode $\mathbf{\Phi_2}$ associated to $\lambda_2 = \rho + i\omega$,

$$\mathbf{\Phi}(x, y, z, t) = Re(\mathbf{\Phi_2})\cos(\omega t) + Im(\mathbf{\Phi_2})\sin(\omega t). \tag{2.8}$$

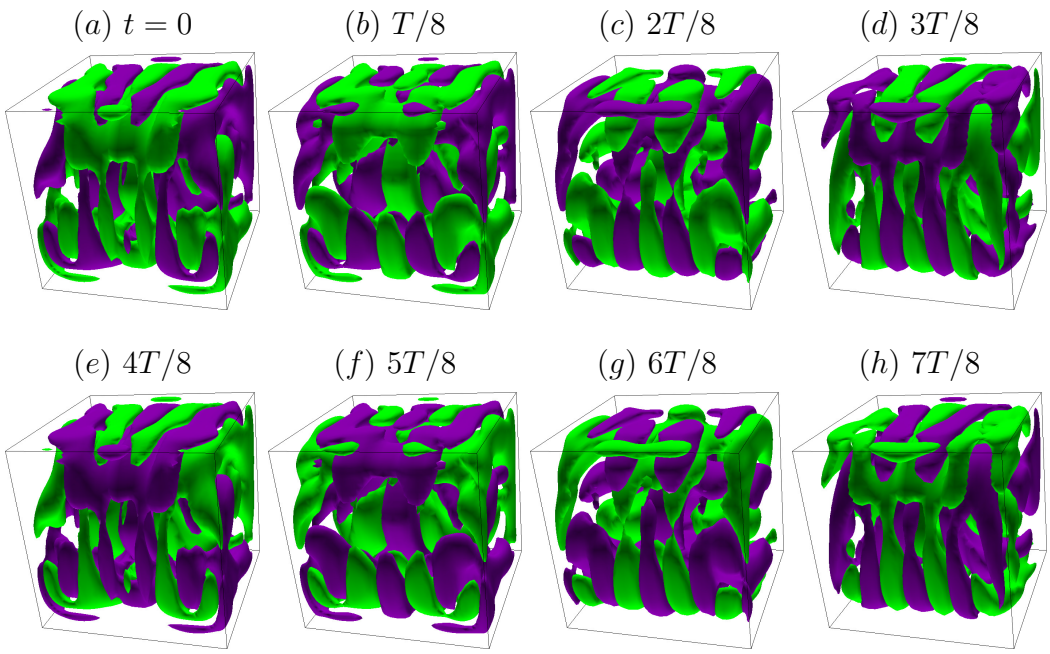

Figure 2.20: Isosurfaces of the y component of $\mathbf{\Phi}$ at Re $= 2090$. The isosurfaces (green is positive and purple is negative) are at $\pm 15\%$ of the maximum over one period. See Supplemental Material [59] for an animation.

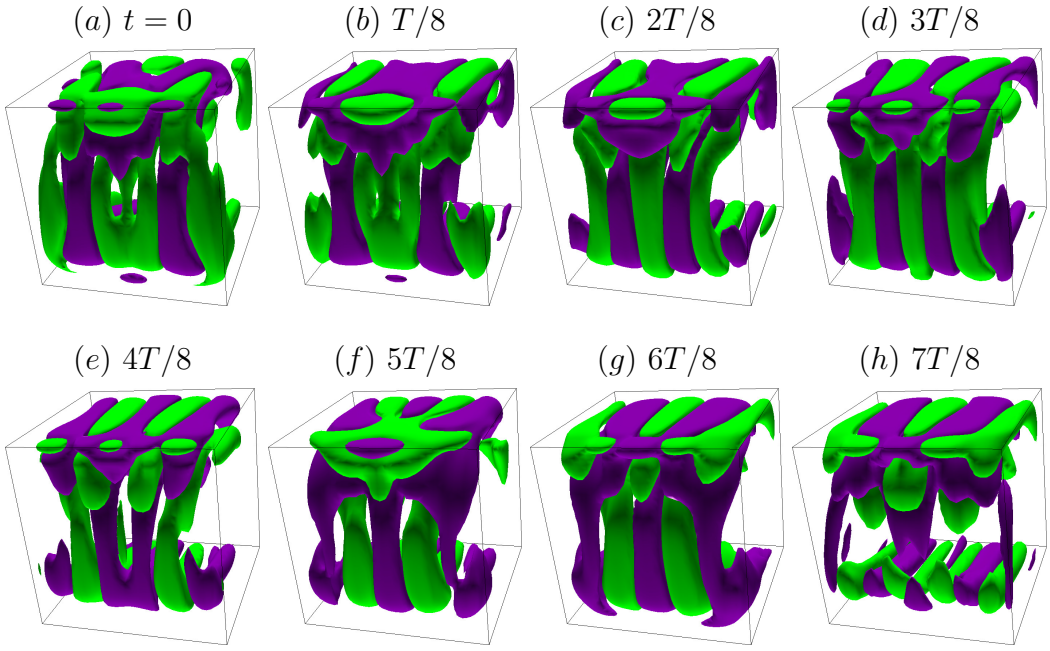

Figure 2.21: Isosurfaces of $v - \langle v \rangle$ at ± 30 at Re $= 2090$ (green is negative and purple is positive). See Supplemental Material [59] for an animation.

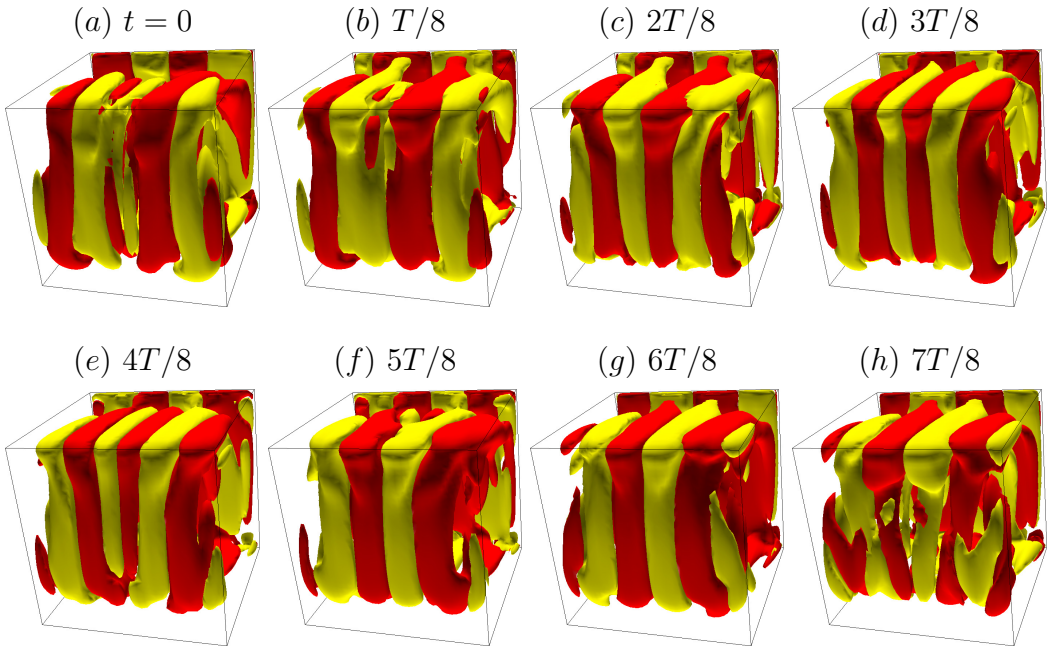

Figure 2.22: Isosurfaces of $\mathcal{H} - \langle \mathcal{H} \rangle$ at $\pm 10^5$ at Re = 2090 (yellow is negative and red is positive). See Supplemental Material [59] for an animation.

The resulting cycle consists of waves coming in symmetrically from lateral walls meeting at the midplane. For comparison purposes, isosurface of $v - \langle v \rangle$ of upper-branch LC2 at Re = 2090 is shown in Fig. 2.21 and exhibits the same type of spatio-temporal behavior. The comparison is even clear from the two corresponding online movies [59]. Figure. 2.22 shows the isosurfaces of $\mathcal{H} - \langle \mathcal{H} \rangle$ of upper-branch LC2 at Re = 2090, which are very similar to those at Re = 1930 shown in Fig. 2.5 and the accompanying online movies.

2.4 Discussion and Conclusions

Symmetries and symmetry-breaking bifurcations play an important role in canonical flows, often leading to spatio-temporal chaos in the neighborhood of primary instabilities, and may be intricately involved in the transition to turbulence. The lid-driven cavity is one such canonical flow, and recent explorations of the onset of

unsteadiness in the cubic cavity have revealed that it comes in the form of bursts at irregular time intervals. With careful consideration of the symmetries of the problem and comparing the flows in the full space and in the symmetric subspace, we have shown that the bursts are excursions away from and back toward the symmetric subspace. These excursions are trajectories in phase space shadowing the stable and unstable manifolds of several saddle states that result following two successive Hopf bifurcations of the basic state as the Reynolds number is increased. Similar complicated dynamics associated with symmetry-breaking bifurcations in a very small neighborhood of parameter space, resulting in slow drifts from one saddle state to another, have been studied in other canonical flows, such as small aspect-ratio Taylor–Couette flow [54, 55, 2, 62, 3] and precessing cylinder flow [63, 56].

Our simulations, both in the full space and in the symmetric subspace, strongly indicate that the onset of unsteadiness in the cubic lid-driven cavity is organized by two successive subcritical Hopf bifurcations of the base state. The two Re at which these occur differ by about 8%. This can lead to the type of intermittency that has been reported; the other ingredient needed in order to rationalize the observation is the breaking of the spanwise reflection symmetry. The subcritical nature of the first Hopf bifurcation along with the symmetry breaking results in all steady, periodic, and quasi-periodic states being unstable local saddle states with a very small number of unstable manifolds in the full space for Re beyond the first bifurcation of the basic state. The lack of any local attractors often leads to intermittent chaotic behavior, with chaotic bursts resulting from repeated divergence away from the (weakly) repelling steady, periodic, or quasiperiodic state, alternating with nearly-periodic phases as the trajectory is re-injected into the vicinity of the weakly unstable local states. However, in the symmetric subspace LC2 is stable, and the intermittent bursting is not present.

Acknowledgements

This work was partially supported by National Science Foundation grant CBET-1336410. The computations were performed on the Saguaro Cluster of ASU Research Computing and School of Mathematical and Statistical Sciences computing facilities.

Chapter 3

VERTICALLY FORCED STABLY STRATIFIED CAVITY FLOW: INSTABILITIES OF THE BASIC STATE

ABSTRACT

The linear stability of a stably stratified fluid-filled cavity subject to vertical oscillations is determined via Floquet analysis. Retaining the viscous and diffusion terms in the Navier–Stokes–Boussinesq equations with no-slip velocity boundary conditions, no-flux temperature conditions on the sidewalls and constant temperatures on the top and bottom walls, we find that the instabilities are primarily subharmonic (as is typical in many parametrically forced systems), except for a few low forcing frequency ranges where the instability is synchronous. When the viscosity is small, the Floquet modes resemble the inviscid eigenmodes of the unforced problem, except in boundary layers. We establish scaling laws quantifying how viscosity regularizes the degeneracy associated with the inviscid idealization, and how it scales the thickness and intensity of the boundary layers. The product of boundary layer thickness and intensity remains constant with decreasing viscosity, leading to a delta distribution of vorticity on the walls in the limit of zero viscosity. This is in contrast to the zero wall vorticity in the inviscid case.

3.1 Introduction

Parametrically-driven internal waves in a laterally enclosed container filled with an initially linearly stratified fluid have received relatively little attention compared to the study of parametrically-driven interfacial waves, known as the Faraday wave

problem [see the review by 75]. For the Faraday wave problem, Benjamin and Ursell [8] showed that the linear stability of the flat-surface solution for an inviscid laterally unbounded fluid of infinite depth that is driven by a single-frequency parametric excitation reduced to the consideration of a Mathieu equation. Kumar and Tuckerman [44] showed that viscosity introduces couplings so that the linear stability is no longer described by a single (damped) Mathieu equation. Edwards and Fauve [27] demonstrated experimentally that in containers of large horizontal-to-depth aspect ratios containing fluids of moderate viscosity, the surface wave response to parametric forcing is not strongly dependent on the lateral boundaries of the container. Yih [114], following the approach of Benjamin and Ursell [8], showed that the linear stability of an inviscid continuously stratified and laterally unbounded fluid subjected to vertical oscillations also reduced to a Mathieu equation.

Thorpe [97] considered the laterally bounded stratified problem. He determined the eigenmodes of a container filled with a linearly stratified inviscid fluid, as well as their leading order nonlinear and viscous corrections, by considering small perturbations about the unforced linearly stratified state. In a rectangular container, the eigenmodes can be obtained via separation of variables and are simply products of trigonometric functions of the independent variables. In the two-dimensional case, these modes are enumerated by their horizontal and vertical half wavenumbers, and the linear dispersion relation gives their frequency (the imaginary part of the eigenvalue; the eigenvalues are purely imaginary complex conjugates in the inviscid case) in terms of their half wavenumbers. The inviscid eigenmodes are infinitely degenerate. Viscosity regularizes this degeneracy, but it also results in all the eigenvalues having negative real part, so in order to observe them in a physical setting the system needs to be continuously forced. A number of different forcing strategies have been considered experimentally. Thorpe [97] introduced plungers in the sidewalls of

a rectangular cavity which oscillated in-and-out of the cavity. In this way, a number of the linear inviscid modes where observed when the plunger frequency was near to half of the mode's eigenfrequency; only modes with the same horizontal parity as that of the forcing were excited. For large amplitude forcing, wave breaking and mixing were observed, as well as wave beams emanating from the edges where the plungers and the sidewalls met.

Motivated to see if the internal wave breaking could be related to triadic resonances between linear inviscid eigenmodes, McEwan [69] constructed an experiment similar to that of Thorpe [97], but instead of using plungers, the sidewalls were made to swing like paddles. Here too, some modes were excited, but again wave beams were generated which compromised the comparison to the linear inviscid modes.

Orlanski [79] conducted experiments in a rectangular container filled with linearly stratified fluid that was forced by a pair of paddles flapping on the top surface. The amplitudes of the paddle oscillations were large so that the response was nonlinear; the objective of the study was to investigate the breaking of the forced standing waves. The experiments were compared with theory and numerical simulations assuming that the flow is inviscid. General agreement between experiments and the model results were obtained, however, secondary circulations observed in the experiments were not captured by the theory nor resolved by the numerics, and this raised questions about the model assumption that the container boundaries were unimportant; the model used stress-free boundary conditions for the velocity.

The experiments of Benielli and Sommeria [7] were ground-breaking in that they parametrically forced linearly stratified fluid in a container without any differential motion of the container walls, thus avoiding the associated generation of wave beams and secondary circulations. The forcing used was the harmonic vertical oscillation of the container, akin to the forcing used in the Faraday wave experiments. In order

to observe a finite response, they needed to use a sizable oscillation amplitude. The responses resembled the two-dimensional linear inviscid modes at early times in the experiment, but as these grew in amplitude, nonlinear effects led to wave breaking. They focused on parametrically exciting the 1:1 mode (eigenmode with one half wavelength in the horizontal and vertical directions), which appeared subharmonically, as expected, within the frequency-amplitude regime theoretically predicted to be the 1:1 resonance horn, but they were unable to determine the edges of the horn. Since their experiments, attention of the response to parametric forcing in contained stratified flows has shifted from exciting the container modes to studying the response to localized forcing, usually driven by a wavemaker in a corner of the container driving wave beams into the interior flow [see the reviews in 93, 22]. This has left many open questions regarding the parametrically-driven internal modes of a contained stratified flow. In this paper, we consider the linear stability problem, accounting for viscous and buoyancy diffusion effects with realistic container boundary conditions, and in particular we quantify how viscous effects (damping of modes and their harmonics, and thickness and intensity of boundary layers) scale with the ratio of the viscous time scale to the Archimedian time scale (a non-dimensional Brunt–Väisälä buoyancy frequency).

3.2 Governing Equations and Numerical Techniques

Consider a fluid of kinematic viscosity ν, thermal diffusivity κ, and coefficient of volume expansion β contained in a square cavity of sidelength L. The cavity sidewalls are thermally insulated, whereas the top and bottom endwalls are held at constant temperatures, T_{T} and T_{B}, respectively. Gravity g acts in the downward vertical direction. In the absence of any other external forcing, the fluid is stationary with a stable, linear thermal stratification. Here, we consider the stability of

this system, subjected to vertical harmonic oscillations with angular frequency Ω and amplitude ℓ. The Navier–Stokes equations under the Boussinesq approximation modeling the system are non-dimensionalized with length scale L, Archimedian time scale $\tau_A = 1/\sqrt{g\beta\Delta T/L} = 1/N$, where N is the Brunt–Väisälä buoyancy frequency, and temperature scale $\Delta T = T_{\mathrm{T}} - T_{\mathrm{B}}$. The non-dimensional governing equations in a reference frame attached to the vertically oscillating cavity are

$$\begin{aligned} &\frac{\partial \boldsymbol{u}}{\partial t} + \boldsymbol{u}\cdot\nabla\boldsymbol{u} = -\nabla P + \frac{1}{R_N}\nabla^2\boldsymbol{u} + [1+\alpha\cos(\omega t)]T\boldsymbol{e}_z, \quad \nabla\cdot\boldsymbol{u} = 0, \\ &\frac{\partial T}{\partial t} + \boldsymbol{u}\cdot\nabla T = \frac{1}{PrR_N}\nabla^2 T, \end{aligned} \tag{3.1}$$

where P is the reduced pressure, $\boldsymbol{u} = (u, w)$ is the velocity in the oscillating cavity frame, $T = (T^* - T_{\mathrm{B}})/\Delta T - 0.5$ is the non-dimensional temperature, with T^* the dimensional temperature, and $(x, z) \in [-0.5, 0.5]^2$ is the Cartesian coordinate system whose origin is fixed at the center of the cavity. The system (3.1) is governed by four independent non-dimensional parameters: Brunt–Väisälä number $R_N = NL^2/\nu$, forcing frequency $\omega = \Omega/N$, forcing amplitude $\alpha = \Omega^2\ell/g$, and Prandtl number $Pr = \nu/\kappa$. Note that $Gr = R_N{}^2$ is the Grashof number. We fix the Prandtl number $Pr = 1$, and consider variations in R_N, ω, and α.

No-slip boundary conditions, $u = w = 0$, are imposed on all cavity walls. The top and bottom endwall temperatures are fixed, $T|_{z=\pm0.5} = \pm0.5$, and the sidewalls are insulated, $\partial T/\partial x|_{x=\pm0.5} = 0$.

The static linearly stratified state in the cavity frame of reference, i.e. the basic state,

$$\boldsymbol{u} = 0, \quad T = z, \quad \text{and} \quad P = 0.5z^2[1+\alpha\cos(\omega t)], \tag{3.2}$$

is an equilibrium solution of (3.1) for all R_N, Pr, ω, and α. Linearizing (3.1) about

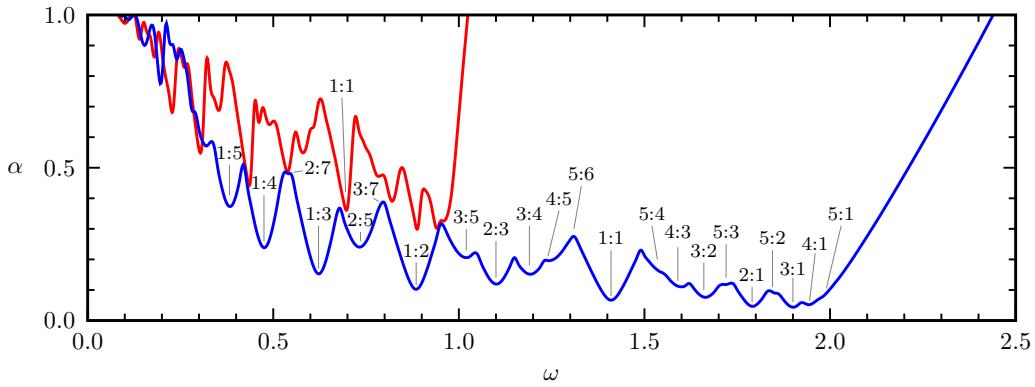

Figure 3.1: Loci of the primary subharmonic (blue curve) and synchronous (red curve) instabilities for $R_N = 2 \times 10^4$. The tips of some low-order $m{:}n$ resonance horns are indicated.

this equilibrium state yields the system

$$\begin{aligned} \frac{\partial \boldsymbol{u}}{\partial t} &= -\nabla p + \frac{1}{R_N}\nabla^2 \boldsymbol{u} + [1 + \alpha\cos(\omega t)]\theta \boldsymbol{e}_z, \quad \nabla \cdot \boldsymbol{u} = 0, \\ \frac{\partial \theta}{\partial t} &= \frac{1}{PrR_N}\nabla^2\theta - w, \end{aligned} \tag{3.3}$$

where $p = P - 0.5z^2[1+\alpha\cos(\omega t)]$ is the perturbation pressure, $\theta = T - z$ is the perturbation temperature, and $\boldsymbol{u}$ is the velocity perturbation away from zero. The boundary conditions are no-slip for $\boldsymbol{u}$ on all walls, no-flux on the sidewalls $\partial\theta/\partial x|_{x=\pm 0.5} = 0$, and $\theta = 0$ on the top and bottom endwalls.

The governing equations (3.3) are discretized in space using a Chebyshev spectral collocation method and in time via a fractional-step improved projection scheme, incorporating the temperature equation as in Mercader *et al.* [74]. Polynomials of degree M in both x and z are used, with $32 \leq M \leq 96$ depending on R_N, and 1000 time steps per forcing period $2\pi/\omega$ are used. The monodromy matrix arising from the Floquet analysis has dimension $3M^2$ and is constructed by evolving a basis for the perturbations (the corresponding identity matrix) over one period.

3.3 Results

We begin by recalling the linear inviscid eigenmodes of the unforced system for the square cavity [97]:

$$\begin{aligned}\psi_{m:n}(x,z,t) &= A_\psi \sin[m\pi(x+0.5)]\sin[n\pi(z+0.5)]\sin(\sigma_{m:n}t),\\ \Theta_{m:n}(x,z,t) &= A_\theta \cos[m\pi(x+0.5)]\sin[n\pi(z+0.5)]\cos(\sigma_{m:n}t),\end{aligned} \tag{3.4}$$

where $\psi_{m:n}$ is the streamfunction such that $(u,w) = (\partial\psi/\partial z, -\partial\psi/\partial x)$, $\Theta_{m:n}$ is the perturbation temperature, A_ψ and A_θ are the corresponding mode amplitudes, $\sigma_{m:n}$ is the eigenfrequency, and $m \geq 0$ and $n > 0$ are the integer half wavenumbers. We shall refer to these inviscid eigenmodes as $\mathrm{I}_{m:n}$. The linear dispersion relation between spatial and temporal frequencies is $\sigma_{m:n}^2 = m^2/(m^2+n^2)$. Note the degeneracy $\sigma_{m:n} = \sigma_{km:kn}$ for any positive integer k; the spatial harmonics all have the same temporal frequency.

We now consider the viscous stability of the static equilibrium to parametric forcing, as described by (3.3), via Floquet analysis over the frequency range $\omega \in [0.05, 2.44]$, amplitudes $0 < \alpha \leq 1$, and $10^3 \leq R_N \leq 10^6$. For a given R_N, there is a critical forcing amplitude $\alpha = \alpha_c(\omega)$, that depends on the forcing frequency, below which the basic state (3.2) is stable. Over the investigated parameter range, Floquet multipliers were found to leave the unit circle either through -1 (subharmonic bifurcation, $\omega_r = \omega/2$) or $+1$ (synchronous bifurcation, $\omega_r = \omega$), where ω_r is the response frequency of the viscous Floquet eigenmode. The loci of these bifurcations, for $R_N = 2\times10^4$, are presented in figure 3.1. It is only in small intervals with $\omega \lesssim 0.3$ that the synchronous bifurcation is primary. The red curve in figure 3.1 is the locus of synchronous bifurcations, with the tip of the 1:1 resonance horn indicated at $\omega \approx 0.7$, which is very close to $\sigma_{1:1} = 1/\sqrt{2}$. This is not the primary bifurcation for forcing frequency $\omega = 0.7$; the basic state (3.2) loses stability at lower α to

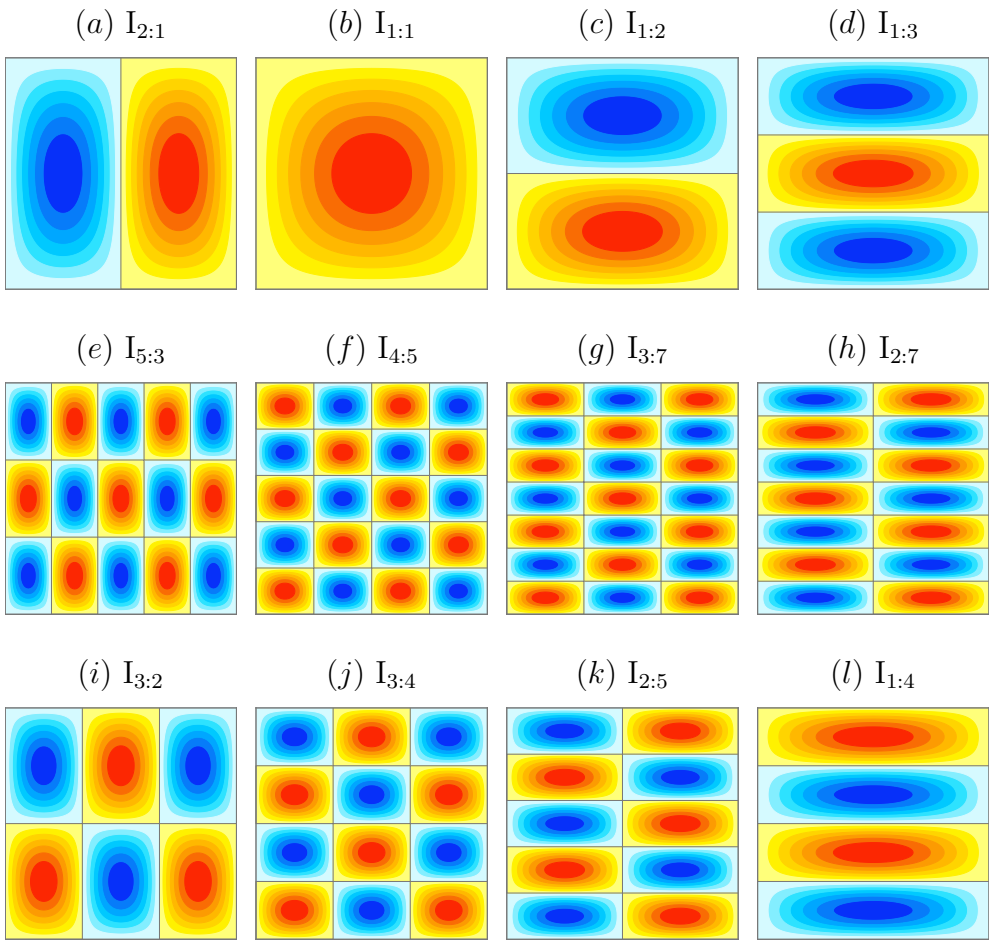

Figure 3.2: Vorticity of inviscid unforced modes with m:n as indicated.

a subharmonic Floquet mode with spatial structure resembling $\mathrm{I}_{2:5}$ and a response frequency $\omega_r = \omega/2 \approx 0.35$, which is close to $\sigma_{2:5} = 2/\sqrt{4+25} \approx 0.37$. The loci of subharmonic bifurcations are the blue curve in the figure.

In the unforced and inviscid linear theory, between any two $\mathrm{I}_{m:n}$ and $\mathrm{I}_{p:q}$, there exists $\mathrm{I}_{m+p:n+q}$ which results in a Farey sequence of eigenmodes. For the forced and viscous results illustrated by figure 3.1, along the loci of the synchronous or the subharmonic primary instabilities exists intersecting resonance horns that are associated with a finite Farey sequence of viscous eigenmodes. The bifurcating modes have m and n cells of alternating sign in the horizontal and vertical directions, and are very

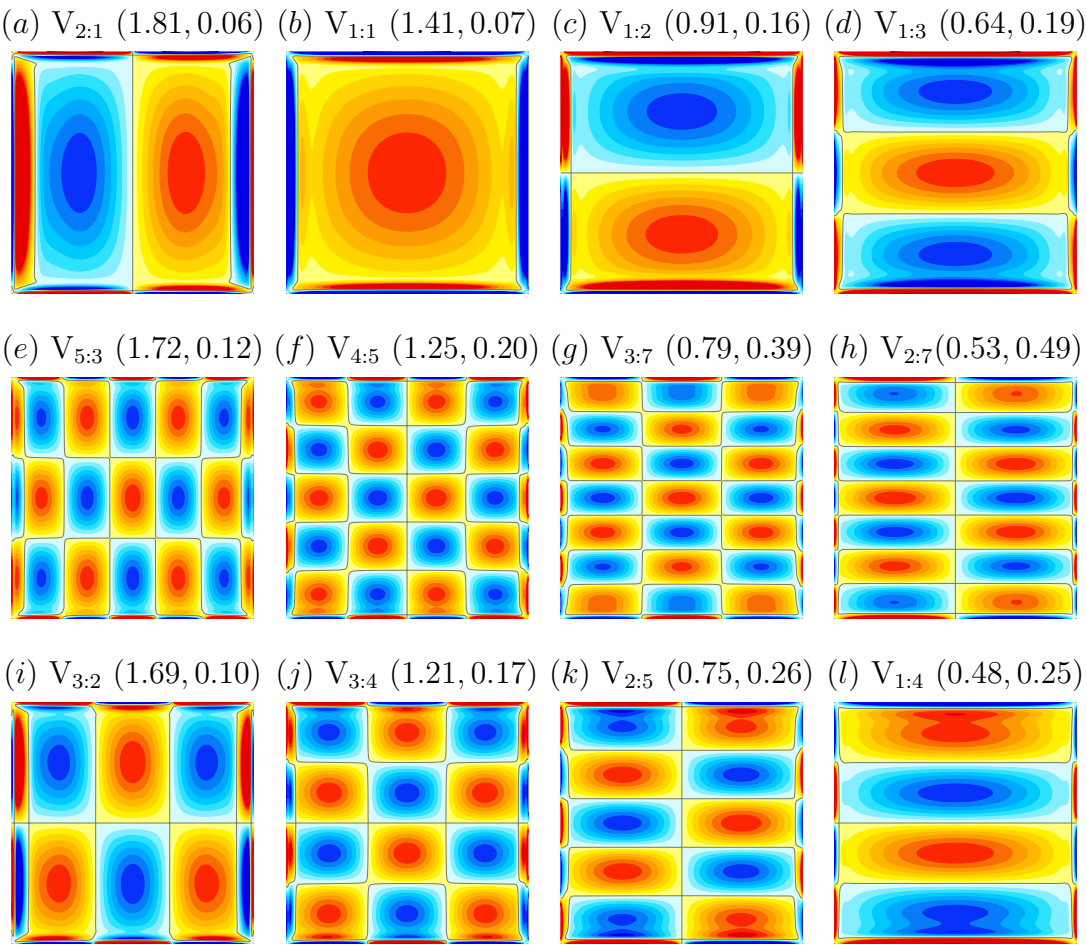

Figure 3.3: Vorticity of the leading subharmonic modes along the primary instability locus for $R_N = 2 \times 10^4$ and (ω, α) as indicated.

similar in structure to the linear inviscid unforced modes $\mathrm{I}_{m:n}$, and we shall call the viscous Floquet modes $\mathrm{V}_{m:n}$. Figure 3.2 shows the spatial structure of the vorticity some of the lower-order unforced inviscid modes together with some intermediate higher-order modes that appear in the Farey sequence, and figure 3.3 shows the same for the viscous Floquet modes at $R_N = 2 \times 10^4$, $\alpha = \alpha_c$ and ω as indicated for subharmonic modes with the same $m{:}n$ structure as the inviscid modes in figure 3.2. The main difference between the inviscid and viscous modes is the presence of viscous boundary layers. Being eigenmodes, their magnitudes are arbitrary, so we have

scaled the modes to have their vorticity maximum in the central region equal to 1. It is clear that the boundary layer vorticity is larger than the interior vorticity for the lower-order modes, and that the interior cells closest to the walls are distorted. Also, for the higher-order modes (e.g. figure 3.3(h) corresponding to a mode $\mathrm{V}_{4:5}$), although the boundary layers are thinner, the viscous distortion of the cells penetrates deeper into the interior.

Within a subharmonic m:n horn, the Floquet mode has half the forcing frequency $\omega_r = \omega/2$, which is close the corresponding frequency $\sigma_{m:n}$ of $\mathrm{I}_{m:n}$, whereas within a synchronous m:n horn the synchronous mode has $\omega_r = \omega \approx \sigma_{m:n}$. Within a given horn, the ratio ω_r/ω is either 1 for a synchronous horn or 1/2 for a subharmonic horn, i.e. the response frequency varies within the horn, but the spatial frequencies, m and n, remain fixed.

Viscosity regularizes the degeneracy in the dispersion relation of the inviscid unforced problem. The bifurcating viscous modes are all simple (of multiplicity one), and the harmonics bifurcate in ascending order as α is increased for a given ω and R_N. That is, for modes $\mathrm{V}_{km:kn}$, $k = 1$ bifurcates first, then $k = 2$, and so on as α is increased. As such, the loci shown in figure 3.1 correspond to the bifurcations of low-order modes.

We now focus our attention on the resonance horn associated with the lowest order mode $\mathrm{V}_{1:1}$ that bifurcates subharmonically. It is the wide horn shown in figure 3.1 with its tip at $\omega \approx 1.41$. A close-up detail of this horn is shown in figure 3.4(a), which also includes the loci of where the $\mathrm{V}_{m:m}$ harmonics bifurcate. Within the horn, the viscous modes have exactly half the forcing frequency, $\omega/2$, which is close to the frequency of $\mathrm{I}_{1:1}$, $\sigma_{1:1} = 1/\sqrt{2}$. It is the spatial frequency rather than the temporal frequency of the response that is locked inside the horn. The m:m subharmonic resonance horns are nested one inside the other with increasing m, as illustrated in

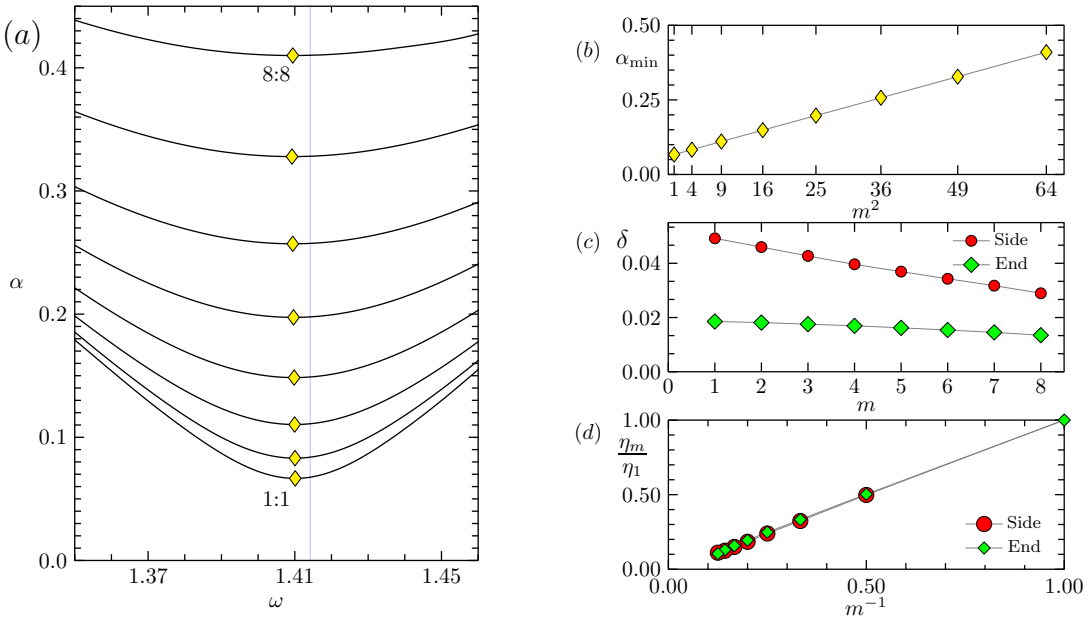

Figure 3.4: (a) Loci of the m:m resonance horns for $R_N = 2 \times 10^4$, with m increasing sequentially from $m = 1$ to $m = 8$ with increasing α; (b, c, d) show the variations of $\alpha_{\min}$, δ and η_m with m.

figure 3.4(a) showing the $m = 1$ to $m = 8$ horns. The tips of the horns are at $\omega_{\min} \approx 1.41 \approx 2/\sqrt{2}$ and $\alpha = \alpha_{\min}$. As shown in figure 3.4(b), $\alpha_{\min}$ increases with m^2. This is an indication of how viscosity progressively dampens the higher harmonics, thus regulating the degeneracy in the inviscid idealization.

Figure 3.5 shows the vorticity of $\mathrm{I}_{1:1}$ and its first seven harmonics, and of the vorticity of subharmonic $\mathrm{V}_{m:m}$, with $m \in [1, 8]$, at $R_N = 2 \times 10^4$, $\omega = 1.41$, and α slightly greater than α_c for each. Again, the most striking difference between the two sets is the presence of viscous boundary layers. For the low-m modes, the difference between interior of the viscous mode (away from the boundary layers) and the interior of the corresponding inviscid mode is minimal, whereas for large m, there are noticeable variations in the local vorticity maxima, indicative of viscous effects permeating deep into the interior for the higher-order modes, so that not only is their instability more viscously damped (larger $\alpha_{\min}$ for larger m), but their structure is

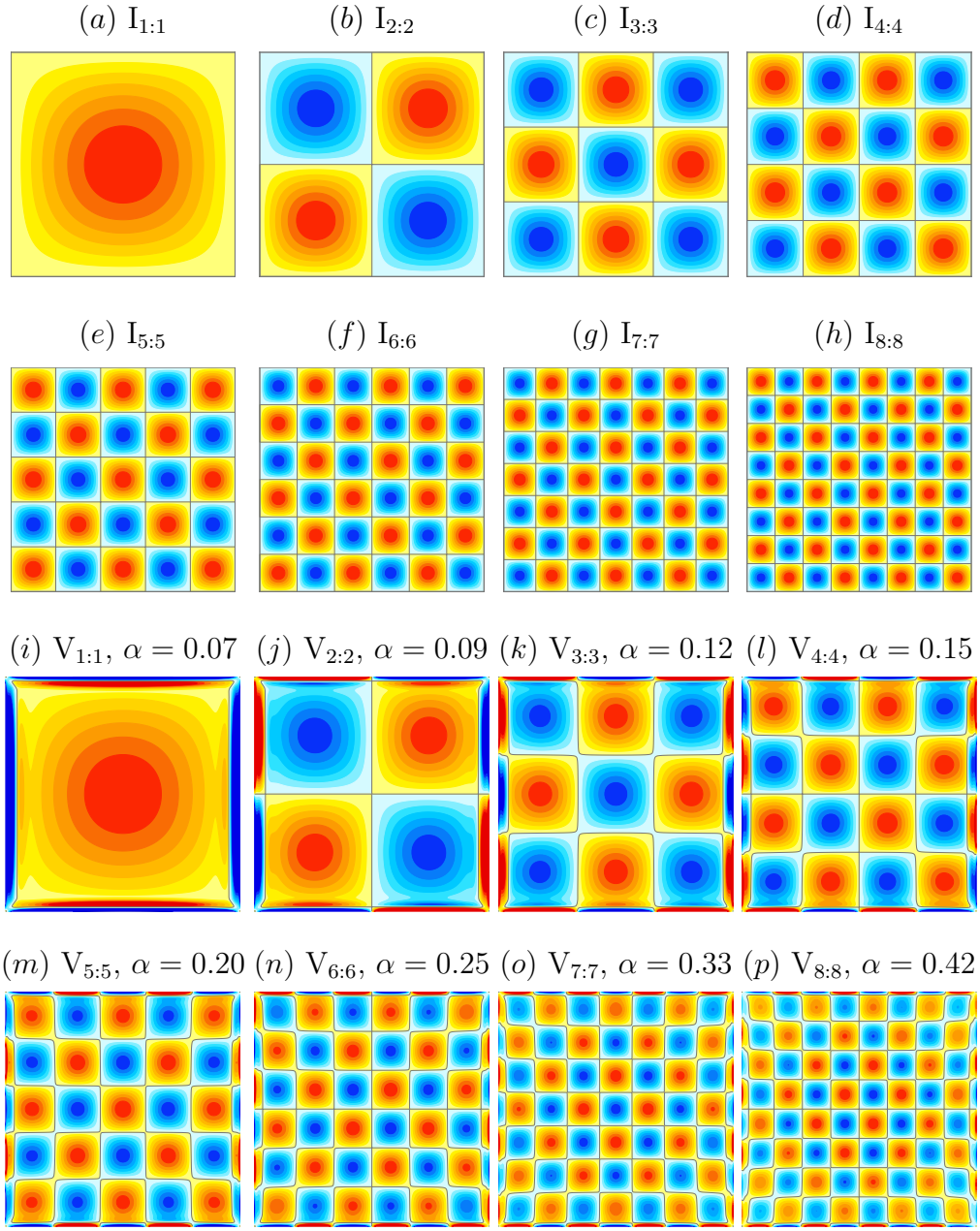

Figure 3.5: Vorticity of the first eight (a–h) $\mathrm{I}_{m:m}$ and (i–p) subharmonic $\mathrm{V}_{m:m}$ at $R_N = 2 \times 10^4$, $\omega = 1.41$, and $\alpha \approx \alpha_{\min}$ as indicated.

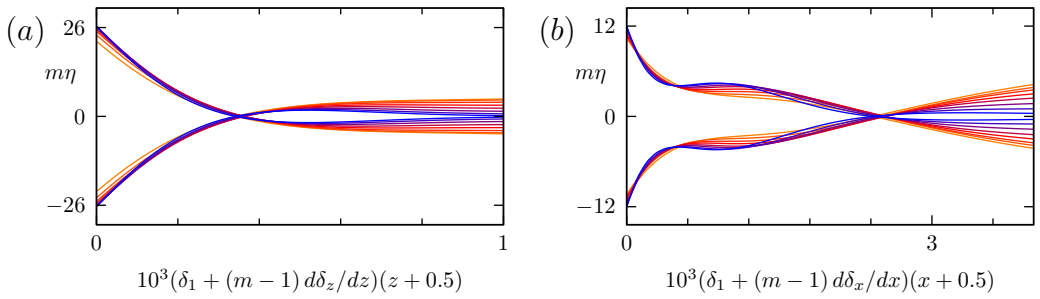

Figure 3.6: Scaled vorticity profiles at their extrema over one period of $\mathrm{V}_{m:m}$ ($m \in [1, 8]$) at $R_N = 2 \times 10^4$, $\omega = 1.41$ and $\alpha \approx \alpha_{\min}$, in (a) endwall and (b) sidewall boundary layers.

more viscously distorted as well.

The variations in the thickness of the boundary layers with m are small. Figure 3.4(c) shows that these decrease linearly with m, where the boundary layer thickness δ is taken to be the distance normal from the wall to the first zero in the vorticity. The sidewall layers are thicker than the top and bottom wall layers, but they decrease faster with increasing m. Figure 3.4(d) shows that the ratio, η_m, of maximum vorticity in the boundary layer to the maximum vorticity in the interior for $\mathrm{V}_{m:m}$, diminishes with increasing m as $\eta_m = \eta_1/m$. Figure 3.6 shows the profiles of the vorticity in the bottom ($z = -0.5$) and sidewall ($x = -0.5$) boundary layers for the subharmonic $\mathrm{V}_{km:km}$. Using the boundary layer scalings with m described in figure 3.4, these profiles collapse to a self-similar profile.

We now turn our attention to how reducing viscous effects (by increasing R_N) acts on the subharmonic $\mathrm{V}_{1:1}$ mode. The 1:1 subharmonic resonance horns for various R_N are shown in figure 3.7(a). With increasing R_N, the tip of the horn $(\omega_{\min}, \alpha_{\min}) \to (2\sigma_{1:1}, 0)$, with the shape of the horn approaching the V-shape that is expected for this horn in the limit $R_N \to \infty$. Figure 3.7(b) shows that $\alpha_{\min} \propto 1/\sqrt{R_N}$. Figure 3.8 shows the vorticity of $\mathrm{V}_{1:1}$ for $R_N \in [10^3, 10^6]$. The interior structure of $\mathrm{V}_{1:1}$ is essentially equivalent to that of $\mathrm{I}_{1:1}$ with the overall difference due to the viscous

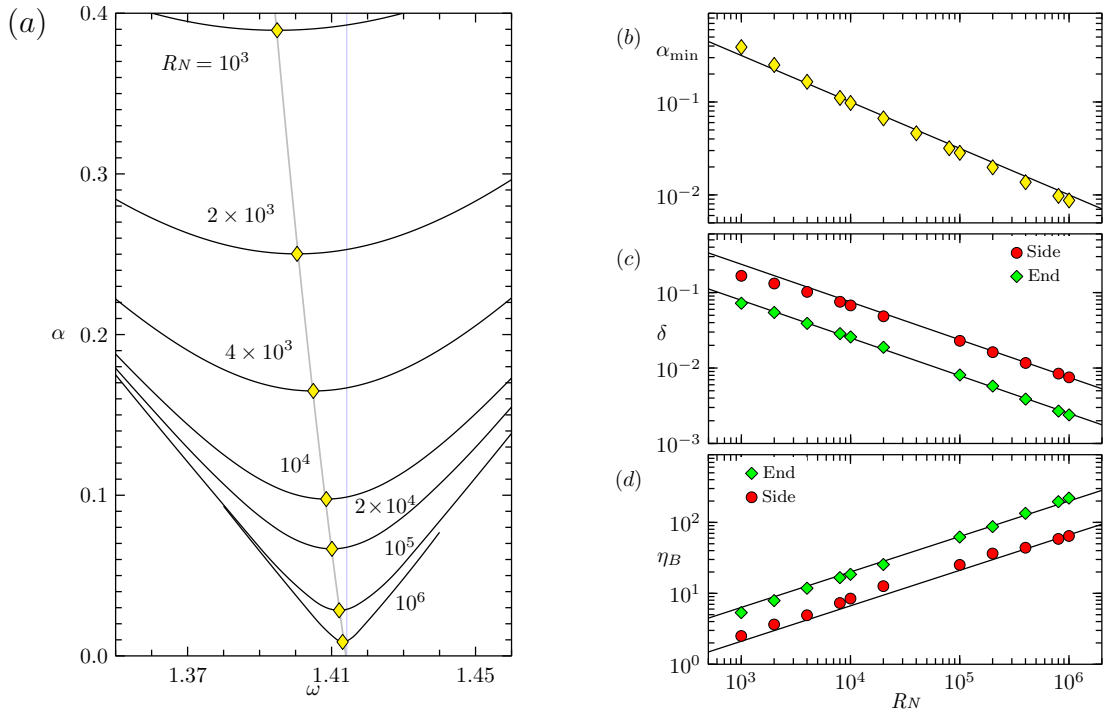

Figure 3.7: (a) Critical (ω, α) for subharmonic $V_{1:1}$ for R_N as indicated. The yellow diamonds are at $(\omega_{\min}, \alpha_{\min})$. Variations with R_N of (b) $\alpha_{\min}$, (c) boundary layer thickness on the top/bottom walls (green diamonds), and on the sidewalls (red circles), and (d) ratio of interior to boundary layer maximum vorticity.

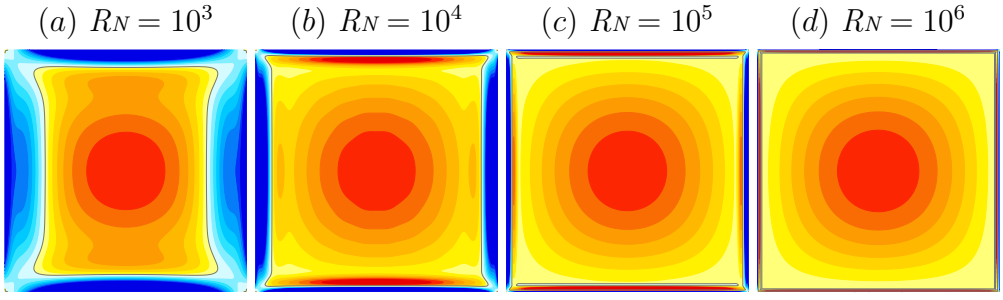

Figure 3.8: Vorticity of subharmonic $V_{1:1}$ for R_N as indicated, near $(\omega_{\min}, \alpha_{\min})$.

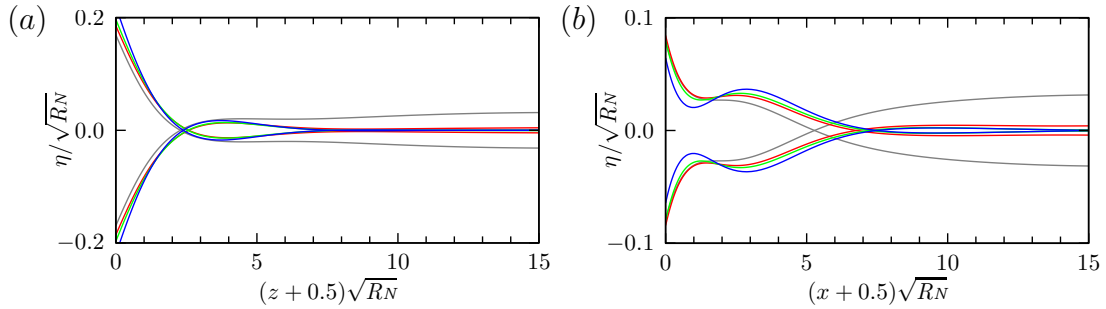

Figure 3.9: Scaled vorticity profiles in (a) the endwall boundary layers and (b) the sidewall boundary layers, at their extrema over one period of subharmonic $V_{1:1}$ at the same (R_N, ω, α) as in figure 3.8, with $R_N = 10^3$ (gray), 10^4 (red), 10^5 (green) and 10^6 (blue).

boundary layers. These boundary layers diminish in thickness as $\delta \propto 1/\sqrt{R_N}$, but their intensity increases as $\eta_1 \propto \sqrt{R_N}$, as indicated in figure 3.7(c, d). Using these scalings, the profiles of the vorticity in the endwall and sidewall boundary layers can be collapsed onto self-similar profiles in R_N, as shown in figure 3.9. The $R_N = 10^3$ deviates somewhat from this, indicating that for that R_N, the response is too viscous, but for $R_N > 10^4$, the response is in the asymptotic regime.

3.4 Conclusions

The linear stability of the static linearly stratified equilibrium in a square cavity subjected to harmonic vertical oscillations has been studied using Floquet analysis on the Navier–Stokes–Boussinesq equations with no-slip boundary conditions and zero-flux temperature conditions on the sidewalls and constant temperature conditions on the top and bottom walls. The analysis considered a large range of forcing frequencies and amplitudes, together with several decades of variation in the non-dimensional parameter R_N (the ratio of viscous to Archimedian time scales). Onset of instability was found to occur when a Floquet multiplier attained modulus greater than one as a critical forcing amplitude was exceeded at a given forcing frequency. Almost all such

primary instabilities were subharmonic, with the multiplier exiting the unit circle through -1, but for a few low frequencies the primary instability was synchronous with the multiplier exiting through $+1$. The spatial structure of the bifurcating modes very closely resembles that of the linear inviscid modes of the unforced square cavity, differing primarily due to the presence of viscous boundary layers. As in the experiments of Benielli and Sommeria [7], we have focused on the subharmonic 1:1 modal response and its harmonics, at forcing frequencies in the neighborhood of $\omega = \sqrt{2}$. We have quantified the impact of viscosity, and in particular obtained scaling laws for the critical forcing amplitude at which the harmonics become unstable, as well as scaling laws for the thickness and intensity of the boundary layers. The critical forced oscillation amplitude depends quadratically on the mode number m of the harmonic, while the boundary layer thickness and the intensity of vorticity in the boundary layer vary as $1/\sqrt{R_N}$ and $\sqrt{R_N}$, respectively, so that their product remains constant independent of R_N as $R_N \to \infty$. This self-similar regime is found to be attained for $R_N \sim 10^4$. This is consistent with the inviscid idealization being a singular limit as viscosity vanishes, with the lower-order viscous and inviscid modes essentially being identical in the interior of the container. Of course, there is a major difference between the zero viscosity approximation, which has zero vorticity at the walls and the limit of vanishing viscosity for which the wall vorticity is a delta distribution. At small R_N, boundary layer effects are localized near the boundaries of the container for lower modes but permeate significantly into the interior for higher-order modes, whose spatial variations in the interior are comparable in size to the boundary layer thicknesses.

It is unlikely that very high-order modes will be observed in full nonlinear simulations or physical experiments, as low-order modes are likely to have already reached an amplitude where nonlinear effects cannot be neglected at the level of forced oscilla-

tion amplitudes needed for the high-order modes to be excited. In their experiment, Benielli and Sommeria [7] observed low-order two-dimensional mode structures as early transients, but as their amplitudes grew, wave breaking and other instabilities became dominant. The study of nonlinear modes interactions and competition beyond onset is currently being addressed.

Acknowledgments

We thank ASU Research Computing facilities and the NSF XSEDE program for providing compute resources, and Ke Wu for the original code.

Chapter 4

MODAL REDUCTION OF A PARAMETRICALLY FORCED CONFINED VISCOUS FLOW

ABSTRACT

An exact reduction of parametrically and periodically forced linear dynamical systems to modal dynamics in low-dimensional subspaces is possible when the operators involved commute with one-another. We describe how a modal analysis may still be possible in the non-commuting case. The approach is illustrated with the determination of neutral curves for a stably and linearly stratified fluid in a square cavity under harmonically modulated gravitational forcing. In this example the non-commutation of operators in the resulting Mathieu system is a direct consequence of the combined action of diffusion and wall effects. An ansatz for modal diffusion is proposed, which enables remarkably predictive estimates of neutral curves via superposition of modal responses.

4.1 Introduction

The dynamics of physical phenomena are often described via Newton's second law. Restoring forces, such as Coriolis effects in rotating flows or buoyancy forces in stratified flows, lead to models that are analogous to coupled spring-mass systems. In the absence of friction and/or spatial confinement, external periodic forcing results in dynamics that can be expressed as a superposition of the modal responses of decoupled oscillators. In the context of surface waves of a homogeneous fluid in a large container subjected to vertical oscillations of angular frequency Ω, Benjamin

and Ursell [8] were the first to make this observation. Their analysis, made under the assumption of vanishing viscosity, led to a Mathieu partial differential equation (PDE) for the free surface elevation. This PDE was reduced to scalar modal Mathieu equations, which satisfactorily reproduced experimental results; small discrepancies were attributed to meniscus and viscous boundary layer effects at the bottom wall of the container. Viscosity dampens the surface oscillations, which can nevertheless be sustained via the parametric forcing if the amplitude is sufficiently large. Internal gravity waves in a fully confined and continuously stably stratified fluid were later studied with similar outcomes [114, 97].

Subsequent studies involving parametric forcing of Faraday waves [44, 106, 61], internal gravity waves [7] and Rayleigh–Bénard convection [17] with viscous fluids in finite-sized containers subjected to harmonic vertical oscillations showed that in order to sustain the waves, larger forcing amplitudes are required to overcome the strong viscous dissipation in the boundary layers of the container walls. These viscous effects are notoriously difficult to quantify. The typical ansatz $-\nu|\boldsymbol{k}|^2$ for the action of $\nu\nabla^2$ representing viscous diffusion, where ν is kinematic viscosity and $|\boldsymbol{k}|$ is the Euclidean magnitude of the wavevector $\boldsymbol{k}$, relies on the existence of a wave-like response that is typically associated with responses in unbounded domains or ideal (inviscid) fluids, and grossly underestimates the viscous contributions in boundary layers. Various corrections based on powers of $\sqrt{\nu|\boldsymbol{k}|^2/\Omega}$ have been proposed to improve comparisons between model and experimental results [43, 76, 83], but those usually assume small ν, $|\boldsymbol{k}|$ and/or large Ω, and introduce non-localization in both space and time due to the fractional powers of $|\boldsymbol{k}|^2$ and Ω, at least for low to moderate viscosity [18, 37]. The global nature of these corrections is ultimately rooted in the non-commutativity of the differential operators involved in the damped Mathieu PDE as a result of viscosity and confinement. The lack of operator commutativity prevents a standard modal

analysis via simultaneous diagonalization of the operators and a simple superposition of scalar Mathieu responses.

We show how responses to scalar damped Mathieu equations can in fact be superposed in confined configurations of viscous fluids under parametric excitation, and obtain a reliable predictive estimate of the instability curves over a wide range of a nondimensional version ω of the forcing frequency Ω, provided an appropriate ansatz for diffusive effects is used. The proposed strategy relies on a simple ad-hoc model of modal diffusion based on data of critical forcing amplitudes at selected forcing frequencies and viscosities, which are obtained from a numerical Floquet analysis. Such a strategy provides an economical alternative to a global Floquet analysis of the parametrically forced Navier–Stokes–Boussinesq equations.

Our approach is illustrated with a study of the onset of instability of a linearly stratified fluid in a square cavity subjected to harmonically modulated gravitational acceleration. It is closely related to the experiments of Benielli and Sommeria [7], and the Floquet analysis of the full problem is presented in Yalim *et al.* [109]. The analogy made in [7] between the stratified fluid's response to the vertical oscillations and that of a parametrically excited pendulum modeled by a Mathieu equation is hampered by two issues: (i) nonlinear effects in the physical experiment lead to subcriticality at the excitation frequency ω considered, which becomes apparent once the predicted threshold for the onset of instability is adjusted (see the discussion in Appendix A), and (ii) the modal expression used for boundary dissipation [7, Eq. (5.5)] vanishes for horizontal wavevectors and neglects viscous effects at lateral walls, whose only role is to quantize these wavevectors. The discrepancies between theory and experiments were correctly attributed to unaccounted friction due to boundary layers effects. Our results show that a proper evaluation of these effects via an ad-hoc modal dissipation model can restore the agreement over a broad range of parameters.

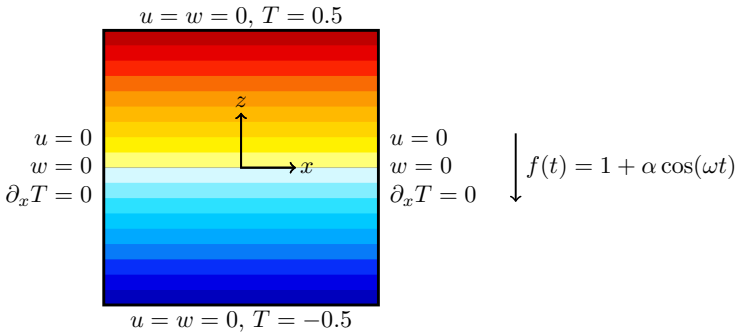

Figure 4.1: Schematic showing the basic state isotherms, boundary conditions, coordinate system, and body forcing.

4.2 Model Formulation

A schematic of the nondimensionalized configuration is shown in Fig. 4.1, where the length, time, and temperature scales are the cavity side length, the Archimedian time, and the imposed temperature difference between the top and bottom walls. Using a frame attached to the oscillating cavity results in a harmonically modulated nondimensional gravity

$$f(t) = 1 + \alpha \cos(\omega t). \tag{4.1}$$

The horizontal and vertical components of the velocity in the $x \in [-0.5, 0.5]$ and $z \in [-0.5, 0.5]$ directions are u and w. The side walls are insulated, and the top and bottom walls are kept at constant nondimensional temperatures $T = 0.5$ and $T = -0.5$, providing a stable temperature stratification in the cavity in the absence of gravity modulation, $\alpha = 0$. The time evolution of small perturbations $(u, w, \theta) = (u, w, T - z)$ about the linearly stratified base state $(u, w, T) = (0, 0, z)$ is governed by the nondimensionalized Navier–Stokes–Boussinesq equations linearized about the

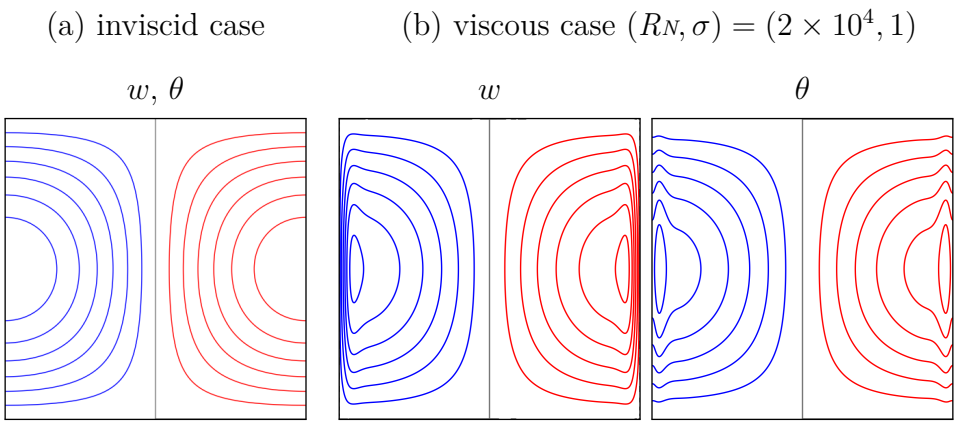

Figure 4.2: Contour levels with red positive and blue negative for the vertical velocity w and thermal perturbation θ obtained at $\omega \approx \sqrt{2}$ for (a) the inviscid and unforced $a_{1:1}$ ($R_N \to \infty$) and (b) the viscous w and θ for α near onset obtained from Floquet analysis. The magnitude of eigenmodes (w, θ) is arbitrary, but that of θ relative to w is not.

base state,

$$\begin{aligned} \partial_t u &= -\partial_x p + \mathrm{R_N^{-1}} \nabla^2 u, \\ \partial_t w &= -\partial_z p + \mathrm{R_N^{-1}} \nabla^2 w + f(t)\theta, \\ \partial_t \theta &= -w + (\sigma R_N)^{-1} \nabla^2 \theta, \\ \partial_x u + \partial_z w &= 0, \end{aligned} \tag{4.2}$$

where p is pressure, the Brunt–Väisälä number R_N is the ratio of viscous and Archimedian time scales, and the Prandtl number σ is the ratio of thermal and viscous time scales. Using the incompressibility condition to eliminate u and p yields the differential system

$$\partial_t \begin{bmatrix} w \\ \theta \end{bmatrix} = \mathcal{A}(t) \begin{bmatrix} w \\ \theta \end{bmatrix}, \qquad \mathcal{A}(t) = \begin{bmatrix} \mathrm{R_N^{-1}} \nabla^2 & f(t)\mathcal{L} \\ -\mathcal{I} & (\sigma R_N)^{-1} \nabla^2 \end{bmatrix}, \tag{4.3}$$

where $\mathcal{I}$ is the identity operator and $\mathcal{L}$ is a bounded linear operator satisfying $\nabla^2 \mathcal{L} = \partial_{xx}$.

The stability of (4.3) depends on the spectrum of the monodromy operator. In

the inviscid limit $Ra \to \infty$, the Laplacian terms vanish. Diagonalization of $\mathcal{L}$ reduces the problem of studying the monodromy operator of (4.3) to studying the 2×2 monodromy matrices of systems

$$\frac{d}{dt}\begin{bmatrix} w_{\boldsymbol{k}} \\ \theta_{\boldsymbol{k}} \end{bmatrix} = A_{\boldsymbol{k}}(t)\begin{bmatrix} w_{\boldsymbol{k}} \\ \theta_{\boldsymbol{k}} \end{bmatrix}, \qquad A_{\boldsymbol{k}}(t) = \begin{bmatrix} 0 & f(t)\lambda_{\boldsymbol{k}} \\ -1 & 0 \end{bmatrix}, \tag{4.4}$$

describing the time evolution of solutions of (4.3):

$$\begin{bmatrix} w \\ \theta \end{bmatrix} = \begin{bmatrix} w_{\boldsymbol{k}}(t) \\ \theta_{\boldsymbol{k}}(t) \end{bmatrix} a_{\boldsymbol{k}}(x, z). \tag{4.5}$$

Here, $a_{\boldsymbol{k}}(x, z) = \cos m\pi(x + 0.5) \sin n\pi(z + 0.5)$ are eigenmodes of $\mathcal{L}$ and are solutions of the generalized eigenvalue problems

$$\lambda_{\boldsymbol{k}} \nabla^2 a_{\boldsymbol{k}} = \partial_{xx} a_{\boldsymbol{k}}, \tag{4.6}$$

with thermal boundary conditions $a_{\boldsymbol{k}}(x, \pm 0.5) = \partial_x a_{\boldsymbol{k}}(\pm 0.5, z) = 0$, quantizing the index $\boldsymbol{k} = (m\pi, n\pi) = m{:}n$ with positive integers m and n, and the corresponding eigenvalues are $\lambda_{\boldsymbol{k}} = m^2/(m^2 + n^2)$ [97]. Note that w obtained from (4.5) only vanishes on the top and bottom boundaries, which is consistent with the impermeability condition imposed at boundaries in the inviscid case. Figure 4.2(a) shows the spatial structure of the inviscid mode $a_{1:1}$, describing both w and θ. In this inviscid setting, w and θ have the same spatial structure.

Eliminating $w_{\boldsymbol{k}}$ in (4.4) leads to the Mathieu equation

$$\theta''_{\boldsymbol{k}} + f(t)\lambda_{\boldsymbol{k}}\theta_{\boldsymbol{k}} = 0. \tag{4.7}$$

This equation has a rich history, dating back to Mathieu's work on Poisson equations in elliptic domains [66]. It has found numerous applications [85, 101] and its theory is well-established [73, 41]. In particular, the eigenvalues of the monodromy matrix

of the system (4.4) with modulus one can only be ± 1, occurring at the edge of an infinite sequence of horns emanating from $(\omega, \alpha) = (2\lambda_{\boldsymbol{k}}^{1/2}/\ell, 0)$, $\ell = 1, 2, \ldots$, in the Ince–Strutt stability diagram, with either subharmonic (ℓ odd) or synchronous (ℓ even) periodic solutions. As an alternative to Floquet analysis, or other asymptotic methods typically used with small α, the subharmonic and synchronous neutral curves for mode $\boldsymbol{k}$ may be efficiently determined as the zero contour level of a Hill continued fraction, which results from applying harmonic balance to Mathieu's equation [41].

4.3 Results

In the viscous case ($R_N < \infty$), a standard stability estimate using the L_2 norm shows that the global perturbation L_2 energy, $\|u\|^2 + \|w\|^2 + \|\theta\|^2$, decreases for $\alpha > 0$ small enough. The onset of instability coincides with the characteristic multipliers crossing the unit circle in the complex plane, which has been observed numerically to occur only through ± 1 in this problem. The first occurrence of a multiplier exiting the unit disk at -1 (subharmonic response) or $+1$ (synchronous response) determines two critical curves in (ω, α) space, illustrated in [109, Fig. 1] for $(R_N, \sigma) = (2 \times 10^4, 1)$, and reproduced here in Figs. 4.3 and 4.4.

At $\omega = 1.41 \approx \sqrt{2}$, the instability occurs at $\alpha \approx 0.07$ via a flip bifurcation (subharmonic response). Contours of the vertical velocity w and temperature θ of the corresponding eigenmode of the monodromy operator are shown in Fig. 4.2(b) and illustrate how viscosity affects the response (w, θ) at onset of instability, compared to the inviscid case. The forced viscous modes w and θ both broadly resemble the inviscid mode $a_{1:1}$, except that the viscous velocity satisfies the no-slip condition $w = 0$ on the side boundaries. The difference in boundary conditions for w on the sidewalls ($\partial_x w = \partial_{xt}\theta = 0$ in the inviscid case and $w = 0$ in the viscous case) introduces distortions due to the formation of boundary layers–these boundary layers

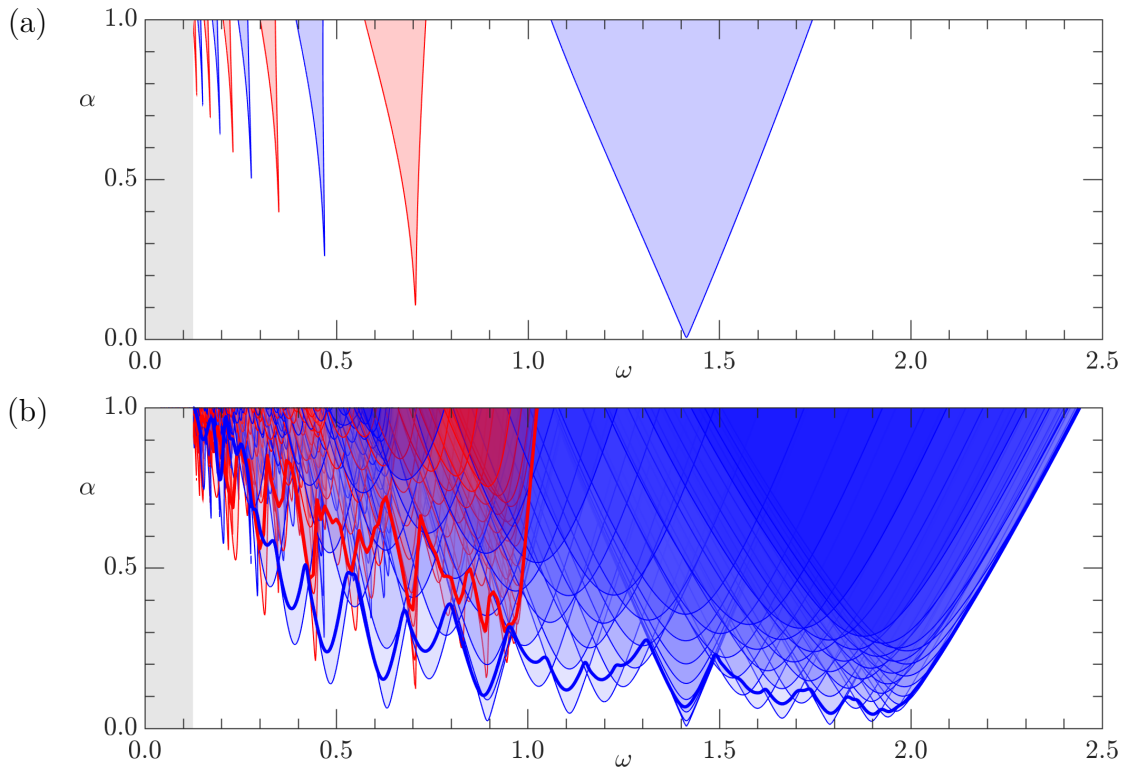

Figure 4.3: (a) Instability tongues of the Mathieu system associated with the $m{:}n = 1{:}1$ mode at $(R_N, \sigma) = (2 \times 10^4, 1)$ in (ω, α) domain. (b) Superposition of viscous Mathieu stability tongues at $(R_N, \sigma) = (2 \times 10^4, 1)$ associated with modes $m{:}n$ for $m, n \geq 1$ and $m^2{+}n^2 \leq 12^2$. Superimposed are the Floquet Navier–Stokes–Boussinesq subharmonic (thick blue) and synchronous (thick red) results from Yalim *et al.* [109]. Tongues accumulating at low frequencies are narrower and more difficult to estimate (gray area).

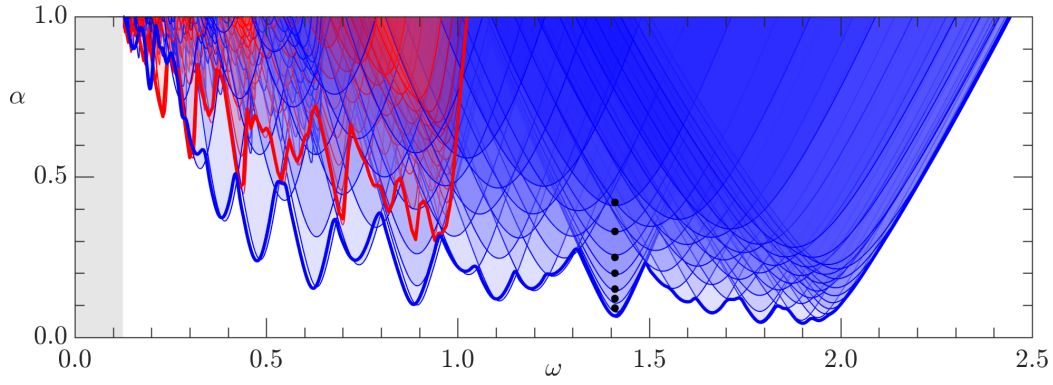

Figure 4.4: Same as in Fig. 4.3(b), but now using the corrected diagonal coefficients (4.11) in (4.8) with $\gamma = 20$. The black dots correspond to critical Floquet results for the viscous $m{:}m$ modes with $1 \leq m \leq 8$.

in w also distort the temperature distribution in the boundary layer regions and even though the boundary condition on θ is the same in both the viscous and inviscid setting, i.e. the sidewalls are insulating with $\theta_x = 0$. These effects lead to the loss of commutativity of the operators ∇^2 and $\mathcal{L}$. This prevents an exact modal reduction of (4.3) to a superposition of first-order Mathieu equations (4.4).

An approximating modal reduction is nevertheless desirable, as it delivers considerable savings in the computational cost of evaluating critical curves over a large range of forcing frequencies, especially when compared to the computation of the monodromy matrix in the Floquet analysis. A widely used approach is to continue replacing, as in the inviscid case, the action of $\mathcal{A}(t)$ on the Floquet eigenmodes by its action on the inviscid modes (4.5). This ansatz leads to a system of the form (4.4) again, but with

$$\frac{d}{dt}\begin{bmatrix} w_{\boldsymbol{k}} \\ \theta_{\boldsymbol{k}} \end{bmatrix} = A_{\boldsymbol{k}}(t)\begin{bmatrix} w_{\boldsymbol{k}} \\ \theta_{\boldsymbol{k}} \end{bmatrix}, \qquad A_{\boldsymbol{k}}(t) = \begin{bmatrix} \mathrm{R_N^{-1}}\delta_{\boldsymbol{k}} & f(t)\lambda_{\boldsymbol{k}} \\ -1 & (\sigma R_N)^{-1}\delta_{\boldsymbol{k}} \end{bmatrix}, \tag{4.8}$$

where $\delta_{\boldsymbol{k}} = -\pi^2(m^2+n^2) > 0$. Elimination of $w_{\boldsymbol{k}}$ in (4.8) yields the second-order equation

$$\theta_{\boldsymbol{k}}'' + c\,\theta_{\boldsymbol{k}}' + g(t)\,\theta_{\boldsymbol{k}} = 0, \tag{4.9}$$

where $c = -\mathrm{trace}[A_{\boldsymbol{k}}(t)]$ and $g(t) = \det[A_{\boldsymbol{k}}(t)]$. The stability diagram of this damped Mathieu equation consists of tongues in (ω, α) space with boundaries alternately corresponding to subharmonic and synchronous periodic solutions [19], is shown in Fig. 4.3(a) for the mode $m{:}n$ = 1:1 at $(R_N, \sigma) = (2\times 10^4, 1)$. Each tongue corresponds to a mode of instability of the linearly stratified base state with the same 1:1 spatial response to different forcing frequencies $\omega_\ell \approx 2\lambda_{1:1}^{1/2}/\ell = \sqrt{2}/\ell$, slightly detuned from the inviscid values, with a minimum forcing amplitude $\alpha_\ell \approx \mu_\ell Q_{1:1}^{1/\ell}$, where $Q_{1:1} = c/\lambda_{1:1}^{1/2}$ measures the dissipation for mode 1:1, and $\mu_\ell \in [1,2]$ is a constant; see Appendix A for details.

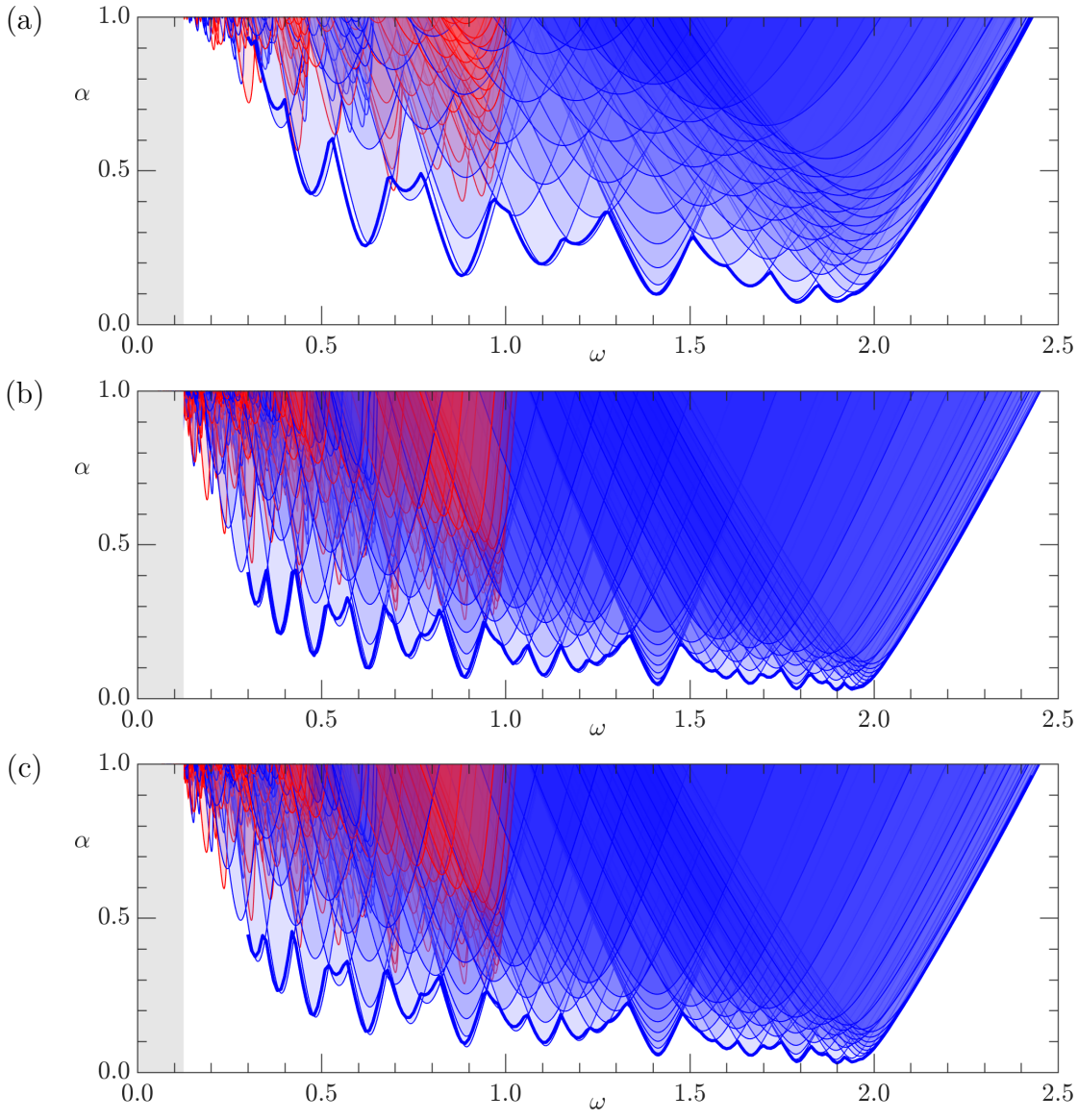

Figure 4.5: Same as in Fig. 4.4 using corrected diagonal coefficients (4.11) in (4.8) with (a) $\gamma = 15$ at $(R_N, \sigma) = (10^4, 1)$, (b) $\gamma = 27$ at $(R_N, \sigma) = (4 \times 10^4, 1)$, and (c) $\gamma = 30.6$ at $(R_N, \sigma) = (2 \times 10^4, 7)$. Only primary subcritical responses at forcing frequencies $\omega \geq 0.3$ were computed via Floquet analysis for the sake of efficiency.

The superposition of the resulting curves for $|\boldsymbol{k}| \leq 12\pi$ (i.e. $m^2 + n^2 \leq 12^2$) are shown in Fig. 4.3(b), together with the subharmonic (thick blue) and synchronous (thick red) critical curves computed via Floquet analysis in [109]. To our knowledge, this figure is the first instance of a frequency-wide model of actual stability boundaries of a base state in an Ince–Strutt diagram. Not surprisingly, the ansatz (4.8), based on the action of spatial operators on inviscid modes, tends to underestimate viscous effects in boundary layers, lowering the critical amplitude α for onset of instability across the whole ω spectrum as a result. This is more so at $\omega \leq \sqrt{2}$, for which the wavevectors $\boldsymbol{k}$ are predominantly vertical ($m \leq n$) and are more affected by the strong boundary layers on the sidewalls.

In order to take the additional diffusion occurring in boundary layers into account, the modal action of ∇^2 is estimated via Rayleigh quotients

$$\frac{(\nabla^2 w, w)}{(w, w)} = -\frac{\|\nabla w\|^2}{\|w\|^2} \quad \text{and} \quad \frac{(\nabla^2 \theta, \theta)}{(\theta, \theta)} = -\frac{\|\nabla \theta\|^2}{\|\theta\|^2}\,, \tag{4.10}$$

evaluated on selected viscous Floquet eigenmodes, where $(\cdot, \cdot)$ is the L_2 inner product. The results, included in Appendix B, suggest replacing $\delta_{\boldsymbol{k}}$ with

$$\delta_{\boldsymbol{k}} \left(1 + \frac{\gamma}{m^2 + n^2}\right) \left(0.75 + \frac{(mn)^2}{(m^2 + n^2)^2}\right). \tag{4.11}$$

The last factor can be expressed as $0.75 + 0.25 \sin^2(2\varphi_{\boldsymbol{k}})$, where $\tan \varphi_{\boldsymbol{k}} = n/m$ measures the inclination of the wavevector $\boldsymbol{k} = m{:}n$. This factor is unity when $m{=}n$ and its role is to moderate (by up to 25%) the modal diffusion when $m{\neq}n$, i.e. for vertical and horizontal wavevectors $\boldsymbol{k}$ associated to forcing frequencies away from $\omega = \sqrt{2}$. The correction (4.11) bears similarities with the expression of the ratio of modal boundary to bulk dissipations from [7, Eq. (5.5)] (e.g. $mn/(m^2{+}n^2) = \sin^2 \varphi_{\boldsymbol{k}} \cot \varphi_{\boldsymbol{k}}$). However, (4.11) does not vanish for horizontal wavevectors ($m \geq n$), whereas boundary dissipation in [7, Eq.(5.5)] does, thus ignoring the contributions from the container's lateral boundaries.

The superposed modal Ince–Strutt stability diagrams are recomputed using diagonal coefficients (4.11) rather than $\delta_{\boldsymbol{k}}$ in (4.8). The results for $(R_N, \sigma) = (2 \times 10^4, 1)$ with $\gamma = 20$, obtained by fitting critical Floquet amplitudes at the m:m modes with $1 \leq m \leq 8$ are shown in Fig. 4.4. They are in excellent agreement with the critical curves obtained via Floquet analysis for both subharmonic and synchronous responses [109]. In particular, our model correctly identifies the rare instances of primary synchronous responses in the lower frequency range. There is a small detuning, particularly for lower ω, which is due to a mild dependence of $\mathcal{L}$ on ω; see Appendix C.

The robustness of the ansatz (4.11) to changes in both R_N and σ was tested by comparing the critical forcing amplitudes obtained at $(R_N, \sigma) = (10^4, 1)$, $(4 \times 10^4, 1)$ and $(2 \times 10^4, 7)$ using the model (4.11) with an adjusted γ, with those obtained via Floquet analysis. Fig. 4.5 shows the results using $\gamma = 15, 27$ and 30.6, resp. Again, the match is very good, especially for wavenumbers $\boldsymbol{k}$ with low m or n. The subharmonic critical curves obtained for $(R_N, \sigma) = (4 \times 10^4, 1)$ and $(2 \times 10^4, 7)$ are very similar. The different values of γ are consistent with a scaling

$$\gamma = \gamma_{R_N,\sigma} \approx 3 + 0.12(\sigma {R_N}^2)^{1/4}, \tag{4.12}$$

illustrating the balance between momentum and thermal diffusion contributions.

At large R_N the ansatz (4.11) shows that diffusion occurs with order $\mathcal{O}({R_N}^{-1/2})$ rather than $\mathcal{O}({R_N}^{-1})$, which is typical of flows dominated by viscous boundary layers. The dependence (4.12) on R_N also yields an estimate of the minimum of the principal 1:1 tongue at $\omega \approx \sqrt{2}$,

$$\alpha_{\min} \approx 2Q = \frac{4\delta_{1:1}}{R_N\sqrt{\lambda_{1:1}}} \approx \frac{279}{R_N} + \frac{6.7}{\sqrt{R_N}} \tag{4.13}$$

at $\sigma = 1$, in good general agreement with the results presented in [109, Fig. 7(b)]. The

balance between the two terms on the right-hand side of (4.13) occurs at a relatively low $R_N \approx 1734$, while the last term accounts for 78% at $R_N = 2 \times 10^4$.

4.4 Conclusions

In summary, confinement together with viscous effects make the determination of neutral curves in large parametric studies of fluid flows subjected to parametric forcing a nontrivial task due to the non-commutation of operators ($\mathcal{L}$ and ∇^2). We have shown how global neutral curves can still be obtained via superposition of modal responses, at a fraction of the cost, provided a suitable model of modal diffusion, based on interpolation of local Floquet data at onset of instability, is used to account for boundary layer contributions. It is expected that this approach can be generalized to other systems, including three-dimensional configurations or more general Hill-type periodic parametric forcings, at least as long as the primary bifurcation of the base state in modal responses occurs in a similar way as it does in the full system (excluding, for example, the possibility of "combination resonances" [19] in Mathieu PDEs, which do not occur in the scalar version).

Acknowledgments

We thank Research Computing at Arizona State University for providing the High Performance Computing and storage resources necessary to conduct the Floquet analysis.

Chapter 5

PARAMETRICALLY FORCED STABLY STRATIFIED CAVITY FLOW: COMPLICATED NONLINEAR DYNAMICS NEAR THE ONSET OF INSTABILITY

ABSTRACT

The dynamics of a fluid-filled square cavity with stable thermal stratification subjected to harmonic vertical oscillations are investigated numerically. The nonlinear responses to this parametric excitation are studied over a comprehensive range of forcing frequencies up to two and a half times the buoyancy frequency. The nonlinear results are in general agreement with the Floquet analysis, indicating the presence of nested resonance tongues corresponding to the intrinsic m:n eigenmodes of the stratified cavity. For the lowest order subharmonic 1:1 tongue, the responses are analyzed in great detail, with complex dynamics identified near onset, most of which involving interactions with unstable saddle states of a homoclinic or heteroclinic nature.

5.1 Introduction

Parametrically forced stratified flows are of both fundamental and practical interest, with many open questions remaining to be addressed, particularly in regards to resonances and internal wave breaking for continuously stratified flows [114, 97, 69, 71, 79, 80, 72, 26, 90, 70, 98, 13, 7, 92, 22]. Even the onset of instability has not been clearly resolved. This is in sharp contrast to the case of parametrically forced interfacial flows, such as the Faraday wave problem [75]. In the inviscid idealization of the Faraday problem, the onset of instability is well characterized by independent

Mathieu equations for each instability mode as the modes are orthogonal [8]. When viscous stress at the interface is taken into account, even though the modes are no longer orthogonal and their damping depends on their wavenumber, the corresponding Floquet analysis [44] gives very good agreement with experiments [29] for the onset of instability.

Yih [114] considered the linear stability of a continuously stratified and laterally unbounded inviscid fluid subjected to vertical vibration. The resultant inviscid Mathieu equations for the instability modes were essentially the same as those of Benjamin and Ursell [8]. Motivated by the question of internal wave breaking, Thorpe [97] built on Yih's work by analytically determining the eigenmodes for a laterally confined stratified system, and set up an experiment with plungers in the two opposing sidewalls to perturb a continuously stratified brine solution. The two-dimensional standing internal wave modes were analytically determined to third order for an inviscid, diffusionless, stably and linearly stratified fluid confined in a rectangular container [97]. Thorpe observed a number of resonantly driven modes near the frequencies predicted by the linear inviscid theory, and qualitatively described wave breaking and mixing for large amplitude forcing. However, he was only able to observe modes of a specific parity and was unable to quantitatively study the large-amplitude responses. Also, his experiment suffered from the presence of internal wave beams emanating from the junctions where the sidewalls and plungers met, which interacted with the driven modes. Also motivated by two-dimensional internal wave breaking and transition to turbulence, and whether triadic resonances are involved, McEwan [69] devised an experiment similar to that of Thorpe [97], but using paddles instead of plungers. Those experiments also generated internal wave beams at the junctions of the paddles and the container.

Benielli and Sommeria [7] also studied linearly stratified flow in a rectangular container, but in contrast to the earlier experiments, they used vertical oscillations to perturb the flow. This had the advantage of not having any differential motion of the container walls, thus avoiding the production of wave beams. They were able to describe the primary and secondary instabilities, observing the fundamental eigenmode and its apparent harmonics lose stability to wave breaking. They considered a small forcing frequency interval covering the resonance interval for the lowest-order spatial mode. Although they were unable to experimentally determine the forcing frequency bounds for the resonance tongue, they did observe intermittent bursting and wave breaking.

The experimental studies [e.g. 97, 69, 70, 7] used salt stratification, which has a very slow diffusivity (the ratio of kinematic viscosity to salt diffusivity, the Schmidt number, is of order 700). The boundary condition for salt at a solid wall is zero flux, so that a constant linear stratification fails in a thin boundary layer on the bottom wall (and at the top wall if it is rigid; some experiments used a free surface). The zero flux condition means that eventually, the system becomes homogeneous. Of course, the time scale for homogenization is very slow compared to the dynamic time scales of interest in the experiments, but for a theoretical analysis both of these effects become problematic. The use of heat rather than salt stratification, with fixed temperatures on the top and bottom walls and insulating (zero flux) sidewall boundary conditions leads to linear temperature stratification as an equilibrium solution for the temperature equation. This, together with no-slip boundary conditions for the velocity, gives a basic state which is linearly stratified and static in the frame of reference of the vertically oscillating container, whose linear stability has been studied using Floquet analysis [109]. When the viscous time scale is large compared to the buoyancy time scale, the viscous Floquet modes resemble the inviscid eigenmodes of the unforced

problem [97], except for the presence of thin boundary layers. While Floquet analysis determines the amplitudes and frequencies at which the basic state loses stability, it provides no information about the nonlinear dynamics that result as perturbations grow to finite amplitudes.

In this paper, we study the nonlinear dynamics via numerical simulations of the two-dimensional Navier–Stokes equations using the Boussinesq approximation. The restriction to two-dimensional flow is motivated by the experimental results of Benielli and Sommeria [7] which showed that the flow remained two-dimensional in their short spanwise aspect ratio container, unless the forcing amplitude is large enough to cause wave breaking. McEwan [70] also noted in his experiments in a similar rectangular container, but with the flow driven by a paddle, that the flow was predominantly two-dimensional, although small patches of fine-scale three-dimensional distortions occurred intermittently due to localized instabilities.

We begin by examining the onset of instability over a wide range of forcing frequencies, from nearly zero to a little over two and a half times the buoyancy frequency. The loci of lowest forcing amplitude for a non-static response flow as a function of forcing frequency broadly agrees well with the Floquet results [109], except that many of the resonance tongues have a hysteretic region on their low-frequency side. Also, complex dynamics are often observed at or very near onset. These two effects contribute to the problems identifying the edges of the resonance tongues experimentally [7]. For the lowest order spatial mode, we then examine in detail the dynamics near the tip of its resonance tongue, reconciling the complex dynamics observed in our nonlinear simulations with what is expected from a dynamical systems perspective near onset.

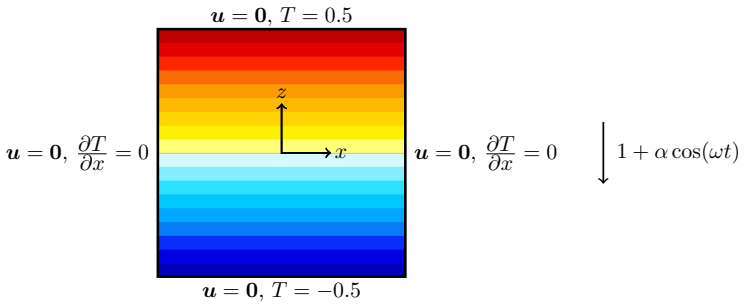

Figure 5.1: Schematic showing the initial isotherms, the boundary conditions, coordinate system, and body force (harmonic gravity modulation).

5.2 Governing Equations and Numerics

Consider a fluid of kinematic viscosity ν, thermal diffusivity κ, and coefficient of volume expansion β contained in a square cavity of side lengths L. The cavity sidewalls are thermally insulated (adiabatic) while the endwalls are held at constant temperatures. The temperature difference between the top and bottom walls is $\Delta T = T_{\mathrm{T}} - T_{\mathrm{B}} > 0$. Gravity g acts downwards in the negative z direction. In the absence of any other external force, the fluid is linearly stratified. The cavity is subjected to harmonic oscillations in the vertical direction with angular frequency Ω and amplitude ℓ. The non-dimensional temperature is $T = (T^* - T_{\mathrm{B}})/\Delta T - 0.5$. The length scale L and time scale $1/N$ are used to non-dimensionalize, where $N = \sqrt{g\beta\Delta T/L}$ is the buoyancy frequency. A Cartesian coordinate system $\boldsymbol{x} = (x, z) \in [\pm 0.5, \pm 0.5]$ is fixed with its origin at the center of the cavity, and the corresponding velocity is $\boldsymbol{u} = (u, w)$. Figure 5.1 is a schematic of the set up. Under the Boussinesq approximation, the non-dimensional governing equations in the frame of reference fixed to the oscillating cavity (the cavity frame) are

$$\begin{aligned} &\frac{\partial \boldsymbol{u}}{\partial t} + \boldsymbol{u}\cdot\nabla\boldsymbol{u} = -\nabla p + \frac{1}{R_N}\nabla^2\boldsymbol{u} + (1 + \alpha\cos\omega t)T\boldsymbol{e}_z, \quad \nabla\cdot\boldsymbol{u} = 0, \\ &\frac{\partial T}{\partial t} + \boldsymbol{u}\cdot\nabla T = \frac{1}{\sigma R_N}\nabla^2 T, \end{aligned} \tag{5.1}$$

where p is the reduced pressure. The system is governed by four non-dimensional parameters:

Brunt–Väisälä number	$R_N = NL^2/\nu$,
Prandtl number	$\sigma = \nu/\kappa$,
forcing frequency	$\omega = \Omega/N$,
forcing amplitude	$\alpha = \Omega^2\ell/g$.

In this study, $R_N = 2 \times 10^4$ and $\sigma = 1$ are fixed, and we consider $0 < \omega \leq 2.5$ and $0 < \alpha \leq 1$.

The velocity boundary conditions are no-slip, and in the cavity frame these are $u = w = 0$ on all four boundaries. The top and bottom endwall temperature boundary conditions are $T|_{z=\pm 0.5} = \pm 0.5$ and on the sidewalls $\partial_x T|_{x=\pm 0.5} = 0$.

Space is discretized via spectral collocation with Chebyshev polynomials of degree M in barycentric form, and time evolution uses the fractional-step improved projection scheme of Mercader *et al.* [74]. We have used this method previously with related problems in Cartesian coordinates [60, 107]. Most of the results presented in this study were obtained with Chebyshev polynomials of degree $M = 72$ in both the x and z directions. For $\omega > 0.30$, the forcing period was discretized into 1000 time steps. For $\omega \leq 0.30$, up to 5000 time-steps per period were used.

The kinetic energy E_K and the normalized thermal $\mathcal{L}^2$ measure E_T are used to monitor the flows,

$$E_K = \frac{1}{2}\int_{-0.5}^{0.5}\int_{-0.5}^{0.5}(u^2 + w^2)\,dx\,dz \quad \text{and} \quad E_T = 12\int_{-0.5}^{0.5}\int_{-0.5}^{0.5}T^2\,dx\,dz; \tag{5.2}$$

E_T is normalized by the thermal $\mathcal{L}^2$ measure of the basic state $\int_{-0.5}^{0.5}\int_{-0.5}^{0.5} z^2\,dx\,dz = 1/12$.

To characterize the amplitude of the flow's response, we compute the temporal standard deviation of the kinetic energy Σ_K and the temporal variance of the horizontal velocity Σ_u^2 at the point $\boldsymbol{x}_p = (x_p, z_p) = (1/\sqrt{8}, 1/\sqrt{8})$.

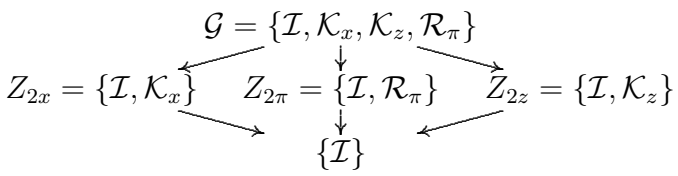

Table 5.1: Hasse diagram of the lattice of subgroups of the group $\mathcal{G} = \{\mathcal{I}, \mathcal{K}_x, \mathcal{K}_z, \mathcal{R}_\pi\}$.

5.3 Symmetries

The governing equations are equivariant to a group symmetry $\mathcal{G}$ generated by reflections in x and in z. The actions of these reflections are

$$\mathcal{K}_x(u, w, T)(x, z, t) = (-u, w, T)(-x, z, t), \tag{5.3}$$

$$\mathcal{K}_z(u, w, T)(x, z, t) = (u, -w, -T)(x, -z, t). \tag{5.4}$$

The symmetry group $\mathcal{G}$ has four elements, $\mathcal{G} = \{\mathcal{I}, \mathcal{K}_x, \mathcal{K}_z, \mathcal{R}_\pi\}$, where $\mathcal{I}$ is the identity and $\mathcal{R}_\pi = \mathcal{K}_x \circ \mathcal{K}_z = \mathcal{K}_z \circ \mathcal{K}_x$ is a π-rotation; $\mathcal{G}$ is a $Z_2 \times Z_2$ group. The lattice of subgroups of $\mathcal{G}$ is presented in table 5.1.

The basic state B is

$$\boldsymbol{u} = 0, \quad T = z, \quad \text{and} \quad p = 0.5z^2(1 + \alpha \cos \omega t), \tag{5.5}$$

in the cavity frame. It is $\mathcal{G}$ invariant. The system, being periodically forced, is invariant to a time translation

$$\mathcal{P}_\tau(u, w, T)(x, z, t) = (u, w, T)(x, z, t + \tau), \tag{5.6}$$

where $\tau = 2\pi/\omega$ is the forcing period. As parameters are varied, instabilities lead to other solutions appearing, which may have broken symmetries. Time dependent states evolve on temporally invariant manifolds. For example, limit cycles have a one-dimensional manifold and 2-tori have a two-dimensional manifold. These states may be pointwise invariant with respect to a spatial symmetry, i.e. at any point in

State	pointwise symmetry	setwise symmetry	temporal type
BS	$\mathcal{G}$	$\mathcal{G}$	limit cycle
$\mathrm{L}_{2m:2n}$	$\mathcal{G}$	$\mathcal{G}$	limit cycle
$\mathrm{L}_{2m:2n+1}$	$\mathcal{K}_x$	$\mathcal{G}$	limit cycle
$\mathrm{L}_{2m+1:2n}$	$\mathcal{K}_z$	$\mathcal{G}$	limit cycle
$\mathrm{L}_{2m+1:2n+1}$	$\mathcal{R}_\pi$	$\mathcal{G}$	limit cycle
$\mathrm{L}_{1:1}$	$\mathcal{R}_\pi$	$\mathcal{G}$	limit cycle
$\mathrm{L}_{2:2}$	$\mathcal{G}$	$\mathcal{G}$	limit cycle
L_L	$\mathcal{R}_\pi$	$\mathcal{R}_\pi$	limit cycle
L_R	$\mathcal{R}_\pi$	$\mathcal{R}_\pi$	limit cycle
T_2	$\mathcal{R}_\pi$	$\mathcal{G}$	2-torus
T_{2L}	$\mathcal{R}_\pi$	$\mathcal{R}_\pi$	2-torus
T_{2R}	$\mathcal{R}_\pi$	$\mathcal{R}_\pi$	2-torus
S_2	$\mathcal{K}_z$	$\mathcal{G}$	2-torus
Q_L	$\mathcal{R}_\pi$	$\mathcal{R}_\pi$	2-torus
Q_R	$\mathcal{R}_\pi$	$\mathcal{R}_\pi$	2-torus
Q	$\mathcal{R}_\pi$	$\mathcal{G}$	2-torus
Q_B	$\mathcal{R}_\pi$	$\mathcal{G}$	2-torus
S_3	$\mathcal{K}_z$	$\mathcal{G}$	3-torus
T_3	$\mathcal{R}_\pi$	$\mathcal{G}$	3-torus
T_{3L}	$\mathcal{I}$	$\mathcal{R}_\pi$	3-torus
T_{3R}	$\mathcal{I}$	$\mathcal{R}_\pi$	3-torus
IB	$\mathcal{I}$	$\mathcal{I}$	erratic

Table 5.2: List of states observed and their symmetries.

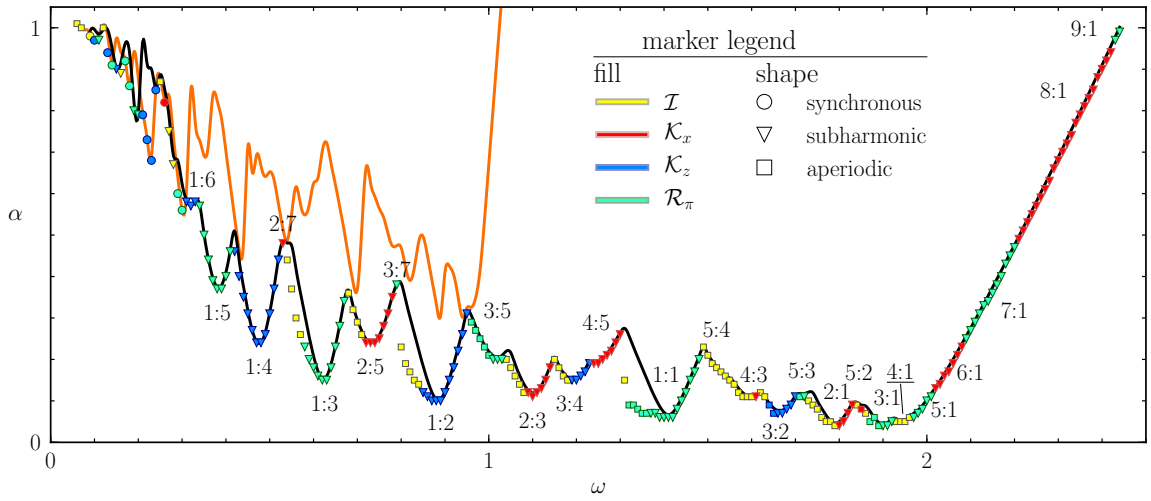

Figure 5.2: Stability boundaries in forcing frequency ω and forcing amplitude α space illustrating internal wave resonance tongues. The black curve is the boundary for subharmonic instability and the orange curve is the boundary for synchronous instability, both determined via Floquet analysis [109]. The symbols are placed at the lowest α for a given ω at which a non-trivial state is found via nonlinear simulations; the color and shape of the symbols correspond to their pointwise symmetry and temporal response, as indicated. Also indicated are the m:n spatial structure of the nonlinear states.

time, the state is invariant to the said symmetry. When $\mathcal{G}$ invariance is broken, the bifurcating state is pointwise invariant to only one of the generators of $\mathcal{G}$. The states may be only setwise invariant, whereby applying the symmetry to the state transforms it onto the same invariant manifold. If the setwise symmetry of a state is broken, applying the symmetry results in another state on a different manifold that is the symmetric image of the original manifold. Also, for any state $\mathcal{S}$ that is not synchronous with the forcing, there is a conjugate state $\mathcal{P}_\tau(\mathcal{S})$.

Table 5.2 is a list of the states that we report on in this study, together with their pointwise and setwise invariances.

5.4 Primary Instabilities

We begin with a broad overview of the flow response for $R_N = 2 \times 10^4$ and $\sigma = 1$ over a large range of forcing frequencies and amplitudes, $\omega \in (0, 2.5)$ and $\alpha \in (0, 1]$. This is summarized in figure 5.2, where the two solid curves are the loci in (ω, α) where the Floquet analysis of the basic state [109] indicates that a single multiplier leaves the unit circle either through $+1$ (synchronous; orange curve) or through -1 (subharmonic; black curve). Below both curves, all Floquet multipliers have modulus less than one (they are all inside the unit circle) and the basic state is stable. The spatial structures of the Floquet modes are very similar to those of the corresponding inviscid eigenmodes of the unforced cavity [97], which consist of m cells in the horizontal and n cells in the vertical directions. Regardless of whether the forced flow is synchronous or subharmonic, its frequency (the response frequency ω_R) is always very close to the eigenfrequency of the corresponding unforced inviscid eigenmode. For synchronous flow $\omega_R = \omega$ and for subharmonic flow $\omega_R = \omega/2$. The forced viscous modes differ from the inviscid eigenmodes primarily due to the presence of viscous boundary layers. The details of these boundary layers are given in Yalim *et al.* [109]. Superimposed on the Floquet stability boundaries in figure 5.2 are symbols indicating the lowest α for each considered frequency ω that a non-trivial state was found. The color and shape of the symbols indicate the symmetry (or lack there of) of the state and whether it is synchronous or subharmonic with respect to the forcing frequency. Synchronous states are only observed for low frequencies, $\omega \lesssim 0.3$, and these are irregularly interspersed with subharmonic states. The figure shows a complicated nesting of resonances tongues, each tongue corresponding to a resonant excitation of an m:n viscous eigenmode. The observed tongues correspond to low values of m and n (typically less than 10), and the finite Farey sequence of

m+p:n+q intermediate tongues nested between m:n and p:q tongues is consistent with the results of the Floquet analysis. More locally, the agreement between the Floquet stability results and the nonlinear simulations is also very good, particularly on the high-ω side of a resonance tongue, indicating that the primary instability is supercritical there. On the low-ω side, there are considerable discrepancies between the two, particularly for the resonance tongues 1:n with $n = 1$, 2, and 3. This is due to the instability being subcritical with the region of hysteresis being larger for smaller n. When nonlinear simulations use the basic state as the initial condition for increasing α at fixed ω, the first non-trivial result agrees very well with the Floquet analysis. The gaps between the nonlinear simulation symbols shown in the figure and the Floquet curve indicate the extent of the hysteresis regions where both the basic state and non-trivial solutions are attracting.

Figure 5.3 shows snapshots of the subharmonic limit cycles $\mathrm{L}_{m:n}$ near the tips of the leading tongues, obtained from the nonlinear simulations at the same forcing amplitudes and frequencies, α and ω, as was used in the Floquet analysis to illustrate the structure of the corresponding viscous modes $\mathrm{V}_{m:n}$ shown in figure 3 of Yalim *et al.* [109]. The structures are very similar, but do show subtle differences due to nonlinear harmonics in $\mathrm{L}_{m:n}$. Linearizing the Navier-Stokes equations about the basic state (5.5) introduces additional symmetries that the nonlinear system is not invariant to. Another distinction between the nonlinear states $\mathrm{L}_{m:n}$ and the corresponding Floquet modes $\mathrm{V}_{m:n}$ is that whereas $\mathrm{V}_{m:n}$ have a time-invariant spatial structure that is harmonically modulated in time, this is not the case for $\mathrm{L}_{m:n}$. The supplemental movie movie-fig503.mp4 shows animations of $\mathrm{L}_{1:1}$, $\mathrm{L}_{1:2}$, and $\mathrm{L}_{2:1}$ over one response period (i.e. two forcing periods), from which it is evident that there is a propagation from the top and bottom endwall boundary layers into the interior accompanied with a propagation from the interior to the sidewall boundary layers. This is more

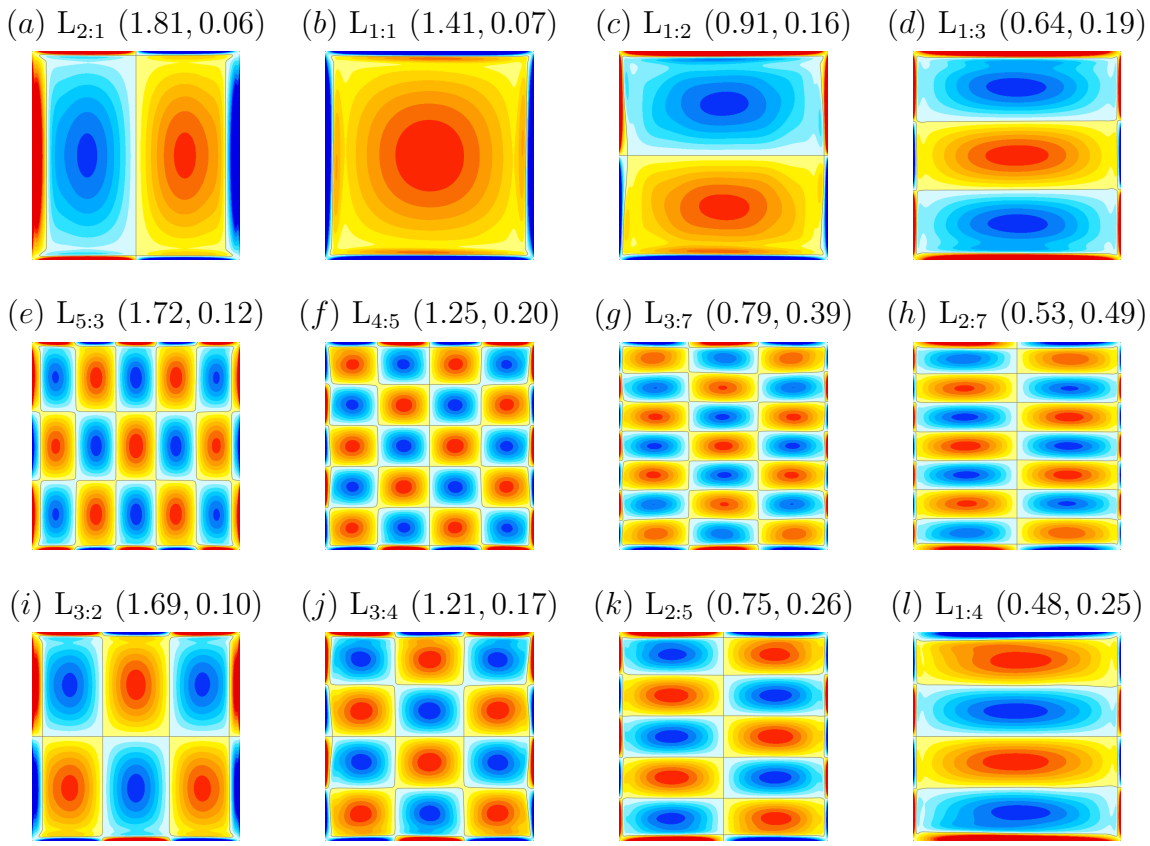

Figure 5.3: Vorticity at phase $\pi/2$ in the forcing for some of the subharmonic limit cycles $L_{m:n}$ at (ω, α) as indicated. See the supplemental movie movie-fig503.mp4 for animations of $L_{1:1}$, $L_{1:2}$, and $L_{2:1}$ over one response period (two forcing periods).

pronounced for larger m and n (movies are not shown). This nonlinearity results in a non-zero mean flow. Figure 5.4 shows the vorticity of the mean flow of the $L_{m:n}$ in figure 5.3; they all have the spatial structure of the corresponding first harmonic, i.e. the mean flow for $L_{m:n}$ has $2m$:$2n$ spatial structure.

5.5 The Tip of the 1:1 Resonance Tongue

We now focus on the 1:1 resonance tongue for the remainder of this study. This is also the resonance tongue which the experimental study of Benielli and Sommeria [7] primarily focused on. This tongue is the one which is least affected by neighboring

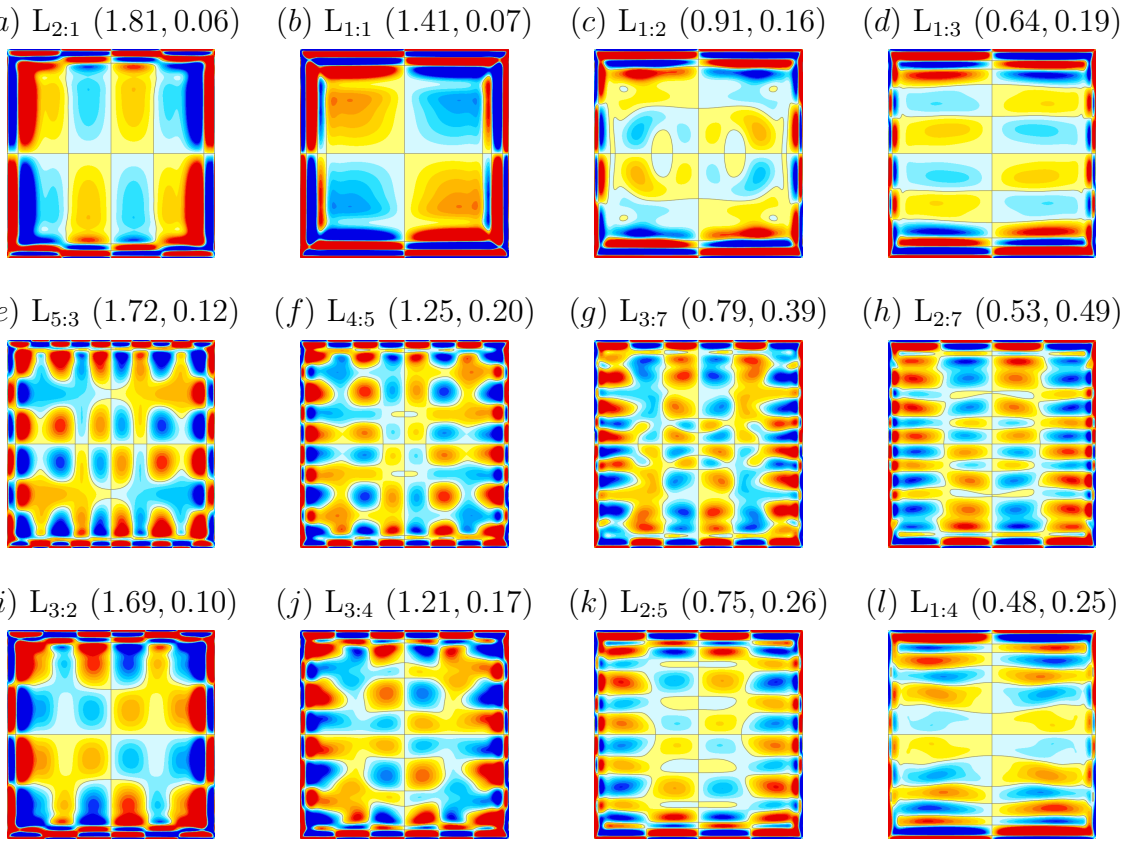

Figure 5.4: Time-averaged vorticity for the subharmonic limit cycle responses at (ω, α) as indicated, corresponding to the states in figure 5.3.

tongues near onset, and is also one of the least viscously damped tongues. Furthermore, as is evident from figure 5.2, the dynamics near the tip of the low-order tongues have many features in common: subcritical flip and fold-Neimark–Sacker bifurcations to the low-frequency side of the tips. In figure 5.5, the primary bifurcation curves found in the neighborhood of the 1:1 tongue tip are illustrated. There are a number of codimension-two points indicated in the figure. The dynamics in the neighborhoods of some of these have been studied theoretically [45], but for some there are only partial known theoretical results. In the following, we describe in some detail the nonlinear dynamics in the various regions of the resonance tongue and, where possible, we relate our nonlinear simulation results to the theoretically expected dynamics.

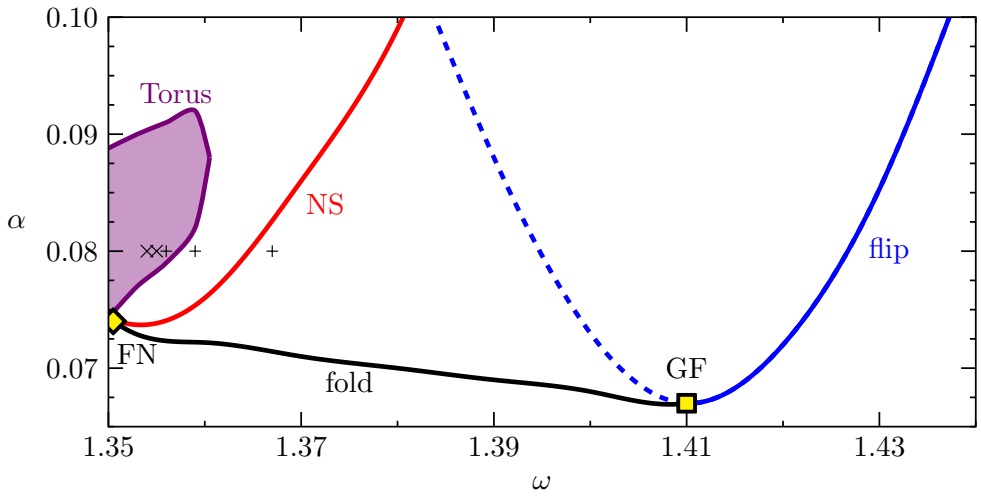

Figure 5.5: Bifurcation curves near the tip of the 1:1 resonance tongue. The flip bifurcation (blue curve) is where the basic state limit cycle period double; this bifurcation is supercritical along the solid blue curve and subcritical along the dashed blue curve. The fold bifurcation (black curve) is a saddle-node bifurcation of limit cycles. At the Neimark–Sacker curve (NS, red curve), the limit cycle bifurcates to a 2-torus, and at the Torus bifurcation (purple curve), the 2-torus bifurcates to a 3-torus. There are two codimension-two points: the generalized-flip (GF) and the fold-Neimark–Sacker (FN) points. The five markers are sampled solutions illustrated in figure 5.10.

At the tip of the tongue, located at $(\omega, \alpha) = (1.41, 0.068)$, the flip bifurcation curve identified via Floquet analysis [109] is found to change from supercritical at higher ω to subcritical at lower ω. The codimension-two point at which this change happens is often called a generalized flip (GF) point [45]. On crossing the supercritical flip bifurcation curve, the trivial basic state loses stability and a non-trivial limit cycle $\mathrm{L}_{1:1}$, whose period is equal to twice the forcing period, is spawned with amplitude growing from zero as the distance from the flip bifurcation curve increases. At the subcritical flip bifurcation, $\mathrm{L}_{1:1}$ is spawned to the 'left' (i.e. to lower ω and α) where the trivial basic state is still stable and the spawned $\mathrm{L}_{1:1}$ is unstable. Near the tip, the stable $\mathrm{L}_{1:1}$ coexists in this subcritical region, and we refer to the co-existing stable and unstable $\mathrm{L}_{1:1}$ as upper and lower branch states.

As in Lopez *et al.* [60], the edge state technique is used to capture the unstable lower branch state. This technique is robust if the unstable state only has one unstable direction. In general, unstable edge states $\mathcal{E}$ can be approached by using convex combinations of two stable states, $\mathcal{S}_0$ and $\mathcal{S}_1$, whose stable manifolds coincide with the unstable manifolds of the target edge state, as initial conditions and refining the weight $\gamma \in (0, 1)$, such that

$$\mathcal{E} = \gamma\mathcal{S}_0 + (1 - \gamma)\mathcal{S}_1. \tag{5.7}$$

To capture the saddle lower-branch $\mathrm{L}_{1:1}$ as an edge state $\mathcal{E}$, we take the stable basic state as $\mathcal{S}_0$ and the stable upper branch $\mathrm{L}_{1:1}$ as $\mathcal{S}_1$ at forcing phase 0.

As the bifurcation curve labelled 'fold' in figure 5.5 is approached from above, the upper and lower branch $\mathrm{L}_{1:1}$ coincide. The bifurcation is a saddle-node of limit cycles, also known as a cyclic-fold, or more simply, a fold bifurcation. This bifurcation curve also emerges from the codimension-two point GF. In the neighborhood of GF, there are no other dynamics involved [45, §9.3].

The limit cycle $\mathrm{L}_{1:1}$ has broken the two reflection symmetries $\mathcal{K}_x$ and $\mathcal{K}_z$. At any instant in time it is neither pointwise $\mathcal{K}_x$ nor pointwise $\mathcal{K}_z$ invariant, but remains pointwise $\mathcal{R}_\pi$ invariant. However, the broken spatial reflections have been replaced by space-time reflections. These are the half-period-flip symmetries $\mathcal{P}_\tau \circ \mathcal{K}_z$ and $\mathcal{P}_\tau \circ \mathcal{K}_x$; the forcing period τ is half of the response period of $\mathrm{L}_{1:1}$. Furthermore, since $\mathrm{L}_{1:1}$ is 2τ-periodic, applying $\mathcal{P}_\tau$ to it at time t_0 results in another 2τ-periodic limit cycle, which is equivalent to $\mathrm{L}_{1:1}$ at $t_0 + \tau$. In other words, there exists two initial value problem solutions $\mathrm{L}_{1:1}(t)$ and $\mathrm{L}_{1:1}(t + \tau)$. Local measures such as a velocity component at a point have time series that repeat every two forcing periods (2τ-periodic), whereas global measures such as E_T or E_K are τ-periodic as a consequence of the half-period-flip symmetries.

5.6 Dynamics in the Subcritical Region of the 1:1 Tongue

In the subcritical region near the tip of the tongue (i.e. in the neighborhood of the generalized flip codimension-two point GF), the stable basic state, the stable (upper branch) $L_{1:1}$, and the unstable (lower branch) $L_{1:1}$ coexist. Increasing α and/or lowering ω, the upper branch $L_{1:1}$ becomes unstable via a Neimark–Sacker bifurcation in which a stable quasiperiodic state T_2 emerges. This T_2 is setwise $\mathcal{G}$ symmetric. The Neimark–Sacker curve (labelled NS in figure 5.5) meets the fold curve emanating from the generalized flip point (GF) at another codimension-two fold-Neimark–Sacker bifurcation point, labelled FN in figure 5.5. It is one of the codimension-two points that only has partially known theoretical results [45, §9.1, case 9].

The fold-Neimark–Sacker bifurcation is sometimes called the Hopf-saddle-node for maps bifurcation. It has been studied by Broer *et al.* [15] in a low-dimensional model problem that was designed to be as "generic as possible." The model was constructed by perturbing the Poincaré map of the truncated normal form for the Hopf-saddle-node bifurcation. In essence, the Hopf-saddle-node bifurcation is treated as being the stroboscopic map of the fold-Neimark–Sacker bifurcation. As such, steady states and limit cycles of the Hopf-saddle-node bifurcation correspond to limit cycles and 2-tori of the fold-Neimark–Sacker bifurcation, and the strobes of those limit cycles and 2-tori are fixed points and cycles in the approximating map. But complications set in due to possible resonances when the frequencies of the 2-tori are in low-order rational ratios. Broer *et al.* [15] provide several conjectures based on numerical studies of their model problem that involve various bifurcations of limit cycles and 2-tori, yielding a cascade of bifurcations of 2-tori, and heteroclinic and homoclinic behavior. The Hopf-saddle-node bifurcation scenario on which their model was based is the one that includes the complex dynamics associated with the breaking of a heteroclinic

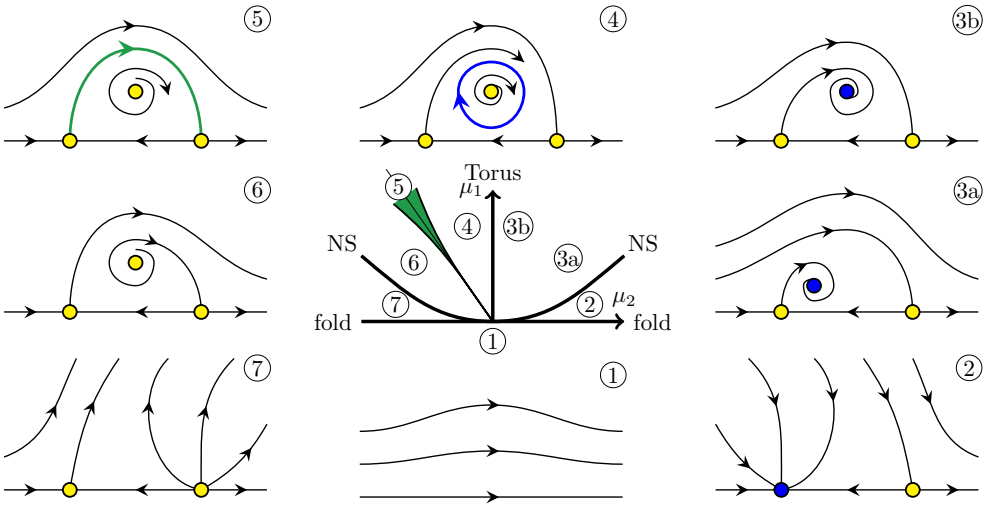

Figure 5.6: Schematic of the Hopf-saddle-node bifurcation, which is used to discuss the fold-Neimark–Sacker (FN) bifurcation.

connection. The nonlinear dynamics in the neighborhood of such a Hopf-saddle-node bifurcation have been studied numerically and experimentally in short aspect-ratio Taylor–Couette flows [57, 1]. Here, we find that much of the simpler dynamics in the neighborhood of the fold-Neimark–Sacker bifurcation FN indicated in figure 5.5 can be diagnosed along these same lines, and as in all Hopf-saddle-node and fold-Neimark–Sacker bifurcations that have been studied, the complex dynamics is very much case dependent, but intrinsically associated with the heteroclinic region. In the following, we describe in some detail such dynamics.

Figure 5.6 is a schematic of a Hopf-saddle-node bifurcation which we adopt to discuss the dynamics in the neighborhood of the fold-Neimark–Sacker point FN in figure 5.5. The FN point is at the origin of the bifurcation diagram, $(\mu_1, \mu_2) = (0, 0)$, where the coordinates μ_1 and μ_2 are the variables in the codimension-two normal form. These are related to the two variables our full problem, ω and α, by linear transformations near the point FN. The bifurcation diagram has a number of bifurcation curves that divide the (μ_1, μ_2) space into various regions, labelled 1–7.

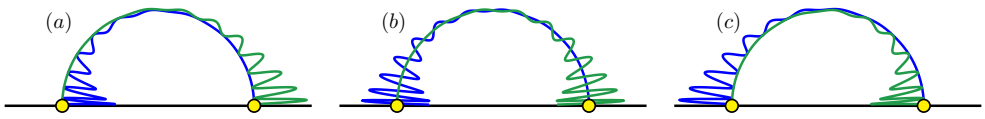

Figure 5.7: Schematic of the transverse across region 5 in figure 5.6.

Typical phase portraits in these regions are provided in the figure. In these phase portraits, the symbols on the horizontal axis are stable (blue) or unstable (yellow) equilibria, which correspond to the upper and lower branch $L_{1:1}$ limit cycles in the full problem. In region 1 ($\mu_1 < 0$), there are no solutions nearby in phase space and all initial conditions evolve away from this region of phase space. In the full problem the evolutions end up at the stable basic state, which is far removed from the neighborhood of the fold-Neimark–Sacker bifurcation in phase space.

Crossing the fold bifurcation curve from region 1 into region 2, the fold bifurcation leads to the creation of the upper and lower branch $L_{1:1}$. Crossing the Neimark–Sacker curve NS from region 2 to region 3, the stable upper branch $L_{1:1}$ loses stability and spawns a stable 2-torus T_2. In the phase portraits for regions 3a and 3b, this 2-torus is indicated as a (blue) equilibrium off the axis. The way to interpret the nature of the equilibria in the phase portraits is that equilibria on the axis have one frequency (corresponding to $\omega/2$ since the $L_{1:1}$ are subharmonic); equilibria off the axis correspond to 2-tori and have an additional frequency (associated with rotations of the equilibria around the axis). The second frequency varies along the Neimark–Sacker curve NS, and may be in a rational ratio with the first frequency ($\omega/2$) at various points along the curve. From such points emerge Arnold tongues into region 3 in which the flow is phase locked.

Crossing from region 3 into region 4, the curve labelled 'Torus' is crossed, at which the 2-torus loses stability (it goes from being blue to yellow) and a stable (blue) invariant circle is spawned in the phase portrait for region 4. This invariant

circle has three frequencies associated with it: two are inherited from the 2-torus and the third is new corresponding to cycling around the blue circle. This indicates the birth of a 3-torus T_3. Below we give descriptions of numerical solutions exhibiting 3-torus dynamics in the corresponding parameter region in figure 5.5. The dynamics in region 5 are not smooth due to various resonances, as suggested by the model case study in Broer *et al.* [15]. In the Hopf-saddle-node normal form, the invariant circle becomes heteroclinic to the two unstable equilibria on the axis (the green curve in the region 5 phase portrait). Even for the Hopf-saddle-node bifurcation, this heteroclinic connection does not persist if higher order terms in the normal form are included. Typically, the higher order terms result in the stable and unstable manifolds emanating from the unstable equilibria on the axis intersecting transversely instead of coinciding. This is illustrated in figure 5.7. The wedge shaped region 5 in green demarcates the region where the transverse intersections occur. It is in this region that very complicated dynamics occurs, some of which we describe below. Continuing from region 5 into regions 6 and 7, all states in the phase space neighborhood of the fold-Neimark–Sacker bifurcation are unstable, and so all initial conditions eventually evolve away from this part of phase space.

Figure 5.5 includes '+' markers, these indicate the (ω, α) locations of some sample states whose time series are shown in figure 5.8. Time is shown in units of n_τ, the number of forcing periods $\tau = 2\pi/\omega$. All are shown at $\alpha = 0.08$ and the variation in ω corresponds to a traverse through the NS and Torus bifurcation curves. For each case, the time series on the left is of T_p, the temperature at the point $(x_p, z_p) = (1/\sqrt{8}, 1/\sqrt{8})$ (a local measure). The one on the right is of the normalized thermal $\mathcal{L}^2$ measure E_T (a global measure). The first case at $\omega = 1.367$ is the upper branch limit cycle $L_{1:1}$. As described earlier, it is a subharmonic response so that the local measure is 2τ-periodic, but it is setwise $\mathcal{G}$ symmetric so its global measure is τ-periodic. The

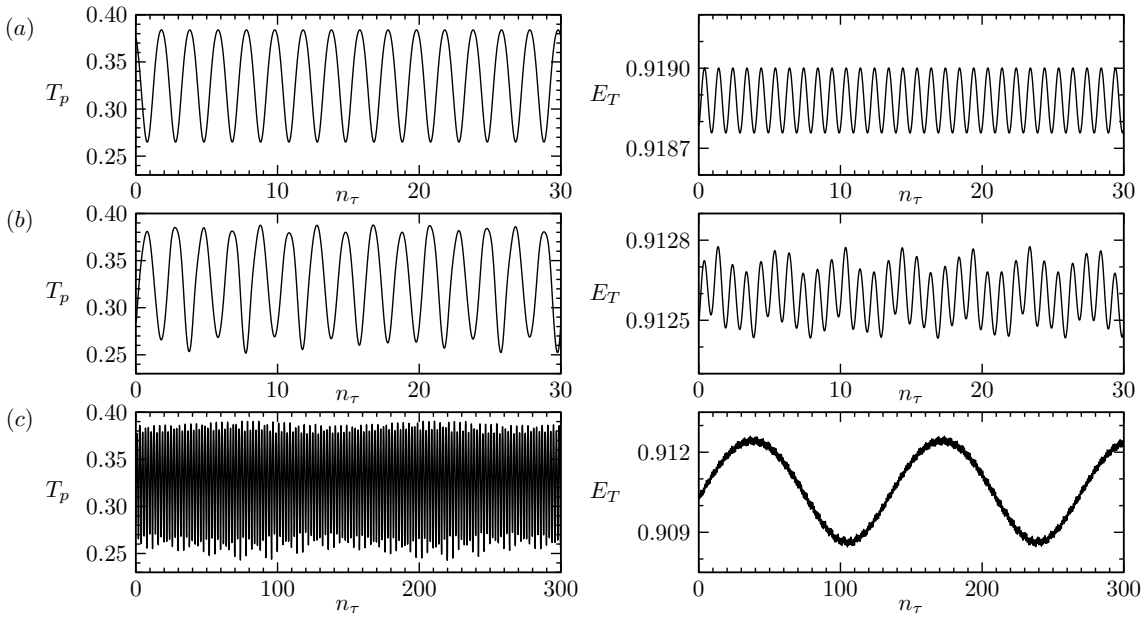

Figure 5.8: Time series of the temperature at $(x_p, z_p) = (1/\sqrt{8}, 1/\sqrt{8})$, T_p (left) and the normalized thermal $\mathcal{L}^2$ measure E_T (right) for (a) $\mathrm{L}_{1:1}$ at $\omega = 1.367$, (b) T_2 at $\omega = 1.359$, and (c) T_3 at $\omega = 1.356$, all with $\alpha = 0.08$, corresponding to the '+' marks in figure 5.5.

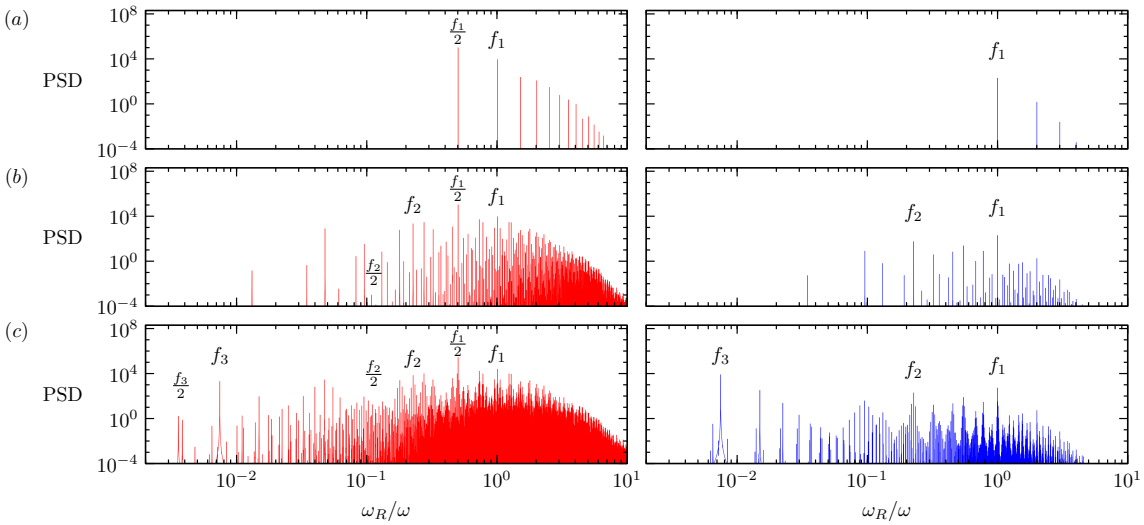

Figure 5.9: Frequency spectra of the time series shown in figure 5.8. The angular response frequency ω_R has been normalized by the forcing frequency ω.

power spectral densities (PSD) of these time series are shown in figure 5.9(a). The spectra of E_T shows a single peak at $\omega_R/\omega = f_1 = 1.0$, plus harmonics, whereas that of T_p also shows a (stronger) peak at $\omega_R/\omega = f_1/2$, plus harmonics. The next state at $\omega = 1.359$ is to the low-ω side of the NS curve. It is a 2-torus T_2 that was spawned at the Neimark–Sacker bifurcation where $\mathrm{L}_{1:1}$ loses stability. The time series of T_2 are very similar to those of $\mathrm{L}_{1:1}$ with a small amplitude modulation. Together with the corresponding spectra, we see that this modulation frequency is $f_2 \approx 0.223 f_1$. The E_T spectra of T_2 consists of peaks at these two frequencies plus their linear combinations. The T_p spectra has many more peaks, corresponding to $f_1/2$, $f_2/2$ and all their linear combinations. This is evidence that T_2 is also setwise $\mathcal{G}$ symmetric. The third case at $\omega = 1.356$ is to the low-ω side of the Torus curve. On crossing the Torus curve, T_2 loses stability and a 3-torus T_3 is spawned. The T_p time series shows multiple frequencies, but the E_T time series of T_3 is essentially that of T_2 with a very large amplitude (about a factor of 10) low frequency modulation. The corresponding E_T spectra of T_3 consists of peaks at f_1 and f_2 (just like that of T_2), together with a very low frequency peak at $f_3 \approx 0.0075 f_1$ (corresponding to a period of approximately 133τ), and all their linear combinations. The spectra of the local measure T_p has many more peaks as it consists of all the linear combinations of $f_1/2$, $f_2/2$, and $f_3/2$.

Figure 5.10 shows strobe maps using both local (panel a) and global (panel c) quantities of the three states just described above (corresponding to the + markers in figure 5.5). The local map uses the horizontal and vertical components of velocity at the point $(x_p, z_p) = (1/\sqrt{8}, 1/\sqrt{8})$ every two forcing periods at forcing phase π. The global map strobes the kinetic and thermal global measures, given in (5.2), also every two forcing periods and at a half period phase shift. The first state is $\mathrm{L}_{1:1}$ at $\omega = 1.367$. Its strobe map is a point (yellow circular symbol). The next state is T_2 at $\omega = 1.359$. Its strobe map is a cycle (closed red loop), which is clearly seen

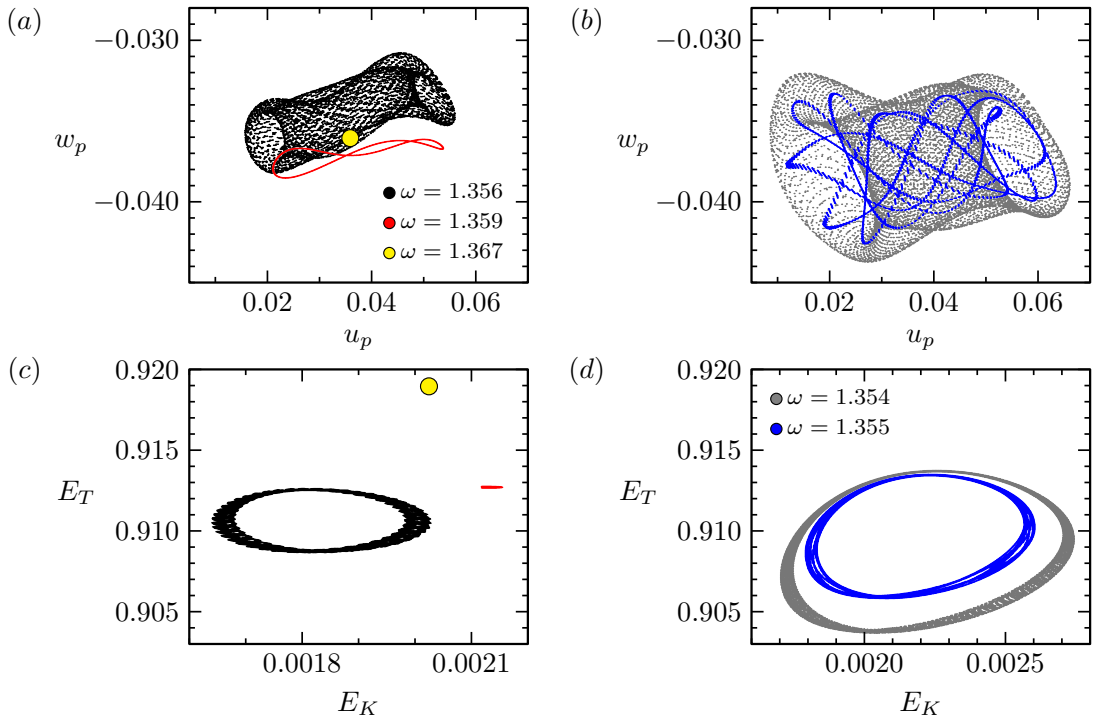

Figure 5.10: Local and global strobe maps of the flows with $\alpha = 0.08$ at the specified forcing frequency ω, showing the strobed behavior of 1-tori, 2-tori, and 3-tori as ω is decreased. The states shown in (a, c) corresponds to the + markers in figure 5.5 and those in (b, d) to the $\times$ markers.

in the local map but requires a significant zoom in to be clearly seen in the global map. The third state is T_3 at $\omega = 1.356$. The global strobe map of T_3 is the black doughnut-shaped structure, typical of a 2-torus; its structure in the local strobe map is also a 2-torus. Figure 5.10(b, d) shows the local and global strobe maps for two other T_3 states. These are indicated by the '$\times$' markers in figure 5.5 at slightly smaller $\omega = 1.355$ and 1.354. Their strobe maps show how they rapidly expand in phase space with very small decreases in ω. Also, the $\omega = 1.355$ case is nearly phase locked; the strobe map is a convoluted cycle on a 2-torus.

We now explore some of the dynamics inside the region enclosed by the Torus curve (shaded purple in figure 5.5). We begin by fixing $\omega = 1.35$. Figure 5.11 is a bifurcation diagram at this ω, using the temporal standard deviation in the

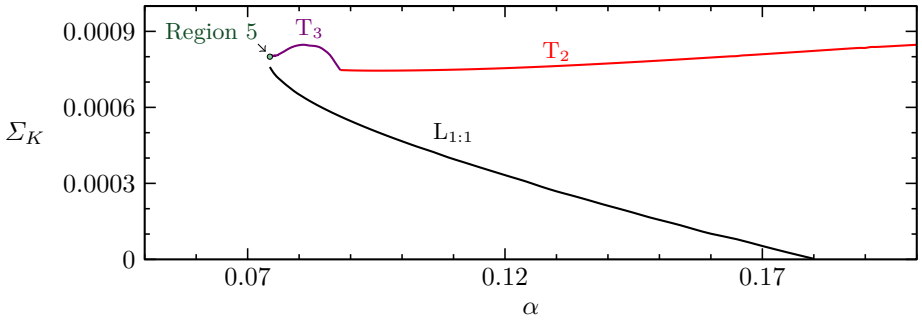

Figure 5.11: Bifurcation diagram for $\omega = 1.35$.

kinetic energy, Σ_K, as a measure of the state. The basic state has $\Sigma_K = 0$. It loses stability at $\alpha \approx 0.181$ in a subcritical flip bifurcation, spawning an unstable limit cycle $L_{1:1}$ to lower α. For larger α, the flow evolves to the quasiperiodic T_2, which we have continued down to smaller α. At $\alpha \approx 0.089$, T_2 loses stability at the Torus bifurcation, and 3-torus T_3 is spawned. Using the stable T_2 and T_3, together with the stable basic state, we have used the edge state technique to capture the unstable $L_{1:1}$. At $\alpha \approx 0.074426$, the T_3 begins a cascade of bifurcations which are described below in some detail. This essentially corresponds to entering region 5 marked in schematic of the Hopf-saddle-node bifurcation in figure 5.6.

Figure 5.12 illustrates some characteristics of a state in the above mentioned region 5. It shows the local phase portrait (figure 5.12a), using the two velocity components at the point $(x_p, z_p) = (1/\sqrt{8}, 1/\sqrt{8})$ and the global phase portrait (figure 5.12c), using E_T and E_K, of the basic state (green dot in the local phase portrait), the unstable $L_{1:1}$ (yellow cycle in the local and global phase portraits; note however that E_T of $L_{1:1}$ is essentially time invariant), and a complicated state that resides in region 5 (black cloud of dots). Further insight is gained by examining the strobed phase portraits, shown in figure 5.12(b, d). In the strobe maps, the limit cycle $L_{1:1}$ is simply a point (yellow dot), and the complicated state in the global strobe map is a thin 2-torus with five loops and in the local strobe map it appears as a wide 2-torus structure with five

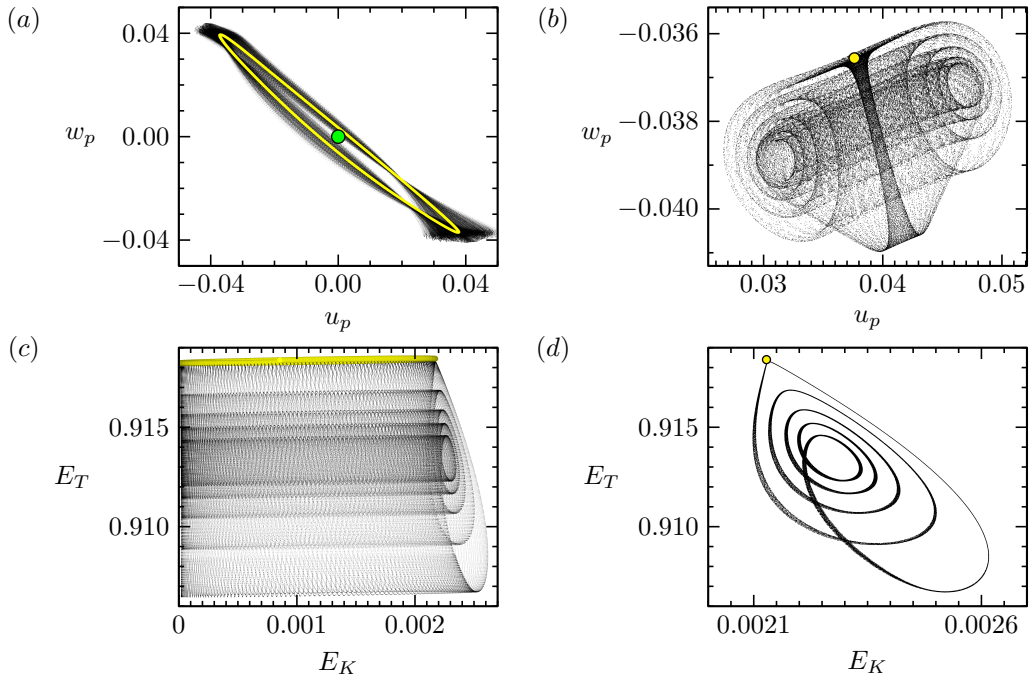

Figure 5.12: (a) Local phase portraits of the basic state (green dot), the unstable lower branch $\mathrm{L}_{1:1}$ (yellow cycle computed using the edge state technique), and the stable attractor (black cloud), and (b) the corresponding strobe map (strobed every two forcing periods at forcing phase $\pi/2$), in which $\mathrm{L}_{1:1}$ is a single (yellow) dot, and the stable attractor is in black, all at at $(\omega, \alpha) = (1.35, 0.074\,317\,8)$. ($c$) and ($d$) illustrate the global data associated with (a) and (b). Note that the basic state is not shown in (c); it is located at $(E_K, E_T) = (0, 1)$.

scrolls. Furthermore, this T_3 is very close to forming a homoclinic connection to the unstable $\mathrm{L}_{1:1}$.

The T_3 for $\omega = 1.35$ and $\alpha \in [0.074\,43, 0.089]$ exhibits behavior which we describe as having $\ell = 1$ loop. Reducing the forcing amplitude just below $\alpha \approx 0.074\,42$, the global strobe map shows that T_3 has $\ell = 2$ loops. In a sense, there has been a period-doubling of the T_3. Further reducing α below approximately $0.074\,374$, there is another period-doubling resulting in an $\ell = 4$ T_3, and an $\ell = 8$ T_3 at $\alpha \approx 0.074\,365$. Further doublings were not resolved in this neighborhood. Examples of T_3 with $\ell = 1$, 2, 4, and 8 are shown in figures 5.13(a–d), which give both the local and global strobe

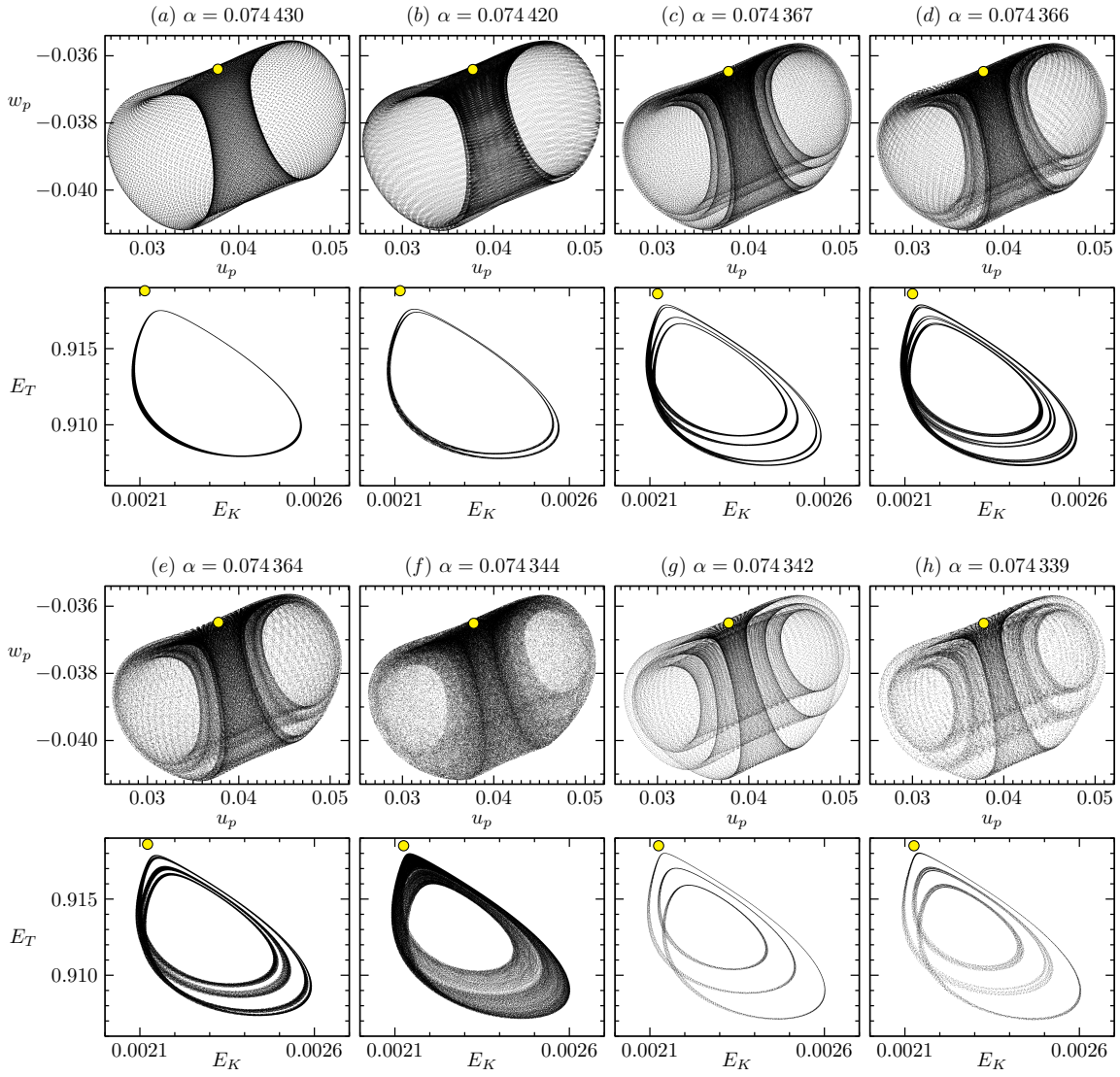

Figure 5.13: Local and global strobe maps (strobed every two forcing periods at forcing phase $\pi/2$) for $\omega = 1.35$ and α as indicated, illustrating states in the period-doubling cascade. The yellow marker corresponds to the strobed unstable $L_{1:1}$, determined using the edge state technique.

maps of the T_3 (they also include the unstable $L_{1:1}$ obtained using the edge state technique, indicated as a yellow dot). The strobe maps for smaller α (figures 5.13*e*–*h*) generally did not show distinct loops or scrolls, except for some very narrow windows in α where an $\ell = 6$ T_3 at $\alpha = 0.074\,359$ and an $\ell = 5$ T_3 at $\alpha = 0.074\,350$ were detected. The start of a second period-doubling cascade with $\ell = 3 \to \ell = 6$ at $\alpha \approx 0.074\,34$ was also found. This behavior of the strobe maps is very reminiscent of the behavior of the logistic map [68].

We further explore the logistic map-like behavior of the strobe maps by taking a Poincaré-like section of the global strobe map. Of course, the strobe map is a discrete-time map and so we cannot simply take a Poincaré section of it. Instead, we define a transverse section, give it a little thickness, and record E_T whenever the strobe map is within this thin transverse rectangular section. The strobe map was iterated (i.e. the flow was simulated) for up to 10^6 forcing periods for each value of α (124 values of $\alpha \in [0.074\,317\,8, 0.074\,520]$). The results (discarding the early transients) are shown in figure 5.14(*a*). The similarity to the logistic map is striking. The supplemental movie movie-fig514.mp4 animates the 124 cases in this small range in α, with each frame corresponding to a different value of α, and consisting of the local and global strobe maps at that α, and a vertical line at the α value of the plot in figure 5.14(*a*). At several of the α values where the strobe maps have distinct ℓ loops/scrolls, we plot in figure 5.14(*b*) the period corresponding to the very low frequency in the T_3, and in figure 5.14(*c*) this period is divided by ℓ, giving essentially the averaged period $1/f_3$ over the ℓ loops. This averaged period $1/f_3$ grows linearly with decreasing α.

The logistic map-like dynamics just described also has much in common with what is theoretically expected in a so-called homoclinic-doubling cascade [78], in which an entire period-doubling cascade collides with a saddle equilibrium. In period-doubling cascades that do not involve homoclinic collisions, the parameter values

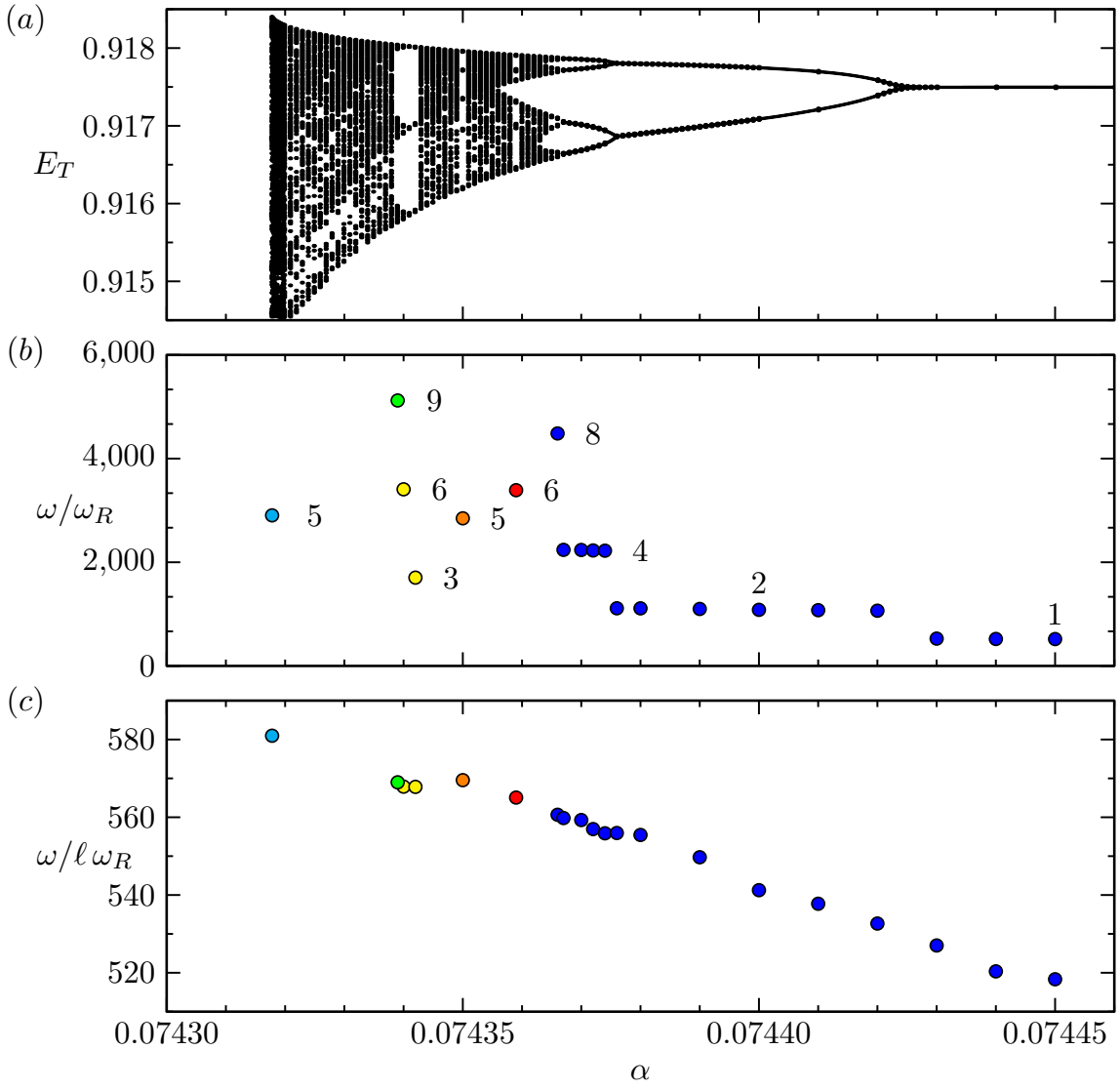

Figure 5.14: (a) Variation with α of E_T strobed every two forcing periods at forcing phase $\pi/2$ for $\omega = 1.35$, (b) response period relative to the forcing period, ω/ω_R, in the periodic windows in (a), with the integer ℓ related to the logisitic map like period-doubling cascade, and (c) $\omega/\ell\omega_R$. See the supplemental movie movie-fig514.mp4, which shows how the local and global strobed phase portraits (shown in figure 5.13) vary with α.

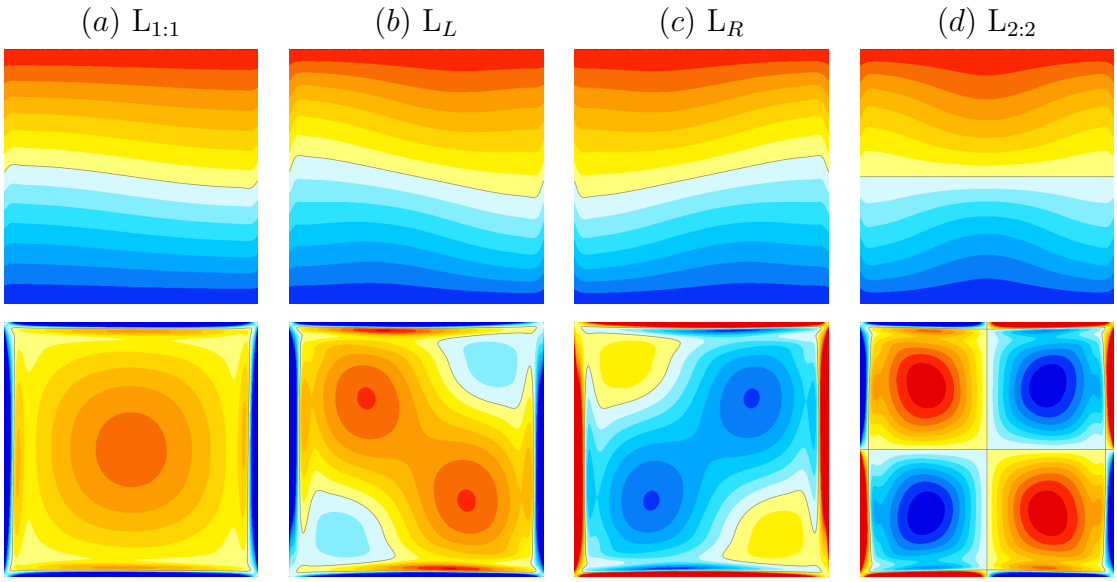

Figure 5.15: Snapshots of the temperature and vorticity for subharmonic limit cycles at $\omega = 1.41$: (a) $\mathrm{L}_{1:1}$ at $\alpha = 0.07$, (b) and (c) L_L and L_R at $\alpha = 0.105$, and (d) $\mathrm{L}_{2:2}$ at $\alpha = 0.105$. The temperature snapshots are at forcing phase $3\pi/2$ whereas the vorticity is shown at $\pi/2$. The supplemental movie movie-fig515.mp4 animates the temperature and vorticity of the four limit cycles over two forcing periods.

at which the period-doubling bifurcations occur follow a self-similar scaling given by the Feigenbaum constant [30]. In contrast, for the homoclinic-doubling cascade, the scaling constants depend on the eigenvalues of the saddle equilibrium. While Oldeman *et al.* [78] studied a system of three ordinary differential equations with quadratic nonlinearity that was constructed to satisfy conditions for the existence of a homoclinic-doubling cascade, they concluded that such a cascade is a generic mechanism that should be found in many physical systems. We believe that the cascade we have found is the first to be reported in a hydrodynamic system.

5.7 Dynamics Associated with Symmetry Breaking and Restoring

So far, all of the flows described in the 1:1 tongue have been pointwise $\mathcal{R}_\pi$ invariant and setwise $\mathcal{G}$ invariant. Keeping our focus within this tongue, we now explore how

these symmetries are broken and restored. We begin by fixing $\omega = 1.41$, which is very close to the frequency at the tip of the 1:1 tongue, and increase α. Upon increasing α across the tongue at $\alpha \approx 0.066$, the subharmonic $\mathrm{L}_{1:1}$ is spawned, as described earlier. As was noted in § 5.3, for any state $\mathcal{S}$ that is not synchronous with the forcing, there also exists a conjugate state $\mathcal{P}_\tau(\mathcal{S})$. This is the case for $\mathrm{L}_{1:1}$ and all states that bifurcate from it. Up to now, this has not been dynamically important, but it will be in some parameter regimes which we now explore.

Increasing α past 0.101, $\mathrm{L}_{1:1}$ loses stability at a pitchfork bifurcation breaking the half-period-flip symmetry, i.e. the setwise $\mathcal{G}$ invariance, where a pair of symmetrically-related limit cycles, L_L and L_R, appear. Applying either $\mathcal{K}_x$ or $\mathcal{K}_z$ to one results in the other:

$$\mathcal{K}_x \,\mathrm{L}_L(x,z,t) = \mathrm{L}_R(x,z,t) \quad \text{and} \quad \mathcal{K}_z \,\mathrm{L}_L(x,z,t) = \mathrm{L}_R(x,z,t). \tag{5.8}$$

Figure 5.15 illustrates snapshots of the temperature and vorticity of $\mathrm{L}_{1:1}$ at $\alpha = 0.066$, and L_L, L_R, and $\mathrm{L}_{2:2}$ at $\alpha = 0.105$ (supplemental movie movie-fig515.mp4 animates these over two forcing periods); these states are all pointwise $\mathcal{R}_\pi$ invariant. Note that $\mathrm{L}_{2:2}$ is unstable. It was computed by restricting the simulations to the $\mathcal{G}$ symmetric subspace.

In fact, much of the dynamics we will describe in this section entails interactions that involve unstable states, such as $\mathrm{L}_{2:2}$. Fortunately, many of these are stable in symmetry subspaces, and so we now explore the dynamics restricted to the various symmetry subspaces before putting it all together in the full space.

5.7.1 Dynamics Restricted to the $\mathcal{G}$ and $\mathcal{K}_z$ Subspaces

$\mathrm{L}_{2:2}$ is pointwise $\mathcal{G}$ invariant. Fixing $\omega = 1.41$ and computing in the $\mathcal{G}$ subspace, $\mathrm{L}_{2:2}$ is found to bifurcate subharmonically (so it is 2τ periodic) from the base state by

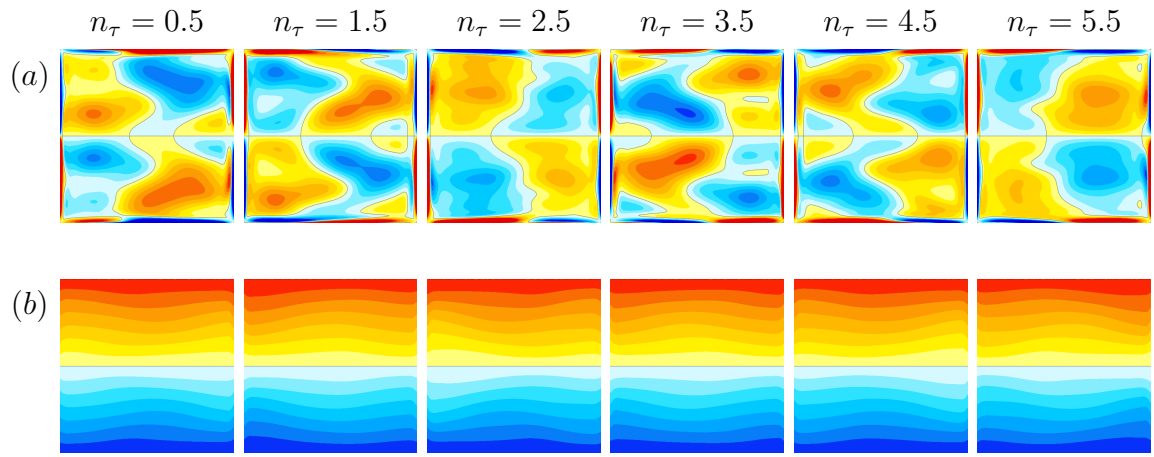

Figure 5.16: Snapshots of (a) the vorticity and (b) the temperature of S_2 at $\omega = 1.41$ and $\alpha = 0.111$ shown at six consecutive forcing periods at phase π. The supplemental movie movie-fig516.mp4 shows the corresponding animations over the six forcing periods.

$\alpha \approx 0.084$, which is very close to the forcing amplitude predicted by Floquet analysis, $\alpha \approx 0.0831$ [109]. It remains stable up to $\alpha \approx 0.155$. However, if the simulations are only restricted to the $\mathcal{K}_z$ subspace, it loses stability at $\alpha \approx 0.087$ via a $\mathcal{K}_x$-symmetry breaking Neimark–Sacker bifurcation. The new frequency f_2 is approximately an order of magnitude smaller than the forcing frequency, $1/f_2 \approx 7$, and corresponds to an internal sloshing state that modulates the $L_{2:2}$ oscillation. Figure 5.16 shows a few snap-shots of the temperature and vorticity of the sloshing state, S_2, at $\alpha = 0.111$ (the supplemental movie movie-fig516.mp4 shows the temporal evolution over six forcing periods). S_2 loses stability at $\alpha \approx 0.114$ at a secondary Neimark–Sacker bifurcation that spawns a 3-torus, S_3, which inherits the two frequencies of S_2 and has a new much lower third frequency, approximately another order of magnitude smaller. Figure 5.17 shows the variations with α of Σ_u^2 and the number of forcing periods ω/ω_R associated with the primary E_T response frequencies of $L_{2:2}$, S_2, and S_3 for $\omega = 1.41$.

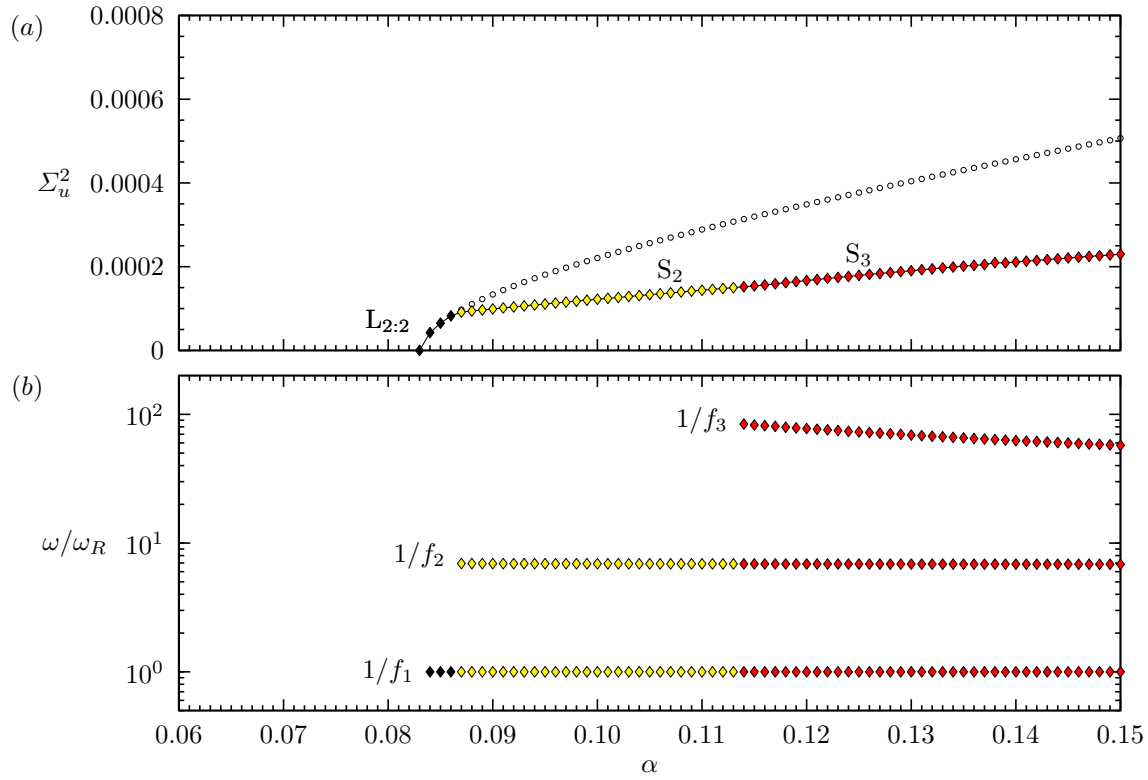

Figure 5.17: Variations with α at $\omega = 1.41$ of (a) the variance of the horizontal velocity Σ_u^2 at the point $(x_p, z_p) = (1/\sqrt{8}, 1/\sqrt{8})$, computed in the $\mathcal{K}_z$ symmetric subspace, and (b) the number of forcing periods corresponding to the E_T response frequencies of $L_{2:2}$ (f_1), S_2 (f_1, f_2) and S_3 (f_1, f_2, f_3). The part of the $L_{2:2}$ branch with open circles is unstable in the $\mathcal{K}_z$, but is stable in the $\mathcal{G}$ subspace.

5.7.2 Dynamics in the $\mathcal{R}_\pi$ Subspace

We now consider what happens in the $\mathcal{R}_\pi$ invariant subspace. L_L and L_R which bifurcated from $L_{1:1}$ at the pitchfork bifurcation at $\alpha \approx 0.084$ are $\mathcal{R}_\pi$ invariant, as is $L_{1:1}$. In the $\mathcal{R}_\pi$ subspace they remain stable until $\alpha \approx 0.1208$, where they lose stability at a Neimark–Sacker bifurcation NS_s. A 2-torus pair, Q_L and Q_R, are spawned and are $\mathcal{G}$ symmetry conjugates. The period associated with the second frequency acquired at NS_s is approximately 400 forcing periods near onset and suddenly becomes unbounded as α is increased. This second frequency corresponds to a slow drift toward and away from the $\mathcal{G}$ symmetry subspace, and at $\alpha = \alpha_{G1} \approx 0.125\,536$, Q_L and Q_R

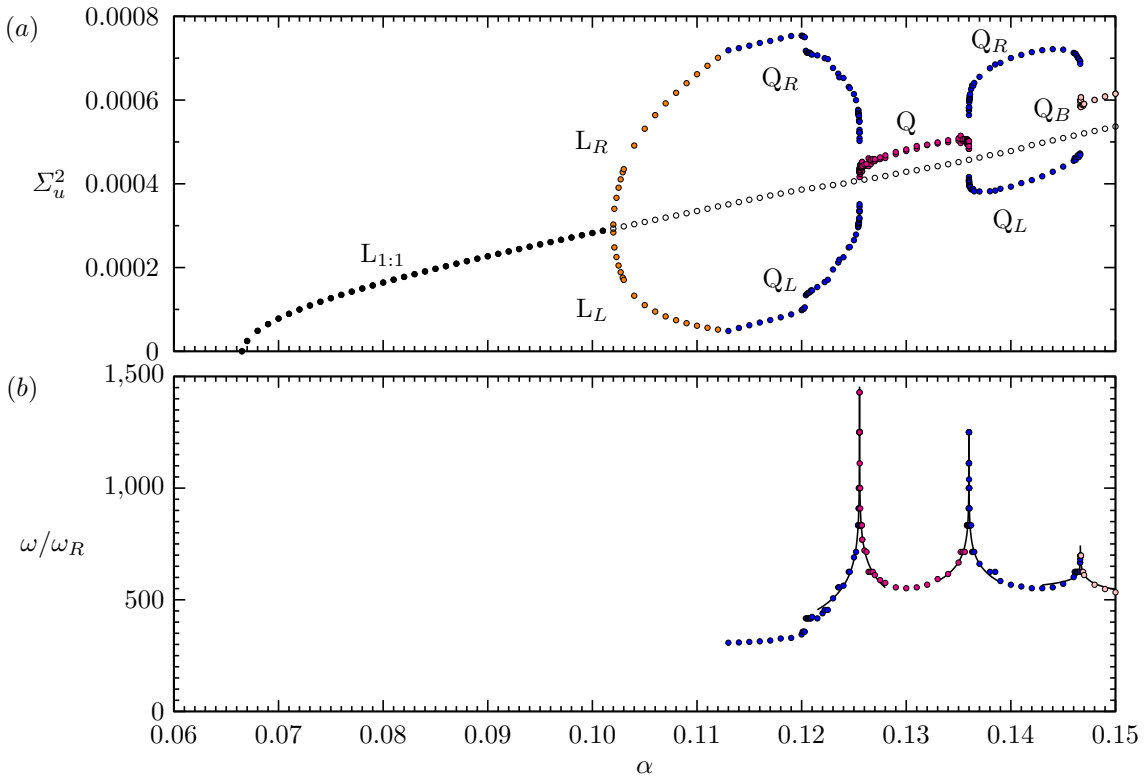

Figure 5.18: Variations with α at $\omega = 1.41$ of (a) variance of the horizontal velocity Σ_u^2 at the point $(x_p, z_p) = (1/\sqrt{8}, 1/\sqrt{8})$ for various observed states in the $\mathcal{R}_\pi$ symmetric subspace, as indicated, and (b) the number of forcing periods of the slow response versus forcing amplitude for 2-tori states in (a). The data are fitted to logarithmic fits $\omega/\omega_R = a_1 \ln(1/|\alpha - \alpha_c|) + a_2$, with $\alpha_{G1} = 0.125\,536$, $\alpha_{G2} = 0.135\,994$, and $\alpha_{G3} = 0.146\,631$. The plotted slow periods were computed by finding the highest amplitude frequency of the E_T power spectral density over 20 000 forcing periods. The supplemental movie movie-fig518.mp4 animates the strobe maps of the states in steps of 0.01 in α.

each become homoclinic to the saddle $L_{1:1}$ which resides in the $\mathcal{G}$ subspace. For $\alpha > \alpha_{G1}$, a single setwise $\mathcal{G}$ invariant 2-torus, Q, results from the homoclinic gluing [33]. The homoclinic gluing bifurcation occurs when two symmetrically-related states simultaneously become homoclinic to a saddle and "glue" together to form a single symmetric state. Figure 5.18 shows the velocity variances of the states involved in the $\mathcal{R}_\pi$ subspace as α is increased, along with the second frequency of the 2-tori states. The critical α_{G1} was determined by using a logarithmic fit $\omega/\omega_R = c_1 \ln(1/|\alpha - \alpha_{G1}|) + c_2$ [32, 53, 65, 57]. Also, the variance Σ_u^2 of the unstable $L_{1:1}$ are included in figure 5.18 as open circular symbols. These were obtained by using the unstable basic state as initial condition; the unstable $L_{1:1}$ appears as a long-lived transient (on the order of hundreds of forcing periods). The flow evolves quickly from the unstable basic state, spirals in toward the saddle-focus $L_{1:1}$, and eventually evolves away from it to a nearby stable trajectory.

Figures 5.19 and 5.20 illustrate the dynamics just before and after the gluing bifurcation at $\alpha = \alpha_{G1}$. At $\alpha = 0.125$, the strobe map of Q_L shows a slow-fast trajectory composed of saddle-focus behavior with the slow behavior being at the focus, followed by a rapid excursion out from the focus. The snap-shots in figure 5.20 show the focus to be $L_{1:1}$, and the trajectory away from the focus resembles L_L, then $L_{2:2}$ briefly as it loops back, again resembling L_L, and spirals in toward the focus again. The numbers labelled on the various strobe maps in figures 5.19 corresponds to the snap-shots in figure 5.20. For Q_R, there is also a spiral into $L_{1:1}$, but the ejection out is via L_R and the $L_{2:2}$-like part of the trajectory at the top of the loop has more of a 'right-hand' bias than the $L_{2:2}$-like part in Q_L. After the gluing, the result is Q which consists of alternating Q_L and Q_R loops, as illustrated in figure 5.20(c) at $\alpha = 0.126$. The supplemental movie movie-fig520.mp4 animates the strobes of Q_L, Q_R, and Q shown in the figures over several hundred forcing periods, mapping out

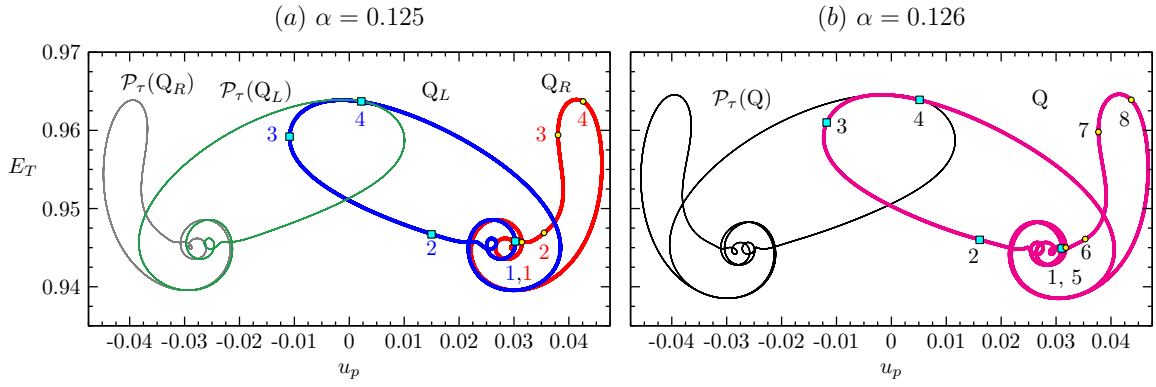

Figure 5.19: Strobe maps (every two forcing periods at forcing phase π) for (a) Q_L and Q_R (thick blue and red curves) as well as $\mathcal{P}_\tau(\mathrm{Q}_L)$ and $\mathcal{P}_\tau(\mathrm{Q}_R)$ (thin green and gray curves) at $\alpha = 0.125$, before the gluing bifurcation, and (b) Q (thick magenta curve) and $\mathcal{P}_\tau(\mathrm{Q})$ (thin black curve) at $\alpha = 0.126$, after the gluing of Q_L and Q_R (and $\mathcal{P}_\tau(\mathrm{Q}_L)$ and $\mathcal{P}_\tau(\mathrm{Q}_R)$). The simulations were restricted to the $\mathcal{R}_\pi$ symmetric subspace.

the near-homoclinic cycles involved in the gluing. Everything just described for Q_L, Q_R, and Q also takes place for $\mathcal{P}_\tau(\mathrm{Q}_L)$, $\mathcal{P}_\tau(\mathrm{Q}_R)$, and $\mathcal{P}_\tau(\mathrm{Q})$, as illustrated by the thin curves in figure 5.19.

Q unglues at $\alpha = \alpha_{G2} \approx 0.135\,994$. This ungluing is essentially like the first gluing at $\alpha = \alpha_{G1}$ in reverse as α is increased. Figures 5.21 and 5.22 illustrate the dynamics just before and after this second gluing bifurcation, as does the supplemental movie movie-fig522.mp4. The essential difference between the first and second gluings is that the flows traverse a larger part of phase space at the larger α. In both the first and second gluing bifurcations, for α close to α_{G1} and α_{G2}, the period $1/f_2$ becomes unbounded smoothly and monotonically.

In figure 5.18(a), at $\alpha_{G3} \approx 0.146\,631$ the period $1/f_2$ again becomes unbounded, but now this process is neither smooth nor monotonic. This gluing event is different to the two gluing bifurcations described above. The most obvious difference is that now Q_R and $\mathcal{P}_\tau(\mathrm{Q}_L)$ glue, i.e. the trajectories that glue have opposing phases at the $\mathrm{L}_{1:1}$ saddle-focus. This is seen both on the strobe maps in figure 5.23 and in the snap

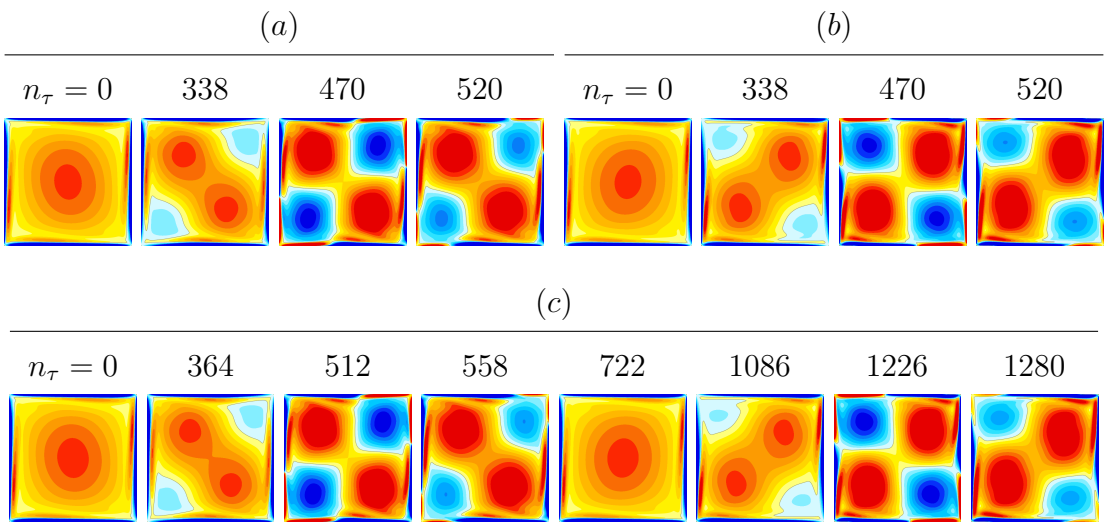

Figure 5.20: Snapshots of the vorticity at forcing phase π with $\omega = 1.41$ at the markers indicated in figure 5.19 (the relative times of the markers are indicated in terms of forcing periods): (a) and (b) Q_L and Q_R at $\alpha = 0.125$ and (c) Q at $\alpha = 0.126$. The supplemental movie movie-fig520.mp4 animates the strobe maps and vorticity of the Q_L, Q_R, and Q states at the respective parameters.

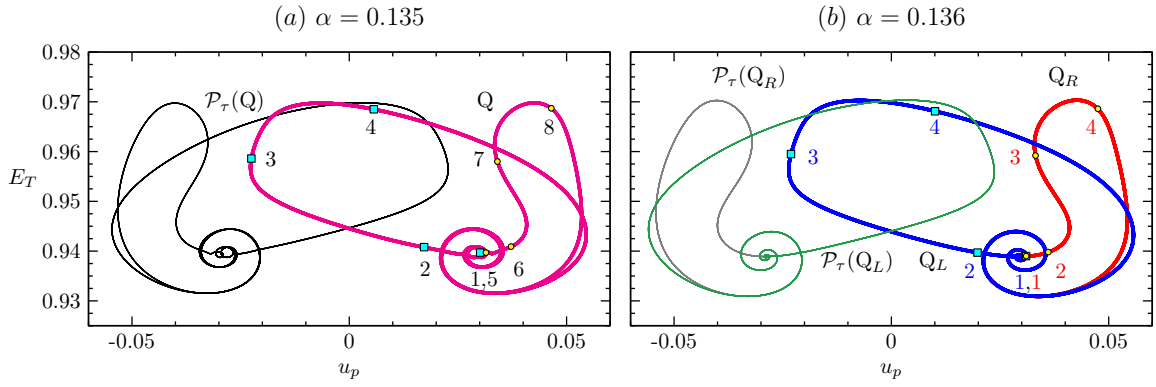

Figure 5.21: Strobe maps (every two forcing periods at forcing phase π) for (a) Q (thick magenta curve) and $\mathcal{P}_\tau(\mathrm{Q})$ (thin black curve) at $\alpha = 0.135$, before the ungluing, and (b) Q_L and Q_R (thick blue and red curves) as well as $\mathcal{P}_\tau(\mathrm{Q}_L)$ and $\mathcal{P}_\tau(\mathrm{Q}_R)$ (thin green and gray curves) at $\alpha = 0.125$, before the gluing bifurcation. The simulations were restricted to the $\mathcal{R}_\pi$ symmetric subspace.

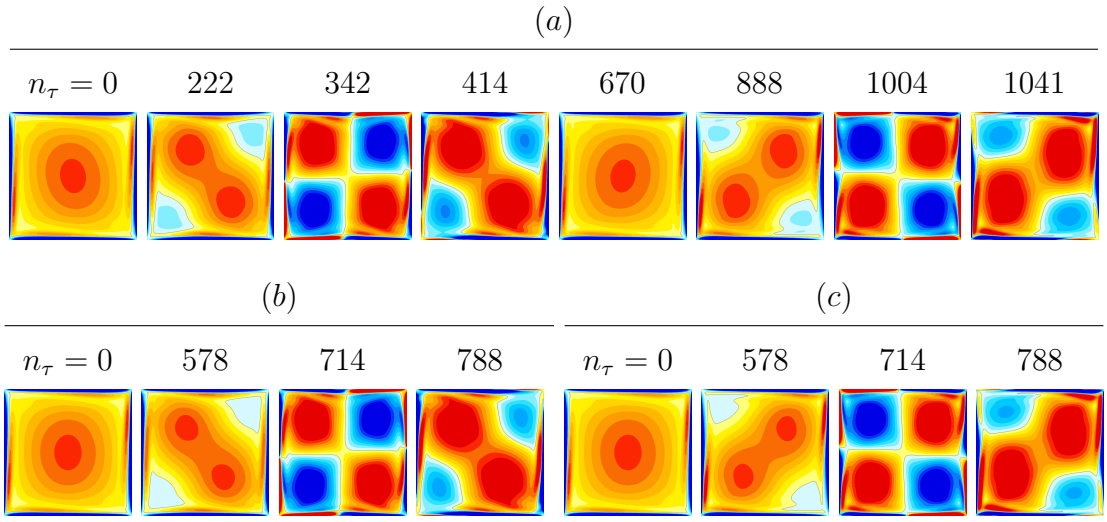

Figure 5.22: Snapshots of the vorticity at forcing phase π with $\omega = 1.41$ at the markers indicated in figure 5.21 (the relative times of the markers are indicated in terms of forcing periods): (a) Q at $\alpha = 0.135$, (b) and (c) Q_L and Q_R at $\alpha = 0.136$. The supplemental movie movie-fig522.mp4 animates the strobe maps and vorticity of the Q, Q_L, and Q_R states at the respective parameters.

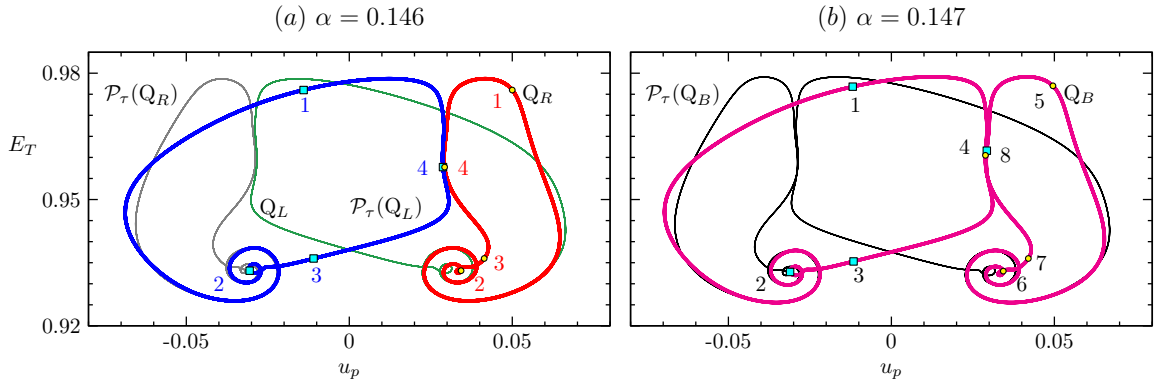

Figure 5.23: Strobe maps (every two forcing periods at forcing phase π) for (a) Q_L and Q_R (thick blue and thin green curves) as well as $\mathcal{P}_\tau(\mathrm{Q}_L)$ and $\mathcal{P}_\tau(\mathrm{Q}_R)$ (thick blue and thin gray curves) at $\alpha = 0.146$, before the gluing bifurcation, and (b) Q_B (thick magenta curve) and $\mathcal{P}_\tau(\mathrm{Q}_B)$ (thin black curve) at $\alpha = 0.147$, after the gluing of Q_L and Q_R (and $\mathcal{P}_\tau(\mathrm{Q}_L)$ and $\mathcal{P}_\tau(\mathrm{Q}_R)$). The simulations were restricted to the $\mathcal{R}_\pi$ symmetric subspace.

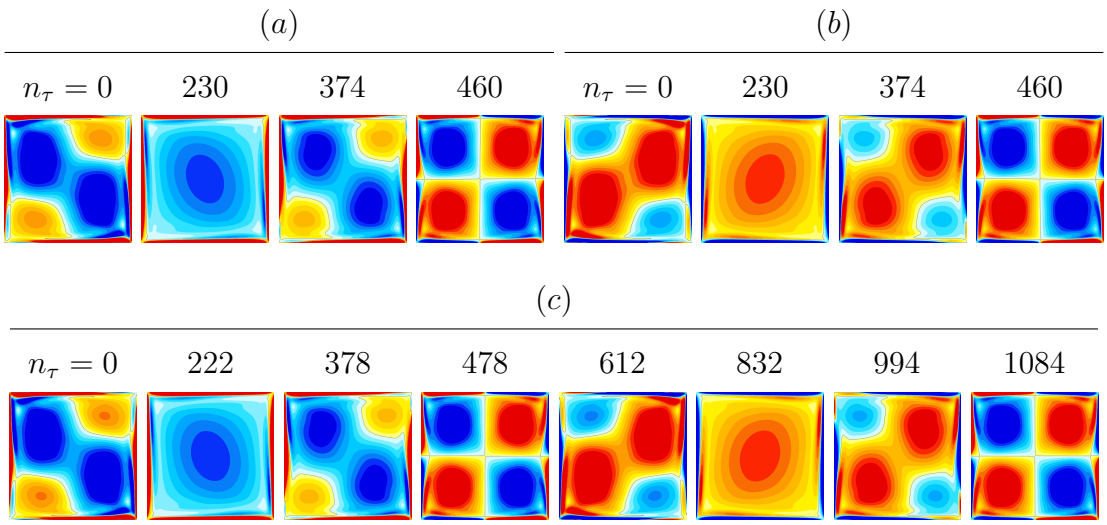

Figure 5.24: Snapshots of the vorticity at forcing phase π with $\omega = 1.41$ at the markers indicated in figure 5.23 (the relative times of the markers are indicated in terms of forcing periods): (a) and (b) Q_L and Q_R at $\alpha = 0.146$ and (c) Q_B at $\alpha = 0.147$. The supplemental movie movie-fig524.mp4 animates the strobe maps and vorticity of the Q_L, Q_R, and Q_B states at the respective parameters.

shots in figure 5.24. There is also the conjugate gluing between Q_L and $\mathcal{P}_\tau(\mathrm{Q}_R)$.

The trajectories at this third gluing are not homoclinic to $\mathrm{L}_{1:1}$ (although they do get very close to $\mathrm{L}_{1:1}$ and $\mathcal{P}_\tau(\mathrm{L}_{1:1})$). Instead, as the trajectories are ejected away from the saddle-foci $\mathrm{L}_{1:1}$ and $\mathcal{P}_\tau(\mathrm{L}_{1:1})$ they approach the stable manifold of the saddle $\mathrm{L}_{2:2}$ and become homoclinic to it at $\alpha_{G3} \approx 0.146\,631$. For $\alpha \gtrsim \alpha_{G3}$, the glued trajectory Q_B spirals around $\mathrm{L}_{1:1}$ and $\mathcal{P}_\tau(\mathrm{L}_{1:1})$, but spends a long time near $\mathrm{L}_{2:2}$ (near points labelled 4 and 8 in figure 5.23*b*). This suggests the existence of heteroclinic connections between the unstable manifolds of $\mathrm{L}_{1:1}$ and $\mathcal{P}_\tau(\mathrm{L}_{1:1})$ and the stable manifold of $\mathrm{L}_{2:2}$, but this connection is structurally unstable and instead of coinciding, the stable and unstable manifolds intersect transversely (much like that shown in the schematic in figure 5.7). This implies the existence of a horse-shoe map and chaos [91]. Indeed, we have found such chaotic dynamics for α very close to α_{G3}, primarily manifesting itself as trajectories with irregular numbers of orbits around $\mathrm{L}_{1:1}$ and $\mathcal{P}_\tau(\mathrm{L}_{1:1})$. Fig-

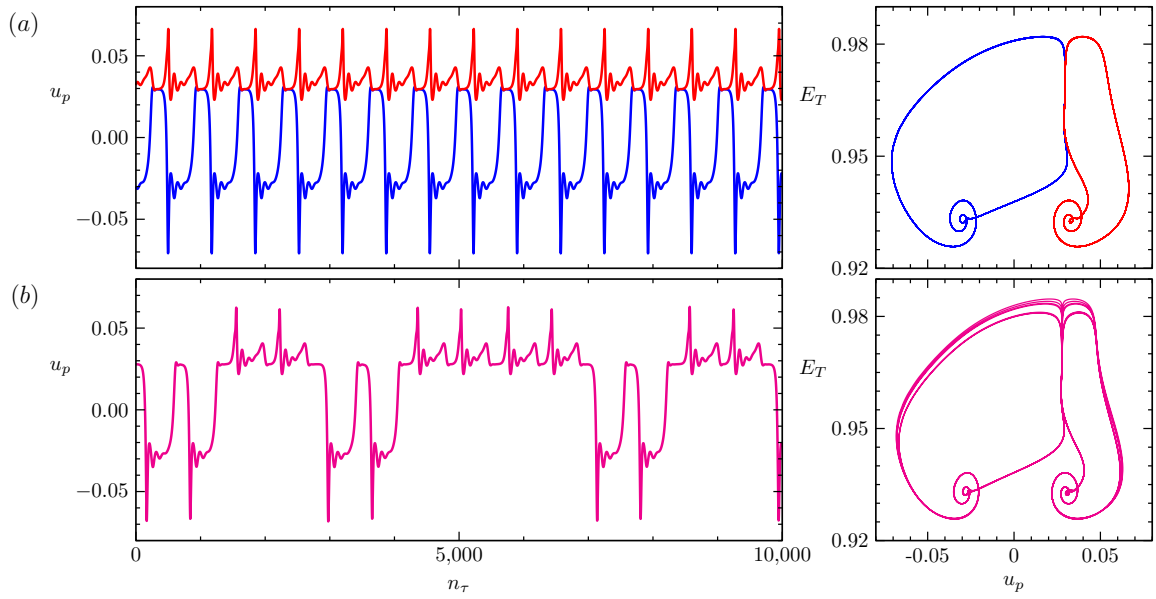

Figure 5.25: Strobed time series of the local velocity u sampled at $(x_p, z_p) = (1/\sqrt{8}, 1/\sqrt{8})$ and corresponding strobe map sampled every two periods at forcing phase π for (a) $\mathcal{P}_\tau(\mathrm{Q}_L)$ and Q_R (blue and red curves) at $\alpha = 0.14663$ before the gluing bifurcation, and (b) Q_B (magenta curve) at $\alpha = 0.14664$, post gluing bifurcation. The simulations were restricted to the $\mathcal{R}_\pi$ symmetric subspace, and only the last 10 000 forcing periods are shown of simulations with 200 000 forcing periods.

ure 5.25(a) shows a strobed time series of $u_p = u(1/\sqrt{8}, 1/\sqrt{8}, t)$ at $\alpha = 0.146\,63$ and $\alpha = 0.146\,64$, either side of the gluing at $\alpha = \alpha_{G3}$. For the lower α case, the responses are very regular Q_L and Q_R states, where as for α slightly beyond the gluing, the Q_B response shows an irregular number of left and right loops, and the accompanying strobe map in panel (b) demonstrates that the loops are also variable especially as they are ejected along the unstable manifolds of $\mathrm{L}_{2:2}$.

As α is increased beyond α_{G3}, the trajectory is farther away from the heteroclinic tangle, and instead follows a smooth path were it executes a single loop around $\mathrm{L}_{1:1}$ followed by a single loop around $\mathcal{P}_\tau(\mathrm{L}_{1:1})$; such a trajectory is illustrated in figure 5.23(b) for $\alpha = 0.147$. The supplemental movie movie-fig524.mp4 animates Q_R and $\mathcal{P}_\tau(\mathrm{Q}_L)$ at $\alpha = 0.146$ and Q_B at $\alpha = 0.147$.

The supplemental movie movie-fig518.mp4 summarizes the dynamics in the $\mathcal{R}_\pi$ subspace at $\omega = 1.41$. It animates the strobe maps in steps of 0.01 in α over the α range in figure 5.18.

5.7.3 Dynamics in the Full Space

We now return to the dynamics in the full space. L_L and L_R lose stability at $\alpha \approx 0.11$ via a Neimark–Sacker bifurcation which breaks the pointwise $\mathcal{R}_\pi$ symmetry (in comparison, L_L and L_R lost stability in the $\mathcal{R}_\pi$ subspace at $\alpha \approx 0.1208$). This Neimark–Sacker bifurcation is designated NS_a. A pair of $\mathcal{G}$ related 2-tori, T_{2L} and T_{2R}, are spawned, which are setwise $\mathcal{R}_\pi$ invariant. They inherit the subharmonic frequency $\omega/2$ and gain a new frequency corresponding to between six and seven forcing periods (in contrast, the 2-tori Q_L and Q_R that were spawned at NS_s in the $\mathcal{R}_\pi$ subspace have a second frequency which is two orders of magnitude smaller). This new frequency corresponds to small oscillations in the degree to which the $\mathcal{R}_\pi$ symmetry is broken. The $\mathcal{R}_\pi$ asymmetry is quantified by

$$A_\pi(\mathcal{S}) = \|T_{\mathcal{R}_\pi(\mathcal{S})} - T_{\mathcal{S}}\|/\|T_{\mathcal{S}}\|, \tag{5.9}$$

where $\mathcal{S}$ is the state, $T_{\mathcal{S}}$ is its temperature, and $\mathcal{R}_\pi(\mathcal{S})$ is the result of the action of $\mathcal{R}_\pi$ on $\mathcal{S}$. For T_{2L} and T_{2R}, $A_\pi \sim 10^{-3}$; in essence they are weakly modulated L_L and L_R.

Figure 5.26 shows the velocity variances of the states involved in the full subspace as α is increased for fixed $\omega = 1.41$, along with the long periods of the some of the quasi-periodic states. It is very similar to figure 5.18, which shows the corresponding measures in the $\mathcal{R}_\pi$ subspace. On the scale of the figure, T_{2L} and T_{2R} are stable only at the symbol shown (in yellow), and they lose stability with a very slight increase in α. A pair of $\mathcal{G}$-related 3-tori, T_{3L} and T_{3R} are spawned. They inherit the two frequencies

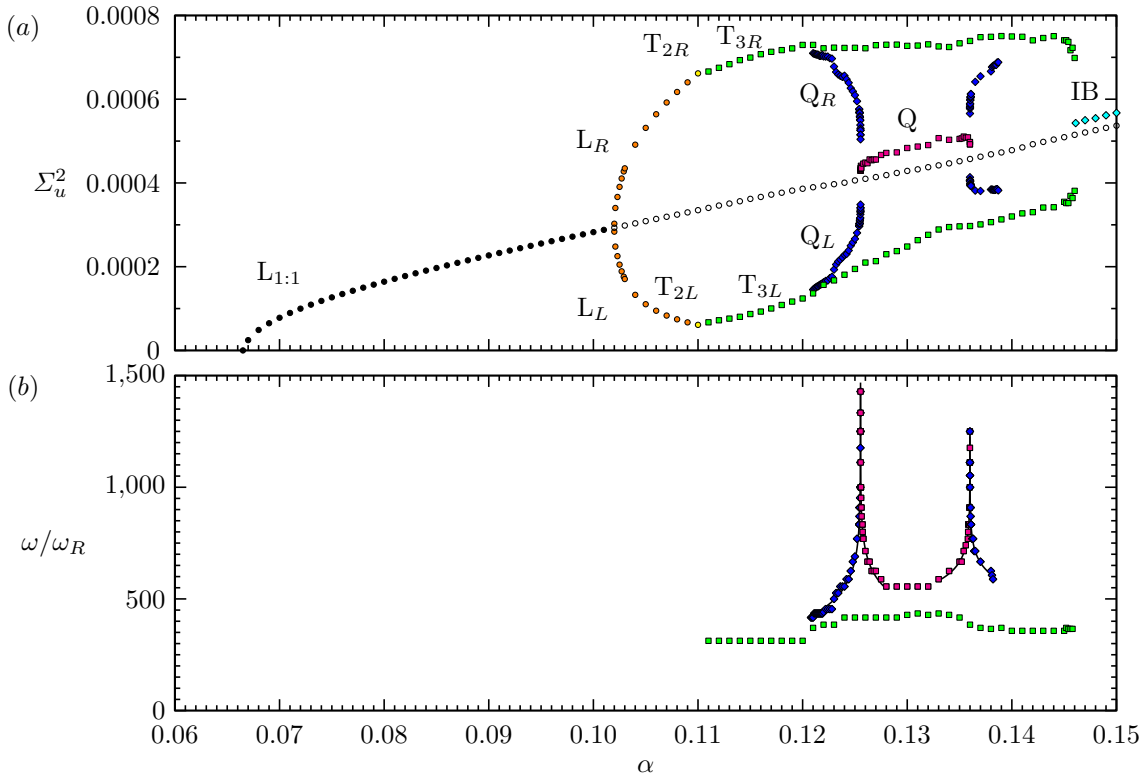

Figure 5.26: Variance of the horizontal velocity Σ_u^2 at the point $(x_p, z_p) = (1/\sqrt{8}, 1/\sqrt{8})$ for $\omega = 1.41$ for various observed states, as indicated. In panel (a), the $L_{1:1}$ is unstable for $\alpha > 0.102$ and is obtained through a transient. The supplemental movie movie-fig526.mp4 animates the strobe maps of the states in steps of 0.01 in α.

from T_{2L} and T_{2R}, and the third new frequency is very low, approximately two orders of magnitude smaller, and corresponds to slow drifts towards and away from the $\mathcal{R}_\pi$ symmetric subspace. During these drifts, A_π varies between $O(10^{-3} - 10^{-4})$ and $O(10^{-1})$.

At $\alpha \approx 0.121$ two new stable 3-tori states are observed. They are very similar to of Q_L and Q_R in the $\mathcal{R}_\pi$ subspace, with the only essential difference is that in the full space they have a very weak drift away from and back to the $\mathcal{R}_\pi$ subspace. As such, we shall simply call them Q_L and Q_R. In contrast, T_{3L} and T_{3R} are never $\mathcal{R}_\pi$ symmetric even though they also drift toward and away from the $\mathcal{R}_\pi$ subspace in a regular fashion. The T_{3L} and T_{3R} also drift toward and away from the $\mathcal{K}_z$ subspace

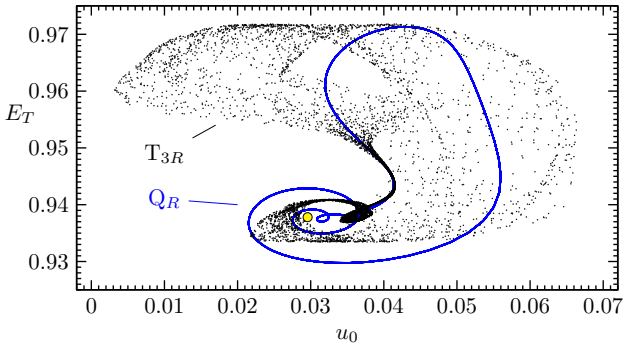

Figure 5.27: Strobe maps for the flow taken every two forcing periods at forcing phase π at $\alpha = 0.138$ for the stable Q_R (blue), stable T_{3R} (black), and unstable $L_{1:1}$ (yellow).

during the $\mathcal{R}_\pi$ subspace drifts. This $\mathcal{K}_z$ subspace excursion gains intensity as the forcing amplitude α is increased, and is associated with the 2-torus S_2 and 3-torus S_3 sloshing flows identified in the $\mathcal{K}_z$ symmetric subspace.

Q_L and Q_R undergo the first and second gluing bifurcations with essentially no difference from what we observed earlier in the $\mathcal{R}_\pi$ subspace. Over the same interval in α, T_{3L} and T_{3R} follow similar trajectories in phase space with two important differences. They do not become homoclinic to $L_{1:1}$ (although they do spiral in close to it), and they have a pronounced excursion to the sloshing S_2 or S_3 (depending on the value of α). Q_L and Q_R are completely oblivious to S_2 and S_3 as S_2 and S_3 do not exist in the $\mathcal{R}_\pi$ subspace. Strobes of Q_R and T_{3R} are shown in the supplemental movie movie-fig527.mp4 at $\alpha = 0.138$; the erratic behavior in T_{3R} is due to the trajectory passing very close by S_3. The corresponding strobe maps are shown in figure 5.27 with the unstable $L_{1:1}$ shown as a yellow marker. Q_L and Q_R are no longer stable for $\alpha \gtrsim 0.139$, and T_{3L} or T_{3R} are the only observed states until $\alpha \gtrapprox 0.146$, the flow then consists of intermittent bursts, displaying behaviour associated with the previously described states for irregular time intervals. This intermittent bursting state IB roughly coincides with the appearance of the Q_B state in the $\mathcal{R}_\pi$ subspace.

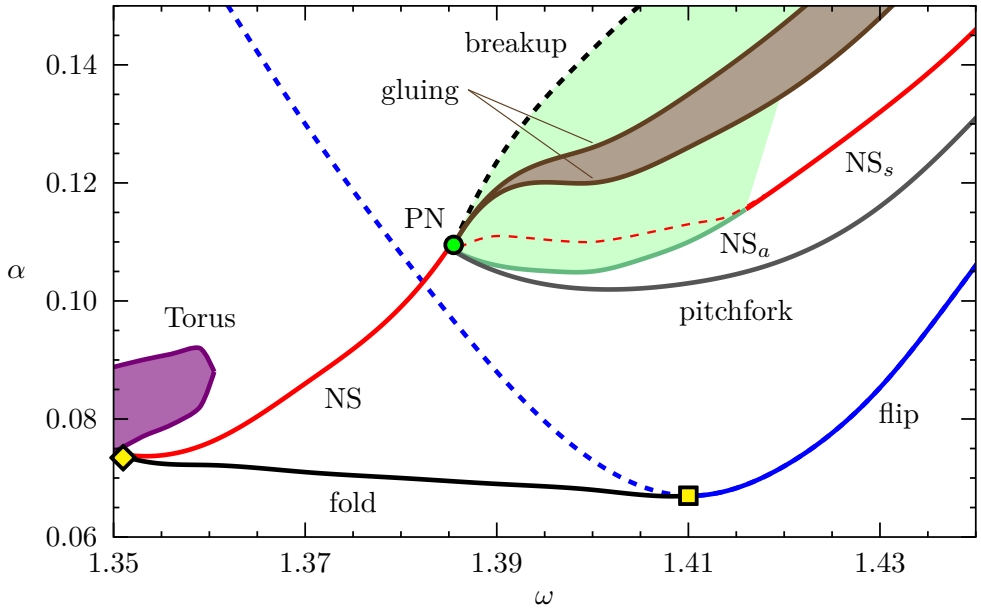

Figure 5.28: Bifurcation curves in the 1:1 resonance tongue.

The supplemental movie movie-fig526.mp4 summarizes the dynamics as α is increased with $\omega = 1.41$ in the full space. The left panel has figure 5.26 for reference and the (u_p, E_T) strobe maps are in the right panel.

5.7.4 The Big Picture of the $L_{1:1}$ Tip

Now, we consider how the various dynamic responses in the different parameter regimes of the tip of the 1:1 horn described earlier are interrelated. We have traced out both the pitchfork bifurcation and the Neimark–Sacker bifurcation NS$_a$ in (ω, α) space, and their loci are shown in figure 5.28. These curves appear to meet the Neimark–Sacker curve NS (described in section 5.6) at a point PN (green circular symbol in the figure). For $\omega \lesssim 1.415$, T$_{2L}$ and T$_{2R}$ are only stable in a very thin wedge region emanating from PN (too thin to see on the scale of the figure). For $\omega \gtrsim 1.415$, the Neimark–Sacker bifurcation does not break the pointwise $\mathcal{R}_\pi$ symmetry. The Neimark–Sacker bifurcation curve is the continuation of NS$_s$ which was identified in

the $\mathcal{R}_\pi$ subspace (see § 5.7.2). It also meets the point PN (it is shown as a dashed red curve for $\omega \lesssim 1.415$). The 2-tori that are spawned at NS_s, Q_L and Q_R, are stable over a larger range in α than those spawned at NS_a. Above the NS_a and NS_s there are multiple stable states, some of which undergo homoclinic bifurcations. The region between these Neimark–Sacker curves and the dashed curve denoted 'breakup' has very complicated dynamics, some of which we describes above for $\omega = 1.41$ (see § 5.7.3). In the middle of the complex region are a pair of homoclinic gluing bifurcation curves along which $\mathcal{G}$-related states simultaneously become homoclinic to a setwise $\mathcal{G}$ invariant saddle state (the unstable $\mathrm{L}_{1:1}$). The green region of figure 5.28 demarcates where pointwise $\mathcal{R}_\pi$ symmetry is broken. In between the second gluing bifurcation curve and the breakup curve, there are multiple states manifesting slow drifts towards and away from various saddle solutions that are related not just to $\mathrm{L}_{1:1}$, but also the secondary instability of the basic state ($\mathrm{L}_{2:2}$), and various secondary instabilities of these that we have been able to identify.

5.8 Discussion and Conclusions

The nonlinear responses of a stably stratified fluid in a square cavity subjected to parametric forcing consisting of vertical harmonic oscillations has been explored numerically. While linear Floquet analysis about the basic state predicts the critical forcing amplitude and frequency for the onset of instability, it does not distinguish between supercritical and subcritical onset, nor to what the instability saturates to nonlinearly. The nonlinear results are in very good agreement with the Floquet analysis in determining the instability of the basic state, in which the viscous eigenmodes of the cavity are excited via parametric resonance.

The present study is in the regime where the product of the buoyancy frequency and the viscous time scale is $R_N = 2 \times 10^4$, in which many of the resonance tongues

corresponding to the lower order eigenmodes are clearly identified. The nonlinear responses clearly demonstrate the subcritical nature of the primary instability from the basic state on the low forcing frequency side of the resonance tongues. The dynamics near the tip of the broadest tongue, the subharmonic 1:1 tongue, were explored in detail. The period-doubled limit cycle response $L_{1:1}$ undergoes both pitchfork and Neimark–Sacker bifurcations, resulting in symmetry conjugate limit cycles and quasi-periodic 2-tori in different part of the tip, and the basic state also loses stability to the first harmonic viscous eigenmode $L_{2:2}$. All of these states undergo secondary bifurcations, resulting in a multiplicity of unstable saddle states. We have identified three codimension-two points that organize the responses.

The first of these is a generalized flip located at the very tip of the tongue, where the instability of the basic state changes from supercritical to subcritical as the forcing frequency is reduced. The subcritical flip bifurcation leads to a fold bifurcation curve along which the unstable saddle $L_{1:1}$ that bifurcates from the basic state is folded back and stabilized. The stabilized upper branch $L_{1:1}$ becomes unstable via a Neimark–Sacker bifurcation as the forcing frequency is increased.

The Neimark–Sacker curve and the fold curve meet at a second codimension-two point that we analyzed. This flow involves heteroclinic behaviour in its normal form, but the heteroclinic behaviour is not structurally stable, and the full Navier–Stokes system reveals a complex homoclinic doubling response, which has some similarities to the dynamics of the logistic map, in the parameter region of the heteroclinics in the normal form. Beyond this region, all states locally associated with the codimension-two bifurcation are unstable, and the flow abruptly collapses to the basic state.

The third codimension-two point is near the center of the tip where the Neimark–Sacker and the pitchfork curves meet. In the neighborhood of this point, to the high frequency side, the symmetry-broken limit cycles undergo Neimark–Sacker bifurca-

tions and then the resulting conjugate 2-tori simultaneously become homoclinic to the saddle $L_{1:1}$ in a gluing bifurcation. The resulting glued symmetric 2-torus unglues as the forcing amplitude is increased. The two curves of gluing bifurcations also meet at the third codimension-two point. There are other complicated states in this regime, and they all involve slow drifts into and out of symmetric subspaces, and near heteroclinic collisions with the various saddle states that have been excited. As the forcing amplitude is increased, the stable and unstable manifolds involved in the heteroclinic behaviour become increasingly tangled, resulting in intermittently bursting flows.

Despite the details the 1:1 resonance tongue obtained in this study, the details of the other resonance tongues remain unresolved. It is likely that the dynamics observed near the generalized flip and fold-Neimark–Sacker codimension-two points will be common to the other tongues, but the symmetry breaking and restoring events will necessarily differ as the primary viscous eigenmodes associated with other tongues have symmetries that differ from those of $L_{1:1}$.

Much of the dynamics we have found are consistent with the experimental observations of Benielli and Sommeria [7], whose focus on the 1:1 resonance tongue motivated our study, even though there are obvious differences between their experimental set-up and our numerical model. They used salt as their stratifying agent, whereas we use temperature. Apart from having a two order of magnitude difference in the Prandtl/Schmidt number, the boundary condition on the horizontal endwalls are different. These differences seem to be of secondary importance. Our simulations are two-dimensional, but the experiments are necessarily three dimensional. However, the spanwise dimension of their cavity was considerably less than the other two dimensions, and in the central tip region they were able to parametrically excite the two-dimensional mode ($L_{1:1}$), and observed some of the dynamics we report on, albeit at higher R_N compared to $R_N = 2 \times 10^4$ used here (presumably to over-

come the viscous damping from the spanwise walls). They observed various m:n modes, and heteroclinic drifts between some these, akin to the heteroclinic intermittency (IB) we reported from the $\mathcal{R}_\pi$ subspace simulations. They also observed localized small-scale three-dimensional flows associated with wavebreaking events at larger forcing amplitudes. We have observed two-dimensional wave breaking in some regimes [110, 111], but these events were short-lived. The breaking produces small scale intense vortices, but these are quickly dissipated. The present study, being restricted to two-dimensional flow, lacks the vortex tilting and stretching mechanism that would allow for intensification of the strength of the small length scales on a time scale that is faster than that in which the viscous dissipation acts on. Studies in the wave breaking regime for three-dimensional flows is currently under investigation and will be reported on subsequently.

5.9 Acknowledgments

We thank ASU Research Computing facilities and the NSF XSEDE program for providing compute resources, Ke Wu for the original solver codebase, and Professor Francisco Marques for his expertise.

Chapter 6

CONCLUSIONS AND FUTURE WORK

This dissertation resolved the behavior of fluid flows confined within various rectangular geometries. The flow of a three-dimensional lid-driven cavity was first studied to validate the numerical solver, whose initial results were compared to the existing body of literature. Techniques were then developed and applied to resolve the previously open problem of intermittent bursting within the cavity near the Reynolds number where the flow went unsteady. Applying dynamical systems theory in combination with symmetric subspace restriction, selective frequency damping, linear stability analysis via Arnoldi iteration, and the edge state technique resulted in clearly identifying two successive subcritical Hopf bifurcations of the steady state, as well as a Neimark–Sacker bifurcation connecting the two branches. LC1 (the first limit cycle to bifurcate from the steady state) was shown to be stable for a small interval in the full space, and ultimately to be unstable to LC2 (the second limit cycle to bifurcate from the steady state). LC2 was then shown to be unstable to symmetry breaking, and this transition away from the symmetric subspace was followed by a fast transition back to the subspace (either toward LC1 or the steady state), resulting in a bursting event. In the full space, by the start of the intermittent bursting phenomenon, no local stable attractor exists. Instead the dynamics are global and the flow consists of trajectories between the saddle equilibria. These methods and realizations served as a basis for the remainder of the dissertation.

The stably stratified fluid flows confined within a square cavity subject to vertical harmonic forcing then became the focus of study. The problem of parametrically forced internal waves are underrepresented in the literature. Only a handful of ex-

periments had been conducted (most notably [7]) and only inviscid theory had been addressed (most notably [97]). Further, the experiments were done with salt as the stratification agent rather than temperature, which leads to dynamical issues. Stratification with concentration requires normal no-flux conditions for the top and bottom walls of the container (rather than constant Dirichlet conditions), which results in the eventual homogenization of the fluid on a timescale related to the Schmidt number (ratio of viscous and concentration diffusivities). Thus, any result without a homogenized density field is transient. As stated, using heat instead of concentration allows for the persistence of the stratification.

In Chapter 3, a linear stability analysis was performed on the basic state of the flow, revealing a multitude of resonance horns in forcing frequency and forcing amplitude parameter space for a prescribed Prandtl number and buoyancy number. Since the basic state is periodic, Floquet analysis was required, and the spectrum with corresponding viscous eigenmodes of the full discretization was obtained. These results are compared to what is expected from the inviscid theory and are found to be in good agreement away from viscous boundary layers and for larger buoyancy numbers. Further, the self-similarity (power laws) of the viscous effects were determined.

In Chapter 4, a modal analysis is conducted allowing for the fast estimation of neutral curves for the basic state's instability. The numerical Floquet analysis required tens of thousands of simulations to resolve the instability loci, each of which took at least four hours of compute time leveraging sophisticated low-level software (computed with a Fortran 2008 implementation). After tuning the modal analysis with a few Floquet analysis results, the neutral curves of an arbitrary m:n mode are instead computed within seconds with high-level software (MATLAB/Python). This resulted from the appropriate ansatz for modal diffusion, permitting the superposition of modal responses.

In Chapter 5, the complex nonlinear behaviors of the flow near onset were determined. First the $R_N = 2 \times 10^4$ Floquet analysis results were validated, and the criticality of the flip bifurcation was determined. Then, the dynamics of the 1:1 resonance tongue were focused on, classified by the codimension-2 behavior observed. The dynamics around these codimension-2 points was then analyzed, and led to the discovery of a homoclinic doubling cascade near the fold-Neimark–Sacker codimension-2 point. In the symmetry-breaking and restoring regime emanating from the pitchfork-Neimark–Sacker codimension-2 point, a pointwise-vertical-reflection symmetric state was isolated bifurcating from the 2:2 mode, a state unobserved in the linear study that interacted with the nonlinear full space flow. Further, a number of gluing bifurcations were observed as well as a gluing bifurcation associated to Lorenz-like heteroclinicity.

6.1 Future Work

The problems discussed in this dissertation established the validity of the numerical methods and techniques for analyzing the dynamics of fluid flows. In particular, the flow of a stably stratified fluid subject to vertical harmonic forcing was well analyzed. The study of the vertically oscillating stratified square cavity was motivated by previous experimentalists noting the apparent two-dimensional nature of response [97, 69, 7]. However, preliminary work has begun on the three-dimensional problem.

Using the aspect ratio of Benielli and Sommeria [7] for the rectangular cavity restricts the three-dimensional instabilities of the flow via viscous damping. Figure 6.1 provides a schematic of the short-spanwise three-dimensional set up. Like the two-dimensional study, heat is used to stably stratify the fluid, with the constant temperature top and bottom walls at warmer and colder temperatures respectively. This provides an explicit basic state for the flow: $\boldsymbol{u} = \mathbf{0}$, $p = 0.5z^2(1 + \cos(\omega t))$, and $T = z$.

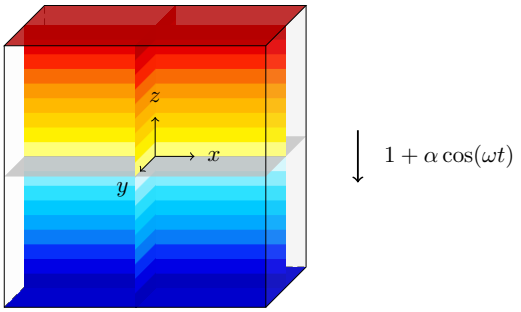

Figure 6.1: Schematic of the vertically oscillating short spanwise rectangular cavity. The isotherms of the basic state are illustrated on the midplanes, as well as the harmonic gravity modulation, constant temperature endwalls, and Cartesian coordinate system.

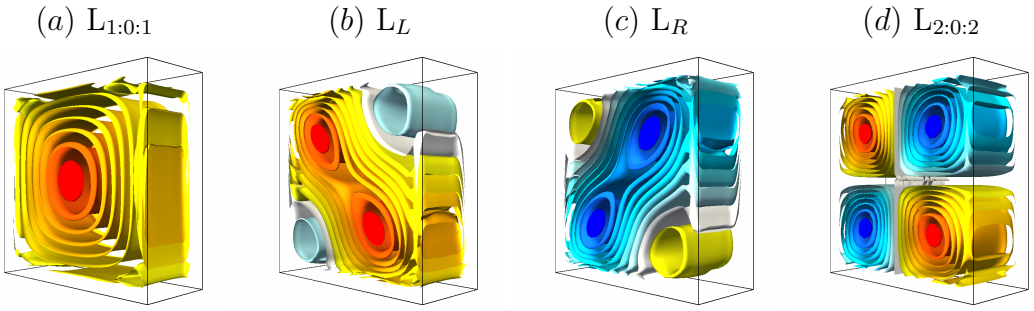

Figure 6.2: Snapshots at forcing phase $\pi/2$ of the spanwise vorticity, η, for subharmonic limit cycles at $\omega = 1.41$: (a) $\mathrm{L}_{1:0:1}$ at $\alpha = 0.15$, (b) and (c) L_L and L_R at $\alpha = 0.17$, and (d) $\mathrm{L}_{2:0:2}$ at $\alpha = 0.17$. Note the $\mathrm{L}_{2:0:2}$ was obtained by restricting the flow to the vertical reflection symmetry subspace.

As is illustrated in figure 6.2, the three-dimensional responses of the flow are indeed close to two-dimensional, and in fact the behavior in parameter space is similar to that of the two-dimensional cavity, with the $\mathrm{L}_{1:0:1}$ and $\mathrm{L}_{2:0:2}$ modes as well as the symmetrically related L_L and L_R handed states essentially being the three-dimensional analogs of the two-dimensional $\mathrm{L}_{1:1}$, L_L, L_R, and $\mathrm{L}_{2:2}$ from figure 5.15.

Figure 6.3 provides a response diagram. Note that there exists glued states, similar to the two-dimensional result summarized in figure 5.26.

Additionally, open problems for stably stratified fluid flows in rectangular con-

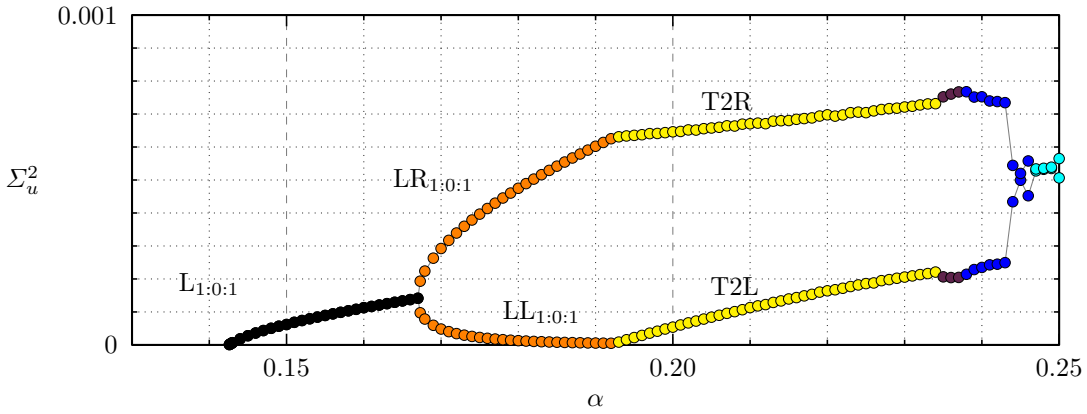

Figure 6.3: Variance of the horizontal velocity Σ_u^2 for $\omega = 1.41$ at the point $(x, y, z) = (\sqrt{2}/4, \sqrt{2}/10, \sqrt{2}/4)$ for various observed states, as indicated.

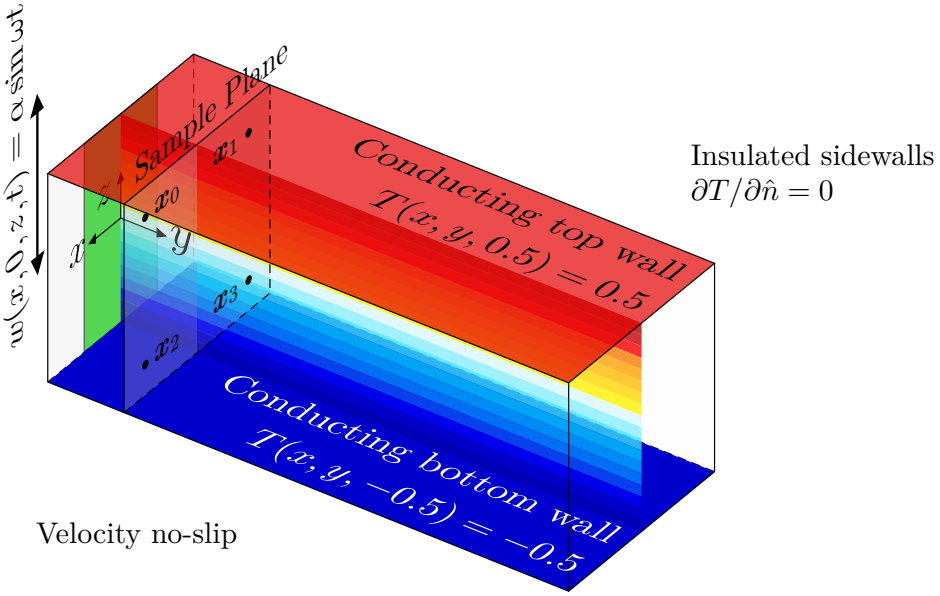

Figure 6.4: Schematic of the oscillating slat-driven rectangular cavity. The isotherms of the initial linear stratification are illustrated on the yz-midplane, as well as the embedded vertically oscillating slat (green) in the frontwall, the boundary conditions, the Cartesian coordinate system, and the four sampled points for local measures. Note that the slat only takes up half of the frontwall's width.

tainers will be studied. For example, the experiment of Robinson and McEwan [84], analysis of von Kerczek and Davis [25, 103, 24], and more recent work by Blanchette et. al [12] has motivated the study of a slat-driven rectangular cavity with stable stratification. In the experimental study, oblique waves were observed emanating from the driving front-wall slat. However, the mechanism for the instability is not resolved by the linear theory.

Figure 6.4 provides a schematic of the stably stratified slat-driven setup. Driving the slat with nondimensional forcing frequency $\omega = 0.71$ at nondimensional forcing amplitude $\alpha = 0.15$ results in a quasiperiodic state with the oblique wave nature as described in the experiments. This was associated with a pointwise-horizontal-reflection symmetry breaking for $\alpha \in (0.14, 0.15)$, and the pointwise-horizontal-reflection symmetric limit cycle for $\omega = 0.71$ with $\alpha = 0.14$ is illustrated in the first row of figure 6.5, which has pointwise-horizontal-reflection symmetric oblique waves. Note that the pointwise-symmetry breaking at this frequency results in two symmetrically related states (one state is obtainable from the other after the action of a symmetry). These are illustrated in the second and third rows of figure 6.5, and these left-handed and right-handed oblique waves are related by the horizontal-reflection symmetry that has broken.

In figure 6.6, the quasiperiodic pointwise-symmetry broken flow at $\omega = 0.71$ and $\alpha = 0.15$ is illustrated strobed every 10 forcing periods at forcing phase $\pi/4$. It's remarkable that two unique configurations of the oblique waves are both visited by the flow over the long sample window of roughly 80 forcing periods.

There is a lot to still resolve for this problem. Currently a large batch of direct numerical simulations are running on the Open Science Grid (OSG) national facilities for different forcing frequencies and forcing amplitudes. Regardless, it is evident that the symmetry breaking and restoring phenomenon discussed in Chapter 5 has a major

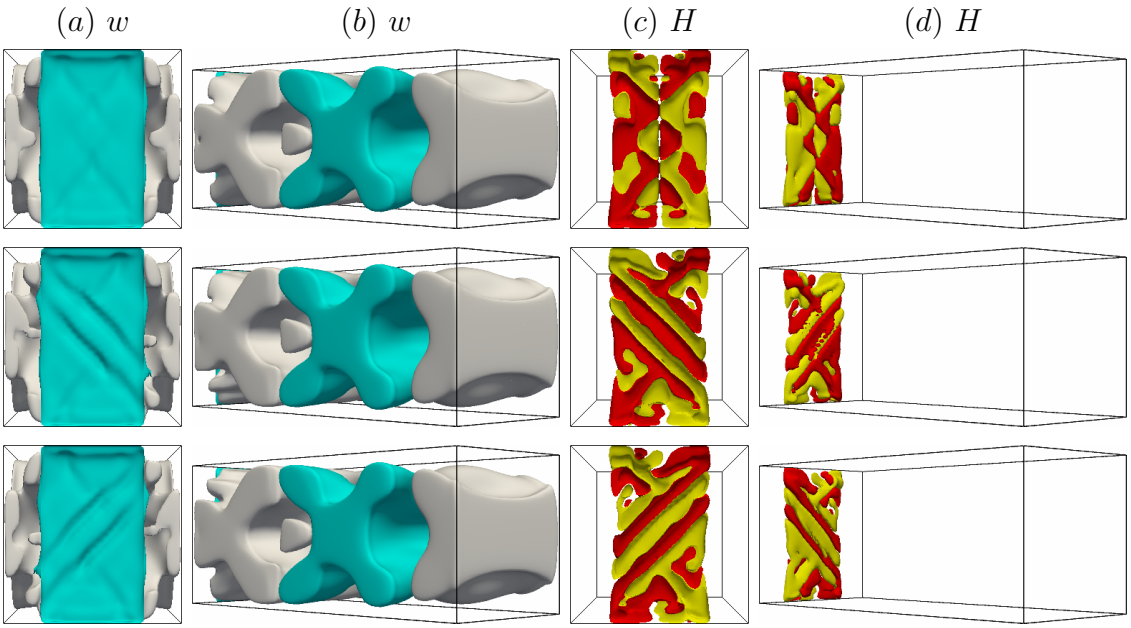

Figure 6.5: Snapshots of the $\omega = 0.71$ flow at forcing phase $\pi/5$ for the synchronous limit cycle at $\alpha = 0.14$ in the first row and the quasi-periodic pointwise-symmetry-broken flow at $\alpha = 0.15$ visiting the left-handed oblique state in the second row and visiting the right-handed oblique state in the third row. Columns (a, c) show the slat driven wall head on, where as (b, d) have the driven wall 'in the back left'. Contour levels are shown at ± 0.01 of the global maximum with cyan (white) contours for the positive (negative) vertical velocity w isosurfaces and red (yellow) contours for the positive (negative) helicity H isosurfaces.

role to play in describing the dynamics of related stably stratified flows contained within rectangular cavities, and that many of the dynamics observed in that two-dimensional study may be generic to a larger class of three-dimensional flows as well.

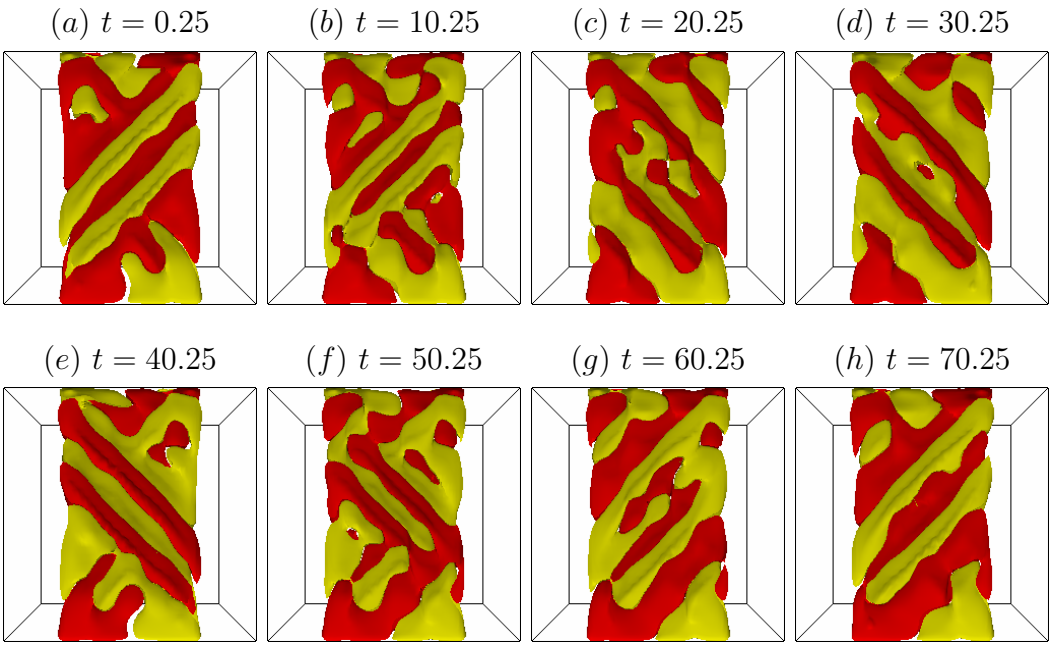

Figure 6.6: Helicity snapshots of the strobed $\omega = 0.71$ flow at forcing phase $\pi/4$ quasiperiodic pointwise-symmetry-broken oblique flow at $\alpha = 0.15$ at various times over the slow frequency. Strobe snapshots are shown ten forcing periods apart.

[1] Abshagen, J., J. M. Lopez, F. Marques and G. Pfister, "Mode competition of rotating waves in reflection-symmetric Taylor-Couette flow", J. Fluid Mech. **540**, 269–299 (2005).

[2] Abshagen, J., J. M. Lopez, F. Marques and G. Pfister, "Symmetry breaking via global bifurcations of modulated rotating waves in hydrodynamics", Phys. Rev. Lett. **94**, 074501 (2005).

[3] Abshagen, J., J. M. Lopez, F. Marques and G. Pfister, "Bursting dynamics due to a homoclinic cascade in taylor–couette flow", J. Fluid Mech. **613**, 357–384 (2008).

[4] Baltensperger, R. and J.-P. Berrut, "The errors in calculating the pseudospectral differentiation matrices for chebyshev-gauss-lobatto points", Comput. Math. Appl. **37**, 41–48 (1999).

[5] Bartels, R. H. and G. W. Stewart, "Solution of the matrix equation $AX+XB = C$", Commun. ACM **15**, 9, 820–826 (1972).

[6] Bayliss, A., A. Class and B. Matkowsky, "Roundoff error in computing derivatives using the chebyshev differentiation matrix", J. Comput. Phys. **116**, 380–383 (1995).

[7] Benielli, D. and J. Sommeria, "Excitation and breaking of internal gravity waves by parametric instability", J. Fluid Mech. **374**, 117–144 (1998).

[8] Benjamin, T. B. and F. Ursell, "The stability of the plane free surface of a liquid in vertical periodic motion", Proc. Roy. Soc. Lond. A **225**, 505–515 (1954).

[9] Berrut, J.-P. and L. N. Trefethen, "Barycentric lagrange interpolation", SIAM Rev. **46**, 3, 501–517 (2004).

[10] Blackburn, H. M. and J. M. Lopez, "The onset of three-dimensional standing and modulated travelling waves in a periodically driven cavity flow", J. Fluid Mech. **497**, 289–317 (2003).

[11] Blackburn, H. M., F. Marques and J. M. Lopez, "Symmetry breaking of two-dimensional time-periodic wakes", J. Fluid Mech. **522**, 395–411 (2005).

[12] Blanchette, F., T. Peacock and R. Cousin, "Stability of a stratified fluid with a vertically moving sidewall", J. Fluid Mech. **609**, 305–317 (2008).

[13] Bouruet-Aubertot, P., J. Sommeria and C. Staquet, "Breaking of standing internal gravity waves through two-dimensional instabilities", J. Fluid Mech. **285**, 265–301 (1995).

[14] Boyd, J. P., *Chebyshev and Fourier Spectral Methods* (Dover, 2001), 2 edn.

[15] Broer, H., C. Simó and R. Vitolo, "Hopf saddle-node bifurcation for fixed points of 3D-diffeomorphisms: Analysis of a resonance 'bubble'", Physica D **237**, 1773–1799 (2008).

[16] Canuto, C., M. Hussaini, A. Quarteroni and T. Zang, *Spectral Methods: Fundamentals in Single Domains*, Scientific Computation (Springer-Verlag Berlin Heidelberg, 2006), 1 edn.

[17] Carbo, R. M., R. W. M. Smith and M. E. Poese, "A computational model for the dynamic stabilization of Rayleigh–Bénard convection in a cubic cavity", J. Acoust. Soc. America **135**, 654–668 (2014).

[18] Certa, E. and E. Tirapegui, "Faraday's instability for viscous fluids", Phys. Rev. Lett. **78**, 859–862 (1998).

[19] Champneys, A., "Dynamics of parametric excitation", in "Mathematics of Complexity and Dynamical Systems", edited by R. A. Meyers, pp. 183–204 (Springer, New York NY, 2012).

[20] Charalambides, M., "The spectrum of the gegenbauer collocation approximation for the second derivative operator", J. Math. Anal. Appl. **433**, 1502–1512 (2016).

[21] Charalambides, M. and F. Waleffe, "The spectrum of the jacobi tau approximation for the second derivative operator", SIAM J. Num. Anal. **48**, 280–294 (2008).

[22] Dauxois, T., S. Joubaud, P. Odier and A. Venaille, "Instabilities of internal gravity wave beams", Annu. Rev. Fluid Mech. **50**, 1–28 (2018).

[23] Davidson, P., *Turbulence in Rotating, Stratified, and Electrically Conducting Fluids* (Cambridge Univ. Press, 2013).

[24] Davis, S. H., "The stability of time-periodic flows", Annu. Rev. Fluid Mech. **8**, 57–74 (1976).

[25] Davis, S. H. and C. von Kerczek, "A reformulation of energy stability theory", Arch. Ration. Mech. Anal. **52**, 112–117 (1973).

[26] Drazin, P. G., "On the instability of an internal gravity wave", Proc. Roy. Soc. Lond. A **356**, 411–432 (1977).

[27] Edwards, W. S. and S. Fauve, "Patterns and quasi-patterns in the Faraday experiment", J. Fluid Mech. **278**, 125–148 (1994).

[28] Faraday, M., "On a peculiar class of acoustical figures: and on certain forms assumed by groups of particles upon vibrating elastic surfaces", Phil. Trans. Roy. Soc. Lond. A **121**, 299–340 (1831).

[29] Fauve, S., K. Kumar, C. Laroche, D. Beysens and Y. Garrabos, "Parametric instability of a liquid-vapour interface close to the critical point.", Phys. Rev. Lett. **68**, 3160–3163 (1992).

[30] Feigenbaum, M. J., "Quantitative universality for a class of nonlinear transformations", J. Stat. Phys. **19**, 25–52 (1978).

[31] Feldman, Y. and A. Y. Gelfgat, "Oscillatory instability of a three-dimensional lid-driven flow in a cube", Phys. Fluids **22**, 093602 (2010).

[32] Gaspard, P., "Measurement of the instability rate of a far-from-equilibrium steady state at an infinite period bifurcation", J. Phys. Chem. **94**, 1–3 (1990).

[33] Glendinning, P., "Bifurcations near homoclinic orbits with symmetry", Phys. Lett. **103A**, 163–166 (1984).

[34] Gómez, F., R. Gómez and V. Theofilis, "On three-dimensional global linear instability analysis of flows with standard aerodynamics codes", Aerospace Science & Technology **32**, 223–234 (2014).

[35] Hugues, S. and A. Randriamampianina, "An improved projection scheme applied to pseudospectral methods for the incompressible Navier–Stokes equations", Intnl J. Num. Meth. Fluids **28**, 501–521 (1998).

[36] Hurley, D., "The emission of internal waves by vibrating cylinders", **36**, 657–672 (1969).

[37] Ibrahim, R. A., "Recent advances in physics of fluid parametric sloshing and related problems", ASME J. Fluid Engng **137**, 090801 (2015).

[38] Itano, T. and S. Toh, "The dynamics of bursting process in wall turbulence", J. Phys. Soc. Japan **70**, 703–716 (2001).

[39] Karniadakis, G. E., M. Israeli and S. A. Orszag, "High-order splitting methods for the incompressible navier-stokes equations", J. Comput. Phys. **97**, 2, 414–443 (1991).

[40] Keunecke, K.-H., "Stehende interne wellen in rechteckigen becken", Deut. Hydr. Zeit. **23**, 61–79 (1970).

[41] Kovacic, I., R. Rand and S. M. Sah, "Mathieu's equation and its generalizations: overview of stability charts and their features", Appl. Mech. Rev. **70**, 020802 (2018).

[42] Kuhlmann, H. C. and S. Albensoeder, "Stability of the steady three-dimensional lid-driven flow in a cube and the supercritical flow dynamics", Phys. Fluids **26**, 024104 (2014).

[43] Kumar, K., "Linear theory of Faraday instability in viscous liquids", Proc. Roy. Soc. Lond. A **452**, 1113–1126 (1996).

[44] Kumar, K. and L. S. Tuckerman, "Parametric instability of the interface between two fluids", J. Fluid Mech. **279**, 49–68 (1994).

[45] Kuznetsov, Y. A., *Elements of Applied Bifurcation Theory* (Springer, 2004), third edn.

[46] Lappa, M., *Rotating Thermal Flows in Natural and Industrial Processes* (John Wiley & Sons, 2012).

[47] Leung, J. J. F., A. H. Hirsa, H. M. Blackburn, F. Marques and J. M. Lopez, "Three-dimensional modes in a periodically driven elongated cavity", Phys. Rev. E **71**, 026305 (2005).

[48] Liberzon, A., Y. Feldman and A. Y. Gelfgat, "Experimental observation of the steady-oscillatory transition in a cubic lid-driven cavity", Phys. Fluids **23**, 084106 (2011).

[49] Linden, P. F., "Introduction: Simulations of natural flows in the laboratory and on a computer", in "Modeling Atmospheric and Oceanic Flows: Insights from Laboratory Experiments and Numerical Simulations", edited by T. von Larcher and P. D. Williams, Geophysical Monograph Series, pp. 1–5 (John Wiley & Sons, 2015).

[50] Loiseau, J.-C., *Dynamics and Global Analyses of Three-Dimensional Flows*, Ph.D. thesis, Paris Institute of Technology (2014).

[51] Loiseau, J.-C., M. A. Bucci, S. Cherubini and J.-C. Robinet, "Time-stepping and krylov methods for large-scale instability problems", in "Computational Modelling of Bifurcations and Instabilities in Fluid Dynamics", edited by A. Gelfgat, vol. 50 of *Computational Methods in Applied Sciences*, pp. 33–74 (Springer, 2019).

[52] Loiseau, J.-C., J.-C. Robinet and E. Leriche, "Intermittency and transition to chaos in the cubical lid-driven cavity flow", Fluid Dynam. Res. **48**, 061421 (2016).

[53] Lopez, J. M. and F. Marques, "Dynamics of 3-tori in a periodically forced Navier–Stokes flow", Phys. Rev. Lett. **85**, 972–975 (2000).

[54] Lopez, J. M. and F. Marques, "Small aspect ratio Taylor-Couette flow: Onset of a very-low-frequency three-torus state", Phys. Rev. E **68**, 036302 (2003).

[55] Lopez, J. M. and F. Marques, "Finite aspect ratio Taylor-Couette flow: Shil'nikov dynamics of 2-tori", Physica D **211**, 168–191 (2005).

[56] Lopez, J. M. and F. Marques, "Nonlinear and detuning effects of the nutation angle in precessionally-forced rotating cylinder flow", Phys. Rev. Fluids **1**, 023602 (2016).

[57] Lopez, J. M., F. Marques and J. Shen, "Complex dynamics in a short annular cylinder with rotating bottom and inner cylinder", J. Fluid Mech. **501**, 327–354 (2004).

[58] Lopez, J. M. and J. Shen, "Numerical simulation of incompressible flows in cylindrical geometries using a spectral projection method", Internat. J. Appl. Sci. Comput **5**, 25–40 (1998).

[59] Lopez, J. M., B. D. Welfert, K. Wu and J. Yalim, see Supplemental Material at https://journals.aps.org/prfluids/abstract/10.1103/PhysRevFluids.2.074401#supplemental for animations corresponding to figures 2.4, 2.5, 2.15, 2.20, 2.21, and 2.22. (2017).

[60] Lopez, J. M., B. D. Welfert, K. Wu and J. Yalim, "Transition to complex dynamics in the cubic lid-driven cavity", Phys. Rev. Fluids **2**, 074401 (2017).

[61] Mancebo, F. J. and J. M. Vega, "Faraday instability threshold in large-aspect-ratio containers", J. Fluid Mech. **467**, 307–330 (2002).

[62] Marques, F. and J. M. Lopez, "Onset of three-dimensional unsteady states in small aspect-ratio Taylor–Couette flow", J. Fluid Mech. **561**, 255–277 (2006).

[63] Marques, F. and J. M. Lopez, "Precession of a rapidly rotating cylinder flow: traverse through resonance", J. Fluid Mech. **782**, 63–98 (2015).

[64] Marques, F., J. M. Lopez and H. M. Blackburn, "Bifurcations in systems with Z_2 spatio-temporal and $O(2)$ spatial symmetry", Physica D **189**, 247–276 (2004).

[65] Marques, F., J. M. Lopez and J. Shen, "A periodically forced flow displaying symmetry breaking via a three-tori gluing bifurcation and two-tori resonances", Physica D **156**, 81–97 (2001).

[66] Mathieu, E., "Mémoire sur le mouvement vibratoire d'une membrane de forme elliptique", J. Math. Pures Appl. **13**, 137–203 (1868).

[67] Åkervik, E., L. Brandt, D. S. Henningson, J. Hœpffner, O. Marxen and P. Schlatter, "Steady solutions of the Navier–Stokes equations by selective frequency damping", Phys. Fluids **18**, 068102 (2006).

[68] May, R. M., "Simple mathematical models with very complicated dynamics", Nature **261**, 459–467 (1976).

[69] McEwan, A. D., "Degeneration of resonantly-excited standing internal gravity waves", J. Fluid Mech. **50**, 431–448 (1971).

[70] McEwan, A. D., "The kinematics of stratified mixing through internal wavebreaking", J. Fluid Mech. **128**, 47–57 (1983).

[71] McEwan, A. D., D. W. Mander and R. K. Smith, "Forced resonant second-order interaction between damped internal waves", J. Fluid Mech. **55**, 589–608 (1972).

[72] McEwan, A. D. and R. M. Robinson, "Parametric instability of internal gravity waves", J. Fluid Mech. **67**, 667–687 (1975).

[73] McLachlan, N. W., *Theory and Applications of Mathieu Functions* (Oxford Univ. Press, 1947).

[74] Mercader, I., O. Batiste and A. Alonso, "An efficient spectral code for incompressible flows in cylindrical geometries", Computers.& Fluids **39**, 2, 215 – 224 (2010).

[75] Miles, J. and D. M. Henderson, "Parametrically forced surface-waves", Annu. Rev. Fluid Mech. **22**, 143–165 (1990).

[76] Müller, H. W., H. Wittmer, C. Wagner, J. Albers and K. Knorr, "Analytic stability theory for Faraday waves and the observation of the harmonic surface response", Phys. Rev. Lett. **78**, 12, 2357–2360 (1997).

[77] Muthiyalu, N. and S. Usha, "Eigenvalues of centrosymmetric matrices", Computing **48**, 213–218 (1992).

[78] Oldeman, B. E., B. Krauskopf and A. R. Champneys, "Death of period-doublings: locating the homoclinic-doubling cascade", Physica D **146**, 100–120 (2000).

[79] Orlanski, I., "On the breaking of standing internal gravity waves", J. Fluid Mech. **54**, 577–598 (1972).

[80] Orlanski, I., "Trapeze instability as a source of internal gravity waves. Part I", J. Atmos. Sci. **30**, 1007–1016 (1973).

[81] Peyret, R., *Spectral methods for incompressible viscous flow*, vol. 148 of *Applied Mathematical Sciences* (Springer Science & Business Media, 2002).

[82] Peyret, R. and T. D. Taylor, *Computational methods for fluid flow* (Springer–Verlag Berlin Heidelberg, 1983), 1 edn.

[83] Rajchenbach, J. and D. Clamond, "Faraday waves: their dispersion relation, nature of bifurcation and wavenumber selection revisited", J. Fluid Mech. **777**, R2 (2015).

[84] Robinson, R. M. and A. D. McEwen, "Instability of a periodic boundary layer in a stratified fluid", J. Fluid Mech. **68**, 41–48 (1975).

[85] Ruby, L., "Applications of the Mathieu equation", Am. J. Phys. **64**, 39–44 (1996).

[86] Saad, Y., *Numerical Methods for Large Eigenvalue Problems* (SIAM, 2011), 2 edn.

[87] Schneider, T. M., J. F. Gibson, M. Lagha, F. De Lillo and B. Eckhardt, "Laminar-turbulent boundary in plane Couette flow", Phys. Rev. E **78**, 037301 (2008).

[88] Shankar, P. N. and M. D. Deshpande, "Fluid mechanics in the driven cavity", Annu. Rev. Fluid Mech. **32**, 93–136 (2000).

[89] Shen, J., T. Tang and L.-L. Wang, *Spectral Methods: Algorithms, Analysis and Applications*, vol. 41 of *Springer Series in Computational Mathematics* (Springer-Verlag Berlin Heidelberg, 2011), 1 edn.

[90] Sherman, F. S., J. Imberger and G. M. Corcos, "Turbulence and mixing in stably stratified waters", Annu. Rev. Fluid Mech. **10**, 267–288 (1978).

[91] Smale, S., "Differentiable dynamical systems", Bull. Amer. Math. Soc. **73**, 747–817 (1967).

[92] Staquet, C., "Gravity and inertia-gravity waves: breaking processes and induced mixing", Surveys in Geophys. **25**, 281–314 (2004).

[93] Staquet, C. and J. Sommeria, "Internal gravity waves: from instabilities to turbulence", Annu. Rev. Fluid Mech. **34**, 559–593 (2002).

[94] Strogatz, S. H., *Nonlinear Dynamics and Chaos* (Addison-Wesley, 2015), 2 edn.

[95] Sutherland, B., T. Dauxois and T. Peacock, "Internal waves in laboratory experiments", in "Modeling Atmospheric and Oceanic Flows: Insights from Laboratory Experiments and Numerical Simulations", edited by T. von Larcher and

P. D. Williams, Geophysical Monograph Series, chap. 10, pp. 193–212 (John Wiley & Sons, 2015).

[96] Sutherland, B. R., *Internal Gravity Waves* (Cambridge Univ. Press, 2010).

[97] Thorpe, S. A., "On standing internal gravity waves of finite amplitude", J. Fluid Mech. **32**, 489–528 (1968).

[98] Thorpe, S. A., "Observations of parametric instability and breaking waves in an oscillating tilted tube", J. Fluid Mech. **261**, 33–45 (1994).

[99] Trefethen, L. N., *Spectral methods in MATLAB* (SIAM, 2000).

[100] Tuckerman, L. S. and D. Barkley, "Bifurcation analysis for timesteppers", in "Numerical Methods for Bifurcation Problems and Large-Scale Dynamical Systems", edited by E. Doedel and L. S. Tuckerman, vol. 119 of *Volumes in Mathematics and its Applications*, pp. 453–466 (Springer, 2000).

[101] Turner, K. L., S. A. Miller, P. G. Hartwell, N. C. MacDonald, S. H. Strogatz and S. G. Adams, "Five parametric resonances in a microelectromechanical system", Nature **396**, 149–152 (1998).

[102] Vanel, J.-M., R. Peyret and P. Bontoux, "A pseudo-spectral solution of vorticity-stream function equations using the influence matrix technique", in "J. Numerical Methods for Fluid Dynamics II", edited by K. W. Morton and M. Baines, pp. 463–475 (Clarendon Press Oxford, 1986).

[103] von Kerczek, C. and S. H. Davis, "The instability of a stratified periodic boundary layer", J. Fluid Mech. **75**, 287–303 (1976).

[104] Weideman, J. A. and S. C. Reddy, "A matlab differentiation matrix suite", ACM TOMS **26**, 4, 465–519 (2000).

[105] Welfert, B. D., "Generation of pseudospectral differentiation matrices I", SIAM J. Numer. Anal. **34**, 1640–1657 (1997).

[106] Wright, J., S. Yon and C. Pozrikidis, "Numerical studies of two-dimensional Faraday oscillations of inviscid fluids", J. Fluid Mech. **402**, 1–32 (2000).

[107] Wu, K., B. D. Welfert and J. M. Lopez, "Complex dynamics in a stratified lid-driven square cavity flow", J. Fluid Mech. **855**, 43–66 (2018).

[108] Wunsch, C. and R. Ferrari, "Vertical mixing, energy, and the general circulation of the oceans", Annu. Rev. Fluid Mech. **36**, 281–314 (2004).

[109] Yalim, J., J. M. Lopez and B. D. Welfert, "Vertically forced stably stratified cavity flow: instabilities of the basic state", J. Fluid Mech. **851**, R6 (2018).

[110] Yalim, J., B. Welfert, J. Lopez and K. Wu, "Fluid flow in a vertically oscillating, stably stratified cubic cavity", in "Amer. Phys. Soc. Div. Fluid Dyn. 2017 Meeting Abstracts", p. L34.010 (2017).

[111] Yalim, J., B. Welfert, J. Lopez and K. Wu, "V0066: Resonant collapse in a harmonically forced stratified cavity", in "Amer. Phys. Soc. Div. Fluid Dyn. 2017 Gallery of Fluid Motion", (2017), https://doi.org/10.1103/APS.DFD.2017.GFM.V0066.

[112] Yalim, J., B. D. Welfert and J. M. Lopez, "Modal reduction of a parametrically forced confined viscous flow", submitted to Phys. Rev. Fluids (2019).

[113] Yalim, J., B. D. Welfert and J. M. Lopez, "Parametrically forced stably stratified cavity flow: complicated nonlinear dynamics near the onset of instability", accepted for publication in J. Fluid Mech. (2019).

[114] Yih, C.-S., "Gravity waves in a stratified fluid", J. Fluid Mech. **8**, 481–508 (1960).

[115] Zang, T. A., "On the rotation and skew-symmetric forms for incompressible flow simulations", **7**, 27–40 (1991).

APPENDIX A

CO-AUTHOR PERMISSIONS

I certify that my co-authors, Professor Juan M. Lopez, Professor Bruno D. Welfert, and Ke Wu, have given me permission, in writing, to include the all material in my PhD thesis for Chapter 2. I further certify that my co-authors, Professor Juan M. Lopez and Professor Bruno have given me permission, in writing, to include the all material in my PhD thesis for Chapters 3, 4, and 5.

APPENDIX B

LID-DRIVEN CAVITY FLOW IN THE CUBE

This appendix provides additional details to the Arnoldi iteration performed to conduct the linear stability analysis for the three-dimensional lid-driven cavity (Chapter 2). This technique resulted in the determining the critical Reynolds number $\mathrm{Re} = 2089$ for the secondary Hopf instability of the basic state, as well as the primary Hopf instability at $\mathrm{Re} = 1929$.

For a given Re, the steady state existed either as a stable or unstable solution to the governing equations (2.1), resulting in steady state velocity $\boldsymbol{u}_s$ and pressure p_s. Linearizing about this state with velocity perturbation $\boldsymbol{U}$ and pressure pertubation q results in the following linearized governing equations for the perturbations

$$\partial \boldsymbol{U}/\partial t + \boldsymbol{U} \cdot \nabla \boldsymbol{u}_s + \boldsymbol{u}_s \cdot \nabla \boldsymbol{U} = -\nabla q + \mathrm{Re}^{-1} \nabla^2 \boldsymbol{U}, \quad \nabla \cdot \boldsymbol{U} = 0. \tag{B.1}$$

Note that the pertubation boundary conditions are no-slip and homogeneous, even for the moving wall.

B.1 Linear Stability Analysis with Arnoldi Iteration

Arnoldi iteration is a commonly applied technique in numerical linear algebra to estimate the eigenvalues and eigenvectors of a matrix A. It is essentially an improved power iteration method, combining Gram-Schmidt orthogonalization with power iteration. This results in convergence to the leading eigenpairs for sufficiently large Krylov-subspace dimension. For a good background on the technique, see [50, §2.3.1.2] or [51]. From those work, the Arnoldi iteration is,

$$MU_k = U_k H_k + \boldsymbol{r}_k \hat{\boldsymbol{e}}_k^T, \tag{B.2}$$

where M is the action of the linearized Navier-Stokes equations over a time-window t_h, U_k is the iteratively obtained set of fields, H_k is an upper Hessenberg matrix, and $\boldsymbol{r}$ is a residual vector. An outline of implementation steps is presented below:

1. Take a basic state solution as input for the linearization.
2. Create a uniformly random perturbation of mean 0 and order 10^{-8} as the initial condition, u_0.
3. Evolve u_0 for some time leading to transient state u_1.
4. Store $u_1/||u_1||_2$ as q_0.
5. For $k \in [1, N]$,
   (a) Evolve q_{k-1} for t_h to v_k.
   (b) Set $du_k = v_k$.
   (c) Orthonormalize du_k to set of existing q.
   (d) Let $H'_{jk} = (q_j, du_k)$ for $j \in [0, k]$.

6. Compute eigenvalues of H, λ_j, such that H is H' with its last row removed.
7. $\lambda_j = \log(\lambda_j)/t_h$

The previous timestep velocity states are set equal to the current timestep velocities at the beginning of each iteration (i.e., $u(t_{-1}) = u(t_0)$), as is prescribed by the semi-implicit linear multistep method adopted from [35].

Also, the choice of t_h is very important. Due to Nyquist's theorem, any signals being approximated will be aliased if not properly sampled. Thus, modes with periods over two times the time window will be aliased. For the application here, the Krylov subspace had dimension $m = 96$, and the time-window was chosen to be 2×10^{-3} viscous times long, which provided a sufficiently large period to capture the dynamics of the leading order modes. This time-window was discretized into 10^3 timesteps.

Note that running a Gram-Schmidt process on the resultant H prior to computing the eigenspace may be prudent for improving numerical accuracy.

It's important to note that a nonlinear implementation of this method was also applied: rather than solving the linearized Navier-Stokes about the basic state, the nonlinear governing equation (2.1) was instead integrated with the steps outlined above. Remarkably, the nonlinear technique resulted in a nearly identical leading spectrum relative to the linearized method. However, the corresponding eigenvectors obtained with the nonlinear technique were polluted and far from converged.

Figure 2.9 demonstrates the spectral results of the linearized Arnoldi implementation. As Re increases, it becomes unstable through a Hopf bifurcation to LC1 at Re = 1929 and then unstable through another Hopf to LC2 at Re = 2089. Figures 2.20 and 2.21 illustrate components of the eigenvector associated to the instability at Re = 2089. Utilizing direct numerical simulation (DNS), specifically with the edge state technique (EST) detailed in Chapter 2, the subcritical aspect of these bifurcations was then resolved.

APPENDIX C

VERTICALLY FORCED STABLY STRATIFIED CAVITY FLOW: INSTABILITIES OF THE BASIC STATE

This appendix provides additional details to the Floquet analysis performed to conduct the linear stability analysis for the two-dimensional vertically forced cavity confining a stably stratified fluid (Chapter 3). This technique resulted in the determination of neutral curves for the basic state in parameter space.

C.1 Symmetry

The basic state is given by equation (3.2), which is recalled here

$$\boldsymbol{u} = 0, \quad T = z, \quad \text{and} \quad P = 0.5z^2[1 + \alpha\cos(\omega t)],$$

and the governing equations linearized about the basic state are given by recalled equation (3.3):

$$\begin{aligned}
\frac{\partial \boldsymbol{u}}{\partial t} &= -\nabla p + \frac{1}{R_N}\nabla^2\boldsymbol{u} + [1 + \alpha\cos(\omega t)]\theta\boldsymbol{e}_z, \quad \nabla\cdot\boldsymbol{u} = 0,\\
\frac{\partial \theta}{\partial t} &= \frac{1}{\sigma R_N}\nabla^2\theta - w,
\end{aligned}$$

where $p = P - 0.5z^2[1+\alpha\cos(\omega t)]$ is the perturbation pressure, $\theta = T - z$ is the perturbation temperature, and $\boldsymbol{u}$ is the velocity perturbation away from zero. The boundary conditions are no-slip for $\boldsymbol{u}$ on all walls, no-flux on the sidewalls $\partial\theta/\partial x|_{x=\pm 0.5} = 0$, and $\theta = 0$ on the top and bottom endwalls. The linearized system is invariant to the symmetries,

$$\mathcal{K}_x(u, w, p, \theta)(x, z, t) = (-u, w, p, \theta)(-x, z, t), \tag{C.1}$$
$$\mathcal{K}_z(u, w, p, \theta)(x, z, t) = (u, -w, p, -\theta)(x, -z, t), \tag{C.2}$$
$$\bar{\mathcal{K}}_x(u, w, p, \theta)(x, z, t) = (u, -w, -p, -\theta)(-x, z, t), \tag{C.3}$$
$$\bar{\mathcal{K}}_z(u, w, p, \theta)(x, z, t) = (-u, w, -p, \theta)(x, -z, t), \tag{C.4}$$

where $\bar{\mathcal{K}}_x$ and $\bar{\mathcal{K}}_z$ are not symmetries of the nonlinear governing equations. Further, the compositions and implied commutations of the four reflections results in the operators

$$\begin{aligned}
\mathcal{R}_\pi &:= \mathcal{K}_x \circ \mathcal{K}_z = \bar{\mathcal{K}}_x \circ \bar{\mathcal{K}}_z,\\
\bar{\mathcal{R}}_\pi &:= \mathcal{K}_x \circ \bar{\mathcal{K}}_z = \bar{\mathcal{K}}_x \circ \mathcal{K}_z,
\end{aligned}$$

which are associated with reflections by π of the flow. Again, note that $\bar{\mathcal{R}}_\pi$ is not a symmetry of the nonlinear governing equations (the nonlinear advection term breaks the bar-conjugate-symmetries). Also, note that the system in the inviscid limit is additionally invariant to a time reversal symmetry,

$$\mathcal{T}(u, w, p, \theta) = (-u, -w, -p, \theta)(-x, -z, -t),$$

that (reflexively) diffusion breaks. The inviscid (and infinitely degenerate) eigenmodes provided by Thorpe [97] satisfied all of these symmetries, whereas the viscous

modes discovered here do not have time reversal invariance, but do possess the bar-conjugate-symmetries. This is emphasized as the nonlinear governing equations of Chapter 5 do not satisfy the bar-symmetries and neither do the observed nonlinear modes.

C.2 Implementation

As discussed in Chapter 3, a linear stability analysis study was performed on system (3.3) with buoyancy number $R_N \in [10^3, 10^6]$ by performing a Floquet analysis using the linearized Poincaré map $\mathcal{P}$. The monodromy matrix A was constructed directly and in full.

Instabilities (modes with multiplier of magnitude greater than unity) were first estimated automatically, and then verified manually. Classification becomes an extremely tedious manual verification and estimation process for the larger R_N, which also require denser discretizations of the parameter space.

The study was conducted in the following manner: for a given R_N number and forcing frequency ω, a monodromy matrix A would be obtained for each forcing amplitude α in the discretized interval $[a, b]$. The eigenspectrum $(\mu, \boldsymbol{v})$ of A would then be analyzed by isolating multipliers μ that crossed the unit circle. The critical forcing amplitude α_C that the basic state would lose stability to mode $\boldsymbol{v}$ was then estimated with linear interpolation.

In practice, ω and α were discretized with resolution 0.01, $\omega \in [1.33, 1.48]$ and $\alpha \in [0, 0.50]$ for most R_N. An approximately constant timestep was used of $\delta t = (2\pi/1000) \cdot \lfloor \omega/1.41 \rfloor$, so that near the tip of the 1:1 resonance tongue there would be 1000 timesteps per forcing period. Space was discretized using Chebyshev polynomials of no less than degree 32 or no more than degree 96 in both the x and z directions, and the Floquet analysis was performed for the three fields, u, w, and T, resulting in a monodromy matrix $A \in \mathbb{R}^{3(M+1)^2, 3(M+1)^2}$ for each point in the discretized parameter space (the meshsize was dependent on the size of R_N, as larger R_N resulted in thinner boundary layers, requiring more resolution). Then, after computing the eigenpairs of A and taking a verification snapshot of its spectrum, the leading sixteen μ on the negative real axis (by magnitude) were parsed and stored along with their corresponding modes $\boldsymbol{v}$. Other eigenpairs of A were ignored because (a) they were stable, (b) as figure C.1 illustrates sixteen modes provided sufficient detail, and (c) Floquet multipliers were only observed to leave the unit circle through ± 1.

The sixteen saved eigenpairs were then sorted by magnitude of the eigenvalue and the corresponding eigenvector's T was parsed and $T_x = \partial T/\partial x$ was computed, plotted, and saved (derivative computed with the Chebyshev collocation method as in the numerical scheme [99, §6]). The integer mode vector $m{:}n$ for T was also estimated for multipliers just before and after crossing the unit circle through ± 1. The estimation was done by projecting the T field onto the first order perturbation

temperature modes $\boldsymbol{\Theta}$ derived by [97], with $(X, Z) \in [0, \pi]^2$

$$\Theta_{m:n}(X, Z) = B\, \cos(mX) \sin(nZ),$$

where B is a wave amplitude. The projection coefficients for the basis transformation are given by,

$$c_{m:n} = \frac{(T, \Theta_{m:n})}{||\Theta_{m:n}||^2},$$

with L_2 inner product on $[-1, 1]^2$ defined as $(q, v) = \iint q \cdot v \, d\boldsymbol{x}$ for arbitrary real fields q, v. Since space is defined on a Chebyshev-Gauss-Lobatto grid, the L_2 inner product was estimated with the Clenshaw-Curtis quadrature. The unstable mode was associated with the $m{:}n$ of the corresponding absolute maximum projection coefficient $c_{m:n}$.

For a given R_N and ω, when a multiplier μ crossed the unit circle its critical forcing amplitude α_C was estimated through linear interpolation, i.e. by solving for ± 1 with the two nearest α and μ pairs before and after the bifurcation. Due to the size of the spectrum, tracking the multipliers for each observed mode was difficult. The leading sixteen eigenpairs along the positive and negative real axis were stored in separate compressed files (multipliers were only observed to leave the unit circle through ± 1). These signed and real eigenpairs were then sorted by multiplier magnitude which increased tractability, but the mode $\boldsymbol{v}$ prior to and post bifurcation required verification. For the vast majority of the presented cases this was a clean and efficient process and the selected eigenpairs would not be greatly affected by the sorting. That is, the leading eigenpair prior to bifurcation would remain leading post bifurcation. However, it was observed that two conditions needed to be met for the automation to not need manual correction:

(a) (anchor condition) the discretization of α was sufficient so that the bifurcating mode's multiplier was observed on the real axis prior to bifurcation,

(b) (degeneracy condition) the (R_N, ω, α) basic state would only lose stability to a single mode or its harmonics.

In general, condition (a) may seem to be a linear interpolation issue–at least two data pairs are necessary. More subtly, the anchor condition is necessary to decrease pollution from the estimation of α_C. The observed behavior of the multiplier was only linear within a neighborhood of the multiplier sufficiently distant from where it first spawned on the real axis. This implies that there is significant curvature near the collision point. As R_N increased, the noncritical magnitude of the complex conjugate pairs also increased. Thus when the high R_N pairs rotated toward the real axis with increasing α, they'd spawn into the real axis relatively close to unity. Without a sufficiently dense α discretization, the real-axis eigenpairs would be more likely to catch a bifurcated mode only after bifurcation, where the nearly linear behavior has saturated.

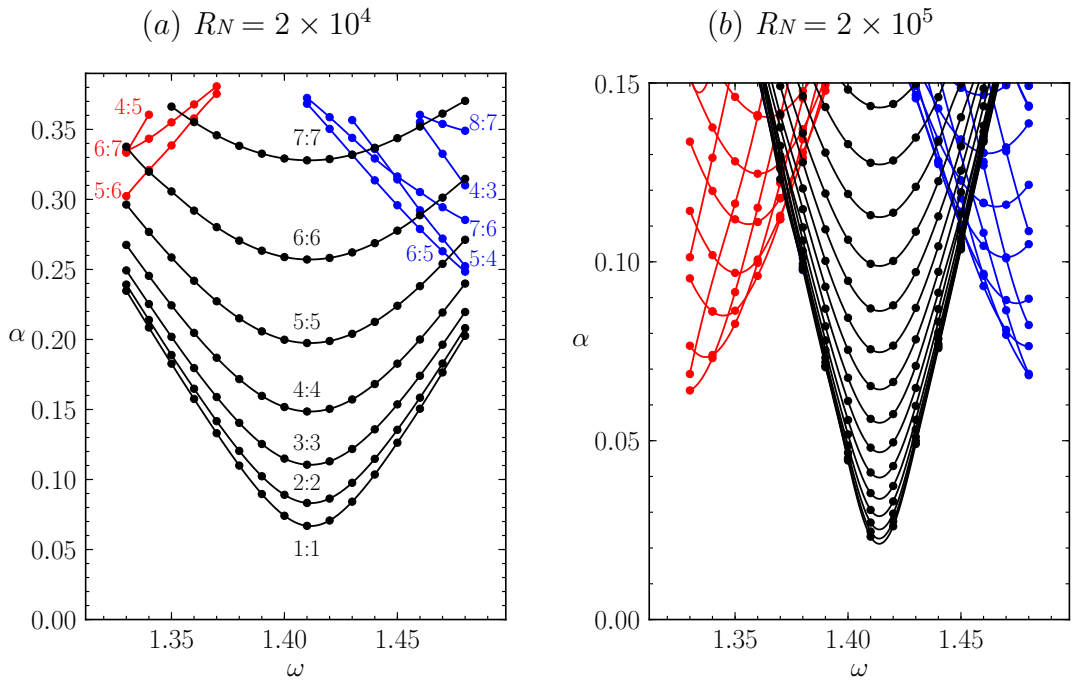

Figure C.1: Linear stability analysis results of the basic state for the buoyancy number indicated. The curves are the approximate locus instability of the basic state to the indicated m:n mode. Note the different y-axis scales for the two plots–the basic state for $R_N = 2 \times 10^4$ requires a larger α relative to $R_N = 2 \times 10^5$.

Figure C.1 demonstrates the complications of the process. Note that a resonance tongue begins to overlap with neighboring resonance tongues the further away from the tongue minimum and the higher the larger the forcing amplitude.

C.3 Spectral Convergence

Figure C.2 shows the spectra of the Monodromy matrix for $\omega = 1.41$ and $\alpha = 0.25$ for various discretizations (Chebyshev polynomials of degree 16 to 96). By $M = 20$ the leading (unstable) spectra are well converged (to four decimal places) and by $M = 64$ the visual spectra are as well.

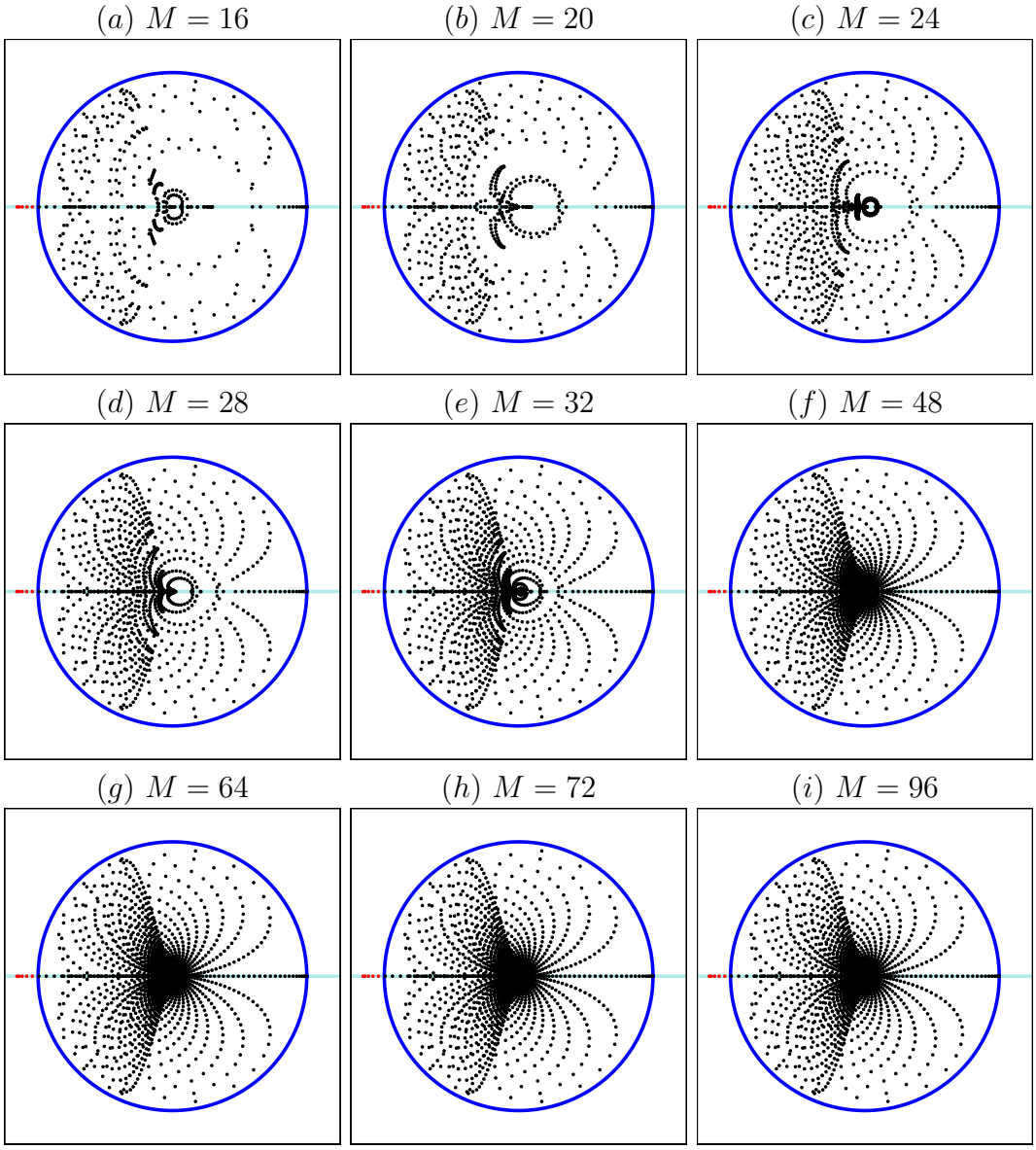

Figure C.2: Floquet multipliers for $(R_N, \omega, \alpha) = (2 \times 10^4, 1.41, 0.250)$ at the Chebyshev polynomial degree indicated. Unit circle in blue, real axis in light blue, and the five unstable multipliers with magnitude greater than one in red.

APPENDIX D

MODAL REDUCTION OF A PARAMETRICALLY FORCED CONFINED VISCOUS FLOW

This is a supplementary appendix containing appendices that were submitted to be published [112].

Supplement

The estimated value of the first ten coefficients $\mu_\ell \approx \alpha_\ell Q_{1:1}^{-1/\ell}$, using α_ℓ measured from the ten tongues visible in Fig. 4.3(a) and $Q_{1:1} \approx 2.8 \times 10^{-3}$ for mode 1:1 at $(R_N, \sigma) = (2 \times 10^4, 1)$, are listed in Table D.1. The value $\mu_1 = 2.00$ relating the minimal critical amplitude α to the friction coefficient c at the principal 1:1 tongue is well-known, for example see [19, p. 1256]. This factor leads in particular to the increased estimate

$$F2 = 2.00 \left(\frac{2Q}{\Omega} \right) = \frac{4Q}{\Omega} \approx 0.077$$

rather than $F2 \approx 0.045$ in [7, Fig. 8], at $\Omega \approx \Omega_e/2 = 2\pi f_e/2 \approx 0.432\pi \approx 1.36$ Hz, where $F2$ denotes the minimal forcing amplitude (α) for instability of the 1:1 mode, $2Q = 0.052$ Hz is the friction coefficient, and Ω represents the natural angular frequency of the undamped unforced oscillator.

ℓ	1	2	3	4	5	6	7	8	9	10
μ_ℓ	2.00	2.00	1.84	1.72	1.63	1.55	1.49	1.45	1.41	1.38

Table D.1: μ_ℓ vs. ℓ for mode 1:1.

The Rayleigh quotients (4.10) were evaluated for viscous Floquet modes $(w_{\boldsymbol{k}}, \theta_{\boldsymbol{k}})$ for $\boldsymbol{k} = m{:}m$ with $1 \le m \le 8$ at or close to the tip of the corresponding tongues (these modes were computed in [109] at $(R_N, \sigma) = (2 \times 10^4, 1)$). The results yield the fits

$$\frac{(\nabla^2 w_{\boldsymbol{k}}, w_{\boldsymbol{k}})}{(w_{\boldsymbol{k}}, w_{\boldsymbol{k}})} \approx \delta_{\boldsymbol{k}} \left(1 + \frac{14}{2m^2} \right) \quad \text{and} \quad \frac{(\nabla^2 \theta_{\boldsymbol{k}}, \theta_{\boldsymbol{k}})}{(\theta_{\boldsymbol{k}}, \theta_{\boldsymbol{k}})} \approx \delta_{\boldsymbol{k}} \left(1 + \frac{1}{2m^2} \right), \tag{D.1}$$

suggesting the form of the second factor in (4.11). Note however that the value $\gamma = 20$ used in Fig. 4.4 is larger than the values $\gamma = 14$ or $\gamma = 1$ in (D.1).

The action of $\mathcal{L}$ on the viscous modes $\theta_{\boldsymbol{k}}$ can be quantified using a Rayleigh quotient

$$\frac{(\mathcal{L}\theta_{\boldsymbol{k}}, \theta_{\boldsymbol{k}})_{-\nabla^2}}{(\theta_{\boldsymbol{k}}, \theta_{\boldsymbol{k}})_{-\nabla^2}} = \frac{(-\nabla^2 \mathcal{L}\theta_{\boldsymbol{k}}, \theta_{\boldsymbol{k}})}{(-\nabla^2 \theta_{\boldsymbol{k}}, \theta_{\boldsymbol{k}})} = \frac{(-\partial_{xx}\theta_{\boldsymbol{k}}, \theta_{\boldsymbol{k}})}{\|\nabla \theta_{\boldsymbol{k}}\|^2} = \frac{\|\partial_x \theta_{\boldsymbol{k}}\|^2}{\|\nabla \theta_{\boldsymbol{k}}\|^2}. \tag{D.2}$$

In the inviscid limit, this quotient reduces to $\lambda_{\boldsymbol{k}} = m^2/(m^2 + n^2)$ for Floquet mode $\boldsymbol{k} = m{:}n$. Viscous effects were evaluated on the modes obtained from Floquet analysis at various forcing frequencies ω for the case $(R_N, \sigma) = (2 \times 10^4, 1)$. Figure D.1 shows the deviation of the Rayleigh quotients, scaled by $\lambda_{\boldsymbol{k}}$, from unity (dots), together with a fit $(\omega/\sqrt{2})^{-4/3}$. In particular, $\lambda_{\boldsymbol{k}}$ underestimates (overestimates) $\mathcal{L}$ for $\omega < \sqrt{2}$

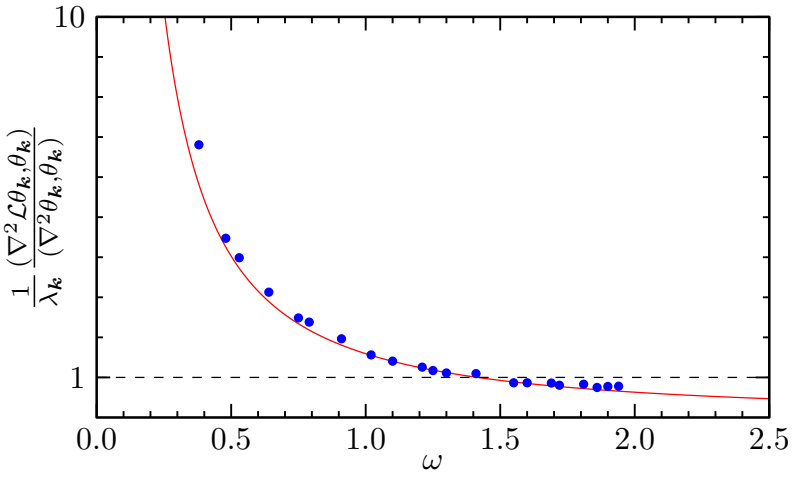

Figure D.1: Scaled operator $\mathcal{L}/\lambda_{\boldsymbol{k}}$ applied to viscous Floquet mode $\theta_{\boldsymbol{k}}$ vs. forcing frequency ω, together with the fit $(\omega/\sqrt{2})^{-4/3}$.

$(\omega > \sqrt{2})$ corresponding to modes $\boldsymbol{k}$ with $m < n$ $(m > n)$. This discrepancy causes a small detuning towards the frequency $\omega = \sqrt{2}$, which is clearly visible at lower ω in Figs. 4.4 and 4.5, of the modal tongues compared to the Floquet critical curves.

APPENDIX E

PARAMETRICALLY FORCED STABLY STRATIFIED CAVITY FLOW

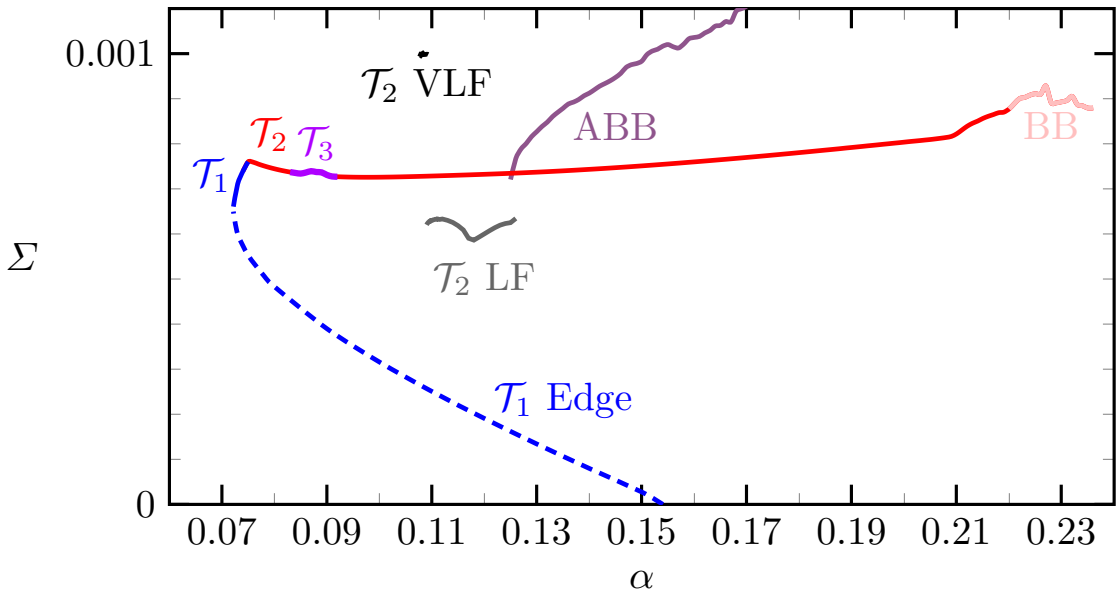

Figure E.1: Standard deviation of the kinetic energy Σ for $\omega = 1.36$ observed states.

This appendix includes additional nonlinear results.

E.1 Additional Nonlinear Results

The results obtained for $\omega = 1.36$ were the most comprehensive for the states not already included in Chapter 5. In figure E.1, the response of these states is illustrated. The 1-torus T_1, 2-torus T_2, and 3-torus T_3 were already discussed in detail within Chapter 5. However, the 2-torus T_2LF and T_2VLF as well as the chaotic BB, and ABB states are shelved nonlinear responses. The T_2VLF is a very low frequency 2-torus that takes exactly 94 forcing periods to complete a cycle when phase-locked, and is remarkably illustrated in figure E.2(a)–the phase-locked flow regularly wave-breaks. The T_2LF is a low frequency 2-torus that takes exactly 14 forcing periods to cycle when phase-locked, suggesting a 1–7 resonance with the forcing (note that the primary response frequency is subharmonic, resulting in the factor of 2), and is illustrated in figures E.2(c) and E.3(c) (phase-locked in latter). A relatively large portion of the observed loci of stability for these states corresponded to being phase-locked. The chaotic flows were either observed to be pointwise-$\mathcal{R}_\pi$ symmetric (BB) or not (ABB). The ABB is illustrated in figure E.3(a).

The stability of the $\mathcal{G}$ symmetric subspace is also investigated. Figure E.4 overlays the flip, fold, and Neimark-Sacker loci for the subspace with those obtained from the full space. The instabilities of subspace are qualitatively the same as the full space but at larger α_C. Note that the flip bifurcation aligns well with the Floquet results obtained in Chapter 3.

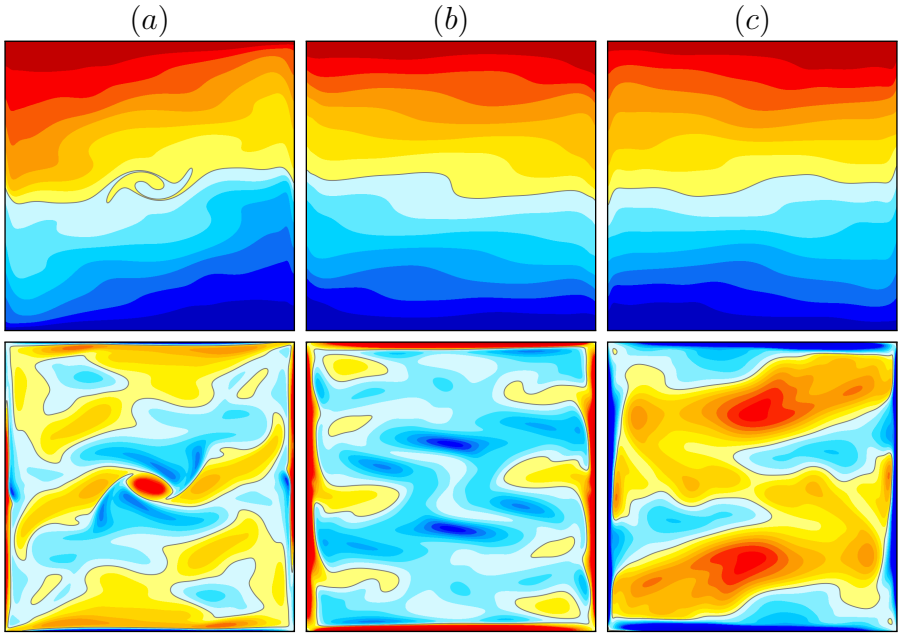

Figure E.2: Snapshots of the isotherms and vorticity at $\omega = 1.36$ illustrating three states (a) T_2VLF at $\alpha = 0.10895$ $t = 33.72$, (b) T_2 at $\alpha = 0.109$ $t = 7.25$, and (c) T_2LF at $\alpha = 0.1095$ $t = 10.25$, where t is the time in number of forcing periods. The QPVLF state is phase locked and takes 94 forcing periods to complete a cycle.

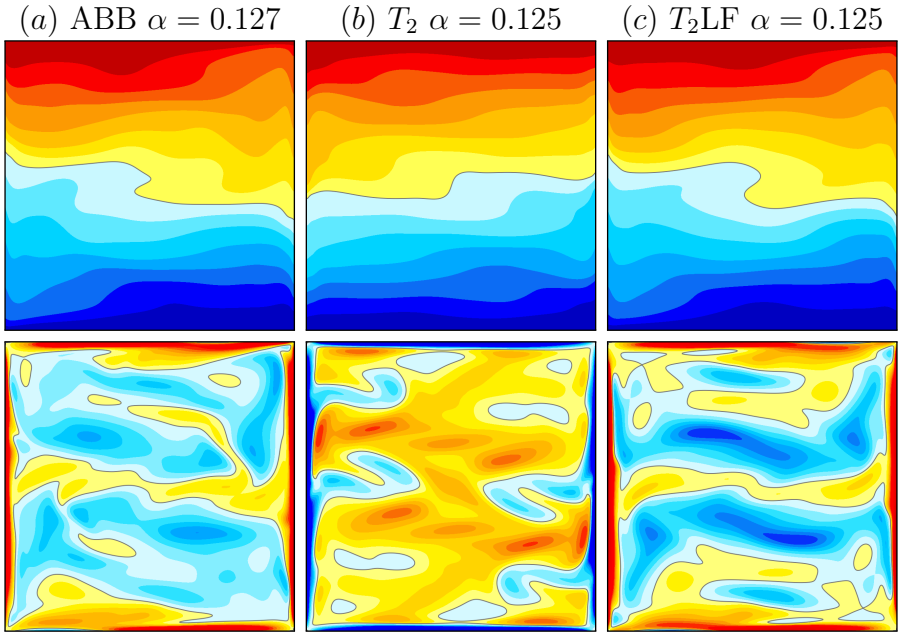

Figure E.3: Snapshots of the isotherms and vorticity at $\omega = 1.36$ illustrating the three states at times (a) $t = 1.25$, (b) $t = 2.25$, and (c) $t = 7.25$, The T_2LF state is phase locked and takes 14 forcing periods to complete a cycle.

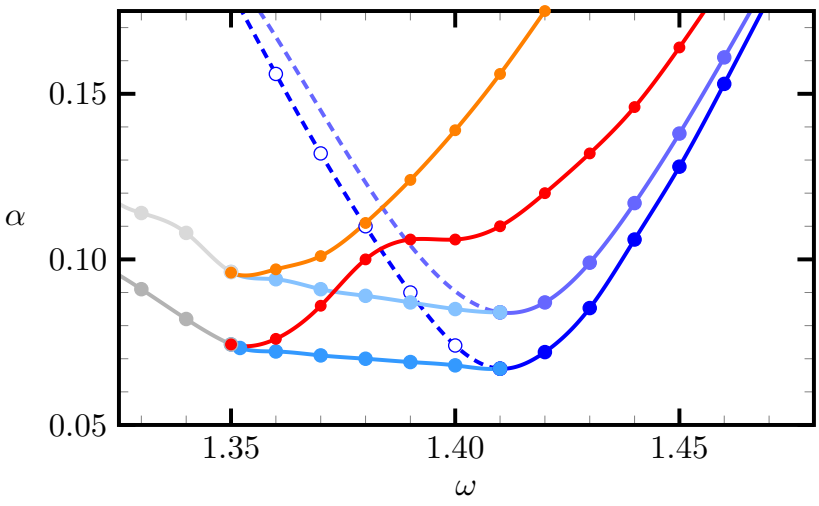

Figure E.4: Stability curves for the full space and $\mathcal{G}$ symmetric subspace. Loci were obtained with quasi-static continuation for fixed ω and decreasing α in the respective spaces. Only the fold, flip, and Neimark–Sacker curves are illustrated.

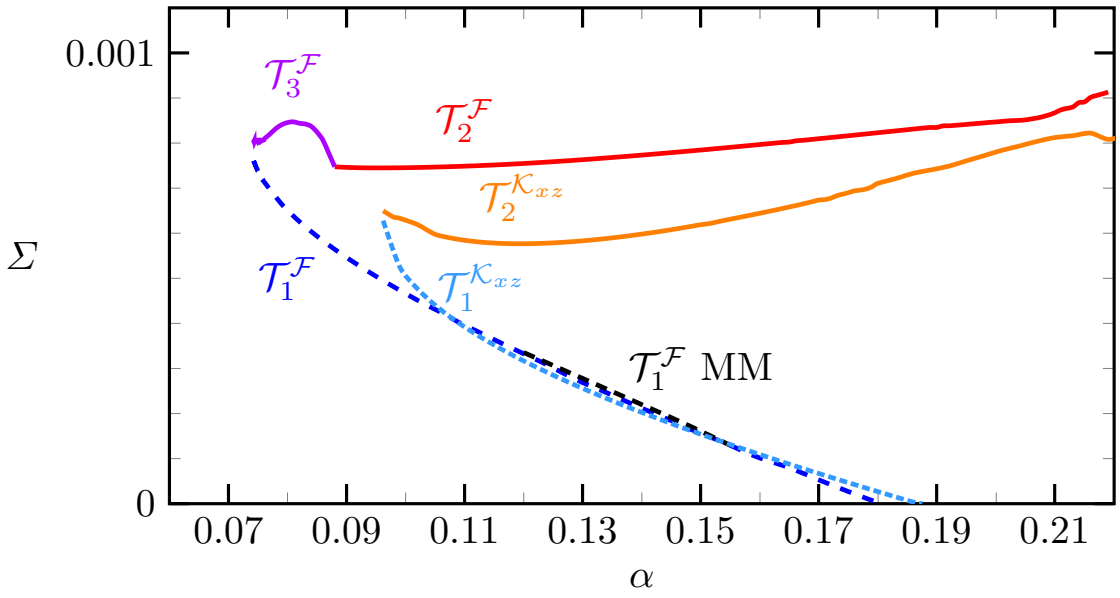

Figure E.5: Standard deviation of the kinetic energy for $\omega = 1.35$ observed states. The superscript of $\mathcal{F}$ implies a full space result, where as the superscript of $\mathcal{K}_{xz}$ indicates a $\mathcal{G}$ subspace result.

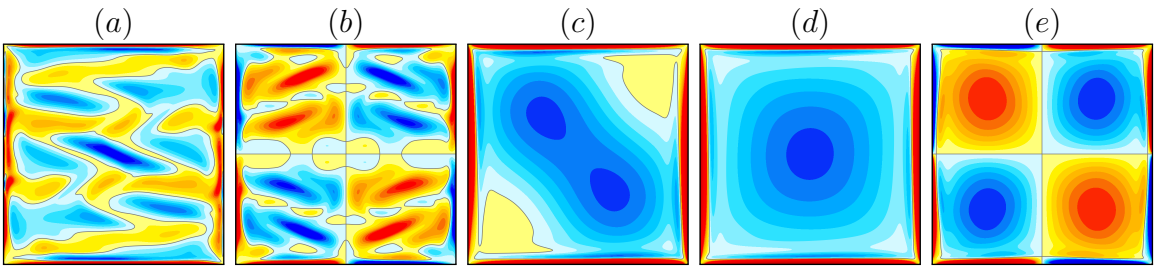

Figure E.6: Snapshots of the vorticity at $(\omega, \alpha) = (1.35, 0.145)$ illustrating the five observed states (a) a full space stable T_2, (b) a $\mathcal{G}$ subspace stable T_2, (c) a full space unstable mixed mode T_1 of the 1:1 and 2:2, (d) a full space unstable 1:1 T_1, and (e) a $\mathcal{G}$ subspace unstable 2:2 T_1. The full space states are shown at forcing phase 0, whereas the $\mathcal{G}$ symmetric subspace states are shown at forcing phase π. The magnitude of Σ decreases from left to right.

The bifurcation diagram E.5 for $\omega = 1.35$ illustrates the some of the dynamics of the full space as well as the $\mathcal{G}$ symmetric subspace. Besides the trivial basic state, the only stable state in the full space is a quasiperiodic flow that retains its $\mathcal{R}_\pi$ symmetry over the examined forcing amplitude interval. For $\alpha \in (0.088, 0.204]$ the flow is nicely characterized by this description although it experiences phase locking in several short amplitude sub-intervals. For $\alpha > 0.204$ the flow becomes chaotic, and for $\alpha \in [0.074\,318, 0.088]$ a low frequency sets in and goes to infinite period as α decreases. The frequency-response of the quasiperiodic flow is nicely summarized by figure E.7. Using this quasiperiodic state and the basic state as an initial conditions, EST was able to obtain the unstable 1:1 limit cycle edge state which was observed for $\alpha \in [0.074\,318, 0.018]$.

By restricting to the $\mathcal{G}$ symmetric subspace, we obtained the quasiperiodic stable state which behaved similarly to the full space quasiperiodic state with infinite period growth near the cyclic fold, phase locking, and broadband behavior. Using the $\mathcal{G}$ quasiperiodic solution and the basic state as initial conditions, EST was again utilized to obtain the unstable 2:2 limit cycle edge state, which was observed for $\alpha \in [0.0962, 0.187]$.

Finally, by using the full space T_2 and $\mathcal{G}$ symmetric subspace T_2 as initial conditions, EST was employed in the full space to obtain an unstable T_1 of the spatially mixed 1:1 with 2:2 mode. This mode was well described in Chapter 5, where it was observed to be asymptotically stable after a setwise-symmetry breaking pitchfork bifurcation. All of these states are shown in figure E.6.

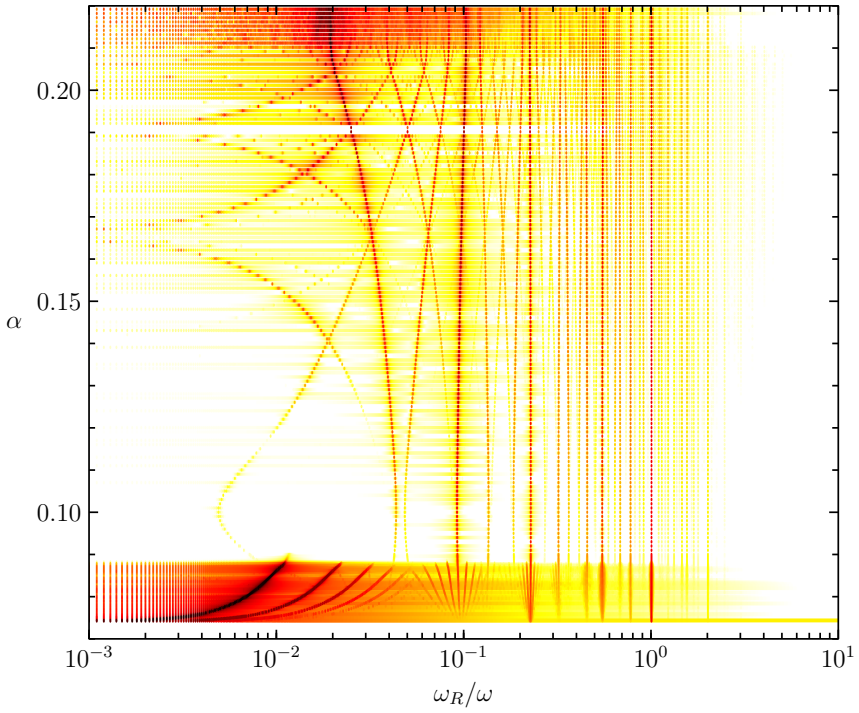

Figure E.7: Spectogram of the E_T timeseries data for $\omega = 1.35$, with colormap set to normalized response power. The response frequency ω_R was normalized by the input frequency ω, and response power was normalized globally by the strongest response. Any response less than 10^{-5} in normalized power was set to zero.

The spectogram in figure E.7 for $\omega = 1.35$ shows how the full space 2-torus T_2 would become phase-locked. Also, it nicely illustrates the very low frequency going to zero for the 3-torus T_3 as α approached the first T_3 state. It is important to note that the fold bifurcation was not observed for $\omega = 1.35$ as the T_3 is the first nontrivial state captured. This frequency is beyond the fold-Neimark–Sacker point, and what happens in the neighorhood of that first T_3 is a homoclinic doubling cascade (this is well discussed in Chapter 5).

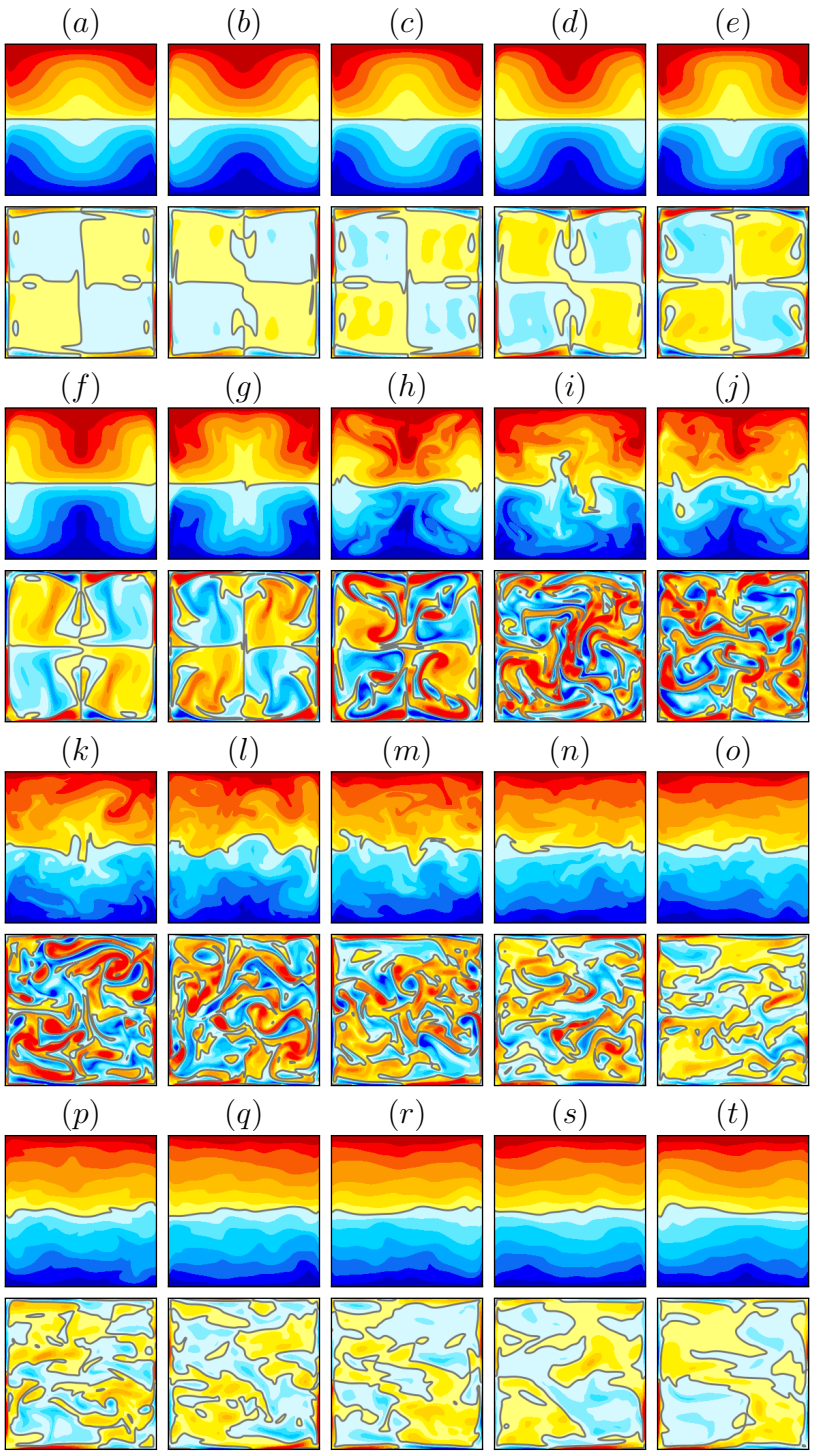

Figure E.8: Temperature and vorticity at phase $\pi/2$ in the forcing for $(\omega, \alpha) = (1.3, 0.3)$. Each labeled column is one forcing period away from the previous, with the isotherms in the first row and the vorticity in the second row of the subfigure.

Finally, figure E.8 illustrates what happens in general for sufficiently large forcing amplitudes, especially on the subcritical side of a resonance tongue. In this regime, the only observed modes are transient and are unstable. The basic state, while still a solution of the system, is unstable to perturbations which develop into parametrically resonated m:n modes. These modes eventually saturate, but the level of forcing is so strong that they violently undergo symmetry breaking via internal wave breaking. These events lead to Rayleigh-Taylor like instabilities that are associated with an exponential decay in the kinetic energy. The flow will relaminarize to various m:n modes of the system, but these undergo parametric resonance and the process intermittently repeats. The dynamics may be explained as was in [60]–saddle states are observed in abundance and the observed flow simply bounces from one to the next. For the flow depicted in figure E.8, the slightly perturbed basic state was used as an initial condition, which transitioned to a transient 2:2 mode. Figure E.8(a) shows the initial transient 2:2 near peak kinetic energy, and the remaining panels follow the flow through the violent pointwise-symmetry breaking.

E.2 Supplementary Material Information

This section contains information on the supplementary material for Chapter 5.

movie-fig503

Animation of the vorticity η of three limit cycle states corresponding to figure 5.3 over one response period (two forcing periods). The three limit cycles are $L_{1:2}$ at forcing frequency $\omega = 0.91$ with forcing amplitude $\alpha = 0.16$, $L_{1:1}$ at $\omega = 1.41$ with $\alpha = 0.07$, and $L_{2:1}$ at $\omega = 1.81$ with $\alpha = 0.06$.

movie-fig514

Animation corresponding to figure 5.14, illustrating how the local and global strobe maps of the flow at forcing frequency $\omega = 1.35$ vary with forcing amplitude α. Demonstrates the homoclinic doubling cascade as α is decreased.

movie-fig515

Animation of the isotherms T (first row) and vorticity η (second row) of the four indicated limit cycles over two forcing periods at forcing frequency $\omega = 1.41$. The limit cycles shown are $L_{1:1}$ at forcing amplitude $\alpha = 0.07$ (first column), L_L at $\alpha = 0.105$ (second column), L_R at $\alpha = 0.105$ (third column), and $L_{2:2}$ at $\alpha = 0.105$ (fourth column). Corresponds to figure 5.15.

movie-fig516

Animation of the isotherms T (left column) and vorticity η (right column) for the S_2 state at $(\omega, \alpha) = (1.41, 0.111)$ over six forcing periods. Obtained by restricting the direct numerical simulation to the $\mathcal{K}_z$ symmetry subspace. Corresponds to figure 5.16.

movie-fig518

Animation summarizing the dynamics observed in the $\mathcal{R}_\pi$ symmetry subspace as an indicated forcing amplitude α is increased by 0.01 for fixed forcing frequency $\omega = 1.41$, with the variance of a horizontal velocity at a point Σ (first row, first column), the number of forcing periods ω/ω_R associated with the slow response of the 2-tori states (second row, first column), and the associated strobe map sampling a horizontal velocity at a point u_p and a global measure of the temperature E_T every two forcing periods at forcing phase π (second column). Corresponds to figure 5.18.

movie-fig520

Animation of the strobe maps of a horizontal velocity at a point with a global measure of the temperature (u_p, E_T) and strobed vorticity η of Q_L, Q_R, and Q at fixed forcing frequency $\omega = 1.41$ and indicated forcing amplitude α near the first gluing. Q_L and Q_R are shown at $\alpha = 0.125$, and Q is shown at $\alpha = 0.126$. The strobe is taken every two forcing periods at forcing phase π. Corresponds to figure 5.20.

movie-fig522

Animation of the strobe maps of a horizontal velocity at a point with a global measure of the temperature (u_p, E_T) and strobed vorticity η of Q, Q_L, and Q_R at fixed forcing frequency $\omega = 1.41$ and indicated forcing amplitude α near the second gluing. Q is shown at $\alpha = 0.135$, while Q_L and Q_R are shown at $\alpha = 0.136$. The strobe is taken every two forcing periods at forcing phase π. Corresponds to figure 5.22.

movie-fig524

Animation of the strobe maps of a horizontal velocity at a point with a global measure of the temperature (u_p, E_T) and strobed vorticity η of Q_L, Q_R, and Q_B at fixed forcing frequency $\omega = 1.41$ and indicated forcing amplitude α near the third gluing. Q_L and Q_R are shown at $\alpha = 0.146$, and Q_B is shown at $\alpha = 0.147$. The strobe is taken every two forcing periods at forcing phase π. Corresponds to figure 5.24.

movie-fig526

Animation summarizing the upper-branch dynamics observed in the full space as an indicated forcing amplitude α is increased by 0.01 for fixed forcing frequency $\omega = 1.41$, with the variance of a horizontal velocity at a point Σ_u (first row, first column), the number of forcing periods ω/ω_R associated with the slow response of the 2-tori and 3-tori states (second row, first column), and the associated strobe map sampling a horizontal velocity at a point u_p and a global measure of the temperature E_T every two forcing periods at forcing phase π (second column). Corresponds to figure 5.26.

movie-fig527

Animation comparing strobed full space dynamics of Q_R (left column) and T_{3R} (right column) at forcing frequency $\omega = 1.41$ and forcing amplitude $\alpha = 0.138$ with a two forcing period strobe map of a horizontal velocity at point and a global measure of the temperature (u_p, E_T) at forcing phase π (first row) and the strobed vorticity η (second row). Corresponds to figure 5.27.